Characterisation of exoplanetary atmospheres

from target selection to feature recognition using deep learning

Tiziano Zingales

Submitted for the degree of **Doctor of Philosophy**

Department of Physics and Astronomy

University College London

December 3, 2018

I, *Tiziano Zingales*, confirm that the work presented in this thesis is my own.

Where information has been derived from other sources, I confirm that this has been indicated in the thesis.

Abstract

On the day of writing this thesis, we know about 4000 exoplanets beyond the Solar System. We have a wide variety of known exoplanets, from very hot giant planets to cold Earths. Planetary detections, nevertheless, are not enough to thoroughly investigate the history and chemistry of the exoplanets. For this reason, atmospheric characterisation is becoming more critical than ever in exoplanetary science. In the next decade, many space missions such as JWST, Twinkle, ground-based instruments (ELT, TMT), and ARIEL, will study spectroscopically exoplanetary atmospheres and will help us examining more-in-depth planetary formation and dynamics.

Today, the Hubble/WFC3 camera represents the state-of-art for transit spectroscopy. State of the art inverse models to interpret the observed exoplanetary spectra are based on Bayesian analysis, able to sample a sizeable parameter space and to converge on a possible real set of parameters that can explain the structure of exoplanetary spectra. In this thesis, I present the results obtained by applying the UCL Bayesian inverse model, TauREx, to the largest catalogue observed to date. I will demonstrate how it is possible to find water vapour in 16 out of 30 planets chosen from the WFC3 planetary dataset. Often the input spectra are too noisy to obtain a result statistically significant. For this reason, I will introduce the ADI (Atmospheric Detection Index) index, able to quantify the "goodness" and the significance of molecular detection.

The use of complex atmospheric models on Bayesian analysis tools can require a prohibitive amount of time. For this reason, it is crucial to improve the analysis efficiency of complex atmospheres and accelerate their computations. To speed up the computation of atmospheric spectroscopic retrievals, I developed ExoGAN (Exoplanetary Generative Adversarial Network), a new-generation deep learning algorithm able to learn how to generate atmospheric spectra and retrieve the best set of parameters that can explain the observed spectrum. It consists of a deep convolutional generative adversarial network able to recognise molecular features, abundances and physical atmospheric parameters.

Finally, after describing more "traditional" atmospheric retrieval tools, their optimisation using deep learning algorithm and their application to real data-sets (i.e. the HST/WFC3 camera), I introduce a possible target list of planet candidates for a space mission dedicated to transit spectroscopy: the ARIEL space mission. Target selection is a crucial task to optimally select the planets with different basic parameters to sample uniformly the whole orbital and physical parameters space. The generation of an optimal target list is highly dependent on the type of instrument, and it will critically influence the science return of the mission.

Research impact statement

Exoplanetary science is at its Golden Age. The analysis of exoplanetary atmospheres is, today, the cutting edge. Transit spectroscopy is currently the most successful technique to probe exoplanetary atmospheres.

This thesis represents an original investigation of exoplanetary atmospheres through three steps:

1. Study of exoplanetary atmospheres with the current state-of-art instrument, the WFC3 camera on Hubble;

2. Optimisation of the standard retrieval methods using Deep Learning algorithms able to return more efficiently the parameters space associated to each exoplanetary observation.

3. The optimal choice of the targets for a space mission dedicated to transit spectroscopy, the ARIEL ESA M4 mission;

Each of the three steps serves as a novel and interdisciplinary application of modern techniques in space science, radiative transfer and AI. I explained what the current technology could do, demonstrating that with the Hubble/WFC3 camera it is possible to discover water in the upper atmosphere and some other trace gases. This exercise was essential to establish the reliability of the standard approach. Furthermore, I focused on the use of Artificial Intelligence algorithms to optimise the computation efficiency of the standard codes. Atmospheric analysis often requires computationally intensive algorithms to sample the parameters space correctly and retrieve atmospheric parameters. I developed ExoGAN, a Generative Adversarial Network trained on 10 million exoplanetary spectra and able to recognise molecular features and abundances, physical parameters and reconstruct possible missing parts of the spectrum. The atmospheric analysis made with ExoGAN reduces the computational time significantly from about 10 hours to 2 minutes.

Acknowledgements

Many people deserved my most profound gratitude and contributed to making this thesis possible.

First of all, I would like to thank my family, which has supported me for my entire life and always allowed and encouraged me to pursue my interests even during difficult times. All of the travels together, your teaching and the books you gave me, helped me for all of my life and allowed me to reach this point so far.

To my girlfriend, who always supported me patiently for many years.

I would like to express my special gratitude to my two first supervisors: Giovanna Tinetti and Giusi Micela. It has been an enormous privilege working with you and thanks to you I grew up as a scientist and as a person. I could not imagine two better supervisors, and I cannot express with any word my immense gratitude to both of you. It was and it will be a great privilege working with you.

To Ingo Waldmann, my second supervisor and friend, he made the realisation of most of this thesis possible. It was, is and will be an absolute pleasure to work with you and I am looking forward to many years to come.

To Professor Giovanni Peres my Bachelor and Master supervisor, I owe a special thanks. He showed me the world out of the undergraduate life and always pushed me to give the best part of me.

To my PhD brothers, Mario Damiano, Angelos Tsiaras, Marco Rocchetto, Billy Edwards and Gordon Yip who made my working environment more comfortable and pleasant.

And last but not least, I would like to thank all my close friends, you know who you are, for making these last years the most enjoyable of my life so far.

Contents

List of Figures

List of Tables

Acronyms

In the following list are defined only the most important acronyms.

AI Artificial Intelligence

ANN Artificial Neural Network

ARIEL Atmospheric Remote-sensing Infrared Exoplanets Large-survey

ASPA Atmospheric Spectrum and Parameters Array

CNN Convolutional Neural Network

DBN Deep Belief neural Network

DCGAN Deep Convolutional Generative Adversarial Network

ESA European Space Agency

ExoGAN Exoplanets Generative Adversarial Network

ExoMol molecular line lists for exoplanet atmospheres

GAN Generative Adversarial Network

GPU Graphic Processor Unit

HITEMP HIgh-TEMPerature molecular spectroscopic database

HITRAN HIgh-resolution TRANsmission molecular absorption database

HST Hubble Space Telescope

ILSVRC ImageNet Large Scale Visual Recognition Challenge

JWST James Webb Space Telescope

lReLU leaky Rectified Linear Unit

LTE Local Thermodynamic Equilibrium

MCMC Markov Chain Monte Carlo

NASA National Aeronautics and Space Administration

NN Neural Network

NS Nested Sampling

RBM Restricted Boltzmann Machine

ReLU Rectified Linear Unit

RoBErt Robotic Exoplanet Recognition

SRGAN Super Resolution Generative Adversarial Network

SSTL Surrey Satellite Technology Ltd

TauREx Tau Retrieval for Exoplanets

TESS Transiting Exoplanet Survey Satellite

TPU Tensor Processor Unit

VAE Variational Auto Encoder

Glossary

In the following notation vectors are represented in bold. Units are expressed in centimetre-gram-second (cgs) system.

Symbol	Description	Units
A_{if}	Einstein Coefficient for a spontaneous emission from the energy level i to the energy level f	s^{-1}
$A_{eq}(\lambda)$	Equivalent Area at wavelength λ	cm^2
A	Geometric albedo	-
α	Particle equivalent radius	cm
a_{sp}	Orbital separation between the star and the planet	cm
a	Semi-major axis of the planetary orbit	cm
$B_\lambda(T)$	Black-body radiation at temperature T and wavelength λ	$\mathrm{erg\,s^{-1}\,cm^{-2}\,sr^{-1}\,cm^{-1}}$
$\beta_{e\,,s\,,a}$	Extinction/scattering/absorption coefficient	cm^{-1}
b	Impact parameter	-
$\mathcal{B}_{21}$	Bayes factor of the model 2 compared to model 1	-
c	Speed of light	$\mathrm{cm\,s}^{-1}$
χ_c	Haze particle molar fraction	-
χ_i	Mole fraction of the i-th molecular species at wavelength λ	-
$D(\lambda)$	Transit depth	-
ΔF	$\frac{F_{\text{no transit}}-F_{\text{transit}}}{F_{\text{no transit}}}$	$\mathrm{erg\,s^{-1}\,cm^{-2}}$
$\Delta\lambda$	Spectral shift	cm
δ	Transit depth	-
$D(\mathbf{x})$	Discriminator: probability that $\mathbf{x}$ came from the data rather than p_g	-
$E_{\mathrm{low}\,j}$	Energy of the lower level	cm^{-1}
ε	Atmospheric emissivity	-

Symbol	Description	Units
$\boldsymbol{\varepsilon}$	Error vector	-
$F_{\rm ecl}[\lambda_1, \lambda_2]$	Dimensionless eclipse flux for a given bandpass $[\lambda_1, \lambda_2]$	-
$F_{\rm no\ transit}$	Flux received out of a transit	$\mathrm{erg\,s^{-1}\,cm^{-2}}$
F_p	Planetary flux	$\mathrm{erg\,s^{-1}\,cm^{-2}}$
F_*	Stellar flux	$\mathrm{erg\,s^{-1}\,cm^{-2}}$
$F_{\rm transit}$	Flux received during a transit	$\mathrm{erg\,s^{-1}\,cm^{-2}}$
$G(\lambda)$	Instrumental spectral response function	-
G	Gravitational constant	$\mathrm{cm^3\,g^{-1}\,s^{-2}}$
g	Gravity accelerator factor	$\mathrm{cm\,s^{-2}}$
$g_{{\rm up}\,j}$	Degeneracy of the j-th energy level	-
$G(\mathbf{z})$	Generator: mapping from latent variable to generated data	-
H	Atmospheric scale height	cm
h	Planck constant	$\mathrm{erg\,s}$
I_λ	Radiation Intensity at wavelength λ	$\mathrm{erg\,s^{-1}\,cm^{-2}\,sr^{-1}\,cm^{-1}}$
i	Inclination of the orbital plane	degrees
J_λ	Source function	$\mathrm{erg\,s^{-1}\,cm^{-2}\,sr^{-1}\,cm^{-1}}$
$\boldsymbol{J}$	Jacobian matrix	-
j_λ	Source term	$\mathrm{erg\,s^{-1}\,mol^{-1}\,sr^{-1}\,cm^{-1}}$
$J^{(D)}$	Discriminator's loss function	-
$J^{(G)}$	Generator's loss function	-
k_B	Boltzmann constant	$\mathrm{erg\,K^{-1}}$
K_*	Semi-amplitude of the radial velocity curve	$\mathrm{cm\,s^{-1}}$
$\xi(\boldsymbol{y})$	Bayesian evidence	-
l	Atmospheric chord length crossed by the radiation flux	cm
l_o	Optical path	$\mathrm{mol\,cm^{-2}}$
$\mathcal{L}(\boldsymbol{x})$	Likelihood function, notation from Feroz et al. (2009)	-
μ_g	g-th quadrature point	-
μ	$\cos\phi$	-
$\mu_{\rm atm}$	Mean molecular mass of the atmosphere	mol
M_p	Mass of the planet	g
M_*	Mass of the star	g
$M(\mathbf{x})$	Model vector	-

Symbol	Description	Units
N_{gas}	Number of gases used in the model	-
N_{layers}	Number of layers used to model the atmosphere	-
N_{quad}	Number of Gaussian quadrature points	-
ν_{if}	Frequency associated to the emitted/absorbed photon	cm^{-1}
N_p	Number of planets	-
$\tilde{\omega}$	β_s/β_e	-
P_i	Atmospheric pressure at layer i	Ba
$P(\boldsymbol{y}\|\boldsymbol{x}, M)$	Likelihood function for the vector $\boldsymbol{y}$, given the state vector $\boldsymbol{x}$ and the model M	-
$P(\mu, \phi; \mu', \phi')$	Redirection function for a radiation flux flux coming from direction μ', ϕ' to the direction μ, ϕ	-
$P(\boldsymbol{x}\|\boldsymbol{y}, M)$	Posterior distribution of the state vector $\boldsymbol{x}$, given the input vector $\boldsymbol{y}$ and the model M	-
P	Orbital period	s
$\pi(\boldsymbol{x})$	Prior distribution, notation from Feroz et al. (2009)	-
$P(\boldsymbol{x}, M)$	Prior distribution	-
$\mathfrak{p}$	p-value	-
p_{data}	Data distribution	-
P_{geom}	Geometrical probability of a planetary transit	-
p_g	Generator distribution	-
$\Phi(\alpha)$	Orbital phase function	-
ϕ	Angle between the radiation direction and the normal to the surface tangent plane	-
Q_{ext}	Extinction coefficient	-
$Q(T)$	Partition function	-
Q_0	Peak of the Q_{ext} coefficient	-
R	Spectral resolution	-
ρ_N	Number density of the medium	$\text{mol}\,\text{cm}^{-3}$
ρ_*	Stellar density	$\text{g}\,\text{cm}^{-3}$
R_p	Radius of the planet	cm
R_*	Radius of the star	cm
σ_{Mie}	Mie cross section	cm^2
σ_λ	Absorption cross section	$\text{cm}^2\,\text{mol}^{-1}$

Symbol	Description	Units
s	Distance traversed by the radiation inside the planetary atmosphere	cm
$\sigma_{\lambda,i}$	Absorption cross section of the i-th molecular species at wavelength λsort	$\mathrm{cm^2\,mol^{-1}}$
T	Temperature	K
$\mathcal{T}_\lambda$	Monochromatic transmittance	-
$\tau_{\lambda,i}$	Optical depth of the i-th molecular species at wavelength λ	-
τ_s	Total optical depth at the planetary surface	-
τ_λ	Total optical depth at wavelength λ	-
t_I	Start ingress time	s
t_{II}	End ingress time	s
t_{III}	Start egress time	s
t_{IV}	End egress time	s
t_F	$t_{III} - t_{II}$	s
$\boldsymbol{\theta}^{(D)}$	Discriminator's hyperparameters	-
$\boldsymbol{\theta}^{(G)}$	Generator's hyperparameters	-
T_p	Planetary temperature	K
t_T	$t_{IV} - t_I$	s
V	Value function	-
v_p	Planetary tangent velocity	$\mathrm{cm\,s^{-1}}$
v_*	Stellar tangent velocity	$\mathrm{cm\,s^{-1}}$
w_g	g-th quadrature point weight	-
$X(\lambda)$	Prior volume inside a region with likelihood lower then λ, with $\lambda \in \mathbb{R}$	-
$\mathbf{x}$	State vector	-
$\boldsymbol{x_0}$	A priori state	-
$\mathbf{y}$	Output vector	-
z_∞	Altitude at the top of the atmosphere	cm
z	Altitude level in the atmosphere	cm

Chapter 1

Introduction

The sky and its beauty have always inspired the humankind. In ancient Attic Greece, the term human is ἄντροπως, which means "the one who looks up and moves forward", highlighting the nature of human beings as an open-minded and curious form of life. Curiosity is a peculiar characteristic of our species, that pushed us into understanding the basic principles that rule the universe and make possible the existence of our world. "Are we alone?", "Are there other worlds?" These are just two of the fundamental questions that pressed us to observe the sky, looking for another planet similar to ours. In our Solar System, there are eight planets, all of them are unique, and even though some of them have similar radii and masses, they all have their peculiar physical and orbital properties, spanning a broad spectrum of possibilities. For answering the fundamental questions spelt out above, we need to look further away and study what is beyond the Solar System.

One of the most remarkable discoveries in the last century occurred in 1992 when Wolszczan and Frail (1992) published the very first detection of a planetary system around a pulsar. They detected two planets with 2.8 and 3.4 Earth masses orbiting the 6.2 ms pulsar PSR1257 + 12 at a distance of, respectively, 0.47 AU and 0.36 AU. Three years later, Mayor and Queloz (1995) reported the discovery of the first exoplanet around a main sequence star. It was a Jupiter mass planet around the G-type star 51 Pegasi, inferred by periodic variations in the star's radial velocity curve. This discovery was unexpected and challenged all the planetary formation models. Indeed Jupiter-mass planets were expected to orbit far away from their star contrary to 51 Peg b. Since 1995 the number of discovered exoplanets increased dramatically and our understanding of planetary science changed with it.

On the day of writing this thesis, we know ∼4000 exoplanets beyond the Solar System (Fig

1.1). We have a wide variety of known exoplanets, from very hot giant planets to cold Earths.

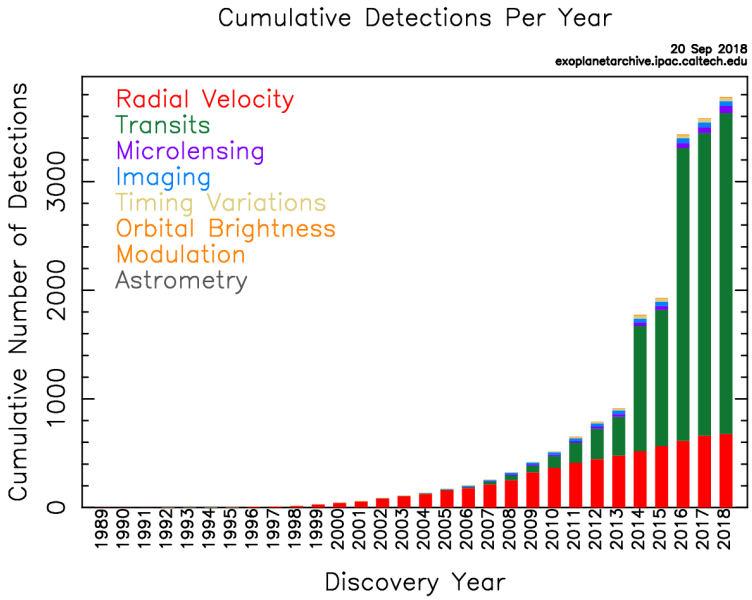

Figure 1.1: Cumulative number of discovered planet per year. Known exoplanets are represented with different colours using different detection methods. (Image generated from `https://exoplanetarchive.ipac.caltech.edu`)

Depending on the detection method some planetary categories are more accessible to discoveries and atmospheric characterisation.

1.1 Detection methods: A general view

Since 1995, year of the discovery of the first exoplanet orbiting a main-sequence star, many other methods have been introduced to the search of exoplanets. We can separate them into two main classes: direct and indirect methods. Direct imaging methods require very sensitive instruments and adaptive optics. So far, these have revealed a few tens of giant, young exoplanets.

The vast majority of known exoplanets have been detected using indirect methods, i.e. by measuring the effects of the planetary presence on the star and inferring planetary physical and orbital properties. Indirect methods use, for example, micro-lensing phenomena, timing variations and astrometry measurements. The most successful methods that revealed most known exoplanets are the Radial Velocity (section 1.1.1) and the transit method (section 1.1.2).

1.1.1 The Radial Velocity method

Radial Velocity uses the Doppler shift of the star which interacts gravitationally with the planet. Mayor and Queloz (1995) successfully detected for the first time an exoplanet using this method, although the scientific community have been speculating about this detection method for many

years (Marcy and Butler, 1992; Cochran and Hatzes, 1994; McMillan et al., 1994; Walker et al., 1995).

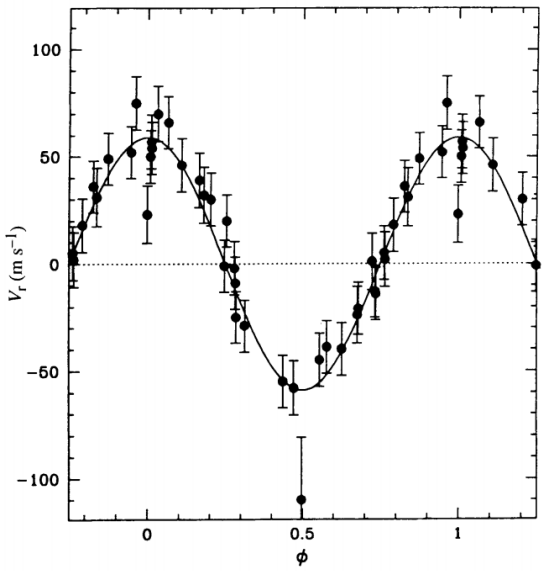

Figure 1.2: Radial Velocity curve of 51 Pegasi used for the detection of the first planet (from Mayor and Queloz (1995)).

Figure 1.2 shows the radial velocity curve measured by Mayor and Queloz (1995). From this measurement it is possible to infer the minimum mass of the planet, its orbital period and its eccentricity. From a Doppler shift of the stellar features we can infer the radial velocity of the star v_*, for a non-relativistic source:

$$\frac{\Delta\lambda}{\lambda_0} = \frac{v_*}{c}, \tag{1.1}$$

where $\Delta\lambda = \lambda - \lambda_0$ is the spectral shift of the line at λ_0 and c is the speed of light. Assuming a circular orbit and $M_p \ll M_*$ with M_p and M_* the masses of, respectively, the planet and the star. From the third Kepler law, the semi-major axis of the orbit, a, is related to the orbital period P as follows:

$$a^3 = \frac{GM_*}{4\pi^2} P^2 \tag{1.2}$$

where G is the gravitational constant. From the conservation of momentum:

$$M_p v_p = M_* v_* \tag{1.3}$$

with v_p and v_* are the planetary and stellar tangent velocity. The semi-amplitude of the radial velocity is:

$$K_* = v_* \sin i = \frac{M_p v_p \sin i}{M_*} \tag{1.4}$$

where i is the orbital inclination. Since, for a circular orbit, $v_p = 2\pi a/P$:

$$K_* = v_* \sin i = \frac{2\pi a M_p \sin i}{M_*}. \tag{1.5}$$

By solving Eq 1.5 for the mass of the planet M_p, we have:

$$M_p \sin i = \frac{K_* M_* P}{2\pi a}. \tag{1.6}$$

1.1.2 Transit method

We observe a transit when the planet, during its orbital motion, passes in front of the host star as seen from the observer position. In this case, the planet blocks part of the stellar light, and the observer measures a dim in the light-curve (see Fig 1.3).

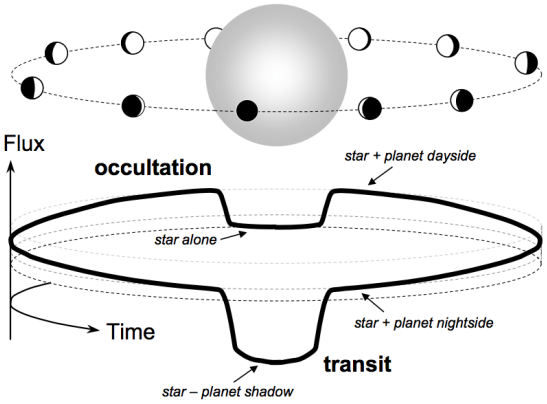

Figure 1.3: Planetary transit and occultation (from Winn (2010)).

A planetary transit gives us information on the planetary radius R_p in units of stellar radii R_*, the orbital semi-major axis a, the orbital period P and the inclination i. In the following section, we derive these parameters assuming, for simplicity, a circular orbit and a single star with one companion in the system.

The ratio R_p/R_* is given by

$$\frac{R_p}{R_*} = \sqrt{\frac{F_{\text{no transit}} - F_{\text{transit}}}{F_{\text{no transit}}}} = \sqrt{\Delta F}, \tag{1.7}$$

where F_{transit} ($F_{\text{no transit}}$) is the measured flux when the planet is (not) transiting. The quantity ΔF defined in Eq 1.7 is dimensionless. Eq 1.7 shows how we can directly measure the planetary radius from a transit observation.

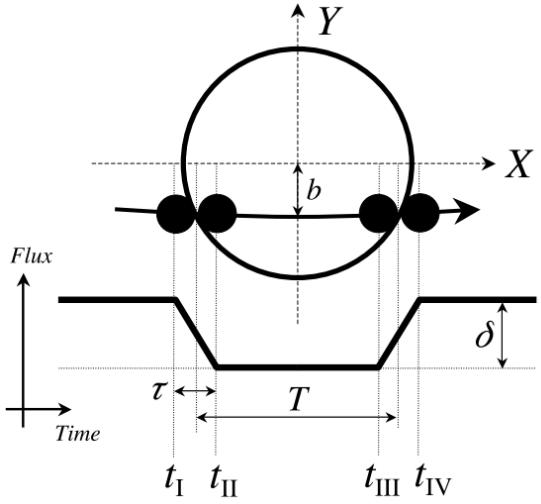

Figure 1.4: Geometry of a transit(from Winn (2010)).

By measuring the time at the egress/ingress of the planetary transit, we can infer the impact parameter b. It represent a dimensionless parameters which quantify the distance between the transit trajectory from the centre of the star (see Fig 1.4), and can be expressed as follows:

$$b = \left[\frac{\left(1 - \sqrt{\Delta F}\right)^2 - (t_F/t_T)^2 \left(1 + \sqrt{\Delta F}\right)^2}{1 - (t_F/t_T)^2} \right]^{\frac{1}{2}} \tag{1.8}$$

where $t_T = t_{IV} - t_I$ and $t_F = t_{III} - t_{II}$, with $t_{I,II,III,IV}$ the time in which the planet starts/ends and ingress/egress, as shown in Fig 1.4.

The ratio a/R_* is given by:

$$\frac{a}{R_*} = \frac{2P}{\pi} \frac{\Delta F^{1/4}}{\left(t_T^2 - t_F^2\right)^{1/2}}. \tag{1.9}$$

Using the third Kepler law it is possible to express the stellar density ρ_* as:

$$\rho_* = \frac{3\pi}{GP^2} \left(\frac{a}{R_*}\right)^3. \tag{1.10}$$

Substituting Eq 1.9 in 1.10 it is possible to represent the stellar density as follows:

$$\rho_* = \frac{24P}{G\pi} \frac{\Delta F^{3/4}}{\left(t_T^2 - t_F^2\right)^{3/2}}. \tag{1.11}$$

Using the impact parameter defined in Eq 1.8 and the third Kepler's law, we can calculate the orbital inclination as:

$$i = \cos^{-1}\left(b\frac{R_*}{a}\right). \tag{1.12}$$

The transit method has been the most successful for discovering exoplanets beyond the Solar system. CoRoT was the first space mission dedicated to study stellar interiors and search for exoplanets (Almenara et al., 2013). The satellite had a 27 cm telescope, and it was launched in 2006 and active until 2013 [1].

The NASA's Kepler space mission [2] (Borucki et al., 2010; Koch et al., 2010), was launched in 2009 into a Earth-trailing heliocentric orbit. With a 0.95m telescope, and a photometer, Kepler could monitor the light from 150000 stars in a single area of the sky in the Cygnus constellation. In the whole mission lifetime (over 9 years), it observed more than 530000 stars, and detected more than 2600 planets and additional 2200 candidates (as shown in the online catalogue tool from Akeson et al. (2013)). Two of the primary goals of the mission were detecting Earth-like planets and providing the first statistics of the occurrence rate of planets. Fressin et al. (2013) published a planetary occurrence rate table based on the observations done during the first six quarters of the spacecraft's operations. With additional spectroscopic observations of the host stars from the ground, Fulton et al. (2017) could complete the previous statistics using sixteen quarters. As shown in Figure 1.5 it was noticed a gap between Super Earth-sized planets and Neptunes. This result also confirmed the observations from Fressin et al. (2013): small planets are more frequent in our galaxy than the giant ones.

In April 2018 the Transiting Exoplanet Survey Satellite[3] (TESS) was launched (Ricker, 2014; Ricker et al., 2015; Sullivan et al., 2015; Ricker et al., 2016; Clery, 2018). In two years TESS will look for the presence of exoplanets around $\sim$ 200000 stars in the Solar System neighbourhood, within 200 light years from the Sun. It will look at the entire sky dividing it into 26 sectors.

The PLATO space mission (Rauer et al., 2014) will find and study a large number of extra-solar planetary systems, focusing on terrestrial planets in the habitable zone around solar-like stars, with an expected launch date in 2026 [4].

[1] http://sci.esa.int/corot/
[2] https://www.nasa.gov/mission_pages/kepler/overview/index.html
[3] https://tess.gsfc.nasa.gov/
[4] http://sci.esa.int/plato/

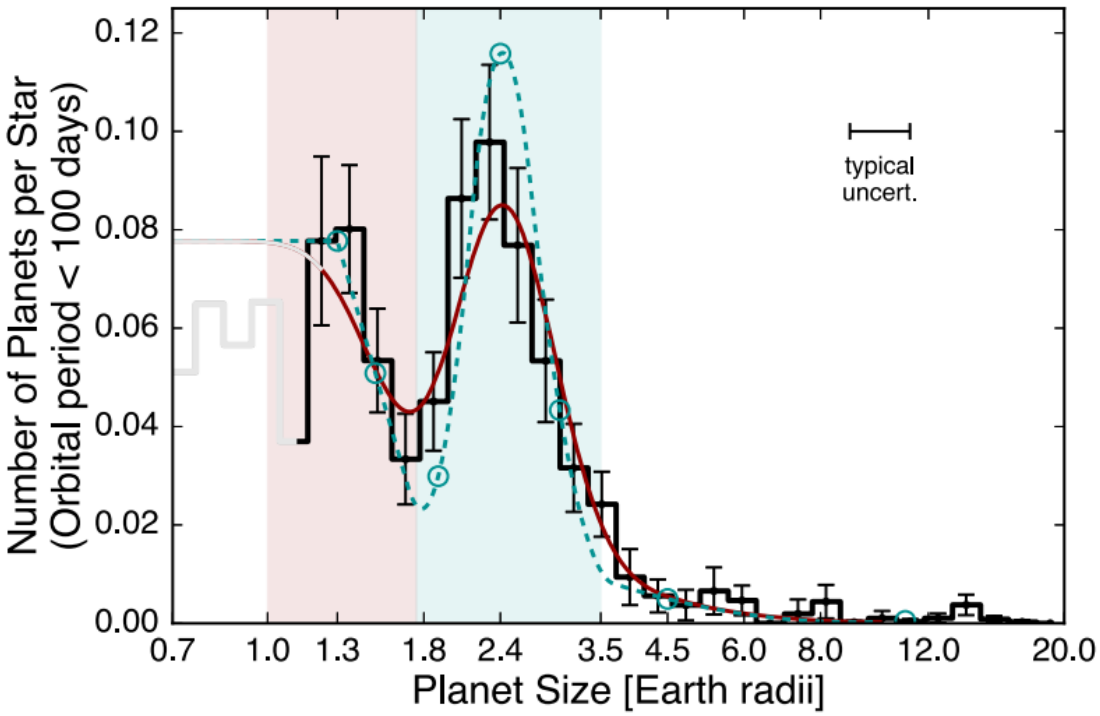

Figure 1.5: Number of planets per star with an orbital period of less than 100 days. The solid red line represents the best-fit spline model (from Fulton et al. (2017)).

1.2 Bulk composition

The transit and radial velocity methods combined allow us to infer the bulk density of the exoplanets. In figure 1.6 is shown a mass-radius relationship for the known planets with a mass up to $30M_{\oplus}$. The coloured lines, indicate different bulk densities for each planets. Each planet has been labelled with its name and a colour scale, indicating its equilibrium temperature. Grey planets are those of the Solar System. It is noticeable that Venus and the Earth are in the lower-left part of the graph, indicating that they are mainly made of Iron. Cold Icy planets, such as Uranus and Neptune, are in the upper-right part of the graph.

The bulk density of the planet is not enough to constrain a model of the interior, due to the degeneracy of the solutions and the uncertainty of the observed parameters (Adams et al., 2008; Valencia, 2007; Valencia et al., 2013; Dorn et al., 2015; Suissa et al., 2018). The chemical composition of the atmosphere, obtained with observations, can provide additional constraints, especially for warm and hot planets, where the interior and the atmosphere are more connected.

1.3 Atmospheric spectroscopy introduction

Exoplanetary atmospheres are crucial to investigate formation and evolution processes, weather and even habitability. In most cases, it is not possible to spatially resolve the exoplanet from

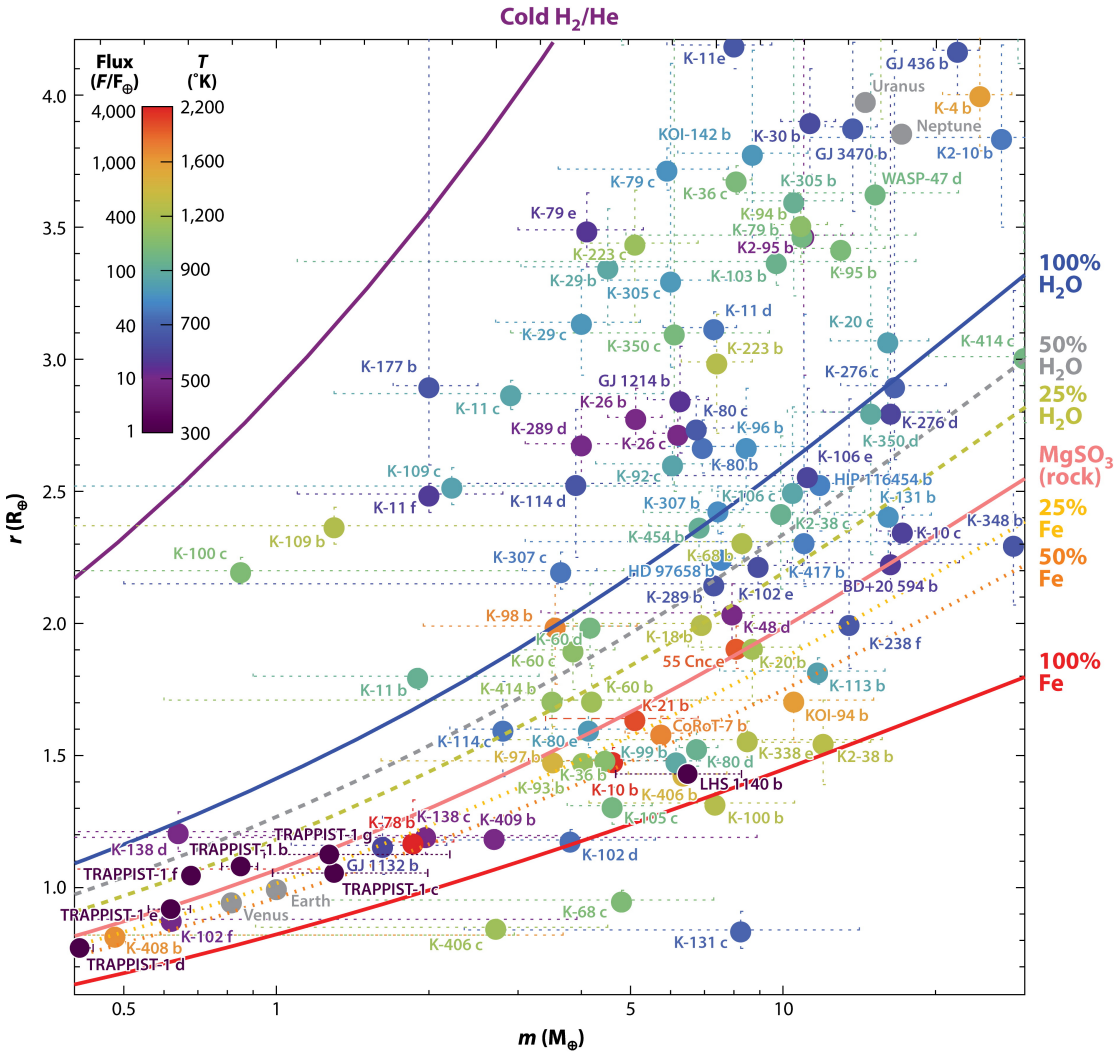

Kaltenegger L. 2017.
Annu. Rev. Astron. Astrophys. 55:433–85

Figure 1.6: Mass-Radius relationship for the known planets up to $30M_\oplus$. With different colours are indicated density lines associated with various bulk compositions (from Kaltenegger (2017)).

its star, as the star is much brighter than the planet by orders of magnitude. In recent years, different solutions have been proposed to study the atmosphere and bypass these difficulties. The most successful techniques can be applied to transiting planets which periodically pass in front and behind their host star. During a transit, the planetary atmosphere filters the stellar light depending on its chemistry, and physical properties. Only a small fraction of the incident light passes through it. During an eclipse, the star blocks the exoplanetary thermal emission and reflection which are otherwise detectable in other orbital phases. With very precise observations, it is possible to separate them from the stellar light.

1.3.1 Transit spectroscopy

During the transit, part of the stellar light is filtered through the exoplanetary atmospheres (see Figure 1.7). The light is absorbed by the atmosphere depending on its chemistry and physical properties. By measuring the transit light-curves at different wavelengths, it is possible to obtain the transit depth as a function of wavelength, see e.g. Figure 1.8 from Fraine et al. (2014).

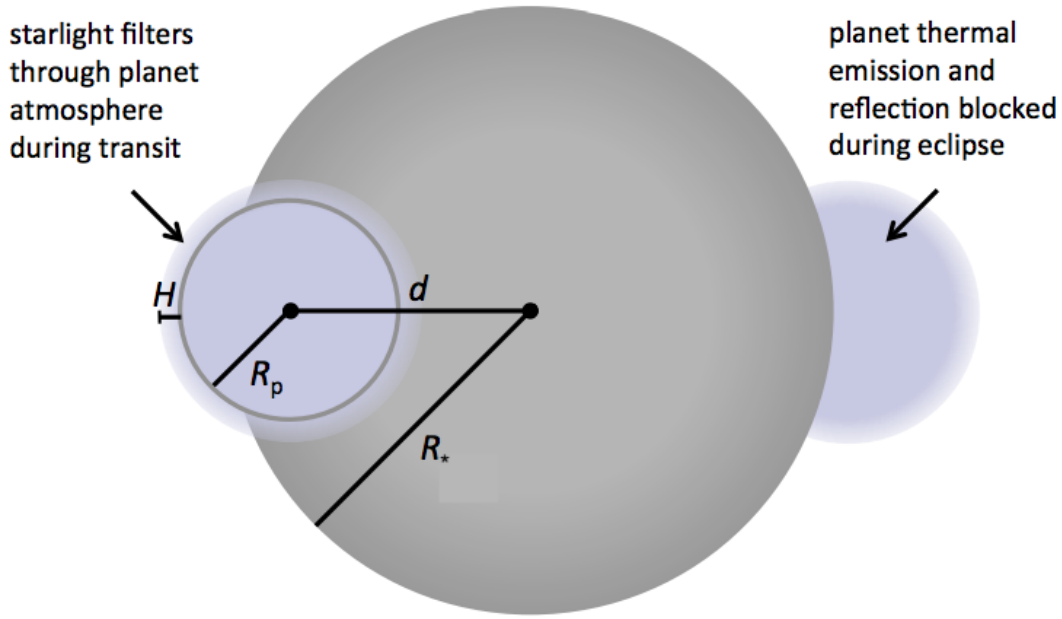

Figure 1.7: Geometry of the transit and eclipse, where R_p is the planetary radius, R_* is the stellar radius, d is the distance between the centres of the two bodies and H is the planetary scale height (from Kreidberg (2017)).

The interpretation of transmission spectra requires the solution of the radiative transfer equations of the stellar light through the planetary atmosphere, which is a computationally-intensive problem. Nevertheless, it is possible to estimate heuristically the amplitude of the atmospheric signal observed during the transit. A key parameter is the scale height H:

$$H = k_B T_p / \mu_{\rm atm} g, \tag{1.13}$$

with k_B the Boltzmann constant, T_p the planetary temperature, $\mu_{\rm atm}$ the mean molecular weight of the atmosphere and g the gravity acceleration factor.

An approximation of the atmospheric signal during a transit is:

$$\delta(\lambda) = \frac{(R_p + nH)^2}{R_*^2} - \frac{R_p^2}{R_*^2} \approx n R_p H / R_*^2, \tag{1.14}$$

For cloud-free atmospheres and low spectral resolution, where $n \in \mathbb{R}$, and $n \sim 5$ (Zellem et al., 2014). In Chapter 2 I will explain more-in-depth the rationale behind this formula (Equation 2.33).

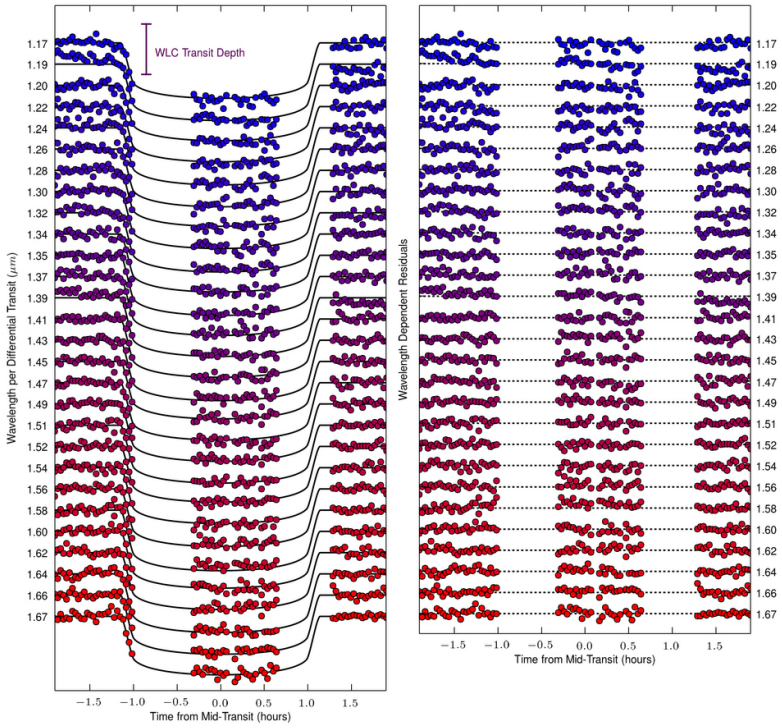

Figure 1.8: Light-curves of a HAT-P 11 transit. Each light curve has been binned in wavelength according to the Hubble WFC3 camera and fitted with a transit model (from Fraine et al. (2014)).

1.3.2 Eclipse spectroscopy

During the eclipse, or secondary transit, or occultation, it is possible to measure the flux of the host star alone. Comparing the star's flux with the one measured just before or after the occultation, it is possible to study more in detail the thermal emission of the planet, and the reflected light.

Thermal Emission

The first mission able to analyse the thermal structure of exoplanetary atmospheres was the Spitzer Space Telescope (Werner et al., 2004). By observing the planets during their eclipse, the Spitzer Space Telescope recorded photometric measurements and emission spectra of exoplanets orbiting their stars (Deming et al., 2005; Charbonneau et al., 2005b,a; Richardson et al., 2007; Grillmair et al., 2007; Wheatley et al., 2010).

To analyse the thermal emission from an exoplanet, we need to measure the eclipse depth as a function of wavelength. Following the notation of Esteves et al. (2015), defining the planetary and stellar surface fluxes, respectively, F_p and F_*, the eclipse depth $F_{\rm ecl}[\lambda_1, \lambda_2]$, at a given bandpass $[\lambda_1, \lambda_2]$, can be calculated as:

$$F_{\rm ecl}[\lambda_1, \lambda_2] \simeq \left(\frac{R_p}{R_*}\right)^2 \frac{\int_{\lambda_1}^{\lambda_2} F_p(\lambda) G(\lambda) {\rm d}\lambda}{\int_{\lambda_1}^{\lambda_2} F_*(\lambda) G(\lambda) {\rm d}\lambda}, \tag{1.15}$$

with R_p and R_*, respectively, the planetary and stellar radius and $G(\lambda)$ is the instrumental spectral response function, i.e. the mapping between the incoming photon flux and the detected one. For the Spitzer space telescope $G(\lambda) = S(\lambda)(\lambda/hc)$, with $S(\lambda)$ the IRAC spectral response function [5], h is the Planck's constant and c is the speed of light in vacuum.

Since the planet is colder than the star, the flux ratio is larger at longer wavelengths, assuming a black-body distribution for both objects. The emission radiation comes from zones in the atmosphere of the planet where the optical depth is of the order of the unity. The optical depth is a measure of the extinction coefficient up to a specific 'depth' of the atmosphere, this measure depends on the wavelength and it is defined in equation 2.4 of chapter 2. Figure 1.9 shows an example of emission spectrum from Kreidberg et al. (2015) of the planet WASP-43 b, were a water absorption feature is visible in the wavelength range between 1.3μm and 1.5μm.

Reflected Light

There are two different planetary fluxes that need to be taken into account when observing a planetary system: the planetary thermal emission, and the reflected light by its surface or atmosphere. The planet also reflects stellar light, especially at shorter wavelengths. To model the total eclipse depth, we need to take into account an additional term describing the reflection from the planetary atmosphere. For simplicity, the planet is considered as a perfect Lambertian surface, i.e. a flat disk with a radius equal to that of the planet R_p, diffusing isotropically light scattered from the star. Assuming a geometric albedo equal to A_g, the total reflected light is:

[5] `http://irsa.ipac.caltech.edu/data/SPITZER/docs/irac/calibrationfiles/spectralresponse/`

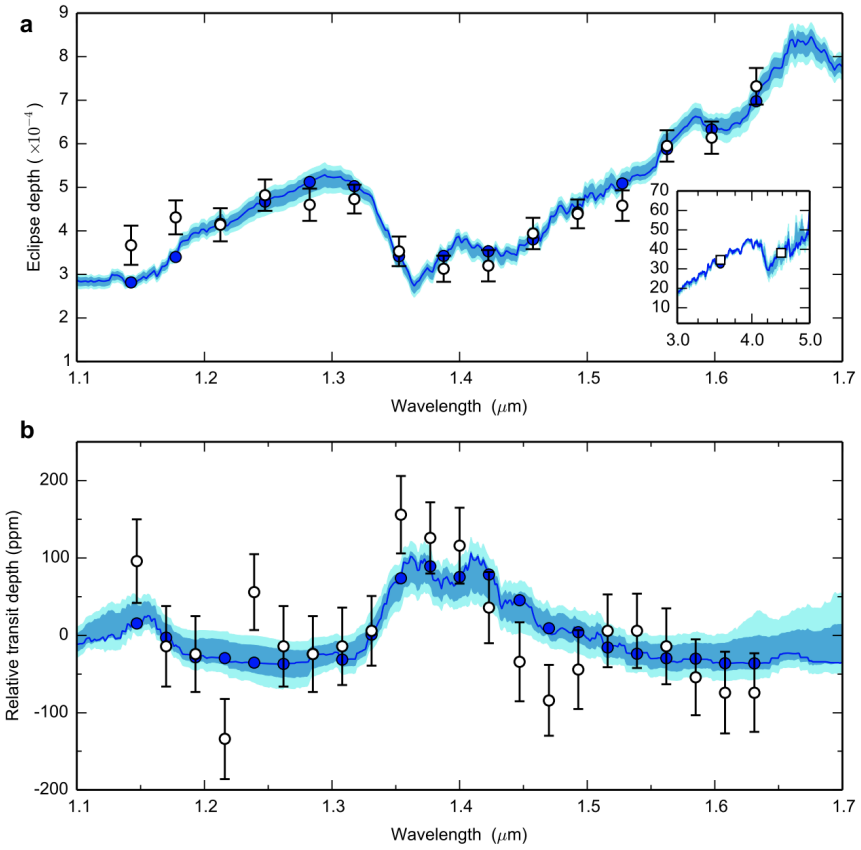

Figure 1.9: Example of thermal emission (top) from the hot-Jupiter WASP-43 b and transmission spectrum (bottom). Data are obtained with the Hubble WFC3 camera (between 1.1 and 1.7 μm) and the Spitzer IRAC camera (between 3.6 - 4.5 μm). The blue line is the best fit to the two spectra with 1-σ confidence (dark blue) and 2-σ confidence (light blue). The water absorption is visible in the wavelength range between 1.3μm and 1.5μm (Kreidberg et al., 2015).

$$F_{\text{reflected}} = A_g \left(\frac{R_p}{a_{sp}}\right)^2 \Phi(\alpha), \tag{1.16}$$

with a_{sp} being the orbital separation between the two bodies and $\Phi(\alpha)$ the orbital phase function, i.e. the intensity of the reflected light at the phase angle α, which depends on the scattering properties of the atmosphere. The orbital phase function is define such as $\Phi(\alpha) = 1$ during the mid eclipse time, and $\Phi(\alpha) = 0$ during the mid transit time. Reflected light models are available e.g. in Madhusudhan and Burrows (2012). The reflected light is important especially in the optical part of the spectrum.

During the secondary eclipse, $\Phi(\alpha) = 1$, then we can define the total eclipse depth as (Esteves et al., 2015):

$$F_{\text{ecl}}[\lambda_1, \lambda_2] \simeq \left(\frac{R_p}{R_*}\right)^2 \frac{\int_{\lambda_1}^{\lambda_2} F_p(\lambda) G(\lambda) \mathrm{d}\lambda}{\int_{\lambda_1}^{\lambda_2} F_*(\lambda) G(\lambda) \mathrm{d}\lambda} + A_g \left(\frac{R_p}{a}\right)^2 \tag{1.17}$$

for a given bandpass $[\lambda_1, \lambda_2]$.

In chapter 2, I describe more in detail the physics of thermal emission 2.1.2 and multiple scattering from the planetary atmospheres 2.1.3.

Phase-curves

Seager et al. (2000); Knutson et al. (2007); Stevenson et al. (2014a); de Wit et al. (2012) showed how it is possible to infer information of the atmospheric dynamics and cloud distribution by observing a full-orbit phase-curve. This technique consists of observing photometrically or spectroscopically the exoplanet/star system over the orbit, using the occultation as the baseline to measure the stellar flux alone. The best planets to study with this technique are the short-period planets, typically tidally locked to their host star. For these planets, the rotation period is equal to the orbital period. Phase-curves offer a tool to probe into the exoplanetary atmosphere at different longitudes (Showman and Polvani, 2011).

The HD 189733 planet/star system shows a sinusoidal phase curve which can be explained by the presence of bright regions on the planet HD 189733 b, towards the observer position during the orbital motion (Knutson, 2007).

Spectrally resolved phase-curves are very useful to infer the vertical structure of a planetary atmosphere as a function of its surface coordinates (Keating and Cowan, 2017). Stevenson et al. (2014c) retrieved the temperature-pressure profile of WASP 12 b as a function of phase using the dataset from HST/WFC3 and Spitzer/IRAC cameras therefore, covering the wavelength between visible and infrared.

Direct imaging

Using spectroscopy on the image of a planet it is possible to study the atmospheric composition and thermal structure (Burrows and Lunine, 1995; Burrows et al., 1997; Marley et al., 1999; Sudarsky et al., 2000, 2003; Burrows et al., 2004).

In the analysis of directly imaged exoplanetary spectra, a key concept is the geometric albedo, i.e. the ratio of light measured from a planet observed at a full phase to that of an ideal fully reflecting Lambertian disk with the same cross-section (πR_p^2) of the planet. Theoretical calculations of reflected spectra for giant exoplanets have been done e.g. by Marley et al. (1999); Burrows et al. (2004); Cahoy et al. (2010); Burrows (2014); Greco and Burrows (2015); Lupu et al. (2016).

The Gemini Planet Imager (GPI) (Macintosh et al., 2014) is a next-generation coronograph designed for direct imaging and spectroscopy. The instrument is mounted on an 8m telescope in Cerro Pachon. Figure 1.10 shows the images of 51 Eri and 51 Eri b observed with the GPI from Macintosh et al. (2015). The extracted spectra show strong signatures of water and methane. Nevertheless, with this technique there are significant uncertainties on the planetary radius and mass, which may lead to model degeneracies.

Another instrument used for direct imaging is SPHERE at VLT (Beuzit et al., 2008).

In principle, for directly imaged planets it is possible to study the polarisation of the signals (Stam et al., 2006; Marley and Sengupta, 2011; de Kok et al., 2011b), which is helpful to study clouds in the atmospheres and atmospheric inhomogeneities. Polarised signals are very challenging, though, since they require contrast ratios sensitivities $\ll 10^{-6}$.

1.3.3 High-resolution atmospheric spectroscopy

High-resolution atmospheric spectroscopy works with resolving powers $\lambda/\Delta\lambda > 50000$. Using planetary radial velocity, or Doppler cross-correlation, it is possible to obtain high-resolution spectra of planetary atmospheres from ground-based spectrographs such as CRIRES (Kaeufl et al., 2004), GIARPS (Claudi et al., 2016), SPIRou (Artigau et al., 2011), IGRINS (Oh et al., 2010) and iSHELL (Rayner et al., 2012).

The absorption lines from the stellar atmosphere and the atmosphere of the Earth must be corrected. Since the exoplanet is moving around its host star, the lines emitted/absorbed by the planetary atmosphere can be distinguished, as they have very different Doppler shifts.

The corrected spectra are correlated with models obtained by assuming the presence of molecules expected to be in the planetary atmosphere.

Snellen et al. (2010) proposed this technique for the first time, discovering CO in the at-

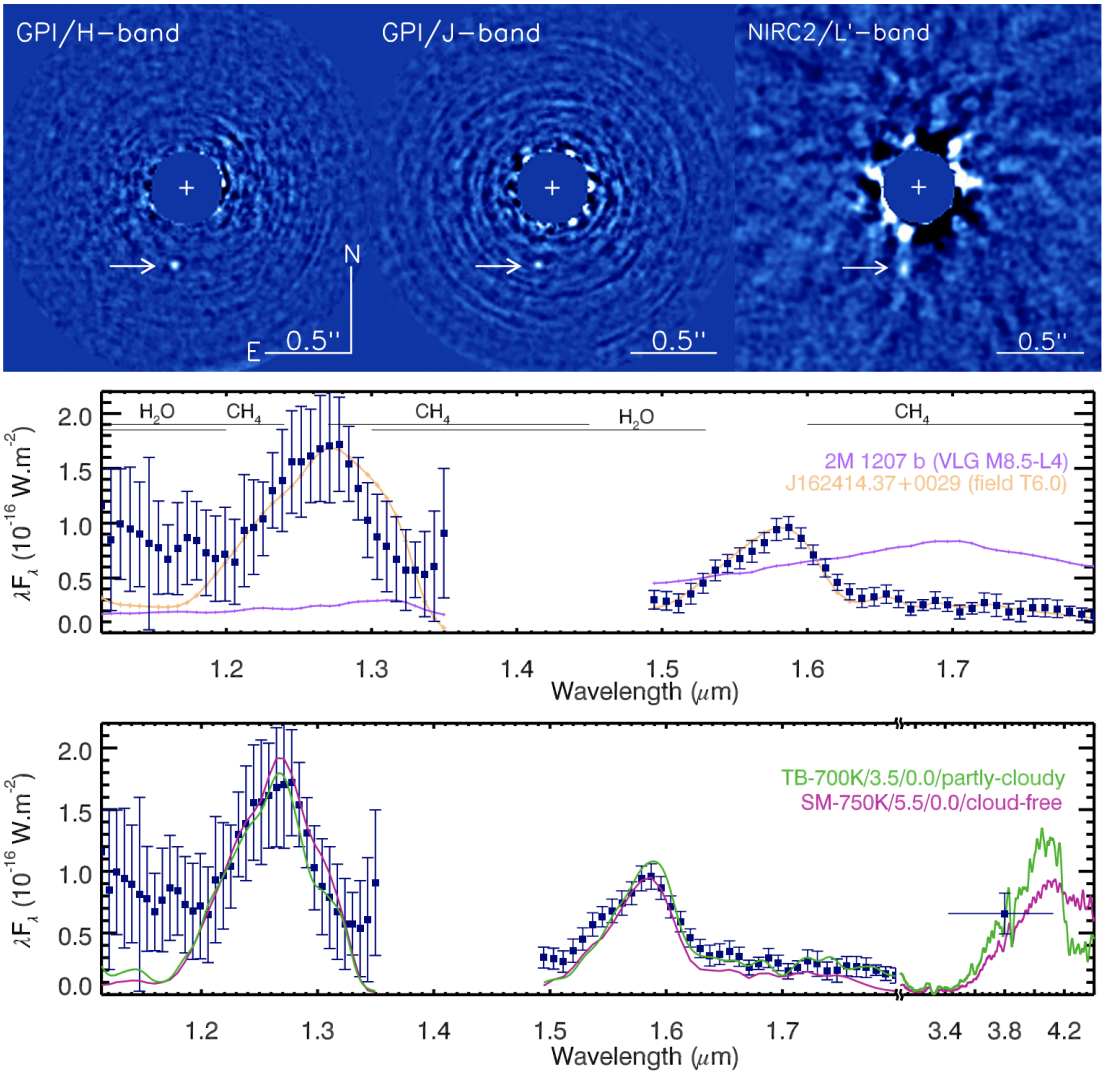

Figure 1.10: 51 Eri and 51 Eri b observed with the Gemini Planet Imager in the H, J and L band (top). Eri b J and H band spectrum from GPI (bottom) (results from Macintosh et al. (2015)).

mosphere of the hot-Jupiter HD 209458 b. Since then, the exoplanetary community started to apply this method to transiting and non-transiting exoplanets, detecting CO and H_2O. Planets studied with this technique are: τ Boo b (Brogi et al., 2012; Rodler et al., 2012; Lockwood et al., 2014); HD 189733 b (de Kok et al., 2013; Birkby et al., 2013; Rodler et al., 2013; Brogi et al., 2016); 51 Peg b (Brogi et al., 2013; Birkby et al., 2017); HD 179949 b (Brogi et al., 2014) and β Pic b (Snellen et al., 2014) (shown in Figure 1.11).

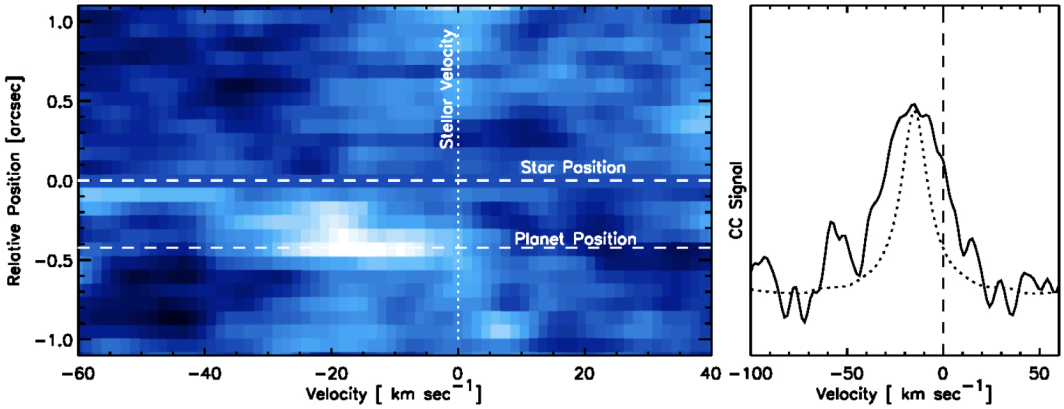

Figure 1.11: (Left) cross-correlation with the molecular signals of CO and H_2O as a function of different velocities (the horizontal axis). The bright area is the best correlation with the model, occurring at the radial velocity of the planet. (Right) the total cross-correlated signal at the planetary velocities. From the broadening of the line, it is possible to infer the rotation of the planet (Image from Snellen et al. (2014)).

1.3.4 Space-based low-resolution spectroscopy

Currently, thanks to the Hubble Space Telescope (HST) and Spitzer we can infer the molecular composition of a few tens of exoplanets, mostly hot Jupiters. Giant planets' spectra appear to be dominated by water vapour (Iyer et al., 2016; Sing et al., 2016a; Tsiaras et al., 2018) (Figure 1.12).

As shown in Sing et al. (2016a) and Tsiaras et al. (2018), the spectral features are weaker than expected. Clouds or a metal-rich atmosphere can explain the flatness of two sub-Neptunes GJ-436 b and GJ-3740 b (Stevenson et al., 2010; Knutson et al., 2011; Fukui et al., 2013; Ehrenreich et al., 2014). There are only two HST datasets recording super-Earths: GJ-1214 b and 55 Cnc e (Bean et al., 2010; Berta et al., 2012; Kreidberg et al., 2014; Tsiaras et al., 2016a; Demory et al., 2016).

Bean et al. (2010); Berta et al. (2012) and Kreidberg et al. (2014) suggest either a metal-rich or a fully cloudy atmosphere for GJ-1214 b. Tsiaras et al. (2016a) suggested a hydrogen-rich atmosphere for 55 Cnc e and a possible presence of HCN detectable with future observations.

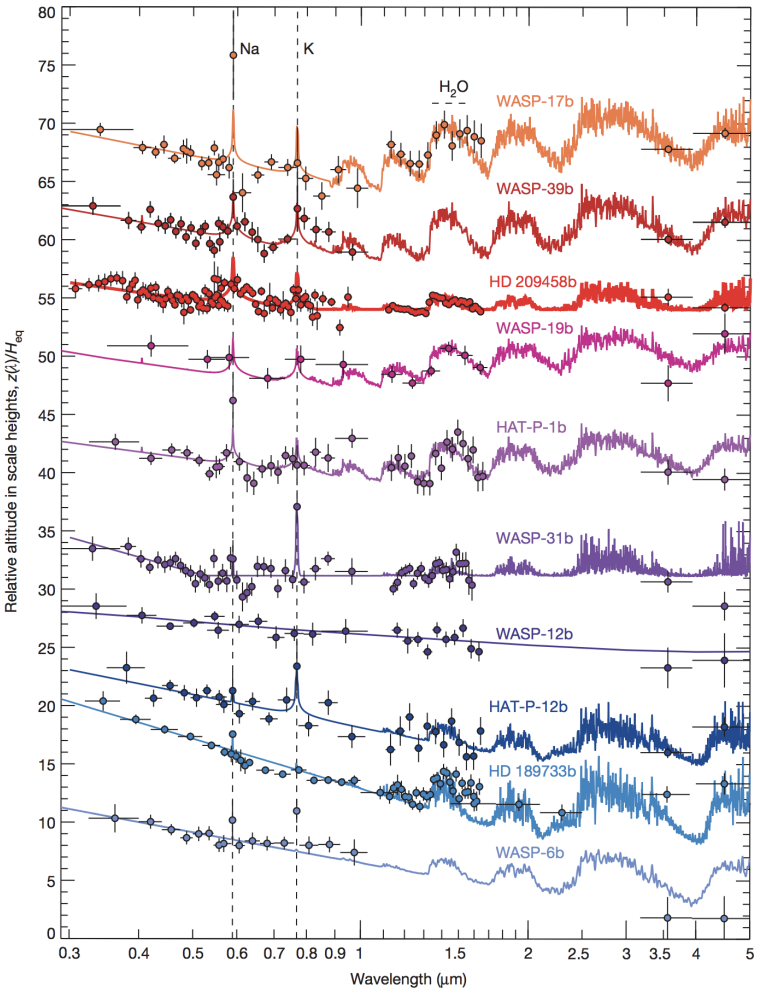

Figure 1.12: Atmosphere of giant planets using a combination of HST/Spitzer data. The presence of water dominates the atmosphere of most of the planets. (from Sing et al. (2016a)).

1.4 Next generation of space instrumentation for exoplanet spectroscopy

To understand what the planetary formation and evolution mechanisms are, we need to observe and characterise the atmospheres of a statistically significant sample of exoplanets. It is important to use instruments dedicated to atmospheric spectroscopy to pursue this aim.

Currently, most of the exoplanetary atmospheric spectra have been recorded with the WFC3 (Wide Field Camera 3) on the Hubble Space Telescope which allows us to probe a very limited spectral range, i.e. $1.1\mu\text{m} - 1.7\mu\text{m}$. That explains why water features are the most evident. Detection of other molecules like carbon monoxide and methane have been proposed immediately upon other instruments have been used (Swain et al., 2008a; Désert et al., 2009; Swain et al., 2009; Tinetti et al., 2010). Low-amplitude features can be interpreted as noise or presence of clouds. In some WFC3 spectra the features a wavelengths lower than 1.5μm can be interpreted either with TiO/VO signature (see Figure 1.13) or with Mie scattering.

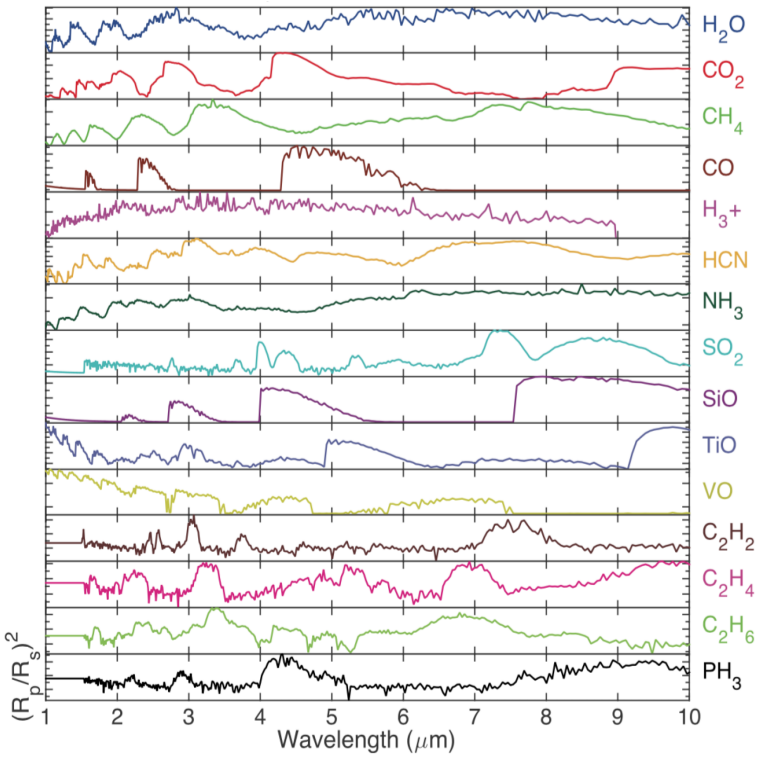

Figure 1.13: Spectral features in the wavelength range $1.0\mu\text{m} - 10.0\mu\text{m}$ from different molecules st resolution $R = 100$ (courtesy of Dr I.P. Waldmann)

Solutions found in the WFC3 spectral range are not well constrained. It is therefore imperative to increase either the instrument resolution or the wavelength range. The analysis of better spectra will reduce the degeneracy of spectral features, i.e. a non-unique solution explaining the

same input spectrum, and confirm the presence of many molecular features suggested today.

The next generation of exoplanetary spectra, with a broader wavelength range and higher accuracy, will come with James Webb Space Telescope (JWST) (Beichman et al., 2014; Cowan et al., 2015; Batalha et al., 2015; Barstow et al., 2015; Greene et al., 2016; Barstow and Irwin, 2016), a NASA/ESA space mission scheduled for launch in March 2021.

In order to characterise exoplanetary atmospheres, there are two dedicated space missions, scheduled for launch in the next decade: Twinkle (Tessenyi et al., 2017) and ARIEL (Tinetti et al., 2016).

1.4.1 JWST: James Webb Space Telescope

JWST[6], with a 6 metre-class telescope, is a NASA/ESA space mission scheduled for launch in 2021 towards the L2 Lagrangian point (see Fig 1.14). It will have four instruments on board: a near-infrared camera, a near-infrared multi-object spectrograph and a tunable filter imager which will cover the wavelength range between 0.6μm-5.0μm, while the mid-infrared instrument is designed to do both imaging and spectroscopy in the wavelength range between 5.0μm-29.0μm (Gardner et al., 2006).

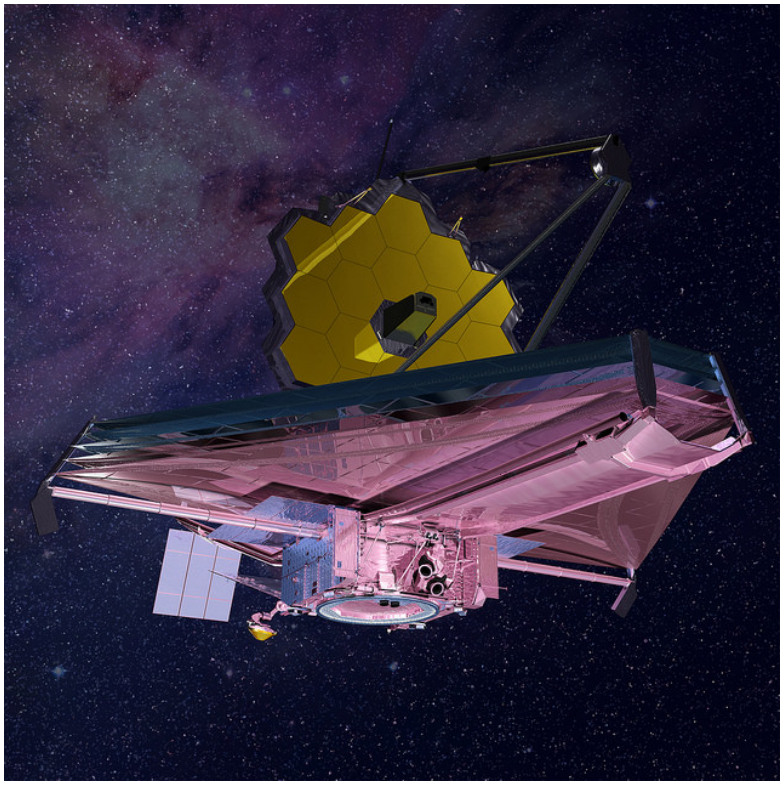

Figure 1.14: Artistic Image of the James Webb Space Telescope. Image credit: Northrop Grumman.

[6] `https://jwst.nasa.gov/`

The JWST mission concept is divided into 4 main themes (Gardner et al., 2006):

1. The End of Dark Ages: this theme seeks to identify the first luminous source to form and determine the ionization history of the early universe;

2. The Assembly of Galaxies: this theme seeks to determine how galaxies and the dark matter, gas, stars, metals, morphological structures and active nuclei within them evolved from the epoch of ionization to the present day;

3. The Birth of Stars and Protoplanetary Systems: this theme seeks to study the birth and early evolution of stars;

4. Planetary Systems and the Origins of Life: this them seeks to determine the physical and chemical characteristics of planets, including the Solar System planets. Furthermore, it will investigate the potential of the origin of life in the planetary systems.

Within the fourth theme, Planetary Systems and the Origins of Life, JWST will use the Near-Infrared Spectrograph (NIRSpec). This instrument was developed by the European Space Agency (ESA). The instrument have seven disperser covering the wavelength range from 0.6μm-5.3μm, with spectral resolution from $R \sim 100$ to $R \sim 2700$, and will allow to study about one hundreds of planetary atmospheres (Birkmann et al., 2016).

1.4.2 Twinkle

The Twinkle space mission [7] consists of a 45 cm telescope (see Fig 1.15), is a low cost mission expected to be launched in late 2020 in a low-Earth orbit (Sun-synchronous polar orbit).

The twinkle space mission will study hundreds of exoplanets with two available wavelength channels in the visible and the infrared wavelengths. The visible channel will span the wavelength range between 0.4μm-1.0μm, while the infrared channel will be sensitive in the wavelength range between 1.3μm-4.5μm. Twinkle maximum resolving power is $R = 300$ (Tessenyi et al., 2017).

1.4.3 ARIEL: The Atmospheric Remote-sensing Infrared Exoplanet Large-survey

The ARIEL space mission[8], consists of a 1-metre class telescope (see Fig 1.16) and it is a ESA space mission dedicated to characterise the atmosphere of ∼1000 exoplanets (Tinetti et al., 2018). It is scheduled for a launch in mid-2028 towards the L2 Lagrangian point.

[7] http://www.twinkle-spacemission.co.uk
[8] https://ariel-spacemission.eu/

Figure 1.15: Model representation of the Twinkle space telescope. Image credit: Twinkle/SSTL.

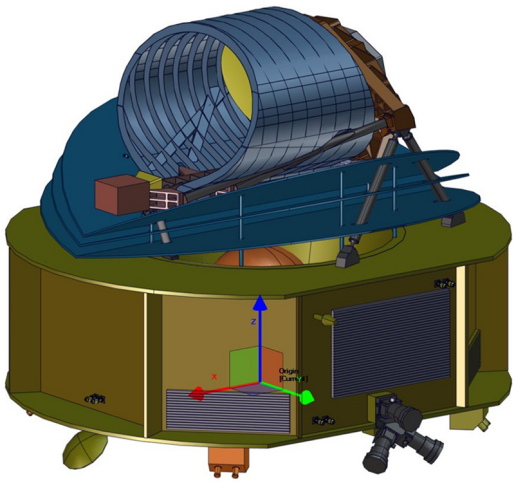

Figure 1.16: Model representation of the ARIEL space telescope. Image credit: ARIEL team.

The wavelength coverage between 0.5μm and 7.8μm, will allow to distinguish molecular bands in the medium-infrared wavelengths. In the infrared channel, from 1.95μm and 7.8μm the spectral resolution will vary from $R \sim 30$ to $R \sim 200$ (Pascale et al., 2018).

1.5 Comparison between the current state-of-art technology and future space instrumentation

The current state-of-art technology in exoplanetary atmospheric spectroscopy is represented by the WFC3 camera mounted on board of the Hubble Space Telescope (HST). WFC3 camera wavelength range is between 1.1μm and 1.8μm (Stiavelli and Robberto, 2003). In order to constrain uniquely a parameter solution related to an input spectrum it is important the coverage of the wavelength range and/or the spectral resolution. New-generation space missions which will characterise the atmosphere of the exoplanets, will return better results than WFC3 camera, since they have a wider wavelength coverage and a higher spectral resolution.

In Figure 1.17 I show the results of the atmospheric analysis for a Hot-Jupiter atmosphere, using simulated observations from WFC3/HST, ARIEL and JWST. Each cell corresponds to the space in which a parameter lies. Using a Bayesian approach (see chapter 3) it is possible to sample and constrain the parameter space according to the quality of the input spectrum. Figure 1.17 shows in green the constraints of the parameters space related to the input spectrum of WFC3. In yellow and red are shown the constraints given from, respectively, the ARIEL and JWST observations. We see that, while WFC3 camera spectrum does not manage to constraint the atmospheric parameters space. On the contrary, ARIEL and JWST will identify a unique solution with a higher precision than Hubble.

1.6 Analysis methods: From Bayesian analysis to Deep learning

Atmospheric analysis can be done using computationally intensive Bayesian models (see chapter 3). On the other hand, it is possible to optimise current Bayesian modelling using 'intelligent' algorithms. Nowadays, Artificial Intelligence (AI) algorithms are becoming very popular and spreading out in many fields including scientific research. Poole et al. (1997) defined the term "Artificial Intelligence" as "Computational Intelligence", that is the study of the design of intelligent agents. An intelligent agent is a system that acts intelligently (Poole et al., 1997). Machine learning (ML) is a sub-field of AI that uses statistical techniques to give computer systems the

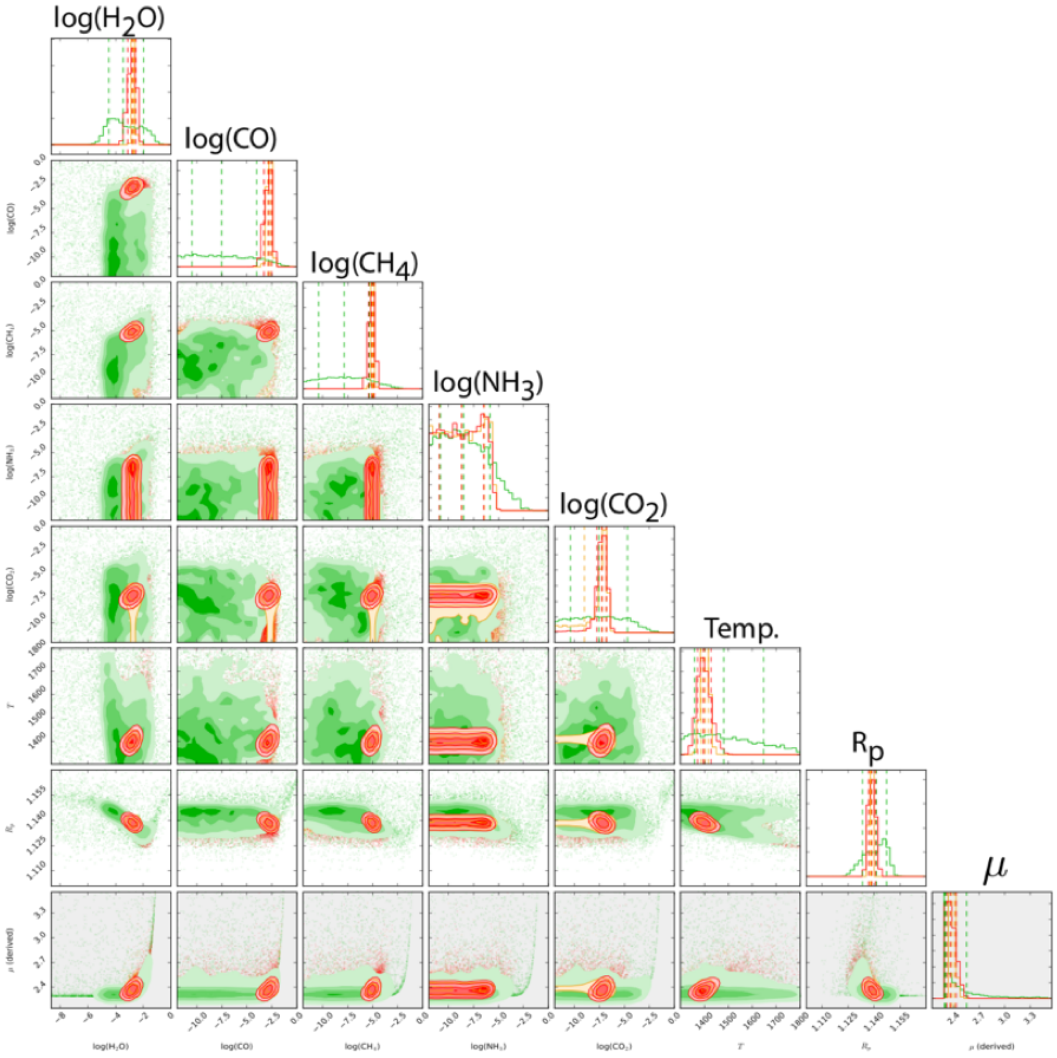

Figure 1.17: Comparison of retrieved parameters with three different space missions instrumentations: **green:** WFC3 on Hubble, **red:** JWST and **yellow:** ARIEL (Image courtesy of Dr Ingo Waldmann).

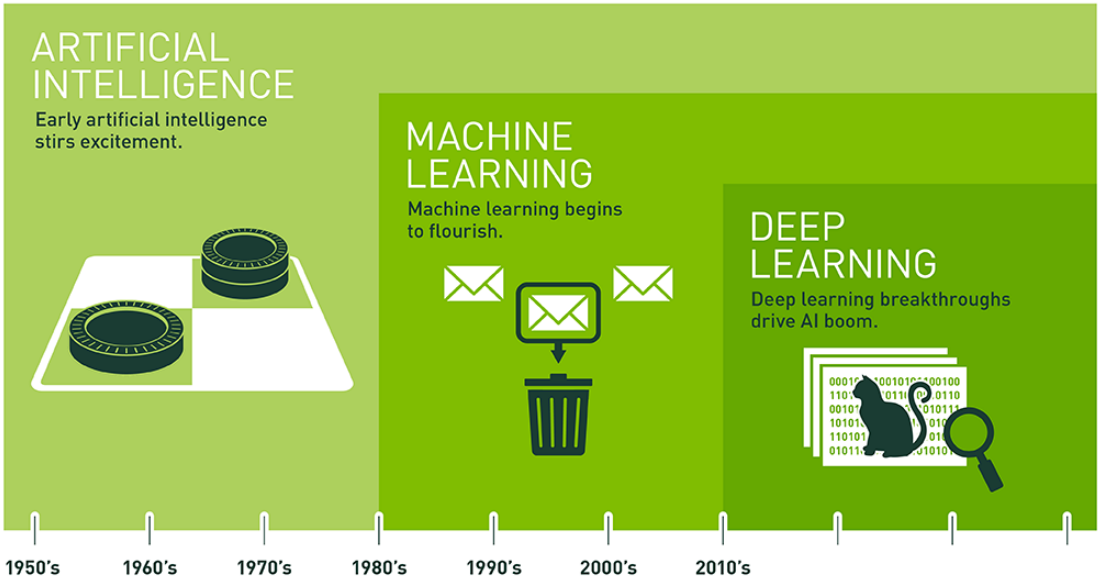

Figure 1.18: Time line of artificial intelligence. AI is a broad class of algorithms which learn some information from an input dataset. Machine Learning is a subset of the Artificial Intelligence. Deep Learning is a subset of the Machine Learning class algorithms. Credit Image: NVIDIA.

ability to learn, i.e. progressively improve performance on a specific task, from data, without being explicitly programmed (Samuel, 1959). Deep Learning (DL) is a sub-field of Machine Learning and, according to Deng and Yu (2014), it is a class of algorithms that:

- Use a cascade of multiple layers of non-linear processing units for feature extraction and transformation;
- Learn in supervised and/or unsupervised manners;
- Learn multiple levels of representation that correspond to different levels of abstraction; the levels form a hierarchy of concepts.

AI is then a broad class of algorithms which include many different approaches that make possible for an artificial machine to learn and generalise an information from a dataset. ML and DL are both sub-field of a more general class of AI algorithms (see Fig 1.18).

Deep Learning is helping people to shape and model very complex problems. Just ten years ago no one could have predicted that today machines can surpass human-level performances in feature recognition and detection on an image (Uçar et al., 2017; Deng and Yu, 2014; Szegedy et al., 2013; Krizhevsky et al., 2012; Russakovsky et al., 2015; Berg et al., 2010; Yan et al., 2016), speech recognition (Higy et al., 2018; Schatz et al., 2018; Izumi et al., 2018; Jiang et al., 2017; Edwards et al., 2017) or mimic realistically the human voice (Michaely et al., 2017; Kleijn et al., 2017; van den Oord et al., 2017).

Deep learning algorithms are fundamentally different from any other traditional approach to data analysis. These algorithms learn quickly directly from a raw image or dataset. Deep learning algorithms will be introduced in chapter 5 as I will apply it to atmospheric spectroscopy in chapter 6.

In 2010 began the ImageNet Large Scale Visual Recognition Challenge (ILSVRC). Since then tens of teams have tested their algorithms on a given dataset, competing to achieve the highest accuracy on visual recognition tasks, i.e. image classification or fine feature extraction tasks (Russakovsky et al., 2015; Berg et al., 2010), using deep neural networks like Convolutional Neural Networks (CNN). As of today, CNNs outperform recognition performances of traditional feature extraction methods (Yan et al., 2016; Ouyang et al., 2015; Zhang et al., 2015; Ren et al., 2015). In the following section, I list just some of the possible application of deep learning to science, showing how powerful and efficient can be such algorithms to help us understand more from nature.

Studying dark energy with generative models of galaxy images

Dark energy accelerates the universe expansion, and it is one of the major problems in modern cosmology. New cosmological surveys will study how dark energy works but all of them are affected by unavoidable biases, and therefore a precise and robust instrumental calibration is required for the analysis. Calibration is a big challenge in cosmology and requires a considerable number of galaxy images with high quality to be addressed. Ravanbakhsh et al. (2016) proposed to use a set of realistic generated galaxy images (Figure 1.19) using a conditional generative network in order to improve calibration challenges without needing a vast amount of high-quality real images.

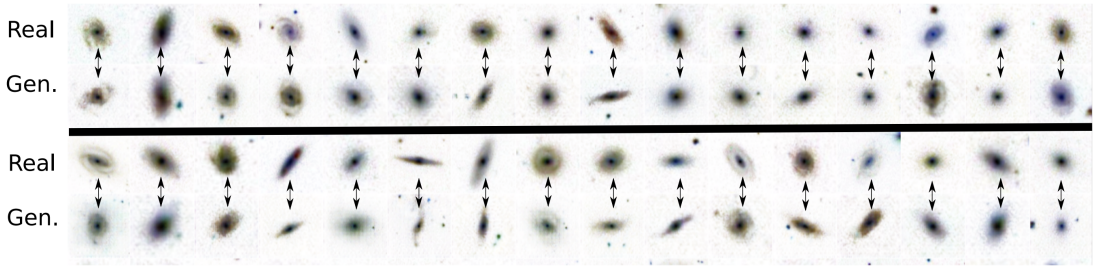

Figure 1.19: Comparison between real galaxy images from the GALAXY-ZOO dataset (upper part) and generated images using a trained conditional generative adversarial network (image from Ravanbakhsh et al. (2016)).

Climate simulations

Deep learning algorithms have been helpful also in climate simulations. Racah et al. (2016) used semi-supervised algorithms to find extreme weather events in large-scale climate simulations. This field is essential to predict potentially hazardous weather events and act promptly to save the ecosystem and inhabited areas. In their work, they use a CNN able to recognise many different types of spatially localised weather feature like hurricanes, extra-tropical cyclones, weather fronts and others.

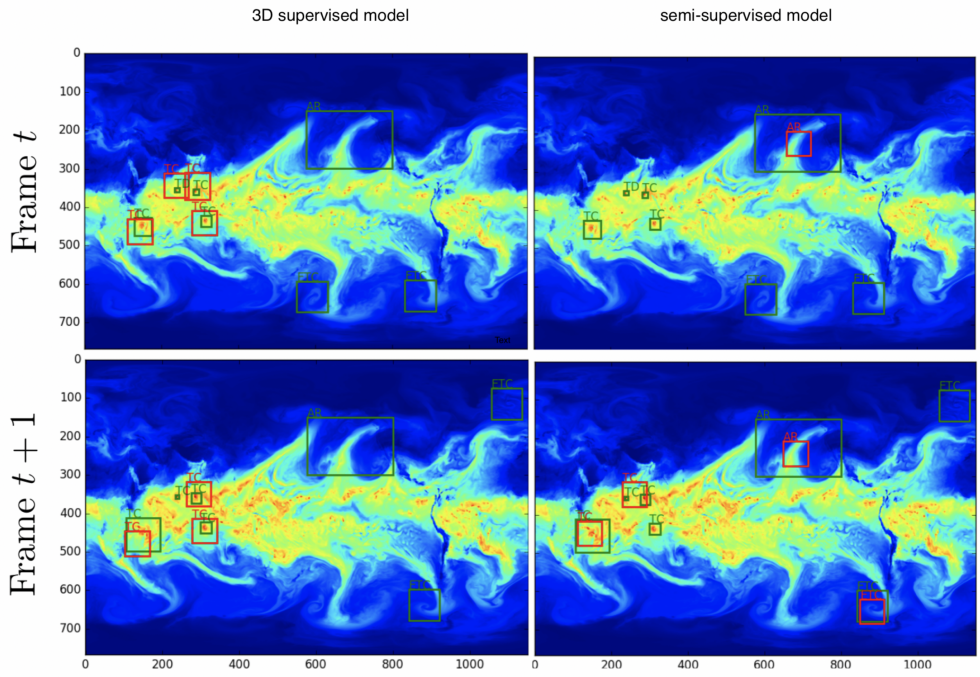

Figure 1.20: Simulation of a water vapour column evolution over 6 hours. In green, there is the ground truth and in red the high confidence predictions of the appearance of atmospheric features. On the left, there is a 3D supervised model, and on the right, there is the prediction of a semi-supervised algorithm (image modified from Racah et al. (2016)).

The trained CNN can be used to predict the spatiotemporal evolution of these features. Figure 1.20 shows the evolution of water vapour in 6 hours. A trained CNN can predict with high confidence the position and properties of the atmospheric features.

Exoplanetary atmospheres characterisation

Waldmann (2016) introduced RoBErt (Robotic Exoplanet Recognition), a Deep Belief Network (DBN, see chapter 5) able to recognise molecular structure in an exoplanetary atmosphere.

RobERt tries to recognise molecular features with a deep belief network trained on hundreds of thousands of atmospheric spectra generated by TauREx (Waldmann et al., 2015a,b). Once

trained it manages to associate to an input spectrum a label corresponding to the presence of a particular set of molecules. More details of this first, recent application of a deep learning algorithm to planetary atmospheres are shown in chapter 5.

Following the idea of Waldmann (2016), I will introduce in chapter 6 ExoGAN (Exoplanet Generative Adversarial Network), a neural network which detects the presence of molecular species estimates the abundance of them and also retrieve physical parameters from an input spectrum.

1.7 Thesis outline

The main goal of this thesis is to offer a new approach to the study of exoplanetary atmospheres. I show how the "classical" tools are currently used in this field and test their limits. Atmospheric spectroscopy analysis is currently possible using computationally intensive Bayesian algorithms. With this thesis I offer a different algorithm, ExoGAN, i.e. an alternative method which can speed up significantly decrease the computational time for an exoplanetary atmosphere analysis. ExoGAN can be used either as a stand-alone algorithm or in synergy with Bayesian modelling. In both cases, ExoGAN is able to reduce significantly the computational time. As I will explain more-in-detail in chapter 6, ExoGAN consists of a very popular DL algorithm extensively used in many fields of human knowledge.

This thesis is focused on the characterisation techniques of exoplanets. Starting from the description of classical retrieval methods, their application to HST/WFC3 camera and their optimisation using deep learning. After the description of conventional retrieval techniques, I describe an optimal target list of planets which maximise the scientific return using a space mission dedicated to transit spectroscopy.

In chapter 2, I describe the atmospheric models that can be used to interpret exoplanetary atmospheric spectra. These models can be used as forward models for a fully Bayesian code. In chapter 3 I explain the rationale behind the Bayesian analysis and I introduce TauREx, a retrieval code for transmission and emission spectroscopy.

In chapter 4, I show some classical retrieval techniques applied to some real cases thanks to the data extracted from the WFC3 camera on the Hubble Space Telescope. I used the fully-Bayesian TauREx retrieval code to do such analysis.

Usually, a Bayesian analysis is highly computationally intensive, the use of deep learning algorithms can help in speeding up the computational time significantly if used correctly. In the last few years, Deep Learning became more pervasive in astrophysics, and it can be used to do a preliminary atmospheric analysis. In chapter 5, I explain the rationale behind deep learning

techniques and show the utility of Deep Learning algorithms in astrophysics.

In chapter 6, I introduce ExoGAN (Exoplanets Generative Adversarial Network), a new generation neural network able to retrieve the parameters of an exoplanetary atmosphere returning a probability distribution for each retrieved parameter that can be used either as final solution for out analysis or as an input informative prior distribution for a next Bayesian analysis of the same spectrum.

Finally, the optimal target choice for space mission dedicated to transit spectroscopy like ARIEL has been explained in chapter 7. The choice of targets is essential to maximise the scientific return of a space mission.

Chapter 2

Atmospheric spectroscopy

Radiation propagates from the host star, travels through vacuum space and, after it travelled between the star-planet distance, it interacts with the planetary atmosphere, where light is absorbed, scattered and emitted by the atmosphere depending on its chemical and physical properties. The interaction between matter and radiation is a fundamental topic in astrophysics and planetary science. In this chapter, I focus on basic concepts of radiative transfer which are important to analyse a planetary atmosphere I will use the notation of (Liou, 2002).

2.1 Radiative transfer of planetary atmospheres: basic concepts

2.1.1 Transmission spectroscopy

When radiation passes through a medium, it becomes fainter because of the interaction with the molecules in it. Let s be the distance (in cm) traversed by the radiation inside the planetary atmosphere. Let I_λ be the incoming radiation as a function of the wavelength λ (in units of $\mathrm{W\,m^{-2}\,sr^{-1}\,m^{-1}}$) and $I_\lambda + \mathrm{d}I_\lambda$ the radiation after the interaction with a medium of thickness $\mathrm{d}s$ in the direction of propagation. then:

$$\mathrm{d}I_\lambda = -\sigma_\lambda \rho_N I_\lambda \mathrm{d}s, \tag{2.1}$$

where σ_λ is the absorption cross section as a function of wavelength λ (in units of $\mathrm{cm^2 mol^{-1}}$) and ρ_N is the number density of the medium (in units of $\mathrm{mol\,cm^{-3}}$) . Eq 2.1 can be re-written:

$$\frac{\mathrm{d}I_\lambda}{I_\lambda} = -\sigma_\lambda \rho_N \mathrm{d}s. \tag{2.2}$$

We define the optical path l_o as:

$$l_o = \int \rho_N \mathrm{d}s, \tag{2.3}$$

and the optical depth τ_λ:

$$\tau_\lambda = \int \sigma_\lambda \rho_N ds = \sigma_\lambda l_o. \tag{2.4}$$

At a wavelength λ, the radiation intensity from the top of the atmosphere z_∞ to altitude z is:

$$I_\lambda(z) = I_\lambda(0) \exp\left(-\int_z^{z_\infty} \sigma_\lambda(z')\rho_N(z')\mathrm{d}z'\right). \tag{2.5}$$

This is known as the Lambert-Beer-Bouguer law:

$$I_\lambda(z) = I_\lambda(0) e^{-\tau_\lambda(z)}. \tag{2.6}$$

The radiation intensity can increase if we consider the possible emission by the atmospheric medium or multiple scattering processes in the atmosphere. These phenomena can contribute to increasing the number of photons at a particular wavelength in a certain direction. To take into account emission, we can add a source term in Equation 2.1:

$$\mathrm{d}I_\lambda = -\sigma_\lambda \rho_N I_\lambda \mathrm{d}s + j_\lambda \rho_N \mathrm{d}s. \tag{2.7}$$

For convenience, we define the source function J_λ:

$$J_\lambda = \frac{j_\lambda}{\sigma_\lambda}, \tag{2.8}$$

so that Equation 2.7 can be rewritten as:

$$\frac{\mathrm{dI}_\lambda}{\sigma_\lambda \rho_N \mathrm{d}s} = -I_\lambda + J_\lambda. \tag{2.9}$$

Equation 2.9 is also known as Schwarzschild's equation.

2.1.2 Emission spectroscopy

The source term in Equation 2.9 can describe re-emission from planetary atmospheres. Assuming a non-scattering atmosphere in LTE (Local Thermodynamic Equilibrium) the radiative transfer equation is:

$$\mu \frac{\mathrm{d}I_\lambda(\tau,\mu)}{\mathrm{d}\tau} = I_\lambda(\tau,\mu) - B_\lambda(T), \tag{2.10}$$

where I_λ is the radiation intensity as a function of wavelength λ, $B_\lambda(T)$ the black-body radiation at temperature T, $\mu = \cos\phi$, with ϕ the angle between the radiation direction and the normal to the surface tangent plane. τ_λ is the total optical depth, defined by:

$$\tau_\lambda(z) = \sum_{i=1}^{N_{\mathrm{gas}}} \tau_{\lambda,i}(z), \tag{2.11}$$

where $\tau_{\lambda,i}$ is the optical depth of the i-th species defined as:

$$\tau_{\lambda,i} = \int_z^{z_\infty} \sigma_{\lambda,i}(z')\chi_i(z')\rho_N(z')\mathrm{d}z', \tag{2.12}$$

with $\sigma_{\lambda,i}$ the absorption cross-section, χ_i the mole fraction of the i-th molecules and ρ_N the density of the atmosphere at altitude z. By solving Equation 2.10 we have:

$$I_\lambda(\tau_\lambda,\mu) = I_\lambda(\tau_s)e^{-(\tau_s-\tau_\lambda)/\mu} + \int_{\tau_\lambda}^{\tau_s} B_\lambda\left(T_{\tau'_\lambda}\right) e^{(\tau'_\lambda-\tau_\lambda)/\mu}\frac{\mathrm{d}\tau'_\lambda}{\mu}. \tag{2.13}$$

The first term in Equation 2.13 is the radiation emitted at the planetary surface and the second term is the integrated emission for each atmospheric layer. The monochromatic transmittance is defined as:

$$\mathcal{T}_\lambda\left(\tau_\lambda/\mu\right) = e^{-\frac{\tau_\lambda}{\mu}}, \tag{2.14}$$

and then:

$$\frac{\partial\mathcal{T}_\lambda(\tau_\lambda/\mu)}{\partial\tau_\lambda} = -\frac{1}{\mu}e^{-\tau_\lambda/\mu}. \tag{2.15}$$

Using the definition of transmittance in Equations 2.14 and 2.15, the integrated radiation at the top of the atmosphere ($\tau = 0, z = \infty$) is:

$$I_{\lambda,0} = I_\lambda(\tau_\lambda = 0) = B_\lambda(T_{\mathrm{s}})e^{-\tau_{\mathrm{s}}/\mu} + \int_{\tau_{\mathrm{s}}}^{0} B_\lambda(T_{\tau_\lambda})\frac{\partial\mathcal{T}_\lambda(\tau_\lambda/\mu)}{\partial\tau_\lambda}\mathrm{d}\tau_\lambda. \tag{2.16}$$

To estimate numerically 2.16, we need to discretise these integrals, introducing $N_{\rm layers}$ atmospheric layers and $N_{\rm gas}$ molecules:

$$\begin{aligned} I_{\lambda,0} = 2\pi \sum_{j}^{N_{\rm layers}} \sum_{g}^{N_{\rm quad}} B(T_{\rm surf}) \left[\exp\left(- \sum_{k=0}^{N_{\rm layers}} \sum_{t}^{N_{\rm gas}} \sigma_{t,k} \rho_{Nk} dz_k \right) \right] \mu_g w_g + \\ + 2\pi \sum_{j}^{N_{\rm layers}-1} \sum_{g}^{N_{\rm quad}} B(T_j) \left[\exp\left(- \sum_{k=j+1}^{N_{\rm layers}} \sum_{t}^{N_{\rm gas}} \sigma_{t,k} \rho_{Nk} dz_k \right) - \right. \\ \left. - \exp\left(- \sum_{k=j}^{N_{\rm layers}} \sum_{t}^{N_{\rm gas}} \sigma_{t,k} \rho_{Nk} dz_k \right) \right] \mu_g w_g. \end{aligned} \tag{2.17}$$

The integration is calculated at the zenith angle using the Legendre-Gauss quadrature method with $N_{\rm quad}$ points. μ_g is the gth quadrature point and w_g is the corresponding weight, dz_k is the width of the kth atmospheric layer. A good compromise between accuracy and computational speed is the use of $N_{quad} = 4$. The first part of the equation represents the atmospheric emission, from the surface, at the top of the atmosphere. The second term is the emission from the remaining layers.

2.1.3 Scattering processes in the atmosphere

In this section, I briefly discuss the diffusion of stellar radiation in planetary atmospheres. With the word "diffusion" I mean multiple scattering of the stellar radiation. Scattering, absorption and re-emission depend on the chemical and physical properties of the particulate composing the atmosphere.

Let us define the coefficients (in units of length) β_e, β_s and β_a related to, respectively, extinction, scattering and absorption, as:

$$\beta_{e\,,s\,,a} = \int_{\Delta z} \sigma_{e,s,a}(z) n(z) \mathrm{d}z / \Delta z, \tag{2.18}$$

where $\sigma_{\cdot}$ is the cross-section related to the '$\cdot$' phenomenon and n is the particle number in the volume considered. We call phase function $P(\mu, \phi; \mu', \phi')$, the redirection of a ray of the incoming flux from a direction (μ', ϕ') to the outgoing direction (μ, ϕ). By defining the differential length $\Delta s = \Delta z / \mu$, we can define the differential intensity

$$\begin{aligned} \frac{\Delta I(z;\mu,\phi)}{\Delta z/\mu} = \beta_e I(z;\mu,\phi) + \beta_s F_* e^{-\tau/\mu} \cdot P(\mu,\phi;-\mu_0,\phi_0)/4\pi \\ + \beta_s \int_0^{2\pi} \int_{-1}^{1} I(z,\mu',\phi') \cdot P(\mu,\phi;\mu',\phi')/4\pi \mathrm{d}\mu' \mathrm{d}\phi' + \beta_a B(T(z)), \end{aligned} \tag{2.19}$$

where F_* is the stellar flux density. The integration in Equation 2.19 is made over the 4π solid angle and assuming radiative equilibrium, the absorption is equal to the emission, according to the Kirchhoff's and Planck laws (Liou, 2002).

Let us define the single-scattering albedo as the ratio of the scattering coefficient to the extinction coefficient:

$$\tilde{\omega} = \frac{\beta_s}{\beta_e} \qquad \text{or} \qquad 1 - \tilde{\omega} = \frac{\beta_a}{\beta_e}, \tag{2.20}$$

and the optical depth as:

$$\tau = \int_z^\infty \beta_e \mathrm{d}z'. \tag{2.21}$$

Then, the Swartzchild's equation can be rewritten as:

$$\mu \frac{\mathrm{d}I(\tau;\mu,\phi))}{\mathrm{d}\tau} = I(\tau;\mu,\phi) - J(\tau;\mu,\phi), \tag{2.22}$$

with the source function given by:

$$\begin{aligned} J(\tau;\mu,\phi) = \frac{\tilde{\omega}}{4\pi} \int_0^{2\pi} \int_{-1}^{1} I(\tau;\mu',\phi') P(\mu,\phi;\mu',\phi') \mathrm{d}\mu' \mathrm{d}\phi' \\ + \frac{\tilde{\omega}}{4\pi} F_* P(\mu,\phi;-\mu_0,\phi_0) e^{\tau/\mu_0} + (1-\tilde{\omega}) B\left(T(z)\right). \end{aligned} \tag{2.23}$$

In the visible and the ultraviolet, multiple scattering phenomena are significant, and atmospheric models need to consider them. In the infrared, they are negligible and can be neglected.

2.1.4 Transit spectroscopy

During transit, the stellar light passes through the atmosphere, and it is absorbed by it depending on its chemistry and structure, as shown in Figure 2.1.

If N_{gas} is the number of gases in the atmosphere, and l is the optical path along the line of sight, the optical depth as a function of the altitude z is:

$$\tau_\lambda(z) = \sum_{i=0}^{N_{\mathrm{gas}}} \left(\int_0^{l(z)} \sigma_{i,\lambda(z')} \chi_i(z') \rho_N(z') \mathrm{d}l \right), \tag{2.24}$$

where χ_i is the mixing ratio of the molecule i and $\sigma_{i,\lambda}$ is the absorption cross section for the i-th molecule at wavelength λ.

As shown in Figure 2.1, in which we define z, z', $\mathrm{d}z$ and the radius of the planet R_p the element $\mathrm{d}l$ can be expressed as a function of the altitude z:

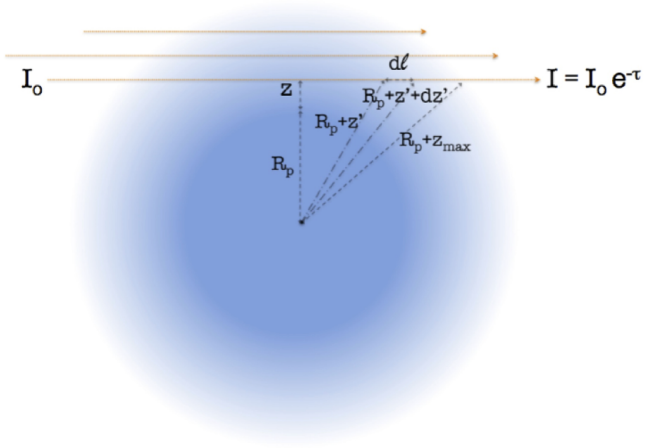

Figure 2.1: Illustration of transit spectroscopy geometry (from Tinetti et al. (2012)).

$$\mathrm{d}l = 2\left(\sqrt{(R_p + z + \mathrm{d}z')^2 - (R_p + z')^2} - \sqrt{(R_p + z)^2 - (R_p + z')^2}\right). \tag{2.25}$$

By integrating Eq 2.24 along the optical path, we can define the equivalent area $A_{eq}(\lambda)$:

$$A_{eq}(\lambda) = 2\int_0^{z_\infty} (R_p + z)\left(1 - e^{-\tau(\lambda,z)}\right)\mathrm{d}z. \tag{2.26}$$

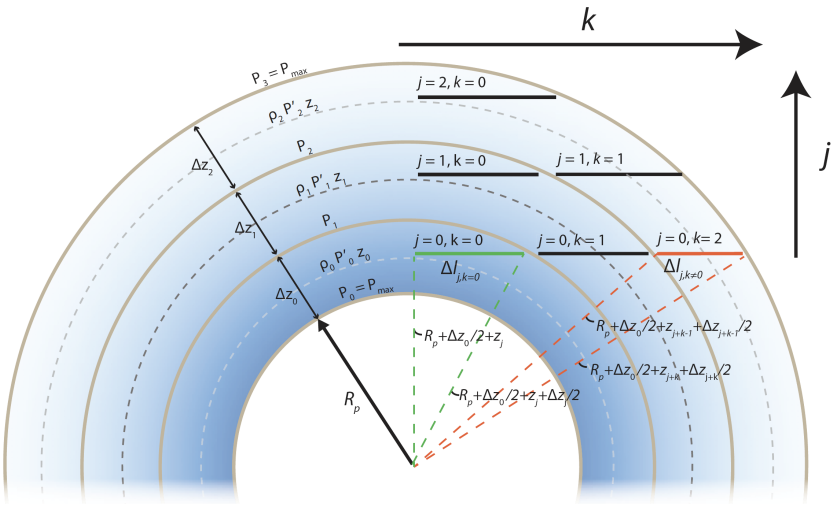

Figure 2.2: Layer division on an atmosphere during a primary transit. Solid circles are the pressure boundaries for each atmospheric layer, and the dashed circles are the middle layer parts for which the pressure P_i', the number density of the i-th species $\rho_{N,i}$ and the altitude z (Figure made by Dr Marco Rocchetto).

In order to integrate numerically Equation 2.26 we divide the atmosphere into N_{layers} layers and N_{gas} molecules:

$$A_{eq}(\lambda) \approx 2 \sum_{j=0}^{N_{\text{layers}}} \left((R_p + z_j) \left\{ 1 - \exp \left[- \sum_{k=0}^{N_{\text{layers}-j}} \left(\sum_{t}^{N_{\text{gas}}} \sigma_{t,j+k}(\lambda) \cdot \chi_{t,j+k} \cdot \rho_{N,j+k} \cdot 2\Delta l_{j+k} \right) \right] \right\} \Delta z_j \right), \tag{2.27}$$

where $\Delta l_{j,k}$:

$$\begin{aligned} \Delta l_{j,k\neq 0} = & \sqrt{\left(R_p + \frac{\Delta z_0}{2} + z_{j+k} + \frac{\Delta z_{j+k}}{2} \right)^2 - \left(R_p + \frac{\Delta z_0}{2} + z_j \right)^2} - \\ & - \sqrt{\left(R_p + \frac{\Delta z_0}{2} + z_{j+k-1} + \frac{\Delta z_{j+k-1}}{2} \right)^2 - \left(R_p + \frac{\Delta z_0}{2} + z_j \right)^2}, \end{aligned} \tag{2.28}$$

and

$$\Delta l_{j,k=0} = \sqrt{\left(R_p + \frac{\Delta z_0}{2} + z_j + \frac{\Delta z_j}{2} \right)^2 - \left(R_p + \frac{\Delta z_0}{2} + z_j \right)^2}. \tag{2.29}$$

The change in altitude Δz_j is:

$$\Delta z_j = -H_i \log \left(\frac{P_{i+1}}{P_i} \right), \tag{2.30}$$

where H_i is the scale height of the i-th layer and P_i, P_{i+1} are the pressure boundaries. We take into account collision-induced-absorption for H_2-H_2 and H_2-He pairs from HITRAN (Richard et al., 2012).

Atmospheric aerosols can be approximated as spheres which scatter the incident light. By defining the parameter $x \cong 2\pi\alpha/\lambda$, with α the radius of the spherical aerosol or cloud particle and λ the wavelength associated to the incident light. If $x \ll 1$ light diffusion can be described by the Rayleigh scattering. When $x \geq 1$ scattering events are described by the Lorenz-Mie scattering from the name of the two physicists who derived a solution for the interaction between a plane wave light and an isotropic homogeneous spherical particle independently (Lorenz, 1890; Mie, 1908).

Mie scattering cross-section can be parametrised according to Lee et al. (2013a) by defining the extinction coefficient Q_{ext}:

$$Q_{\text{ext}} = \frac{5}{Q_0 x^{-4} + x^{0.2}}, \tag{2.31}$$

where Q_0 determines the exact x-value where Q_{ext} peaks. Usually, more volatile materials have $Q_0 \sim 100$ and silicates are better described by $Q_0 \sim 10$ (Lee et al., 2013a). From the extinction coefficient, we can define the Mie cross section as:

$$\sigma_{\text{Mie}} = Q_{\text{ext}} \pi \alpha^2. \tag{2.32}$$

Finally, the equivalent area $A_e q(\lambda)$ can be computed, and the total transit depth as a function of wavelength, $D(\lambda)$ can be defined as:

$$D(\lambda) = \frac{R_p^2 + A_{eq}(\lambda)}{R_*^2}, \tag{2.33}$$

with R_p and R_* the planetary and stellar radius respectively.

2.1.5 The observed flux

After calculating the radiation intensity, we can finally simulate the planetary spectrum as:

$$\frac{F_{p,\lambda}}{F_{*,\lambda}} = \frac{I_{\lambda,0}}{I_{*,\lambda}} \left(\frac{R_p}{R_*} \right)^2, \tag{2.34}$$

where $I_{*,\lambda}$ is the stellar intensity as a function of wavelength.

Equation 2.34 describes the observed planetary flux in units of the stellar flux. It describes in general terms the observation in any phase of the orbit. The $I_{\lambda,0}$ represents the integrated radiation at the top of the planetary atmospher,e and it is calculated by solving the radiative transfer equation taking into account the conditions described for emission (section 2.1.2), reflection (section 2.1.3) and transit spectroscopy (section 2.1.4) Equation 2.34 is elegant and straightforward, however solving the radiative transfer can be very computing intensive. For this reason it is crucial to use of an efficient code to analyse the exoplanetary atmospheres with the modern retrieval tools, which are described in chapter 3. .

2.1.6 Forward models

All the models described in the previous sections, i.e. the emission model (section 2.1.2), the scattering model (2.1.3) and the transmission model (section 2.1.4), describe a planetary atmosphere starting from a set of parameters. They are also called “forward models”, since they generate a unique atmospheric model starting from a set of parameters. In the next chapter I will introduce the “inverse problem” or “retrieval problem”, i.e. a model able to infer the set of parameters from an input atmospheric model. The forward models play a central role in solving the “retrieval problem” (see chapter 3).

2.2 Line Lists

Radiative transfer models require the use of opacity sources and then a series of line lists for every molecule taken into consideration. It is common to use of precomputed molecular opacities in the form of either absorption cross sections or absorption coefficients, as well as k-tables. Line lists are arranged as tables of transitions containing the information to compute molecular cross sections, in particular wavelengths and intensities. Among the line lists in use in the literature, the HITRAN database (Rothman et al., 2013) is mainly useful for Earth-like temperatures. Exoplanetary atmospheres often require temperature much higher of those found in the Solar System ($\sim 600 - 3000$K). At higher temperature, the possible rovibronic states increase: most of existing lab or theoretical data correspond to the low (room) temperature.

In order to solve this problem, there are different attempts to make the existing line lists more complete. The HITEMP (Rothman et al., 2010) database, for example, contains experimental and empirical high-temperature line-lists such as CO, CO_2, NO and OH. One of the most complete line-list databases which include high-temperature transitions and molecules useful to transit spectroscopy is from the ExoMol project (Tennyson et al., 2016), and it includes molecules like CH_4, NH_3, H_2O, HCN, SO_2, H_2S, SiO and others.

Line list databases provide the Einstein coefficients A_{if}, i.e. the probability of spontaneous emission for a particular transition from an initial state i to a final state f, the state degeneracies and lower state energies. The intensity of a transition from i to f can be calculated as:

$$I_{if}(T) = \frac{A_{if} g_{\mathrm{up}\,j}}{8\pi c \nu_{if}^2 Q(T)} \exp\left(-\frac{hcE_{\mathrm{low}\,j}}{k_B T}\right)\left[1 - \exp\left(-\frac{hc\nu_{if}}{k_B T}\right)\right], \tag{2.35}$$

with ν_{if} being the frequency associated with the emitted/absorbed photon, $g_{\mathrm{up}\,j}$ the upper state degeneracy, $E_{\mathrm{low}\,j}$ the lower state energy, A_{if} the Einstein coefficient of the transition, $k_B = 1.3806504 \cdot 10^{-16}\mathrm{erg\,K^{-1}}$ the Boltzmann constant, $c = 2.99792458 \cdot 10^{10}\mathrm{cm\,s^{-1}}$ the speed of light, $h = 6.62606885 \cdot 10^{-27}\mathrm{erg\,s}$ the Planck constant and $Q(T)$ the partition function, defined as:

$$Q(T) = \sum g_j \exp\left(-\frac{hcE_j}{k_B T}\right). \tag{2.36}$$

The cross sections σ_{if} are related to a transition between an initial state i and a final state f:

$$\sigma_{if} = \frac{I_{if}}{\Delta\tilde{\nu}} \int_{\tilde{\nu}-\Delta\tilde{\nu}_i/2}^{\tilde{\nu}+\Delta\tilde{\nu}_i/2} f(\tilde{\nu}; \tilde{\nu}_{0;f}, \alpha_f)\mathrm{d}\tilde{\nu}, \tag{2.37}$$

with I_{if} being defined in Equation 2.35, $f(\tilde{\nu};\tilde{\nu}_{0;f})$ being the line function of the cross-section (usually a Voigt profile, Olivero (1977)), $\nu_{0,f}$ the centre of the line and α_f the half width at half maximum of the line profile.

2.3 Summary and conclusions

In this chapter, I described the physics behind atmospheric spectroscopy. The emission and transit spectroscopy models, in particular, are implemented in the retrieval code I used to analyse real planetary spectra (see chapter 4). These models represent our knowledge about the physics of atmospheres and our way to explain our observations. The complexity of models is the reason why a retrieval code for atmospheric spectroscopy is usually computing-intensive. In the next chapters, I will introduce retrieval algorithms and their applications to transit spectroscopy.

Chapter 3

Atmospheric retrievals

In this chapter, I explain in detail the *retrieval problem*, also known as *inverse problem*. The most general way to define a solution space is to describe a probability distribution over the parameters that define such a space. The elements of the problem are the observable data, the a priori information on the state vector and the forward model parameters and the information on the physical correlations between the observable data and the a priori information. In the *retrieval problem* all these elements are mixed, and the output is a posteriori distribution over the model parameters, from which we can infer the best values (e.g. maximum likelihood or mid variance values) and their uncertainties. *Inverse problems* are widespread in the scientific community, we find them, for example, in astrophysics, in Earth sciences, quantum mechanics and in every field in which we have a complex model depending on a great number of parameters to explain the input dataset.

The way to solve this kind of problem can be divided into three parts:

- Parameterisation of the system: choice of the minimal set of parameters to be retrieved. In this phase, the parameter space is shaped according to the previous knowledge. The boundary conditions need to be defined according to the physics of the system;
- Forward modelling: application of the physical model starting from a set of parameters. The forward model needs to be compared with the observed data, and statistical confidence is applied to it, deciding how precise this model can explain the observation.
- Retrieval modelling or inverse modelling: use of forward models and calculation of the relative confidence interval, according to different algorithms, some of them explained in this chapter, it is possible to constrain the parameters space and the most probable solution, together with the error bars.

The very first retrieval technique applied to planetary atmospheres was in the '50s for Earth studies, with the first meteorological satellites (Kaplan, 1952; King, 1956; Kellogg, 1964; Wark, 1961; Yamamoto and Wark, 1961). A few years later they were improved with dedicated sounders (Chahine, 1977b; Wark, 1961, 1970; Hanel and Conrath, 1970; Conrath et al., 1970; Conrath and Hanel, 1972). Some pioneering work has been done using indirect measurements to study Solar System's planets atmospheres (Irvine and Lenoble, 1974; Chahine, 1977a; Burangulov, 1977; Pavelev, 1980), moons and Saturn's rings (Smith and Doose, 1979; Clark and McCord, 1980a,b). The same retrieval techniques used to solve the inverse problem for Solar System's bodies and the Earth atmospheres are used in exoplanetary science, after the discovery in 1995 of the first exoplanet orbiting a main-sequence star (Terrile et al., 2005; Irwin et al., 2008; Madhusudhan and Seager, 2009; Benneke and Seager, 2012a, 2013; Line et al., 2013; Waldmann et al., 2015a,b).

In the next sections, I explain the retrieval techniques I used to analyse exoplanetary atmospheres, using the forward models explained in the previous chapter and in the last section I describe Bayesian analysis.

3.1 Spectral retrievals

In the previous chapter I described the assumption we make for exoplanetary atmospheres and structured the basis for the TauREx (Tau Retrieval for Exoplanets) retrieval code (Waldmann et al., 2015a,b). Now we need to build an inverse model and try to associate the best set of parameters to an input spectrum. The set of parameters can be described by a vector $\mathbf{x}$, the atmospheric model (or forward model) as a function of the parameters is $M(\mathbf{x})$. Ideally an input spectrum, described by the vector $\mathbf{y}$, can be related to the set of parameters $\mathbf{x}$ by:

$$\mathbf{y} = M(\mathbf{x}) + \boldsymbol{\varepsilon}, \tag{3.1}$$

where $\boldsymbol{\varepsilon}$ is the error vector. Spectral retrievals are, therefore, model-dependent algorithms. The forward model $M(\boldsymbol{x})$ contains all the physics assumed for the atmospheric system, often valid within some degrees of approximation. In the inverse model we try to find the best set of parameters that explain the input spectrum within some physical assumptions. Assuming linearity between $\boldsymbol{x}$ and $\boldsymbol{y}$ and that $M(\boldsymbol{x})$ is linear within the error bars obtained in the retrieval:

$$\boldsymbol{y} - M(\boldsymbol{x}) = \frac{\delta M(\boldsymbol{x})}{\delta \boldsymbol{x}}(\boldsymbol{x} - \boldsymbol{x_0}) + \boldsymbol{\varepsilon} = \boldsymbol{J}(\boldsymbol{x} - \boldsymbol{x_0}) + \boldsymbol{\varepsilon}, \tag{3.2}$$

where $\boldsymbol{J}$ is the weighting function matrix or Jacobian matrix, and $\boldsymbol{x_0}$ is the "a priori" state vector.

Finding a relationship between $\boldsymbol{x}$ and $\boldsymbol{y}$ is often hard as it often depends on underlying physics or unknown processes. Unambiguous measurements, with high signal-to-noise ratio and high accuracy, can help to constrain the solution better. However, in the exoplanetary atmospheric study, we have to deal with low-resolution spectra and low signal-to-noise ratios. In this field, Bayesian inference can help to constrain the parameters space and avoiding too many assumptions on the system. The only disadvantage of Bayesian inference is the computational power required. This approach, described in the following sections, is computationally intensive as it requires several hours of computation to converge to a solution. In chapter 6, I introduce a different approach including deep learning able to reduce the computational time of retrieval.

3.1.1 Bayesian inference

The Bayesian analysis provides a robust and reliable solution for a complex problem as finding the parameters vector that well describes the physics of an input spectrum. The first step is to assume a prior distribution over the parameter space. Usually, in order to avoid assuming a distribution over the parameters space, we use uninformative priors. In this way, we only assume, in the absence of other information, the equiprobability of each parameter value inside a fixed range. As a final result, using the Bayes theorem, it is possible to obtain the posterior distribution over the parameter space, which takes into account both the measurements and the prior distributions information. From the posterior distribution, it is possible to find the best set of parameters that reproduces an input spectrum with their error bars. In the following sections, I briefly explain the method used and implemented in the TauREx retrieval code. Bayesian inference has been discussed widely in literature (e.g. Gelman et al., 2013; Bolstad, 2007) and was extensively applied in cosmology and astrophysics (Trotta, 2008).

Let us define the likelihood function $P(\boldsymbol{y}|\boldsymbol{x}, M)$, the prior distribution $P(\boldsymbol{x}, M)$ representing our knowledge on the state vector $\boldsymbol{x}$ before the analysis and the Bayesian evidence:

$$P(\boldsymbol{y}|M) = \xi(\boldsymbol{y}) = \int P(\boldsymbol{y}|\boldsymbol{x}, M)P(\boldsymbol{x}, M)\mathrm{d}\boldsymbol{x}, \tag{3.3}$$

the Bayes' theorem can be written as:

$$P(\boldsymbol{x}|\boldsymbol{y}, M) = \frac{P(\boldsymbol{y}|\boldsymbol{x}, M)P(\boldsymbol{x}, M)}{P(\boldsymbol{y}|M)}, \tag{3.4}$$

where $P(\boldsymbol{x}|\boldsymbol{y}, M)$ is the posterior distribution of the state given the measurement.

Assuming a normal distribution for the error vector $\boldsymbol{\varepsilon}$ and no correlations between measurements, we can write the likelihood function as:

$$P(\boldsymbol{y}|\boldsymbol{x}, M) = \prod_{k=0}^{N} \frac{1}{\varepsilon_k \sqrt{2\pi}} \exp\left[-\frac{(x_k - y_k)^2}{2\varepsilon_k^2}\right]. \tag{3.5}$$

In order to solve Equation 3.4 there are several techniques and algorithms. In the exoplanetary community, the most used are Markov Chain Monte Carlo (Alfaro et al., 2003) and Nested Sampling (Feroz and Hobson, 2008b).

3.1.2 Calculating the expectation

Let $\boldsymbol{x}$ be a vector of k random variables with distribution p. In Bayesian applications $\boldsymbol{x}$ will include the model and p will be a posterior distribution. We define the expectation of a function $f(\boldsymbol{x})$:

$$E\left[f(\boldsymbol{x})\right] = \frac{\int f(x)p(x)}{\int p(x)}\mathrm{d}x. \tag{3.6}$$

In Bayesian inference we know that $P(\boldsymbol{y}|M) \propto P(\boldsymbol{y})P(M|\boldsymbol{y})$ but it is difficult to evaluate the normalisation constant $\int P(y)P(M|y)\mathrm{d}y$. For simplicity we assume that $\boldsymbol{x}$ is a vector of a k-dimensional Euclidean space, i.e. $\boldsymbol{x}$ can be defined by a set of k continuous variables.

3.1.3 Markov Chain Monte Carlo

Markov Chain Monte Carlo (MCMC) combines Monte Carlo integrations and Markov chains. With the MCMC method the expectation value $E\left[f(\boldsymbol{x})\right]$ is calculated by drawing samples $\{\boldsymbol{x}_t, t = 1, ..., n\}$ from p and approximating Equation 3.6 to:

$$E\left[f(\boldsymbol{x})\right] \approx \frac{1}{n}\sum_{t=1}^{n} f(\boldsymbol{x}_t). \tag{3.7}$$

In this way, the population mean of $f(\boldsymbol{x})$ is evaluated by a sample mean. Assuming independence of samples $\boldsymbol{x}_t$ the approximation can be made arbitrarily accurate by increasing the number n. The $\boldsymbol{x}_t$ can be generated by any process which samples throughout the p distribution in the correct proportions. One way to do it is through Markov chains.

The first step is to generate a sequence of random variables $\{\boldsymbol{x}_0, \boldsymbol{x}_1, \boldsymbol{x}_2, ...\}$ such as at each time $t \geq 0$ the next state $\boldsymbol{x}_{t+1}$ is sampled with a distribution $P(\boldsymbol{x}_{t+1}|\boldsymbol{x}_t)$ that depends just on the current state of the chain, $\boldsymbol{x}_t$. Given $\boldsymbol{x}_t$, the vector state $\boldsymbol{x}_{t+1}$ does not depend further on the history of the chain $\{\boldsymbol{x}_0, \boldsymbol{x}_1, ..., \boldsymbol{x}_{t-1}\}$. This sequence is called *Markov chain* and $P(.|.)$ is called the *transition kernel* of the chain. In our description we assume a time-homogeneous chain as $P(.|.)$ does not depend on t.

Under regularity conditions the chain will gradually lose information about its initial state and $P^{(t)}(.|\boldsymbol{x}_0)$ will eventually converge to a unique stationary (or invariant) distribution ϕ, independent on t or $\boldsymbol{x}_0$.

In general it is defined a number of m *burn-in* iterations after the chain starts converging to ϕ. Now we can use the output of the MCMC to determine the expectation value in Equation 3.7. Burn-in samples are generally discarded in its calculation:

$$\bar{f} = \frac{1}{n-m} \sum_{t=m+1}^{n} f(\boldsymbol{x}_t). \tag{3.8}$$

The quantity in Equation 3.8 is also called *ergodic average*. Convergence to the required-expectation is ensured by the ergodic theorem.

The Metropolis-Hastings algorithm

In Equation 3.8 we show a Markov chain and how it can be used to estimate $E[f(\boldsymbol{x})]$. The problem now is how to construct the Markov chain so that its stationary distribution ϕ is our distribution of interest p. In this section I show one of the simplest methods firstly proposed by Metropolis et al. (1953) and then generalised by Hastings (1970). This method is also called *Metropolis-Hastings* (MH) algorithm. In the MH algorithm each state $\boldsymbol{x}_{t+1}$ is chosen by sampling a $\boldsymbol{u}$ point from a proposal distribution $q(.|\boldsymbol{x}_t)$. The proposal distribution could be a multivariate normal distribution with a fixed covariance matrix. The candidate point $\boldsymbol{u}$ is accepted with a probability $\alpha(\boldsymbol{x}_t, u)$ defined as:

$$\alpha(\boldsymbol{x}_t, \boldsymbol{u}) = \min\left(1, \frac{p(\boldsymbol{u})\, q(\boldsymbol{x}|\boldsymbol{u})}{p(\boldsymbol{x})\, q(\boldsymbol{u}|\boldsymbol{x})}\right). \tag{3.9}$$

When the candidate point $\boldsymbol{u}$ is accepted then the next state becomes $\boldsymbol{x}_{t+1} = \boldsymbol{u}$, if the candidate is rejected then the next chain state is $\boldsymbol{x}_{t+1} = \boldsymbol{x}_t$. Summarising the MH algorithm, we have:

Initialise $\boldsymbol{x}_0$, set $t = 0$.

Repeat {

  Sample a point $\boldsymbol{u}$ from $q(.|\boldsymbol{x}_t)$

  Sample a random variable U from a random uniform distribution between 0 and 1

  If $U \leq \alpha(\boldsymbol{x}_t, \boldsymbol{u})$ set $\boldsymbol{x}_{t+1} = \boldsymbol{u}$

    otherwise set $\boldsymbol{x}_{t+1} = \boldsymbol{x}_t$

  Increment t

}.

Once the algorithm converges to a solution, independently from the form of $q(.|.)$, the stationarity distribution of the chain will be p. Indeed the transition kernel of the MH algorithm is:

$$\begin{aligned} P(\boldsymbol{x}_{t+1}|\boldsymbol{x}_t) &= q(\boldsymbol{x}_{t+1}|\boldsymbol{x}_t)\alpha(\boldsymbol{x}_t, \boldsymbol{x}_{t+1}) + \\ &+ I\left(\boldsymbol{x}_{t+1} = \boldsymbol{x}_t\right)\left[1 - \int q(\boldsymbol{u}|\boldsymbol{x}_t)\alpha(\boldsymbol{x}_t, \boldsymbol{u})d\boldsymbol{u}\right], \end{aligned} \tag{3.10}$$

where I is the indicator function with $I(x) = 1$ if $x =$ true and 0 otherwise. The first term of Equation 3.10 results from the acceptance of a candidate $\boldsymbol{u} = \boldsymbol{x}_{t+1}$ and the second term results from the rejection, for all candidate points $\boldsymbol{u}$. As a consequence of Equation 3.9 we can write:

$$p(\boldsymbol{x}_t)q(\boldsymbol{x}_{t+1}|\boldsymbol{x}_t)\alpha(\boldsymbol{x}_t, \boldsymbol{x}_{t+1}) = p(\boldsymbol{x}_{t+1})q(\boldsymbol{x}_t|\boldsymbol{x}_{t+1})\alpha(\boldsymbol{x}_{t+1}, \boldsymbol{x}_t). \tag{3.11}$$

From Eq 3.11 we obtain the *detailed balance* equation:

$$p(\boldsymbol{x}_t)P(\boldsymbol{x}_{t+1}|\boldsymbol{x}_t) = p(\boldsymbol{x}_{t+1})P(\boldsymbol{x}_t|\boldsymbol{x}_{t+1}), \tag{3.12}$$

and, integrating both sides of Equation 3.12:

$$\int p(\boldsymbol{x}_t)P(\boldsymbol{x}_{t+1}|\boldsymbol{x}_t)d\boldsymbol{x}_t = p(\boldsymbol{x}_{t+1}). \tag{3.13}$$

The left hand side of Equation 3.13 is the marginal distribution of $\boldsymbol{x}_{t+1}$, assuming that $\boldsymbol{x}_t$ is from p. With this assumption, from Equation 3.13 it follows that also $\boldsymbol{x}_{t+1}$ is derived from p. Finally, once we obtain a sample from the stationary distribution, all the subsequent samples will be from that distribution (Gilks et al., 1996).

3.1.4 Nested Sampling and MultiNest

MCMC algorithms provide a posterior distribution for each parameter in our Bayesian model without calculating the Bayesian evidence defined in Equation 3.3. The Metropolis-Hastings algorithm has problems returning multi-modal posterior distributions and finding degeneracies between parameters. MCMC methods usually require tuning on prior distributions to sample the parameters space efficiently and can have convergence problems. With a Nested Sampling algorithm, we can quantify the Bayesian evidence enabling a comparison between different models. With a MULTINEST implementation (Feroz et al., 2009) it is possible to shape multi-modal posterior distributions and find degeneracies between a high number of parameters. MULTINEST is optimised for highly degenerated parameters and multi-modal distributions. It found several

applications in astrophysics (Skilling, 2004; Feroz et al., 2009a; Bridges et al., 2009; White and Feroz, 2010; Feroz et al., 2010, 2011b,a; Graff et al., 2012; Karpenka et al., 2013; Strege et al., 2013). Some relevant works in the exoplanetary atmospheres field can be found in Benneke and Seager (2012b) and Waldmann et al. (2015b).

Nested Sampling

Let us define $\boldsymbol{x}$ as the set of parameters in a model M and $\boldsymbol{y}$ as the measured data. If $\mathcal{L}(\boldsymbol{x}) = P(\boldsymbol{y}|\boldsymbol{x}, M)$ is the likelihood and $\pi(\boldsymbol{x}) = P(\boldsymbol{x}, M)$ the parameter prior distribution, the Bayesian evidence in Equation 3.3 is (Feroz et al., 2009):

$$\xi(\boldsymbol{x}) = \int_{\Omega_{\boldsymbol{x}}} \mathcal{L}(\boldsymbol{x})\pi(\boldsymbol{x})\mathrm{d}\boldsymbol{x}. \tag{3.14}$$

Nested Sampling algorithm estimates the Bayesian evidence by turning the multi-dimensional integral in Equation 3.14 into one-dimensional integral. In order to do that we define the survival function (or "prior volume") as:

$$X(\lambda) = \int_{\{\boldsymbol{x}:\mathcal{L}(\boldsymbol{x})>\lambda\}} \pi(\boldsymbol{x})\mathrm{d}\boldsymbol{x}. \tag{3.15}$$

By defining the survival function it is possible to calculate the integral over the region of space contained within the iso-likelihood contour $\mathcal{L}(\boldsymbol{x}) > \lambda$, with $\lambda \in \mathbb{R}$.

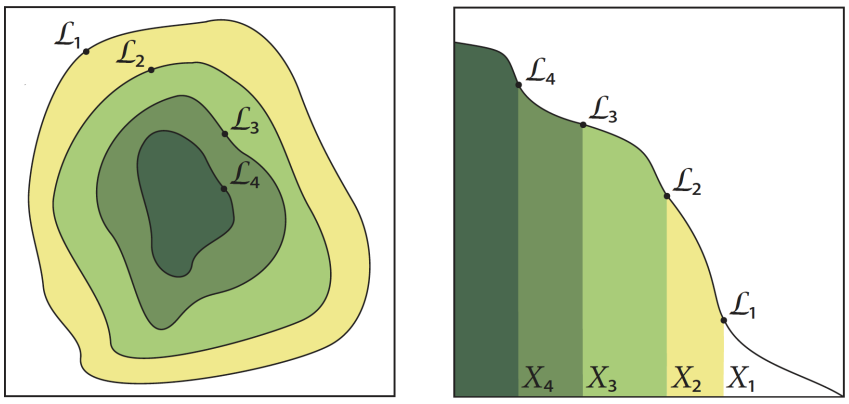

Figure 3.1: **a)** posterior distribution of a two-dimensional problem. **b)** transformed $\mathcal{L}(X)$ function where X_i are the prior volumes and $\mathcal{L}_i$ are the likelihoods (image from Feroz et al. (2009)).

At this point we can calculate the Bayesian evidence:

$$\xi = \int_0^\infty X(\lambda)\mathrm{d}\lambda, \tag{3.16}$$

and then:

$$\xi = \int_0^1 \mathcal{L}(X)\mathrm{d}X. \tag{3.17}$$

As shown schematically in Figure 3.1 the evidence can be approximated numerically to a sum:

$$\xi \equiv \hat{\xi} = \sum_{i=1}^{N} \mathcal{L}_i w_i, \tag{3.18}$$

where w_i are the weights given by the trapezium volume $w_i = 1/2(X_{i-1} - X_{i+1})$. In this algorithm $\mathcal{L}(X)$ is unknown and in the evidence calculation it is possible to use MC methods for probabilistic association of prior volumes X_i with likelihood contours $\mathcal{L}_i = \mathcal{L}(X_i)$.

In a Nested Sampling algorithm the posterior distribution p can be obtained by using the points with the lowest likelihood value at each iteration of the algorithm, i.e.:

$$p_i = \frac{\mathcal{L}_i w_i}{\sum_j \mathcal{L}_j w_j} = \frac{\mathcal{L}_i w_i}{\hat{\mathcal{Z}}}, \tag{3.19}$$

so for which it is possible to calculate the mean and standard deviation.

MULTINEST algorithm

In order to build the posterior distribution, the MULTINEST algorithm draws a set of (possibly overlapping) ellipsoids which surround the set of N_{live} points at each iteration i (Figure 3.2)

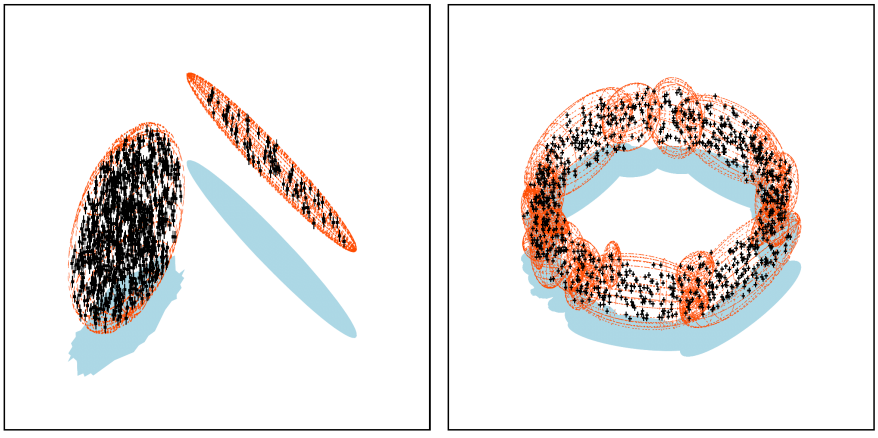

Figure 3.2: Ellipsoidal decomposition from the MULTINEST algorithm with $N_{live} = 1000$ points sampled from: **a)** non-intersecting ellipsoids and **b)** a torus (image from Feroz et al. (2009)).

At each iteration, the live points are redistributed according to a set of ellipsoids. As the

number of iterations increases, the MULTINEST algorithms samples the live points within the ellipsoids with a higher likelihood and probability, obtaining a higher acceptance rate for the new samples.

3.2 TauREx Retrieval code

Modelling an exoplanetary atmosphere is necessary in order to understand how the parameters are correlated with each other and analyse a dataset. Here, such a model is obtained by solving the radiative transfer equation with the TauREx retrieval code (Waldmann et al., 2015a,b). In the TauREx retrieval code assumes a plane-parallel atmosphere and one-dimensional problem. It takes into account the collision-induced absorption and Mie scattering, and it ignores forward scattering, Raman scattering, polarisation and 3D effects. The assumptions made and the ignored effects could introduce some minor biases (de Kok et al., 2011a; de Kok and Stam, 2012; Line and Parmentier, 2016a).

TauREx is a fully Bayesian retrieval code able to reconstruct the parameters space of an input spectrum using a one-dimensional plane parallel atmosphere. It was developed by Dr Ingo Waldmann (Waldmann et al., 2015a,b) and optimised by Dr Marco Rocchetto. TauREx is an object-oriented code written in Python and C++, and thanks to its modular nature is highly scalable.

The transmission and emission forward model is written in C++ to allow a high-speed computation. It is possible to run line-by-line models, including the state-of-art molecular opacity cross sections.

As explained in chapter 6 the molecular and parameters selection and parameters can be done using a trained deep convolutional neural network, working in a GPU cluster and requiring two minutes to determine the model parameters. The current version of TauREx works in a highly parallelised environment using CPU and calculating hundreds of thousands of forward models in a few hours. Thanks to its architecture (Figure 3.3) it is possible to retrieve a high number of model parameters.

The TauREx retrieval code is built in modules which are specialised in completing a particular task. The modular architecture of the TauREx code can be summarised as follows:

1. Input modules: the input of the TauREx code are the model parameters, the observed exoplanetary spectrum and the molecular/atomic line list.

2. Model and Data handling: the input are uploaded in order to provide the requested atmospheric models that are applied to interpret the observation.

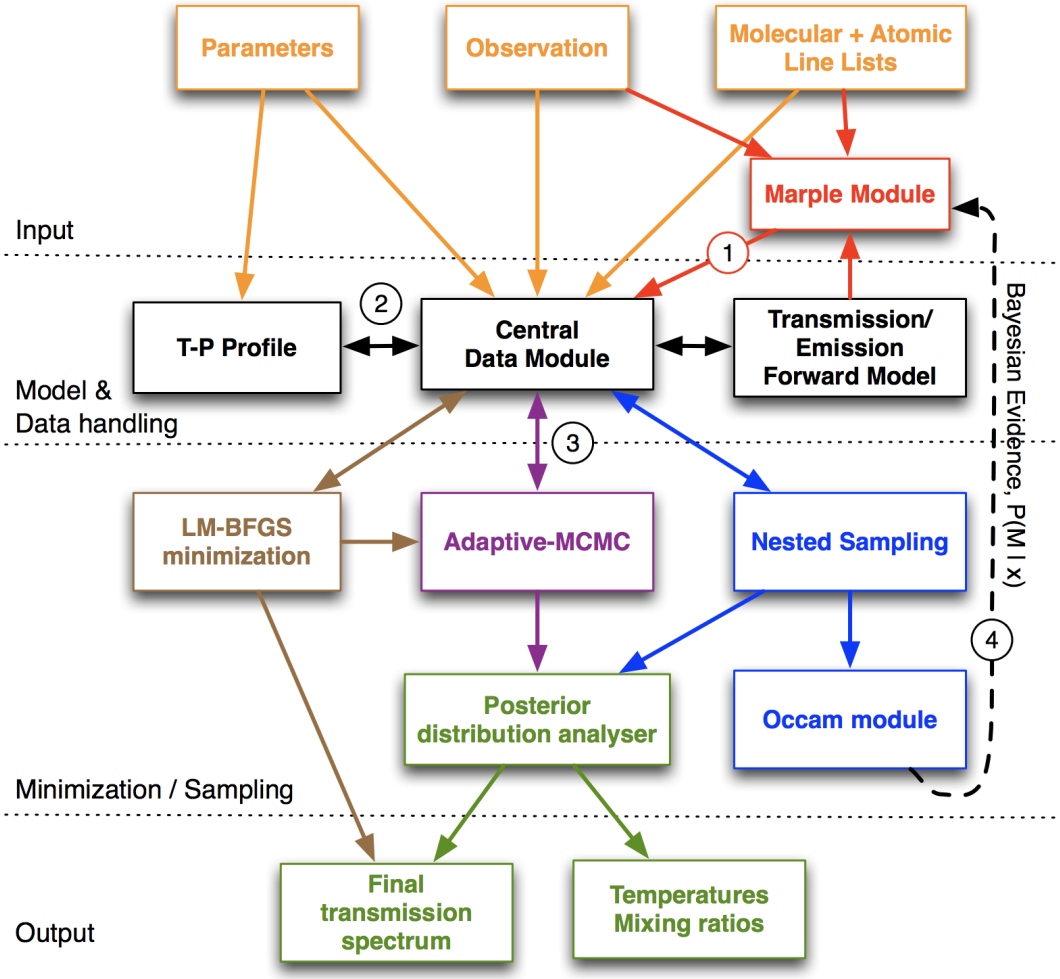

Figure 3.3: Illustration of TauREx architecture (image from Waldmann et al. (2015a)).

3. Minimisation/Sampling modules: Bayesian algorithm to be applied to retrieve the parameters associated to the input spectrum. MCMC and Nested Sampling algorithms are available.

4. Output module: it returns the posterior distribution of the parameters, the temperature-pressure profiles and the final exoplanetary spectrum retrieved.

In the next chapter I show an application of the TauREx retrieval code to analyse the atmosphere of 30 exoplanetary atmospheres obtained with the HST/WFC3 camera Tsiaras et al. (2018).

3.3 Comparison of forward models between TauREx, CHIMERA and NEMESIS

One fundamental part of a retrieval code is the forward model. It is important to evaluate a retrieval code and their forward models by comparing the results from other two retrieval codes. Rocchetto et al. (in prep) compared the TauREx retrieval code with NEMESIS (Irwin et al., 2008) and CHIMERA (Line et al., 2013).

The three models are consistent with each other, as shown in Figures 3.4 and 3.5. The most evident differences were due to:

- Different assumptions of a constant gravity or scale height through the atmosphere altitude. Using a constant value instead of a varying gravity as a function of the altitude can lead to major errors;

- Different definitions of the constants: the use of a different number of decimals can lead to big differences;

- Different numbers of layers (N_{layers}) used to model the exoplanetary atmosphere. A sufficient number of layers (at least 75) is important to approximate accurately the integral in Equations 2.33 and 2.16;

- Use of different line lists.

3.4 Summary and Conclusion

Bayesian algorithms are widely used by the community in order to retrieve the parameters distribution associated with an observation. Markov Chains Monte Carlo and, lately, Nested

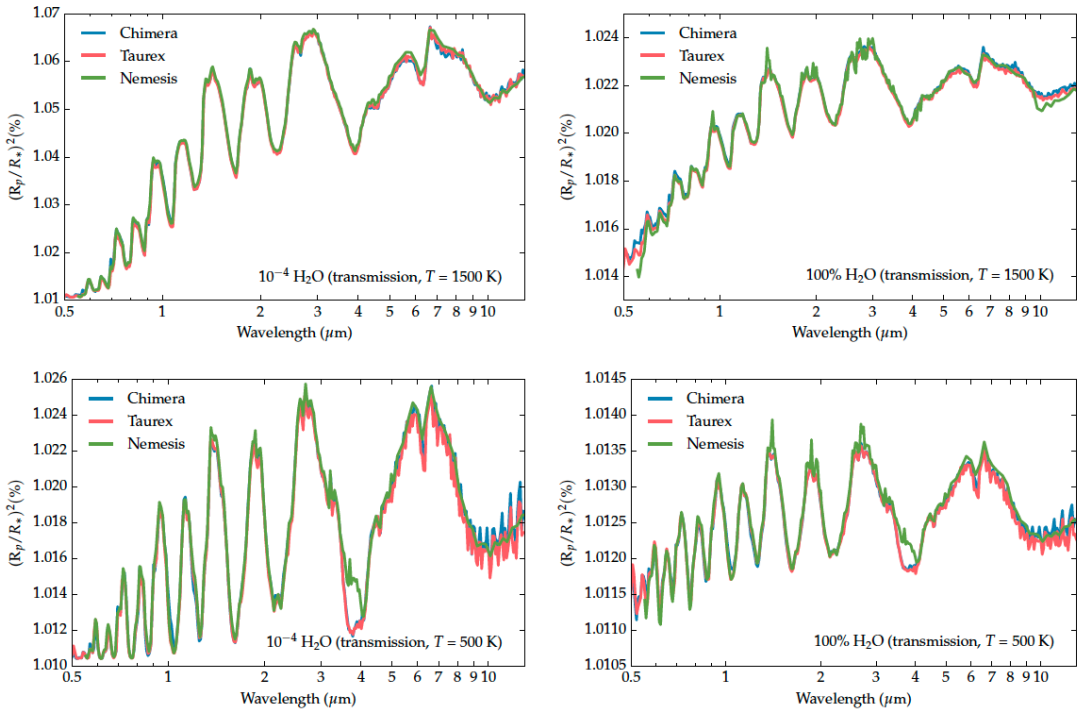

Figure 3.4: Comparison of transmission spectra generated by TauREx, CHIMERA and NEMESIS. On the left part are shown synthetic atmospheres generated assuming $10^{-4}H_2O$ abundance and a temperature of 1500 K (top), and 500 K (bottom). On the right part the water abundance is 100%. For the transmission spectra it has been simulated a planet with mass $M_p = 1M_J$, radius $R_p = 1R_J$ orbiting a star with radius $R_* = 1R_\odot$ (Image courtesy of Dr Marco Rocchetto).

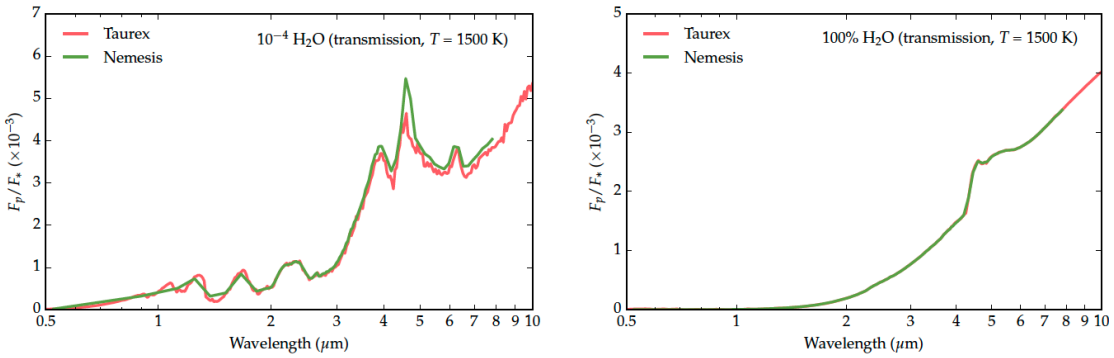

Figure 3.5: Emission spectrum of the same planet shown in Figure 3.4 using TauREx and NEMESIS. The TP profile used in both cases has a high altitude temperature of 2200K and a low altitude temperature of 1260K. It is noticeable that NEMESIS generated a lower resolution emission spectrum. This is due to the use of lower resolution absorption cross section to generate these models (Image courtesy of Dr Marco Rocchetto).

Sampling, are popular algorithms to find the posterior distribution of parameters. Nested Sampling is preferred because it gives a numerical value of the Bayesian evidence and can find possible degenerate solutions. The TauREx retrieval code is an example of fully-Bayesian algorithm applied to exoplanetary atmospheres. In the next chapter I will describe an application of the TauREx code on 30 spectra of giant planets. In chapter 6 I explain a possible improvement for the TauREx retrieval code involving a Deep Learning algorithm.

Chapter 4

Towards a population study of exoplanetary atmospheres

In the Milky Way there are thousands of known planets and the number is expected to grow thanks to future space missions and ground-based surveys. Measuring mass and radius of an exoplanet is not enough to understand its composition or infer the presence of an atmosphere and its properties. A spectroscopic study of exoplanetary atmospheres can give us information on its effective temperature, energy balance and chemistry. Currently the WFC3 camera on the Hubble space telescope has been analysing the atmosphere of several tens of exoplanets. In this Chapter I describe the analysis made for 30 giant planetary atmospheres. I led the effort to calculate the spectral retrievals of the planetary sample and the results were published in Tsiaras et al. (2018). Since the first molecular signatures detected on upper atmospheres of exoplanets (Charbonneau et al., 2002; Richardson et al., 2007; Grillmair et al., 2008; Redfield et al., 2008; Swain et al., 2008b; Tinetti et al., 2007; Knutson et al., 2008) we are moving rapidly towards a comparative study of exoplanets. The first approach of exoplanetary characterisation consisted in studying separately different kind of exoplanets like hot-Jupiters (Konopacky et al., 2013; Macintosh et al., 2015; Brogi et al., 2013; Snellen et al., 2014; de Kok and Stam, 2012; Kreidberg et al., 2015; Stevenson et al., 2014b; Tsiaras et al., 2016b; Todorov et al., 2013; Zellem et al., 2014; Line et al., 2016; Iyer et al., 2016; Deming et al., 2013; McCullough et al., 2014; Mandell et al., 2013), Neptunes (Fraine et al., 2014; Fukui et al., 2013; Ehrenreich et al., 2014; Knutson et al., 2014; Stevenson et al., 2010; Morello et al., 2015) and super-Earths (Bean et al., 2010; Berta et al., 2012; Tsiaras et al., 2016c; Demory et al., 2016; Knutson et al., 2014; Kreidberg et al.,

2014). Analysing the atmosphere of a single planet allows us to infer a possible evolutionary path of the planet itself and maybe infer the properties that an exoplanet should have, given the physical and orbital parameters of the system.

A comparative study of exoplanets can reveal us much more correlations between physical parameters and a first attempt of this kind has been made by Sing et al. (2016b) with 10 hot Jupiters. In order to study more than one planet for a comparative study, the following two points are necessary:

- Follow the same procedure for data analysis, in order to lower the probability of introducing some biases and spectra need to be analysed uniformly;
- Atmospheric modelling should be quantitative and homogeneous, using exactly the same method for each planet and using the same retrieval code. In this way it is possible to have an exact statistical comparability between planetary and atmospheric parameters.

4.1 The dataset

In this work 30 planets (the ones with the highest signal-to-noise ratio) are taken into account. Data extraction from the WFC3 camera has been done using a pipeline wrote by Dr Angelos Tsiaras, publicly available [1]. All of them have temperature between 600 and 2400K and radius between 0.35 and $1.9 R_{Jup}$. Data can be accessed publicly from the NASA Milkulski Archive for Space Telescopes (MAST) archive.

The planets in this study have masses higher than $10 M_{\oplus}$ and signal-to-noise ratios $S/N > 3$. Even though there are other datasets from space missions using HST/STIS, Spitzer/IRAC and ground-based surveys (Danielski et al., 2014; Stevenson et al., 2014a; Snellen et al., 2014; Line et al., 2016; Sing et al., 2016a) we used just HST/WFC3 data in order to compare homogeneously the signal from each planet. The number of transits used and other useful information for the dataset used are shown in Table 4.2.

4.2 Atmospheric modelling

We analysed the atmospheres of 30 exoplanets using the fully Bayesian atmospheric spectral retrieval $\mathcal{T}$-REx (Waldmann et al., 2015a,b). $\mathcal{T}$-REx maps the parameters space using either nested sampling or Markov chains Monte Carlo. For the analysis we used NS (Skilling, 2006; Feroz et al., 2009b) since it is more appropriate to find degenerate solutions whether it is necessary. Using the narrow WFC3 wavelength range, indeed, it is likely to find more than one

[1] `https://github.com/ucl-exoplanets/Iraclis.git`

solution for a single planet. Transmission spectra are modelled using a variety of possible molecular opacities, i.e. H_2O, CH_4, CO, CO_2, NH_3, TiO and VO. For most planets H_2O is the only detectable signal together with clouds/hazes. This detection is helped also from the sensitivity of the WFC3 camera to a significant water bump at its wavelength and resolution. Nevertheless also TiO and VO has been detected in WASP-76 b with a 4.0σ significance and with a lower significance in WASP-121 b.

4.2.1 General setup

In order to analyse exoplanetary atmospheres it is necessary to set up the prior distributions for the Bayesian analysis and the physical parameters for the atmospheric model. In the 30 planetary analyses the pressure was set up in the range from 10^{-4} to 10^{6} Pa and uniformly sampled in a logarithmic scale by 100 atmospheric layers. A sample test done with 250 and 50 confirmed that 100 layers do not introduce significant degradation for the retrieval accuracy for the HST/WFC3 camera and it is a good compromise between accuracy and computational time. All the trace-gas abundances were sampled uniformly from 10^{-8} to 10^{-1} in volume mixing ratios for hot-Jupiters and from 10^{-8} to 1.0 for Neptunes. The temperature was sampled varying the geometric albedos from zero to 0.6 and the emissivity from 0.5 to 1 and calculated as shown in equation 4.1:

$$T_p = T_* \left(\frac{R_*}{2a}\right)^{1/2} \left(\frac{1-A}{\varepsilon}\right)^{1/4}, \tag{4.1}$$

where R_* is the stellar radius, a is the semi-major axis, A is the geometric albedo and ε is the planetary emissivity.

For the temperature prior distributions the albedo and emissivity was varied in order to get the temperature range $[T_p(A = 0.6, \varepsilon = 1) - 500\,K,\ T_p(A = 0, \varepsilon = 0.5) + 500\,K]$. The adoption of a wider temperature range allowed to consider also the cooler temperature of the terminator compared to the expected equilibrium temperature. Indeed with the HST/WFC3 camera it is possible to probe only a very restricted range of planetary temperature-pressure profiles.

For all of the atmospheric retrievals we assumed an isothermal temperature-pressure profile. Whilst this assumption can be oversimple and introduce some retrieval biases (Rocchetto et al., 2016b), the narrow wavelength range of the WFC3 camera (1.1 to 1.8μm) does not allow a differentiation between an isothermal profile from a more complex one.

Concerning the prior distribution for the planetary radius, it was considered, for each observation, the value coming from the maximum and minimum value of the input spectrum, considering their error bars and adding 200 ppm more as a lower and upper bounds.

All the physical and orbital parameters used in the analysis are shown in Table 4.3.

4.2.2 Opacity sources

As a very first assumption we considered a wide range of molecular opacities. Considering the lack of knowledge on these planetary atmosphere, we assumed the presence of 12 different molecule, i.e. H_2O, HCN, NH_3, CH_4, CO_2, CO, NO, SiO, TiO, VO, H_2S, and C_2H_2. For all the 30 planets was not observed any significant contribution from any of these molecules, except for H_2O, TiO and VO. For this reason and the second iteration we proceeded with a second retrieval considering a smaller set of molecules: H_2O (Barber et al., 2006), CO (Rothman et al., 2010), CO_2 (Rothman et al., 2010), CH_4 (Yurchenko and Tennyson, 2014) and NH_3 (Yurchenko et al., 2011). VO (McKemmish et al., 2016) and TiO (McKemmish in prep.) were added to the mix for planets with equilibrium temperatures exceeding 1400 K. The $\mathcal{T}$-REx retrieval code can be computed with either the absorption cross-section or the correlated-k coefficients. The k-tables were computed from very high-resolution ($R > 10^6$) cross-sections, which in turn were calculated from molecular line lists obtained from ExoMol (Tennyson et al., 2016), HITEMP (Rothman et al., 2010) and HITRAN (Rothman et al., 2013). Line-broadening dependent on the temperature and pressure and, where possible, J-dependence (Pine, 1992) were included in the computation.

Absorption cross-sections were binned to a constant resolving power of R = 15000 and the transmission forward models were calculated at this resolution before binning to the resolution of the data. Given the resolutions, wavelength range and uncertainties of the data at hand, we find no differences between the use of cross-section and k-tables in the final retrieval results. Rayleigh scattering and collision induced absorption of H_2-H_2 and H_2-He was also included (Borysow et al., 2001; Borysow, 2002; Rothman et al., 2013).

4.2.3 Cloud parameterisation

In order to model the presence of clouds one can take into account several model of varying complexities such as Benneke and Seager (2012b); Line et al. (2016); Barstow et al. (2013); Griffith (2014). Here we adopted the parameterisation of Lee et al. (2013b), which also finds implementation in an atmospheric retrieval context in Lavie et al. (2016).

In transmission spectroscopy, the optical depth due to clouds as function of wavelength, $\tau_{c1,\lambda}$, is given by:

$$\tau_{c1,\lambda} = \int_0^{l(z)} Q_{ext,\lambda} \pi \alpha^2 \chi_c(z') \rho_N(z') \mathrm{d}l \tag{4.2}$$

where z is the height in the atmosphere, α is the particle size of the cloud/haze, dl is the path

length through the atmosphere, χ_c is the cloud molar fraction, ρ_N is the atmospheric number density, and $Q_{ext,\lambda}$ is the cloud extinction coefficient given by:

$$Q_{ext,\lambda} = \frac{5}{Q_0 x^{-4} + x^{0.2}} \tag{4.3}$$

where $x = 2\pi\alpha/\lambda$ and Q_0 determines the peak of $Q_{ext,\lambda}$. This can be understood as a cloud compositional parameter (Lee et al., 2013b). For $\alpha \ll \lambda$, the formalism reduces to pure Rayleigh scattering. In addition to the above, we implemented an optically thick grey-cloud cover, parameterised as follows:

$$\tau_{c2} = \begin{cases} 1, \text{ if } P < P_{\text{cloud-top}} \\ 0, \text{ otherwise} \end{cases} \tag{4.4}$$

where $P_{\text{cloud-top}}$ is the cloud-top pressure. This dual parameterisation allowed to model optically thick cloud decks with a semi-transparent, hazy, atmosphere above $P_{\text{cloud-top}}$.

We initially kept Q_0, χ_c, α (called R_{cloud} in our retrieval corner plots), and $P_{\text{cloud-top}}$ as free cloud parameters but found HST/WFC3 data to be insufficient to constrain Q_0. In initial tests, this last parameter was with a prior range from 0 - 100 and found that it was not constrained by the data. For this reason, henceforth, its value was fixed to 50 . Moreover it was found that either varying or fixing Q_0, the uncertainty differences on the retrieval were negligible given the quality of the data at hand. We set a log-uniform prior of χ_c ranging from 10^{-40} to 10^{-10}, particle size from 10^{-5} to $10\,\mu$m and cloud top-pressure from 10^{-4} to 10^{6} Pa (Lee et al., 2013b).

4.2.4 Free parameters and model selection

In the end, there were 10-12 free parameters: five molecular abundances (seven when TiO & VO were included), temperature, planet radius, top pressure of the clouds, particle dimension of the haze above the clouds and their molar fraction. Each one of the two spectra per planet at different resolutions was retrieved, yielding 60 retrievals in total. For each of the spectra was also run a separate model assuming a fully cloudy atmosphere, i.e. the flat model. In total the number of atmospheric model runs in retrieval mode and the end of the analysis is 120.

We found no difference between the information retrieved from the two classes of spectra at different resolution. The results reported in the thesis are from the low resolution spectra.

4.3 Bayes Factor and model selection

Data are often noisy and lead us towards a different degenerate solution. The Bayesian analysis offers us a tool to discover the best models and the best set of parameters to include in our reality representation. The choice of the number of parameters must be optimal and, according to the principle of Occam's razor, it is preferable avoiding very sophisticated models and minimise the number of parameters that should be fitted. Under this assumption, we should accept our complicated models just when they significantly differ from a simple model (Trotta, 2007). When it is reached a consistent best fit model, adding more atmospheric parameters does not necessarily add any further information about the analysed spectrum. The Occam's razor principle, can be used for example on the number of molecules that we claim to detect on an exoplanetary atmosphere.

In order to compare to models M_1 and M_2 and quantify Occam's razor principle we can define the Bayes factor:

$$\mathcal{B}_{21} = \frac{P(M_2|\boldsymbol{y})}{P(M_1|\boldsymbol{y})} = \frac{P(M_2)}{P(M_1)} \frac{P(\boldsymbol{y}|M_2)}{P(\boldsymbol{y}|M_1)} = \frac{P(M_2)}{P(M_1)} \frac{\xi_2}{\xi_1}, \tag{4.5}$$

where ξ_1, ξ_2 are the Bayesian evidences of, respectively model 1 and 2.

Assuming that the model priors distributions are identical $P(M_2) = P(M_1)$, Equation 4.5 can be written as the ratio between the two Bayesian evidences:

$$\mathcal{B}_{21} = \frac{\xi_2}{\xi_1}. \tag{4.6}$$

If $\mathcal{B}_{21} > 1$, then $\xi_2 > \xi_1$ and as the Bayes factor increases it means that the simulations run in favour of Model 2. The reverse is true for $\mathcal{B} < 1$. Jeffreys (2008) introduces a scales that gives an empirical estimation of the significance for the strength of evidence (see Table 4.1).

Table 4.1: Jeffreys' scale for the comparison between model M_1 and M_2 (adapted from Trotta (2008)).

$\lvert \ln \mathcal{B}_{21} \rvert$	Probability	Confidence	Notes
< 0.1	< 0.750	$< 2\sigma$	Inconclusive
1.0	0.750	2.1σ	Weak evidence
2.5	0.923	2.7σ	Moderate evidence
5.0	0.993	3.6σ	Strong evidence

It is possible to interpret the Bayes factor as a "goodness" indicator of our model, turning it into a $p-$value $= \mathfrak{p}$ (Sellke et al., 2001; Trotta, 2008). Sellke et al. (2001) obtained an expression to relate the minimum Bayes factor and its relation with $\mathfrak{p}$:

$$\mathcal{B}_{21} \leq \bar{\mathcal{B}}_{21} = -\frac{1}{e\mathfrak{p}\ln\mathfrak{p}}, \tag{4.7}$$

where $e = 2.7182818$ the Euler number. The relation between the p-value, $\mathfrak{p}$ and the sigma significance n_σ is:

$$\mathfrak{p} = 1 - \mathrm{err}\left(\frac{n_\sigma}{\sqrt{2}}\right), \tag{4.8}$$

with $\mathrm{err}(x)$ the error function. In Table 4.1 are shown the columns of $|\ln\bar{\mathcal{B}}_{21}|$, the related probabilities, the sigma confidences calculated through 4.7 and the related interpretation of the result.

Concerning atmospheric retrievals, the Bayes factor is calculated comparing a complex M_2 model with the simplest model possible M_1, i.e. a fully cloudy atmosphere. Indeed if the clouds thoroughly cover the atmosphere, it is difficult to infer chemistry properties. If the detection is clear and evident the Bayes factor is higher than 3 and the evidence is substantial. Otherwise, the simplest model is another statistically equivalent interpretation of our data, and the Occam's razor principle suggests us to keep this model instead of the most complex.

4.3.1 Atmospheric Detection Index (ADI)

The Atmospheric Detection Index (ADI) has been defined in order to quantify the "goodness" or significance of an atmospheric detection. It is essentially the positively defined Bayes factor between the nominal atmospheric model (M_N) and a flat-line model (M_F) or fully cloudy model. As stated above, the nominal model contains molecular opacities, cloud/haze opacities ($\tau_{c1,\lambda}, \tau_{c2}$) collision induced absorption of H_2-H_2/H_2-He and Rayleigh scattering. Other free parameters are the planetary radius, R_p, and the temperature of the isothermal TP-profile, T_iso. The flat-line model contains only grey-cloud opacities, τ_{c2}, R_p and T_iso. This parameterisation always results in a flat-line spectrum but includes the model degeneracies found between cloud top-pressure, planet-radius and temperature. This way we capture both cloudy and clear sky scenarios. As the ADI is a fully Bayesian model selection metric, we naturally impose Occam's razor to our atmosphere detection significance.

We obtained the Bayesian evidence of our nominal model, E_N, and of the pure-cloud/no-atmosphere model, E_F, and calculated the ADI as follows:

$$ADI = \begin{cases} \log(E_\mathrm{N}) - \log(E_\mathrm{F}), \text{ if } \log(E_\mathrm{N}) > \log(E_\mathrm{F}) \\ 0, \text{ otherwise} \end{cases} \tag{4.9}$$

The ADI is a positively defined metric and equivalent to the logarithmic Bayes Factor (Kass and Raftery, 1995) where $\log(E_{\rm N}) > \log(E_{\rm F})$.

4.4 Results and discussion

4.4.1 Atmospheric detectability

The computed posterior distributions and low-resolution spectra with the best-fit model are shown in Appendix A. In Figure 4.1 and Table 4.4 are shown all the spectra with the reported ADI index, ordered by decreasing ADI.

According to the ADI definition (Equation 4.9), an ADI index of 3 and 11 corresponds to an atmospheric detection of, respectively, 3σ and 5σ level. Among the 30 planets 16 out of 30 planets have an ADI index greater than 3 and, thus, they have a statistically significant atmosphere. Even though some planets with ADI < 3 (WASP-80 b, WASP-43 b, HAT-P-12 b, HAT-P-38 b, WASP-31 b, WASP-63 b, GJ 3470 b, WASP-67 b, WASP-74 b) show some water presence in their atmosphere, the model as a whole does not represent a significant detection. ADIs lower than 3 indicate non-detection, i.e. the spectral features are not sufficiently bigger than the error bars of the input spectrum and so it is not possible to distinguish the spectral features from the spectral noise and, therefore, it is not possible to favour the more complex model $M_{\rm N}$ over the simplest lower dimensional flat-line $M_{\rm F}$. Concerning these planets it is necessary to combine additional observations to confirm the presence of water in their atmosphere. In the case of WASP-43 b the presence of water has been confirmed by an additional observation during an eclipse of the planet (Kreidberg et al., 2014).

With the adoption of the ADI index it is possible to infer some general conclusions about an atmospheric detection, quantifying how significant is a measurement from a given dataset. Previous population studies suggested that the observed spectra do not show the strong molecular features expected for a clear sky atmosphere (Iyer et al., 2016; Sing et al., 2016b).

Remarkably, as shown in Figure 4.2 the ADI index does not correlate with the signal-to-noise ratio of the input spectrum. The S/N calculation has been done using the median uncertainty of the final observed low-resolution spectra instead of the pre-calculated uncertainties, I will refer to this quantity as observationally-corrected S/N (o.c. S/N). It is noticeable that for the planets with an o.c. S/N below 20, the ADI index is not correlated to the o.c. S/N (Figure 4.2). In this regime we can find planets that scored highly on paper in terms of potential detections of atmospheric features but turned out to be difficult to interpret (e.g. WASP-101 b), and planets that appeared relatively challenging to observe on paper but delivered very solid detections (e.g.

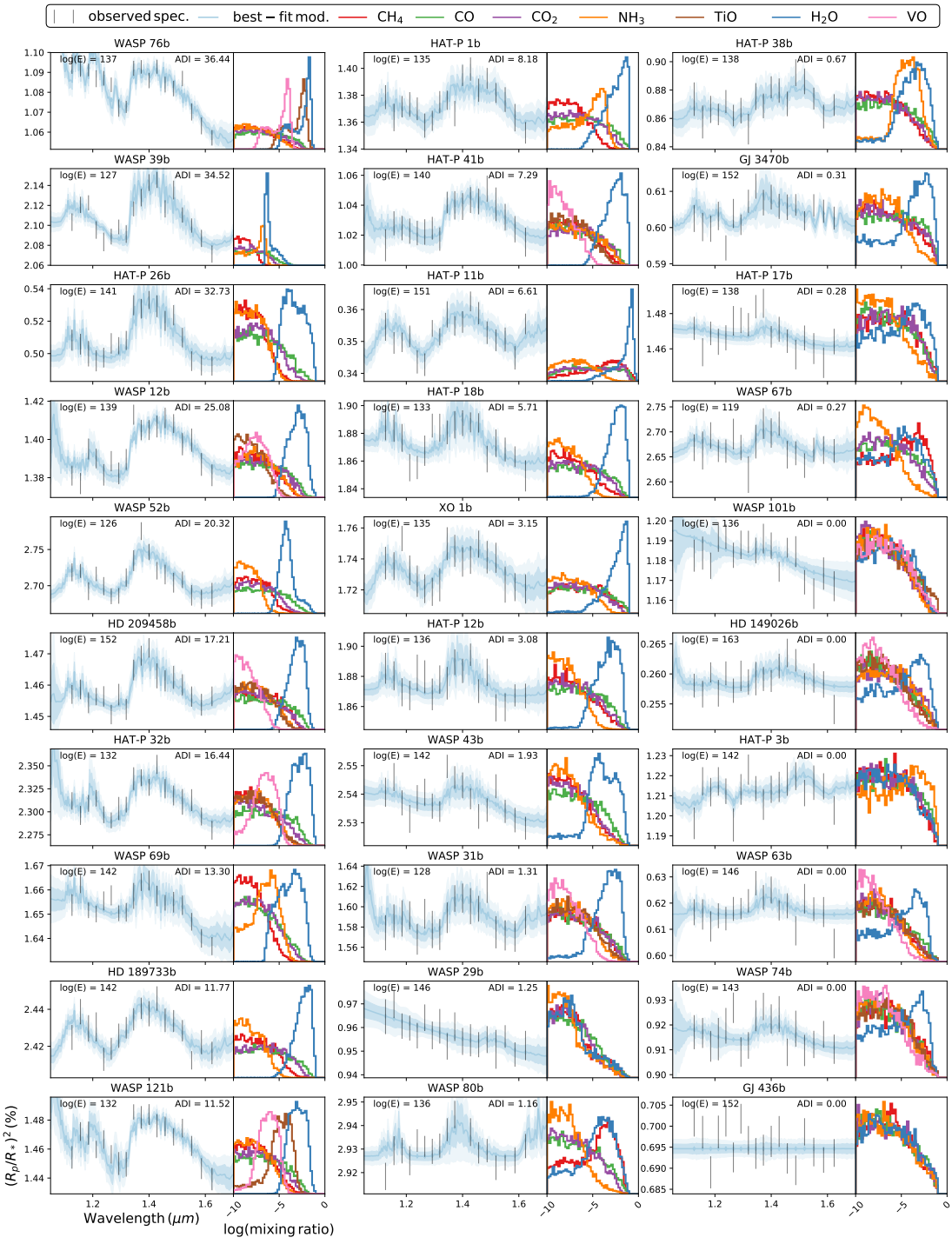

Figure 4.1: Atmospheric modeling results for all 30 planets in the sample. The planets are ordered based on the ADI index. The highest ADI planet is on the upper left part of the graph, the lowest on the lower right. The Bayesian evidence, log(E), of the best-fit model for each planet is also reported. Each panel shows, at left, the spectrum and the best-fit model and, at right, the posterior distributions of the abundances of the different molecules fitted.

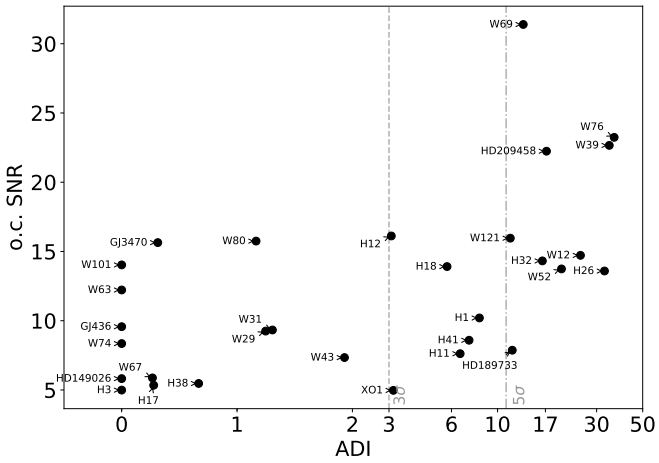

Figure 4.2: The o.c. S/N as a function of the ADI shows that planets with o.c. S/N > **20** are always detectable but no correlation between ADI and o.c. S/N can be found for planets with o.c S/N < **20**.

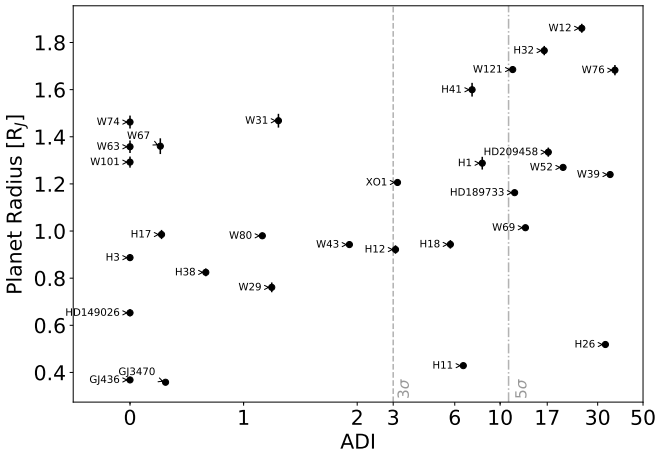

Figure 4.3: A positive trend exists between the planet radius and ADI, with larger planets generally featuring more detectable atmospheres. However, We note an outlying cluster of five planets, including WASP-31 b, WASP-63 b, WASP-67 b, WASP-74 b and WASP-101 b. These low ADIs may indicate high-altitude cloud covers, or water depleted atmospheres.

HAT-P-11 b). This absence of predictability showcases the need for exploratory observations prior to major time investments with large-scale facilities such as the JWST.

Considering the warm and hot Jupiters in our sample ($M > 0.16\,M_{\rm Jup}$, i.e. excluding the Neptunes: GJ 436 b, GJ 3470 b, HAT-P-11 b and HAT-P-26 b), the Pearson correlation coefficient indicates that the ADI is more strongly correlated with the planetary radius (0.51, p-value=0.7%) than the planetary temperature (0.43, p-value=3%) but not correlated with the surface gravity (-0.28, p-value=16%) or the planetary mass (0.20, p-value=32%). These parameters are plotted against ADI in Figures 4.3, 4.4, 4.5, and 4.6. These results indicate that planetary surface gravity is a secondary factor in identifying inflated atmospheres (Laughlin et al., 2011; Weiss et al., 2013; Spiegel and Burrows, 2013).

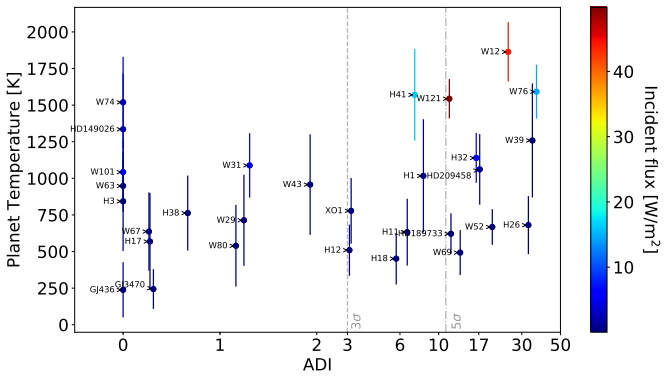

Figure 4.4: Planet temperature vs ADI. Colours show the UV radiation the planet receives in W/m^2. A cluster of outliers at high temperature and high ADI is apparent. These planets are also the highest irradiated.

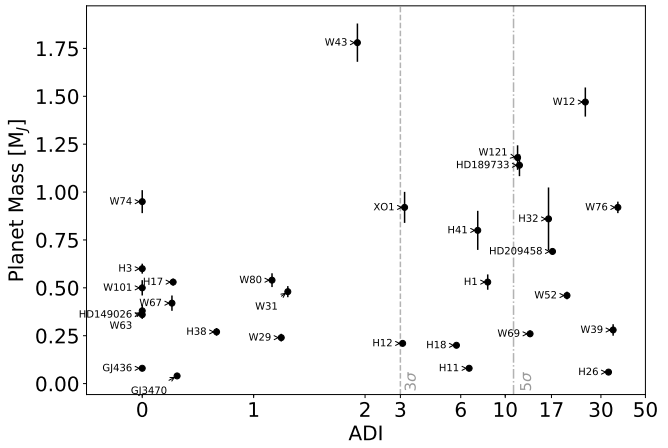

Figure 4.5: Planetary mass as a function of ADI. While the two groups of planets are clearly separated (with or without detectable atmospheres) there is no evident correlation between the planetary mass and the ADI index.

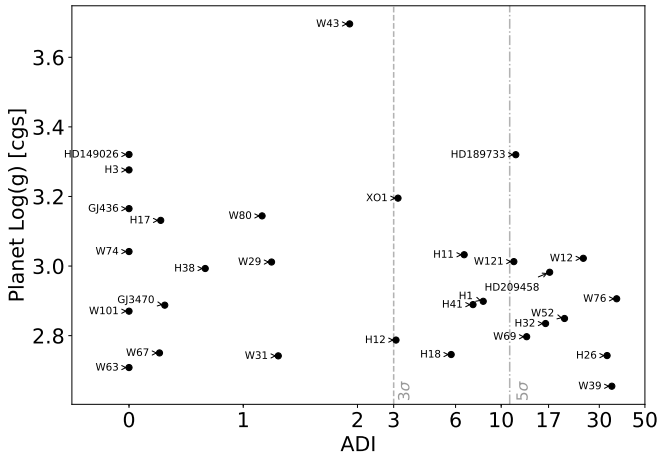

Figure 4.6: Planetary gravity as a function of ADI, with a similar behaviour to the planetary mass.

Another noticeable result is that all the very hot and irradiated planets, thus those with a temperature above 1800 K, have high ADI index. In these planets the retrieved cloud top-pressures are significantly high, i.e. the clouds are deep in the atmosphere. In Table 4.4 there are shown all the results of the quantitative retrievals. Given the narrow wavelength range observed it is not possible to estimate quantitatively the absolute water abundance of the atmosphere. On the contrary it is possible to exclude scenarios where water is significantly destroyed or depleted in the upper atmospheres of irradiated and inflated hot-Jupiters. In addition, the spectra of HAT-P-41 b, WASP-12 b and WASP-121 b show no contribution from photochemical hazes (Zahnle et al., 2009; Kopparapu et al., 2012; Miller-Ricci Kempton et al., 2012). We can conclude that planets with temperatures higher than 1800 K feature clear atmospheres in the terminator regions at HST/WFC3 wavelengths.

In our retrievals we considered a mixture of opaque cloud-deck and hazes, all planets but WASP-69 b are consistent with a grey, opaque cloud-deck. In this study, both opaque clouds and hazes were uniformly distributed along the terminator. Line and Parmentier (2016b) showed that non-uniform cloud coverage can mimic high-molecular weight (hmw) atmospheres. Whilst hmw atmospheres are not observed in our hot-Jupiter retrievals, we note that HST/WFC3 data alone are not sufficient to differentiate between hmw, and low-molecular weight atmospheres with patchy cloud coverage (Line and Parmentier, 2016b). This is particularly relevant for the warm-Neptune HAT-P-11 b, where a hmw atmosphere was postulated by Fraine et al. (2014). Asymmetric cloud coverage can be observed in ingress/egress signatures of the light-curves (von Paris, P. et al., 2016; Line and Parmentier, 2016b) but the incomplete phase coverage of the HST/WFC3 data is insufficient to confirm or reject patchy cloud coverage models.

4.4.2 Molecular opacities detected

All the planets with a statistically significant atmosphere can be described with a model which includes grey-clouds, Mie scattering and presence of water. There are two exceptions, WASP-76 b (see Figures 4.7 and 4.8) and WASP-121 b, which shows a haze free atmosphere and the presence of TiO and VO. The TiO & VO model is favoured with a Bayes Factor of 8.52 (4.44σ significance) when compared to a pure-water and haze dominated atmosphere for WASP-76 b. However, we would like to caution the reader that correlations between H_2O, TiO and VO abundance, planet radius and cloud-top pressure exist in the retrieved posterior distributions. The retrieval features a high-H_2O ($\sim 10^{-2.0}$) and high-TiO ($\sim 10^{-2.5}$) mode, which is likely unphysical. More observations, in particular in the optical wavelengths, are required to fully distinguish between a TiO/VO abundant and high-altitude haze model. In the case of WASP-

121 b, we find both models to be statistically indistinguishable from each other. As discussed above, in this analysis we do not take into account effects due to patchy or non-uniform cloud covers (e.g. MacDonald and Madhusudhan, 2017). In particular, Kempton et al. (2017) shows that non-uniform clouds/hazes on WASP-121 b can cause observable spectral gradients in the HST/WFC3 wavelengths.

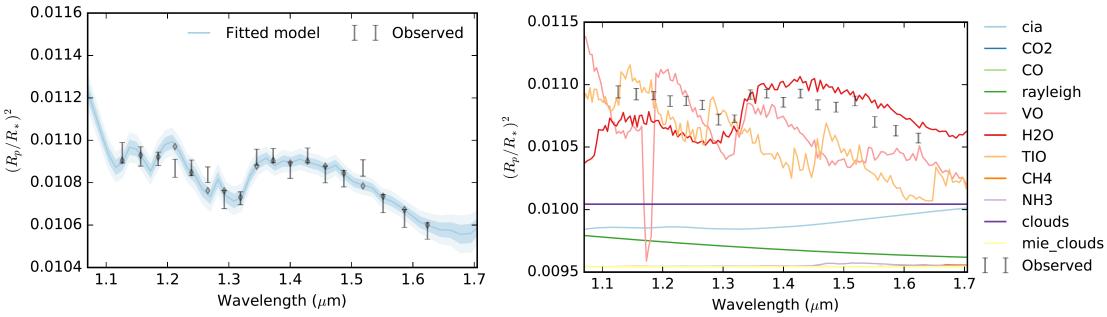

Figure 4.7: Left: Best fit spectra for WASP-76 b transmission spectrum in low resolution. A clear (no haze) upper atmosphere with a deep cloud-top (0.8 bar). Here the main opacities constitute H_2O, TiO and VO.

HST/WFC3 data points are too few to well-constrain the final solution and the wavelength range is not enough to exclude atmospheric haze models for planets which show the presence of TiO and VO. For this reason it is very important to wait for further observations at wider and longer wavelength ranges to determine conclusively the absolute abundance of molecular tracers and obtain an univocal model for each exoplanetary atmosphere.

All the other planets without a statistically significant atmosphere can be explained with either an opaque, high-altitude clouds or low water abundances. The detection has not to be considered strong enough to confirm tracers abundances and often the molecular signature is confused within the error-bars. Given the uncertainties of the input spectra, with HST/WFC3 camera and the $\mathcal{T}$-REx retrieval code it is not possible to retrieve mixing ratios lower than 10^{-8} for clouds free atmosphere. Furthermore, it is not possible to exclude the possibility of having a combination of water depletion and high-altitude clouds. Current space mission and ground-based surveys data are not able to constrain better the absolute tracers abundances. In the future the exoplanetary community can use data from JWST and dedicated space missions (i.e. ARIEL, Twinkle, CHEOPS) will explore a wider wavelength range and will find non-degenerate solutions for each atmosphere.

The spectra of 12 out of the 30 planets in our sample have been previously studied. In particular, these planets are: GJ 436 b (Knutson et al., 2014), HAT-P-1 b (Wakeford et al., 2013), HAT-P-11 b (Fraine et al., 2014), HAT-P-32 b (Damiano et al., 2017), HD 209458 b (Deming et al., 2013), HD 189733 b (McCullough et al., 2014), WASP-12 b (Kreidberg et al., 2015), WASP-31 b

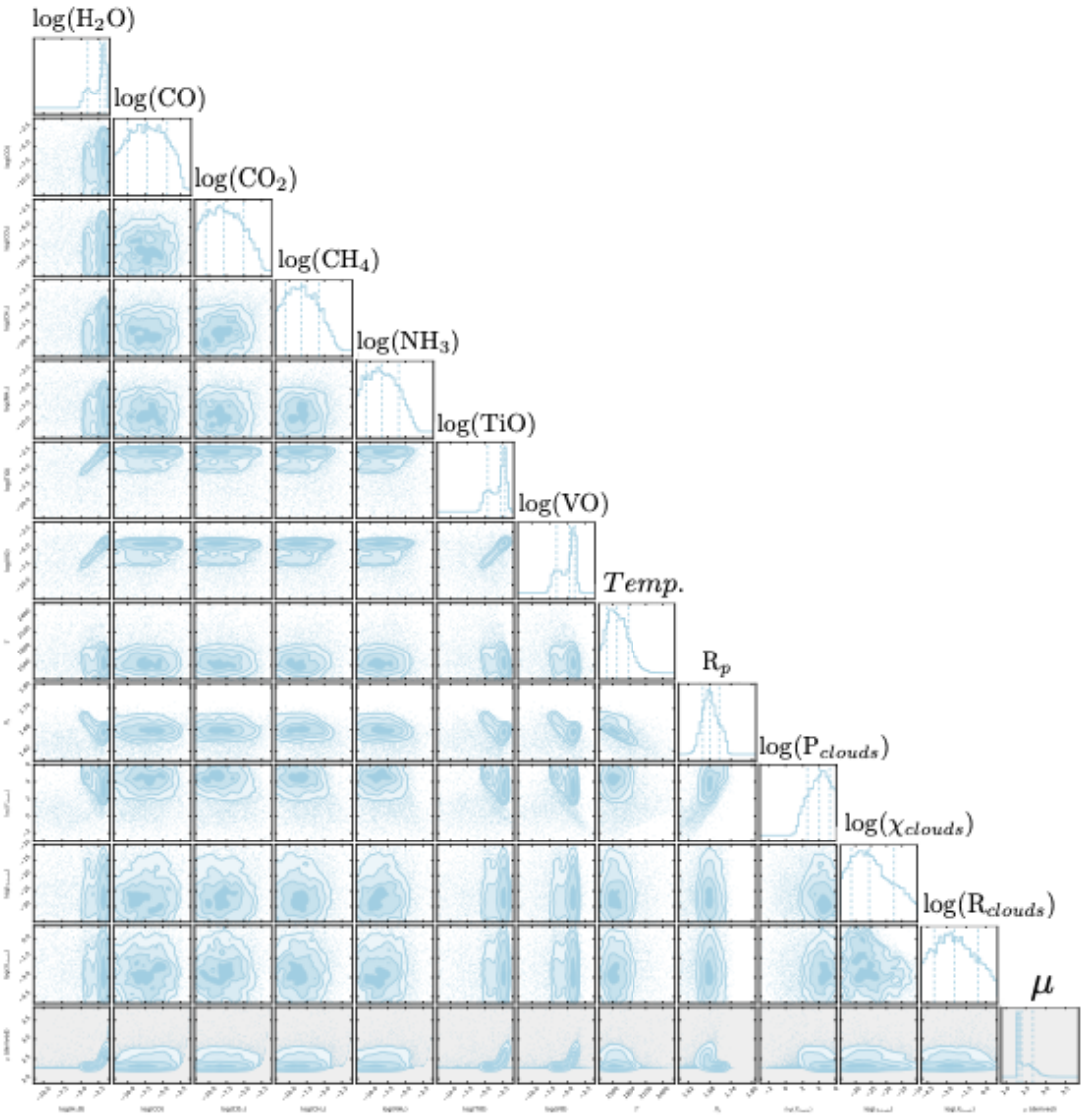

Figure 4.8: The posterior distributions of the Bayesian retrieval for WASP-76 b.

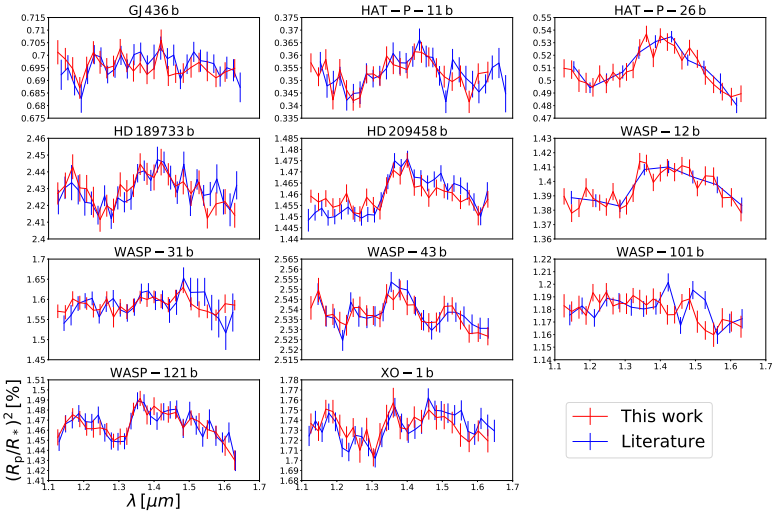

Figure 4.9: Comparison between the spectra presented here (red) and those available in the literature (blue) for 11 planets in our sample. The spectra have been normalized to have the same average transit depth, as they are subject to arbitrary offsets due to different orbital parameters or limb-darkening coefficients used by different studies.

(Sing et al., 2015), WASP-43 b (Kreidberg et al., 2014), WASP-101 b (Wakeford et al., 2017), WASP-121 b (Evans et al., 2016) and XO-1 b (Deming et al., 2013). Figure 4.9 shows a comparison between the extracted spectra here and in the literature. The only noticeable difference is HD 209458 b, which we believe is due to the different calibration method used (Tsiaras et al., 2016b). We plan to further investigate this behaviour is a future study. Concerning the detection of water vapour and other molecules (TiO, VO) and clouds, our results are consistent with previous results in the literature.

3v

Table 4.2: Proposal information for the data used in our analysis.

Planet	Proposal ID	Proposal PI	Transits used	HST orbits used
GJ 436 b	11622	Heather Knutson	4	12
GJ 3470 b	13665	Bjoern Benneke	2	6
HAT-P-1 b	12473	David Sing	1	4
HAT-P-3 b	14260	Drake Deming	2	8
HAT-P-11 b	12449	Drake Deming	1	3
HAT-P-12 b	14260	Drake Deming	2	8
HAT-P-17 b	12956	Catherine Huitson	1	4
HAT-P-18 b	14260	Drake Deming	2	8
HAT-P-26 b	14260	Drake Deming	2	8
HAT-P-32 b	14260	Drake Deming	1	4
HAT-P-38 b	14260	Drake Deming	2	8
HAT-P-41 b	14767	David Sing	1	4
HD 149026 b	14260	Drake Deming	1	4
HD 189733 b	12881	Peter McCullough	1	6
HD 209458 b	12181	Drake Deming	1	4
WASP-12 b	13467	Jacob Bean	3	12
WASP-29 b	14260	Drake Deming	1	4
WASP-31 b	12473	David Sing	1	4
WASP-39 b	14260	Drake Deming	2	8
WASP-43 b	13467	Jacob Bean	6	18
WASP-52 b	14260	Drake Deming	1	3
WASP-63 b	14642	Kevin Stevenson	1	7
WASP-67 b	14260	Drake Deming	1	3
WASP-69 b	14260	Drake Deming	1	3
WASP-74 b	14767	David Sing	1	3
WASP-76 b	14260	Drake Deming	1	4
WASP-80 b	14260	Drake Deming	1	3
WASP-101 b	14767	David Sing	1	4
WASP-121 b	14468	Thomas Evans	1	4
XO-1 b	12181	Drake Deming	1	4

Table 4.3: Parameters used in our analysis. The transit mid-time and depth are not reported as they are fitted in all cases as free parameters.

Planet	$[Fe/H]_*$	T_*	$\log(g_*)$	R_*	M_p	R_p	P	i	a/R_*	e	ω	Reference
		K	cgs	$R_\oplus$	M_{Jup}	R_{Jup}	days	deg			deg	
GJ 436 b	0.02	3416	4.843	0.455	0.08	0.366	2.64389754	86.858	14.54	0.1616	327.2	Lanotte et al. (2014)
GJ 3470 b	0.17	3652	4.78	0.48	0.043	0.346	3.3366487	88.88	13.94	-	-	Biddle et al. (2014)
HAT-P-1 b	0.13	5975	4.45	1.15	0.53	1.36	4.46529	85.9	10.247	-	-	Bakos et al. (2007)
HAT-P-3 b	0.27	5185	4.564	0.833	0.596	0.899	2.899703	87.24	10.59	-	-	Torres et al. (2008b)
HAT-P-11 b	0.31	4780	4.59	0.75	0.081	0.422	4.8878162	88.55	15.58	0.198	355.2	Bakos et al. (2010)
HAT-P-12 b	-0.29	4650	4.61	0.701	0.211	0.959	3.2130598	89	11.77	-	-	Hartman et al. (2009)
HAT-P-17 b	0	5246	4.52	0.838	0.534	1.01	10.338523	89.2	22.63	0.346	201	Howard et al. (2012)
HAT-P-18 b	0.1	4870	4.57	0.717	0.196	0.947	5.507978	88.79	16.67	-	-	Esposito et al. (2014)
HAT-P-26 b	-0.04	5079	4.56	0.788	0.057	0.549	4.234515	88.6	13.44	-	-	Hartman et al. (2011a)
HAT-P-32 b	-0.04	6207	4.33	1.219	0.86	1.789	2.150008	88.9	6.05	-	-	Hartman et al. (2011b)
HAT-P-38 b	0.06	5330	4.45	0.923	0.267	0.825	4.640382	88.3	12.17	-	-	Sato et al. (2012)
HAT-P-41 b	0.21	6390	4.14	1.683	0.8	1.685	2.694047	87.7	5.44	-	-	Hartman et al. (2012)
HD 149026 b	0.36	6160	4.278	1.368	0.359	0.654	2.87598	90	7.17	-	-	Torres et al. (2008b)
HD 189733 b	-0.03	5040	4.587	0.756	1.144	1.138	2.218573	85.58	8.81	-	-	Torres et al. (2008b)
HD 209458 b	0	6065	4.361	1.155	0.685	1.359	3.524746	86.71	8.76	-	-	Torres et al. (2008b)
WASP-12 b	0.33	6360	4.157	1.657	1.47	1.9	1.0914203	83.37	3.039	-	-	Collins et al. (2017)
WASP-29 b	0.11	4800	4.54	0.808	0.244	0.792	3.922727	88.8	12.415	-	-	Hellier et al. (2010)
WASP-31 b	-0.2	6302	4.308	1.252	0.478	1.549	3.4059096	84.41	8	-	-	Anderson et al. (2011)
WASP-39 b	-0.12	5400	4.503	0.895	0.28	1.27	4.055259	87.83	11.647	-	-	Faedi et al. (2011)
WASP-43 b	-0.05	4400	4.65	0.6	1.78	0.93	0.813475	82.6	5.124	-	-	Hellier et al. (2011)
WASP-52 b	0.03	5000	4.582	0.79	0.46	1.27	1.7497798	85.35	7.401	-	-	Hébrard et al. (2013)
WASP-63 b	0.08	5550	4.01	1.88	0.38	1.43	4.37809	87.8	6.773	-	-	Hellier et al. (2012)
WASP-67 b	-0.07	5200	4.5	0.87	0.42	1.4	4.61442	85.8	12.835	-	-	Hellier et al. (2012)
WASP-69 b	0.144	4715	4.535	0.813	0.26	1.057	3.8681382	86.71	11.953	-	-	Anderson et al. (2014)
WASP-74 b	0.39	5970	4.18	1.64	0.95	1.56	2.13775	79.81	4.861	-	-	Hellier et al. (2015)
WASP-76 b	0.23	6250	4.128	1.73	0.92	1.83	1.809886	88	4.012	-	-	West et al. (2016)
WASP-80 b	-0.13	4143	4.663	0.586	0.538	0.999	3.06785234	89.02	12.63	-	-	Triaud et al. (2015)
WASP-101 b	0.2	6380	4.345	1.29	0.5	1.41	3.585722	85	8.445	-	-	Hellier et al. (2014)
WASP-121 b	0.13	6460	4.242	1.458	1.183	1.865	1.2749255	87.6	3.754	-	-	Delrez et al. (2016)
XO-1 b	0.02	5750	4.509	0.934	0.918	1.206	3.941534	88.81	11.55	-	-	Torres et al. (2008b)

Table 4.4: Observationally-corrected S/N, ADI, and main retrieval results (maximum a-posterior).

Planet	o.c. S/N	ADI	R_p R_{Jup}	T_p K	$\log_{10}(P_{cloup})$ Pa	$\log_{10}(H_2O)$
GJ 436 b	9.57	0.00	0.37 ± 0.01	238.25 ± 188.69	1.22 ± 2.12	–6.74 ± 2.70
GJ 3470 b	15.64	0.31	0.36 ± 0.01	243.68 ± 135.42	2.12 ± 1.57	–4.87 ± 2.91
HAT-P-1 b	10.20	8.18	1.29 ± 0.03	1017.09 ± 386.57	3.33 ± 1.35	–2.68 ± 1.22
HAT-P-3 b	4.99	0.00	0.89 ± 0.01	843.00 ± 338.94	1.50 ± 2.01	–6.93 ± 2.73
HAT-P-11 b	7.62	6.61	0.43 ± 0.01	632.37 ± 228.12	4.04 ± 1.11	–1.76 ± 1.41
HAT-P-12 b	16.12	3.08	0.92 ± 0.02	509.25 ± 174.42	2.76 ± 1.23	–3.61 ± 1.48
HAT-P-17 b	5.34	0.28	0.99 ± 0.02	568.69 ± 330.38	1.25 ± 2.12	–5.86 ± 2.89
HAT-P-18 b	13.91	5.71	0.94 ± 0.02	451.61 ± 176.54	2.82 ± 0.91	–2.63 ± 1.18
HAT-P-26 b	13.59	32.73	0.52 ± 0.01	680.56 ± 198.55	3.94 ± 0.74	–3.32 ± 1.10
HAT-P-32 b	14.32	16.44	1.77 ± 0.02	1139.53 ± 169.81	2.34 ± 0.88	–2.84 ± 0.92
HAT-P-38 b	5.47	0.67	0.82 ± 0.02	762.80 ± 256.24	3.32 ± 1.68	–4.29 ± 2.16
HAT-P-41 b	8.59	7.29	1.60 ± 0.03	1570.37 ± 313.42	2.41 ± 1.20	–2.77 ± 1.09
HD 149026 b	5.82	0.00	0.65 ± 0.01	1335.30 ± 379.48	0.75 ± 1.68	–5.75 ± 2.91
HD 189733 b	7.87	11.77	1.16 ± 0.00	621.49 ± 139.05	4.66 ± 0.91	–2.51 ± 0.90
HD 209458 b	22.24	17.21	1.33 ± 0.02	1061.35 ± 241.23	2.14 ± 0.95	–3.19 ± 0.87
WASP-12 b	14.72	25.08	1.86 ± 0.02	1864.01 ± 202.82	2.38 ± 0.95	–3.12 ± 0.92
WASP-29 b	9.25	1.25	0.76 ± 0.02	713.48 ± 311.15	3.29 ± 2.29	–7.93 ± 2.38
WASP-31 b	9.33	1.31	1.47 ± 0.03	1088.35 ± 220.16	1.79 ± 1.27	–3.84 ± 1.90
WASP-39 b	22.66	34.52	1.24 ± 0.01	1258.71 ± 389.53	4.86 ± 0.32	–5.94 ± 0.61
WASP-43 b	7.34	1.93	0.94 ± 0.01	957.27 ± 343.30	2.90 ± 2.12	–4.36 ± 2.10
WASP-52 b	13.74	20.32	1.27 ± 0.01	667.66 ± 121.94	4.84 ± 0.88	–4.09 ± 0.87
WASP-63 b	12.22	0.00	1.36 ± 0.03	948.22 ± 179.13	0.93 ± 1.40	–5.81 ± 2.81
WASP-67 b	5.87	0.27	1.36 ± 0.03	636.58 ± 267.82	2.18 ± 1.91	–6.17 ± 2.82
WASP-69 b	31.39	13.30	1.01 ± 0.01	492.92 ± 153.38	3.93 ± 0.99	–3.94 ± 1.25
WASP-74 b	8.35	0.00	1.46 ± 0.03	1519.36 ± 310.70	-0.05 ± 1.48	–5.91 ± 2.81
WASP-76 b	23.24	36.44	1.68 ± 0.02	1591.88 ± 184.08	3.93 ± 1.22	–2.70 ± 1.07
WASP-80 b	15.75	1.16	0.98 ± 0.01	539.39 ± 278.81	2.17 ± 1.48	–5.34 ± 2.65
WASP-101 b	14.03	0.00	1.29 ± 0.02	1042.55 ± 215.30	0.54 ± 1.75	–6.95 ± 2.61
WASP-121 b	15.96	11.52	1.69 ± 0.01	1543.93 ± 134.06	3.79 ± 1.25	–3.05 ± 0.87
XO-1 b	4.97	3.15	1.21 ± 0.01	778.21 ± 224.04	4.14 ± 1.29	–2.75 ± 1.64

4.5 Summary and Conclusions

In this chapter I showed one of the most complete works of atmospheric spectroscopy on exoplanets. I briefly described the dataset from which it was possible to extract exoplanetary atmospheric spectra as a function of wavelength. HST/WFC3 has been the best instrument up until 2020 and demonstrated the power and potential of atmospheric spectroscopy. I showed the analysis made on 30 exoplanets, most of them hot-Jupiter and explained how water has been detected on at least 16 of them. Future space mission and ground based surveys will help constraining in a better way the parameter space of atmospheric models and will break possible degeneracies.

Furthermore, the state-of-art in atmospheric spectroscopy includes the use of Bayesian analysis to retrieve planetary parameters. The use of efficient codes and algorithms are crucial to obtain an atmospheric model in a reasonable amount of time since Bayesian analysis is time-

consuming and computing-intensive. In the next chapters I will introduce to deep learning and I will apply a neural network to decrease further the computation time in order to retrieve atmospheric parameters.

Chapter 5

Deep Learning methods

Human beings have always tried to create an artificial kind of life, able to move and think autonomously. Some of the first written proof of this attempt comes from ancient Greece, with the myths of the statue of Pygmalion, Daedalus, who created the Minotaur labyrinth and Hephaestus who built automatons of metal to help him work. Galatea, Talos, and Pandora can be considered all artificial kind of life (Ovid and Martin, 2004; Tandy, 1997; Sparkes, 1996)

Deep Learning (DL) is a subset of a broader Machine Learning (ML) algorithms family, based on leaning data representations. This kind of algorithms was defined in the 1940s, and the last seven years they became very relevant and accessible. Figure 5.1 shows all the evolution of deep learning algorithms defined from the beginning until today.

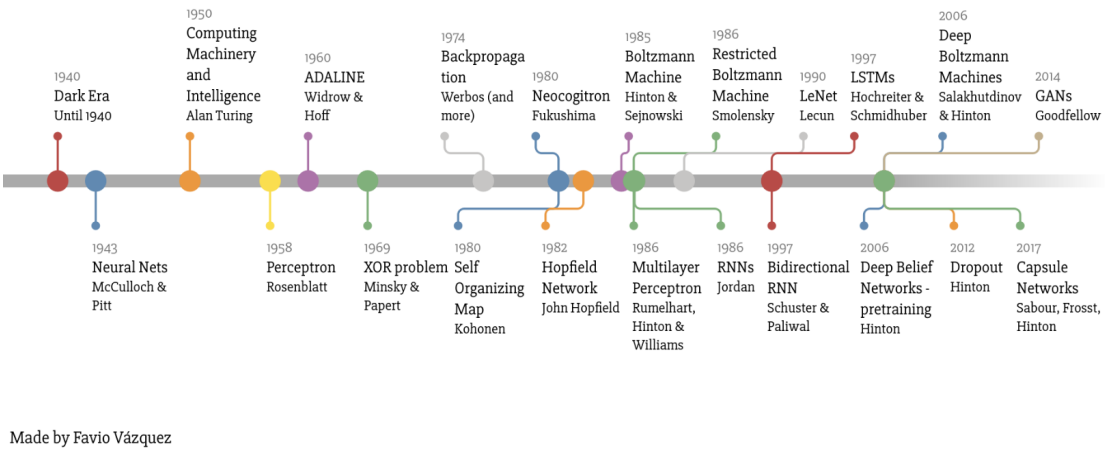

Figure 5.1: Time line of Deep Learning algorithms definition. (Image made by Favio Vàzquez[1])

Deep learning applications are relatively recent because we started having reliable ways of

[1] https://towardsdatascience.com/a-weird-introduction-to-deep-learning-7828803693b0

training deep neural networks. With the technology evolution, especially the advent of Graphic Processor Units (GPUs), and now Tensor Processor Units (TPUs) technology, the development of relevant theoretical and algorithmic improvements and the exponential accumulation of data all over the world, deep learning naturally became the most popular way of understanding the world and changed the way we do machine learning.

More generally, artificial intelligence algorithms can help to solve tasks that are easy for people to solve intuitively but hard to describe formally, i.e., recognising spoken words, faces, images, movements or particular features in an image. In my thesis, I use a deep learning approach to artificial intelligence. In this way, it is possible to allow computers to learn from experience and improves the way they interpret and analyse the world in terms of a hierarchy of concepts. During the phase in which the machine gather information from a dataset, it is essential for the human programmer to specify formally all of the knowledge that the computer needs to interpret correctly the data it sees and return useful information.

One of the first worldwide success of artificial intelligence happened in 1997 when IBM's Deep Blue chess-playing system defeated the world champion Garry Kasparov (Hsu, 2002). Ten years later AlphaGO, a computer program developed by Alphabet Inc's Google DeepMind (Silver et al., 2017) defeated the world champion of the Go game, Lee Sedol, without handicap in a professional board game 19x19.

Artificial intelligence algorithms allowed the computers to deal with problems which involve knowledge of the real world and make a decision as a human being would do. For example, a simple logistic regression algorithm can recommend whether cesarean delivery is necessary or not (Shlomo et al., 1990).

All of these algorithms depend heavily on how data are arranged and on the representation of the data they are given. Many artificial intelligence problems can be solved by designing the exact set of features to extract from a dataset. For example, a useful feature to extract during speaker identification is the size of the speaker's vocal tract. This information can also tell whether the speaker is a man, a woman or a child. The way to represent the dataset is a general problem that appears in every field. The choice of a particular data representation can have severe consequences in term of computing time and usage (Figure 5.2)

One way to solve the representation problem is to use machine learning not only to discover eventual patterns within the dataset but also find the optimal way to represent the dataset. This kind of approach is called representation learning. Representation learning algorithms can rapidly adapt to a new dataset and require minimal human intervention. An excellent example of representation learning algorithm is the autoencoder. The autoencoder is a combination of an

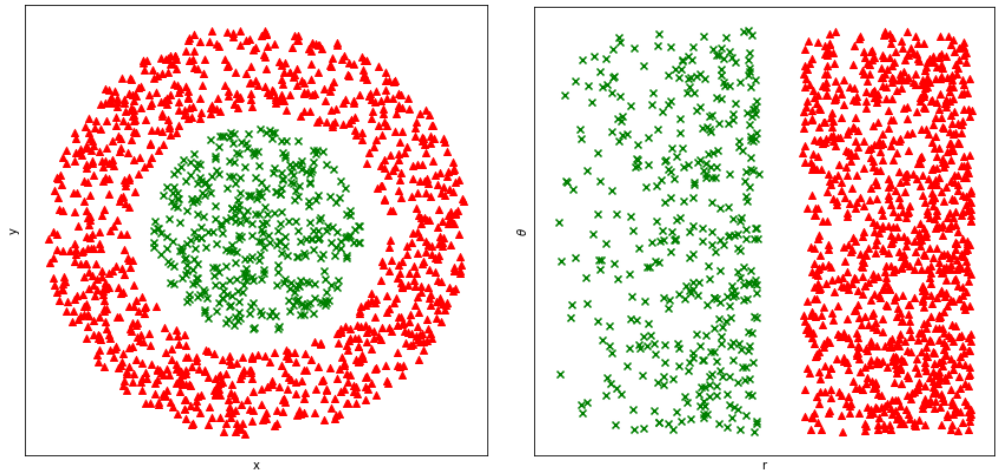

Figure 5.2: Example on the different representation of the same dataset. In order to find a curve separating two subsets of data the easiest solution is to find a line on a polar coordinate system. The same problem can be solved using a Cartesian representation but it is computationally more expansive.

encoder, an algorithm that converts the input data into a compressed basis set, and a decoder, the algorithm that converts the new representation back to the original one.

Extracting many high-level features from raw data can be very difficult. Moreover, it is necessary to take into account many factors of variation (for example, the accent of a speaker or different shapes that a human face can have), to be isolated, understood and interpreted.

Deep learning solves the problem of representation learning, introducing new representations expressed in terms of other more straightforward representations.

In this Chapter, I will briefly explain the theory behind a neural network. I will introduce to Artificial Neural Networks (ANNs), which are essentially the computational backbone of a deep learning algorithm. The fundamental concepts of deep learning are described widely in literature (Pratt, 1993; Anderson, 1995; Hassoun, 1995; Tettamanzi et al., 2001; Goodfellow et al., 2016).

5.1 Biological Neural Networks

Having a basic knowledge about how the human brain works can help us understand the fundamentals of ANNs. The brain is the central part of the nervous system, and it consists of an extensive neural network (NN). A single neuron (Figure 5.3) consists of a central part, the cell body, connected to other neuronal cells through a complex net of axons and dendrites which constitute the synaptic connections.

The activation of a neuron depends on the reception of an electric signal from another neuron through the synaptic connections. After receiving an electric signal, the neuron can, in turn, send another electric impulse towards another neuron. In this way, the information can propagate

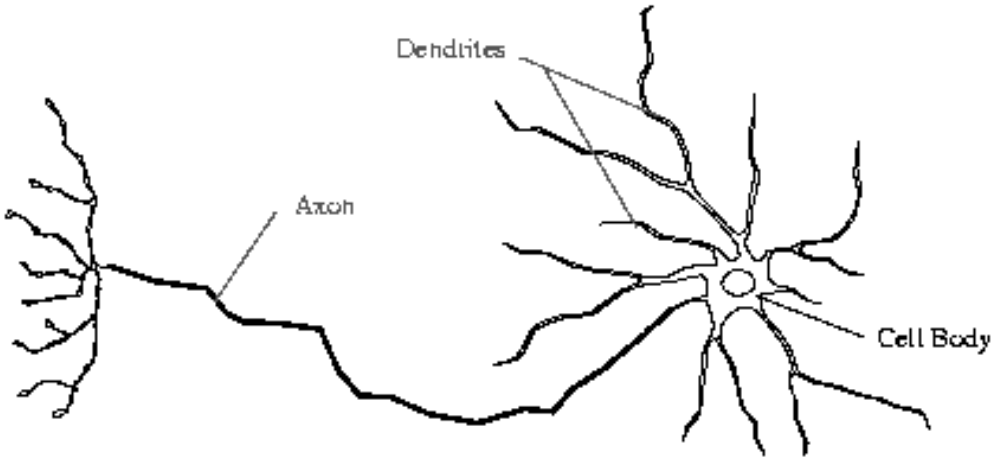

Figure 5.3: Morphology of a neuron.

through a biological neural network.

The human brain consists of 10^{11} neurons, connected through 10^{15} connections (Tettamanzi et al., 2001). The activation of specific neuronal groups can lead to the movement of particular muscles or the generation of thoughts in human beings.

5.2 Artificial Neural Networks

Currently, building an artificial brain is an impossible task, but it is possible to make simplified versions of it, simple artificial neural networks with artificial neurons. ANNs can be good at finding patterns within a dataset and make simple rules from complex problems, but they are still far from being considered "intelligent". They are also good at generalising information from an input dataset. The generalisation skill is the most desirable feature of an ANN currently.

5.2.1 The artificial neuron

The neuron is the most fundamental part of a neural network and it is defined as:

$$y(x) = g\left(\sum_{t=0}^{n} w_i x_i\right) \tag{5.1}$$

where $(x_0, x_1, ..., x_n)$ are the neuron, n is the number of input dendrites, $y(x)$ is the output axon, $(w_0, w_1, ..., w_n)$ are the weights and g is the activation function that control the output coming from a neuron, based on the sum of the input (Figure 5.4).

Similarly to a biological neuron, the g function represents the activation of a particular neuron, and it is a threshold function, returning either 0 or 1. Other activation function can

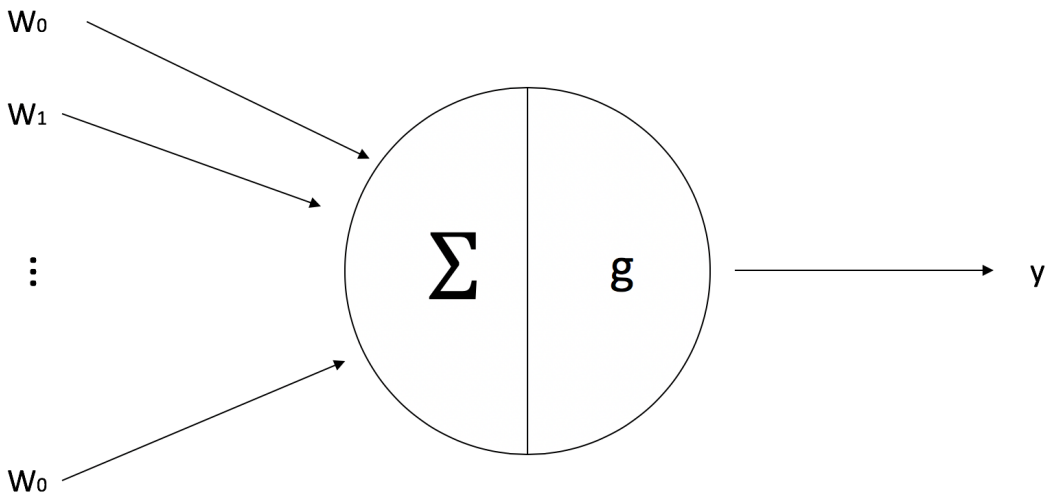

Figure 5.4: Scheme of an artificial neuron.

return output values of either -1 or 1. The weights $w_0, w_1, ..., w_n$ are not as restricted as the output values and can have any real value.

An example of commonly used activation functions are the sigmoid function (Equation 5.2) and the hyperbolic tangent (Equation 5.3). It is important to choose a differentiable activation function to implement many common training algorithms, such as the backpropagation (discussed in section 5.2.3).

$$g(x) = \frac{1}{1 + e^{-2s(x+t)}}, \tag{5.2}$$

$$g(x) = \frac{e^{2s(x+t)} - 1}{e^{2s(x+t)} + 1}. \tag{5.3}$$

During the training phase, the values t and s and the weights are the ones that are adjusted.

5.2.2 ANN description

The multilayer feedforward artificial neural network is a common ANN. In this kind of network, the neurons are assembled in layers, from an input layer to an output layer. Between the input and output layer, there are generally many hidden layers (Figure 5.5). Each connection only goes forward in this representation from layer to layer. The reader interested in other kinds of representation can read Hassoun (1995).

ANNs have two different essential phases: the training phase and the execution phase. The

training phase depends on the input dataset, and at this stage, the ANN is trained to return a specific output given the input. Once it is trained, it is possible to store all the information on the activation function parameters and the weights and can be used for the execution stage.

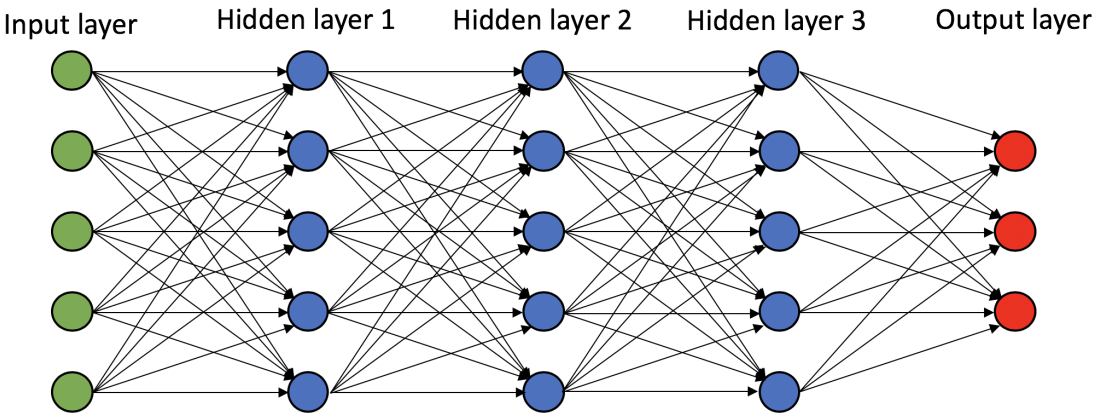

Figure 5.5: Representation of an ANN. In the beginning, there is an input layer, followed by three hidden layers and, finally, the output layers. Each neuron is connected through a weights system, which value is adjusted during the training phase.

In a ANN, during the training phase, the weights $(w_0, w_1, ..., w_n)$ and the t parameters are adjusted.

5.2.3 ANN training - Backpropagation

The training phase is essential to teach the ANN any task. The training phase is necessary to adjust the weights and teach the ANN to return a specific output. At the same time it is important to exclude over-fitting, i.e., the ANN needs to be reliable also with a different dataset and to do that it needs to generalise the information from a dataset. The training phase corresponds to an optimisation problem; indeed the aim is to minimise the mean square error or the neural network's reconstruction of the data, over the entire training set. There are many solutions to this problem, one of the most common approaches include the use of specific gradient descent algorithms like backpropagation. This algorithm has some limitation about the extent of the adjustment of the weights at each iteration. This problem has been solved with the RPROP algorithm (Riedmiller and Braun, 1993), the quickprop (Fahlman, 1989), the wake-sleep algorithm (Hinton et al., 1995) or the dropout algorithm (Baldi and Sadowski, 2014).

As the name suggests, in the backpropagation algorithm the error at the end of an iteration is calculated and propagated back through the network, adjusting all the weights to minimise the error after each iteration. The following explanation is valid for fully connected ANNs, but similar theories can be applied to sparsely connected ANNs.

The most efficient way to minimise the mean square error is training the data sequentially,

one input at a time, completing step by step all the training set, instead of taking the training set as a whole. Proceeding in such a way it is essential to shuffle the training set such as avoiding dependence on the training set order. This approach also avoids being stuck in local minima.

5.3 Convolutional Neural Networks

ANN layers or fully connected layers, can be used to analyse an image. First of all the image needs to be transformed conveniently to optimise the information extraction to give as an input to the ANN. For tackling this problem LeCun et al. (1989) defined a network called Convolutional Neural Network (CNN).

CNNs are a kind of network specialised in analysing data prepared as a grid. It can be, for example, an image made of a 2D-grid of pixels. A CNN is a network that uses an operation called convolution, a kind of linear operation which details are explained in section 5.3.1 (Goodfellow et al., 2016). Convolutional networks are neural networks that use convolution in place of general matrix multiplication in at least one of their layer.

Another common operation used in building a CNN is the pooling. After a convolutional layer usually is used a pooling layer (described in section 5.3.2). After several convolutional and pooling layers, the result is flattened into a one-dimensional array to use as an input for the fully connected layer (the artificial neural network) 5.6.

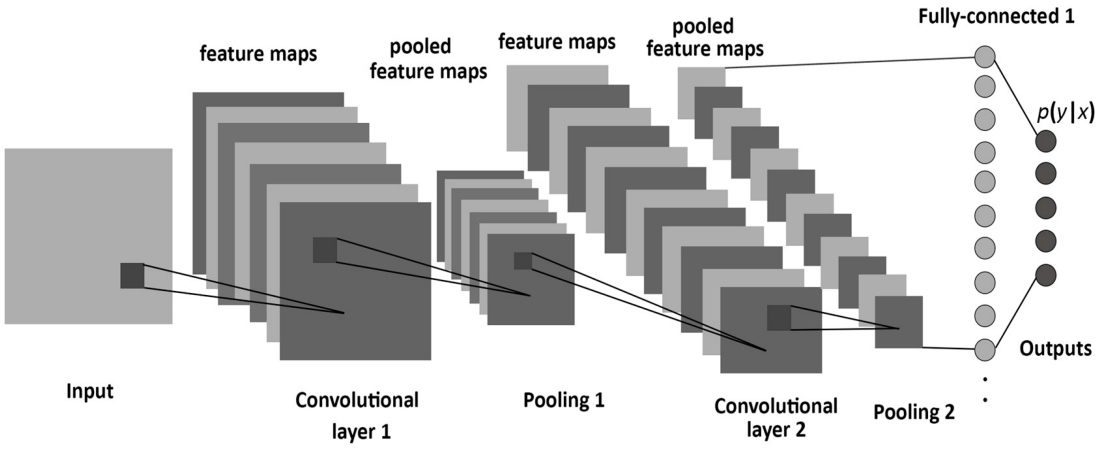

Figure 5.6: CNN structure scheme. The input image, usually a 2D array, is represented through a series of convolutional and pooling layers before being analysed by an artificial neural network (Image from Albelwi and Mahmood (2017)).

5.3.1 The convolution operation

The convolution is an operation between two functions, x and w. It is denoted with the symbol $*$ and defined as:

$$s(t) = (x * w)(\tau) \coloneqq \int_{-\infty}^{\infty} x(\tau)w(t-\tau)\mathrm{d}\tau = \int_{-\infty}^{\infty} x(t-\tau)w(\tau)\mathrm{d}\tau. \tag{5.4}$$

In convolutional network terminology, the function x represents as the input, i.e., a multidimensional array of data and the function w is the kernel, i.e., a multidimensional array of parameters. These multidimensional arrays are referred to as tensors. Another way to refer the output is the "feature map".

Let x and w be two functions of integers t, then the discrete convolution can be expressed as:

$$s(t) = (x * w)(t) = \sum_{\tau=-\infty}^{\infty} x(\tau)w(t-\tau). \tag{5.5}$$

The convolutions are computed over more than one axis at a time. If the user have 2D arrays as input I he wants to use also a 2D kernel K:

$$S(i,j) = (I * K)(i,j) = \sum_m \sum_n I(m,n)K(i-m, j-n) = \sum_m \sum_n I(i-m, j-n)K(m,n). \tag{5.6}$$

The second part of equation 5.6 is a consequence of the commutative property of a convolution, which can be obtained by flipping the kernel relative to the input function, i.e., as m increases, the index into the input increases but the index into the kernel decreases.

Many neural network implementations use a similar function called cross-correlation, which is a convolution function without flipping the kernel (see Figure 5.7):

$$S(i,j) = (I * K)(i,j) = \sum_m \sum_n I(i+m, j+n)K(m,n). \tag{5.7}$$

A discrete convolution is essentially a multiplication by a matrix and usually gives, as a result, a very sparse matrix, i.e., a matrix in which many elements are equal to zero because often the kernel is much smaller than the input image.

5.3.2 Pooling

After performing the convolutions, each activation run through a function which should break some eventual linear correlations between close pixels and run to generalise better the information. This function is called the rectified activation function. This stage is also called the detector stage. In the third phase, a pooling function is used to modify the output of the layer (Figure 5.8) furthermore. The pooling function replaces the output of the layer at a specific

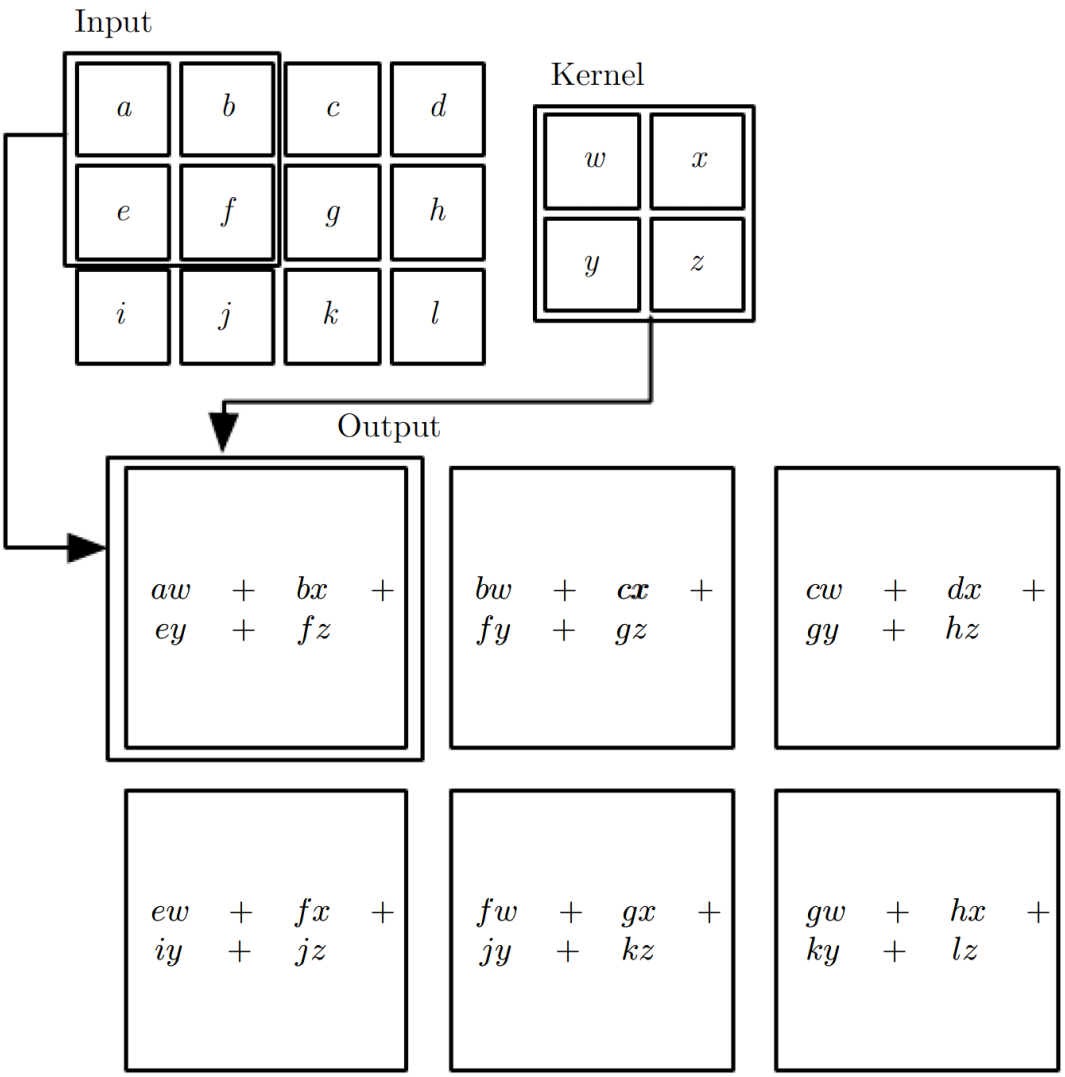

Figure 5.7: Example of a 2D convolution without flipping the kernel (Image from Goodfellow et al. (2016)).

location with a summary of the nearby outputs.

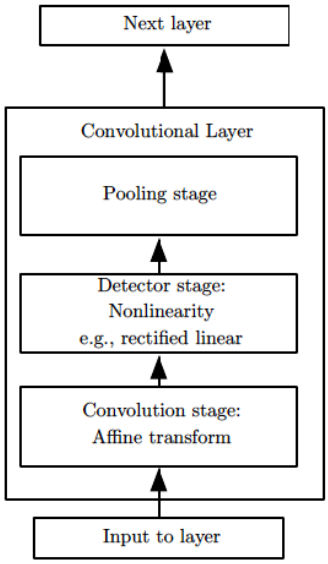

Figure 5.8: Layers of a typical convolutional neural network. From the bottom to the top: the input layer (a bidimensional array or image) is transformed through a series of convolutional layers, then they are modified with the application of a set of rectified functions and pooling layers. After then the output can be used as an input for a fully connected layer or another convolutional layer (Image from Goodfellow et al. (2016)).

A popular pooling method is called max pooling (Zhou and Chellappa, 1988), which consists of reporting the maximum output within a rectangular selection. Another common max pooling method is including the average output over a rectangular selection, the L^2 norm, or the weighted average based on the distance from the central pixel.

After applying several convolutional layers to an image, the output can be linearised and applied to a fully connected layer or artificial neural network.

5.4 First application in exoplanetary atmospheres

Deep learning in exoplanetary science are very recent. The very first application was in 2016 with RoBErt (Robotic Exoplanet Recognition), designed by Waldmann (2016). RoBErt is a pre-trained Deep Belief Network (DBN, Hinton et al. (2006); Hinton (2007)) which mimic human recognition of spectroscopic features. Although complete derivation of a DBN is beyond the scope of this thesis, in Figure 5.9 I show the structure of a DBN compared to a Restricted Boltzmann Machine (RBM) (Waldmann, 2016).

RoBErt can identify the presence of a molecular species in a planetary atmosphere, attributing to them a probability. In Figure 5.10 there are 4 normalised spectra and the identification using RoBErt for 4 input spectra with signal-to-noise ratio of, respectively, 20, 15, 5 and 2

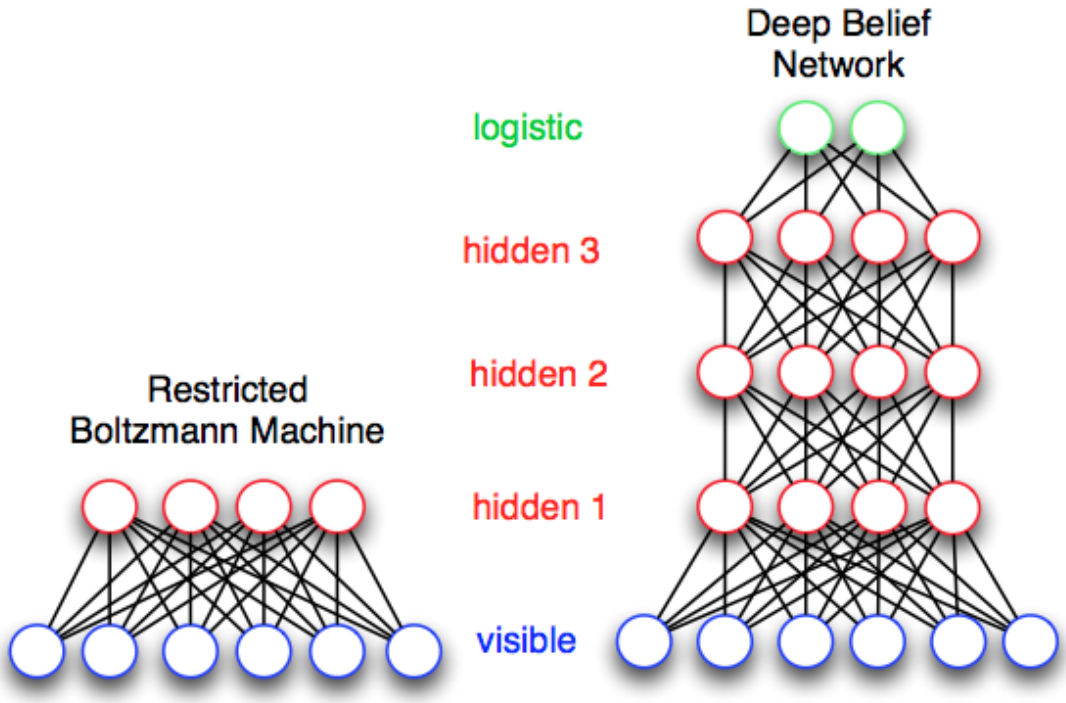

Figure 5.9: Scheme of a restricted Boltzmann machine (left) and a deep belief network (right). The blue layers represent the visible units (like the inputs), and in red, there are the hidden units. The green layers are the logistic units and represent the output of the deep belief network. Black lines represent the connections between all units (image from Waldmann (2016)).

(Waldmann, 2016).

For the atmospheres made with just one main component, RoBErt can identify the main trace gas $> 99\%$ of the time, across the gases considered in Waldmann (2016).

5.4.1 Other applications in exoplanetary atmospheres

At the time of writing this thesis, there are a few attempts of studying exoplanetary atmospheres using AI, more in particular using machine learning algorithms. For exmaple Márquez-Neila et al. (2018) recently presented an atmospheric retrieval algorithm based on random forests regression (Breiman, 2001) and demonstrated the algorithm on Hubble/WFC3 observations.

Waldmann (2016) is the only example of a deep learning method applied to exoplanetary atmospheres. RobERt can, therefore, recognise the presence of some molecular species just by "looking" a single exoplanetary spectrum. In this thesis, in chapter 6, I introduce a more evolved tool, ExoGAN (Exoplanets Generative Adversarial Network). ExoGAN is a deep learning algorithm able not only to recognise molecular species in exoplanetary atmosphere, but also to estimate their abundances. ExoGAN can be considered as the second deep learning attempt in exoplanetary atmosphere (Zingales and Waldmann, 2018).

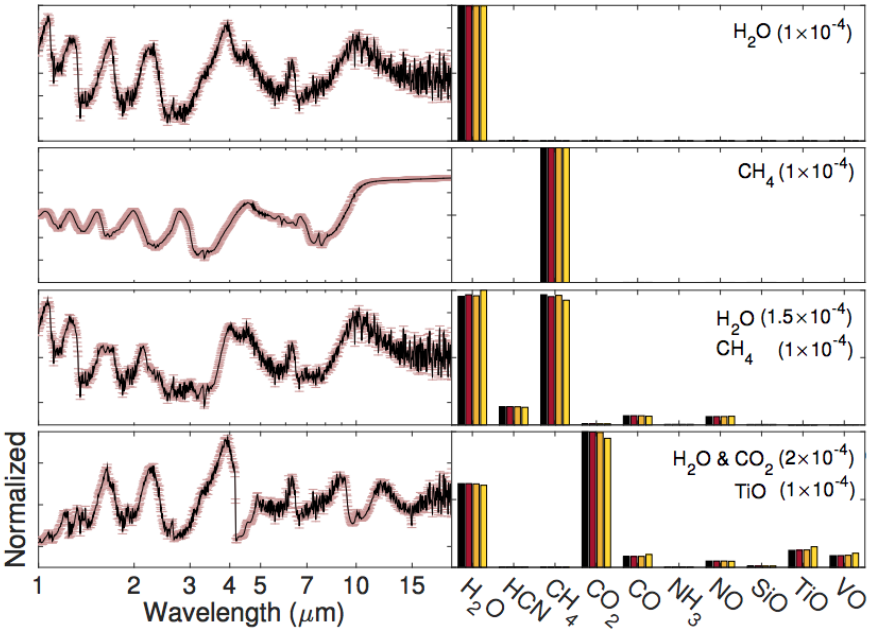

Figure 5.10: On the left side we find an input exoplanetary spectrum. On the right side the histograms represent the probability of the presence of a molecular species given the input spectrum and its error-bars. The real input and the related mixing ratio to generate the spectra on the left are labelled on the top right corner of each simulation (Image from Waldmann (2016)).

5.5 Summary and Conclusions

In this Chapter, I explained the theory behind neural networks focusing on ANNs and CNNs. The field of applicability of these kinds of algorithm is vast, and the astrophysics community started to use them relatively recently. The potential of these algorithms and their reliability leads them to be very common and useful tool for the future generation of scientists. RoBErt was the first neural network trained to recognise molecular features in exoplanetary atmospheres. It is able to detect the presence of molecular species but not their abundances. In the next chapter, I will explain in detail the very first attempt to analyse the exoplanetary atmospheres with a generative net, ExoGAN (Exoplanets Generative Adversarial Network). I will explain more-in-detail the rationale behind a ExoGAN and its application to exoplanetary science and spectral retrievals.

Chapter 6

ExoGAN: Retrieve exoplanetary atmosphere using Deep Convolutional Neural Networks

The modelling of exoplanetary atmospheric spectroscopy through so-called atmospheric retrieval algorithms has become accepted standard in the interpretation of transmission and emission spectroscopic measurements (e.g. Kreidberg et al., 2018; Tsiaras et al., 2018; Bruno et al., 2018; Mansfield et al., 2018; Spake et al., 2018; Sheppard et al., 2017; Barstow et al., 2017; Rocchetto et al., 2016a). These retrieval algorithms are designed to solving the often ill-posed inverse problem of determining atmospheric parameters (such as trace gas abundances for example) from the measured spectra and their corresponding measurement uncertainties (e.g. Irwin et al., 2008; Madhusudhan and Seager, 2009; Line et al., 2013; Benneke and Seager, 2013; Lavie et al., 2017; Gandhi and Madhusudhan, 2018; Cubillos et al., 2016). The associated atmospheric forward model to be fitted varies in complexity from retrieval to retrieval but most times encompasses a high dimensional likelihood space to be sampled. In the era of JWST (Gardner et al., 2006) and ARIEL (Tinetti et al., 2016) observations, said model complexity will have to increase significantly. To date, the most commonly adopted statistical sampling methods are Nested Sampling (Skilling, 2004; Feroz and Hobson, 2008a; Feroz et al., 2009) and Markov Chain Monte Carlo (e.g. Gregory, 2011). These approaches typically require of the order of 10^5 - 10^6 forward model realisations until convergence. The traditional analysis method, which uses Bayesian statistics, creates a precarious bottleneck: to achieve convergence within reasonable time frames (hours to days), we require the atmospheric forward model to be fast and consequently overly

simplistic. The inclusion of disequilibrium chemistry, self-consistent cloud models and the move from 1 D to 2-3 D radiative transfer, are largely precluded by this constraint. In this chapter, I present the first deep learning architecture for exoplanetary atmospheric retrievals and discuss a path towards solving the computational bottleneck using atmospheric retrievals assisted by deep-learning. The work shown in this chapter is part of my work published in Zingales and Waldmann (2018).

Artificial Intelligence has been used extensively to understand and describe complex structures and behaviour in a wide variety of dataset across a plethora of research fields.

In recent years, the field of exoplanets has seen pioneering deep-learning papers on planet detection (Pearson et al., 2018; Shallue and Vanderburg, 2018), exoplanet transit prediction (Kipping and Lam, 2017) and atmospheric spectral identification (Waldmann, 2016). In Waldmann (2016) we applied a deep-belief neural network (DBN) to recognise the atmospheric features of an exoplanetary emission spectrum. This approach provided a qualitative understanding of the atmospheric trace gases likely to be present in a planetary emission spectrum, to then be included in the atmospheric retrieval framework TauREx (Waldmann et al., 2015a,b). In this chapter, I introduce a Generative Adversarial Network (GAN, Goodfellow et al., 2014) to predict the maximum likelihood (ML) of the full retrieval solution given the observed spectrum. As shown in the following sections, this can be used as a stand-alone solution to retrieval or used to constrain the prior parameter ranges for a more standard atmospheric retrieval later.

We design the algorithm following four guiding principles:

- Once trained, the deep or machine-learning algorithm should apply to the widest possible range of planet types.
- Once trained, the algorithm should apply to a wide range of instruments.
- The algorithm should be robust in the presence of unknown 'un-trained' features and be able to generalise to parameter regimes outside its formal training set.
- The design of the algorithm and data format should be modular and easily modifiable and expandable.

In the following sections, I present the Exoplanet Generative Adversarial Network (ExoGAN) algorithm and demonstrate it on a variety of retrieval scenarios.

6.1 Generative Adversarial Networks

Generative Adversarial Networks first introduced by Goodfellow et al. (2014) belongs to the class of unsupervised deep generative neural networks (Goodfellow et al., 2016). Deep generative models can learn the arbitrarily complex probability distribution of a data set, p_{data}, and can generate new data sets drawn from p_{data}. Similarly, they can also be used to fill in missing information in an incomplete data set, so-called inpainting. In this work, I use the data inpainting properties of the GAN to perform retrievals of the atmospheric forward model parameters.

The most common analogy for a GAN architecture is that of a counterfeit operation. The neural network is given a training data set, $\mathbf{x}$, in our case combinations of atmospheric spectra with their associated forward model parameters. I refer to the training set as the 'real' data with the probability distribution p_{data}. Now two deep neural networks are pitted against each other in a `minmax` game. One network, the generator network (G), will try to create a 'fake' dataset (p_g), indistinguishable from the 'real' data. In a second step, a second neural network, the discriminator (D), tries to classify 'fake' from 'real' data correctly. The training phase of the GAN is completed when a Nash equilibrium is reached, and the discriminator cannot identify real from fake any longer. At this stage the generator network will have learned a good representation of the data probability distribution and $p_g \simeq p_{data}$. Unlike for variational inference methods, such as variational autoencoders (VAE; Kingma and Welling, 2013; Jimenez Rezende et al., 2014), the functional form of the data likelihood does not need to be specified but is learned by the Generator. Such implicit latent variable models or likelihood-free networks allow the learning of arbitrarily complex probability distributions in an unsupervised manner while assuming minimal prior assumptions on the data distribution.

GANs have been applied to multiple problems, such as semi-supervised learning, stabilizing sequence learning methods for speech and language, and 3D modelling (Denton et al., 2015; Radford et al., 2015; Salimans et al., 2016; Lamb et al., 2016; Wu et al., 2016). Notable examples of GANs applied in an astrophysical context are given by Rodriguez et al. (2018); Stark et al. (2018); Schawinski et al. (2017), who used GANs trained on existing N-body simulations to efficiently generate new, physically realistic realisations of the cosmic web, learn Point Spread Function from data or de-noise ground-based observations of galaxies.

In the field of exoplanets, the use of GANs or similar deep architectures has not yet been explored. In this work, I base ExoGAN on a Deep Convolutional Generative Adversarial Network (DCGAN, Radford et al., 2015).

DCGANs are an evolution from the classical GAN by replacing the multilayer perceptrons (MLPs; Rumelhart et al., 1986; Bengio, 2009) in the Generator and Discriminator networks

with all convolutional layers. Their characteristics make DCGAN significantly more robust to discrete-mode and manifold model collapse (Metz et al., 2016; Arjovsky and Bottou, 2017) and are found to be stable in most training scenarios (Radford et al., 2015). The use of batch normalisation (appendix B.2) further increases training speed and robustness. Besides, we note that convolutional networks are ideally suited to capturing the highly correlated signals of broad, roto-vibrational spectral bands in NIR and IR wavelengths.

The fundamental part of a GAN are two differentiable functions G and D called, respectively, generator and discriminator. The two nets are locked in a game with different roles. The generator tries to reproduce an output as similar as possible to the training set. The discriminator at the same time is trained to recognise whether the generator is reproducing a real image and associate a probability to it. When the GAN is thoroughly trained, the discriminator will not realise whether the output of the generator is a fake image or not and it will return a probability of 1/2 (Figure 6.1).

In perfect training, the generator manages to catch the distribution of the training set and returns realistic realisations of it. The determinator ensures the plausibility of the output. In the following section, I will describe a particular kind of GAN used in Chapter 6 to detect the best set of parameters for a retrieval.

6.2 Deep Convolutional Generative Adversarial Networks

In this chapter, I use a particular kind of GAN called Deep Convolutional Generative Adversarial Network (DCGAN), presented for the first time in Radford et al. (2015), characterised by:

- All convolutional netwotks: it emphasises the convolutions, getting rid of the pooling layers (see chapter 5 for more details). They increase (or decrease in the case of the discriminator) the feature's spatial dimensions as shown in Figure 6.1.
- Batch Normalisation: the algorithm normalises the feature vector (a function of the input image which indicates the activation of the hidden neurons output from the layer), to have a zero mean and unit variance in all the layers. The normalisation is helpful to stabilise the learning phase and to handle the poor weight initialisation problem. Batch Normalisation is described in Appendix B.2

In the following, I describe intuitively the rationale behind generator and discriminator networks.

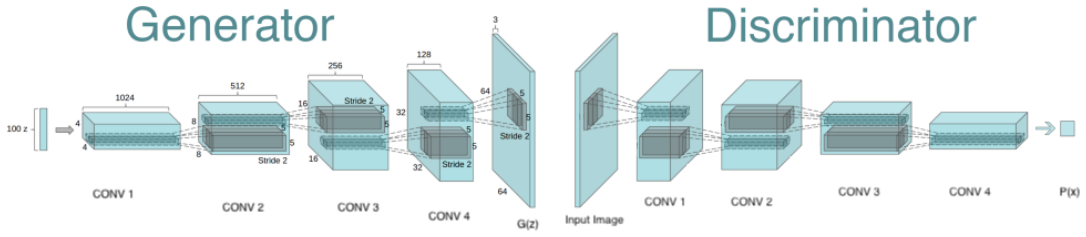

Figure 6.1: Example of Generator (on the right) and Discriminator (on the left) architecture in a DCGAN working with 64x64 pixels image. The generator starts in the image is composed by 5 layers. It starts from a latent vector of dimension 100 and samples 3D arrays which change their dimensions at each layer. The first layer has dimensions 1024x4x4, the second 512x8x8, the third 256x16x16, the fourth 128x32x32 The final layer represents the output and it is 3x64x64 RGB image. The Discriminator works in a perfectly specular way, starting from a 3x64x64 RGB image and returning a probability, P(x), as output, with x the input image. (Image modified from Radford et al. (2015)).

6.2.1 The Generator

The network uses m_g all convolutional layers with m_g an integer number > 1. All of them are followed by batch normalisation and a rectified linear unit (ReLU) activation. The ReLU function is defined as:

$$ReLU(x) = \begin{cases} x & \text{if } x > 0 \\ 0 & \text{if } x \leq 0 \end{cases} \tag{6.1}$$

The input for the generator is a random vector z generated from a normal distribution. After defining the z vector, the generator needs to upsample (extend the dimension of input image) until it returns an image with the same dimensions of the training set images.

The up-sampling layers represent a transpose convolution with stride s. Usually, convolutions go from a broad input to narrower outputs, transpose convolutions (or fractionally stridden convolutions) behave the opposite way.

The stride of a transpose convolution determines the dimension of the output image. If the stride has a dimension s, the output image will double the size of the input image. Indeed by moving one pixel in the input layer, the convolution kernel is moved by s pixels on the output layer (Figure 6.2).

After each transpose convolution, the generator returns a z output, changing every time the dimension of the input image until it returns a final image with the same dimensions of the training set image (see figure 6.1). The final layer is, assuming a dataset arranged as an image with nxn pixels, a nxn image, where each pixel value is between 0 and 1 (using a sigmoid function) or -1 and 1 (using a hyperbolic tangent function)

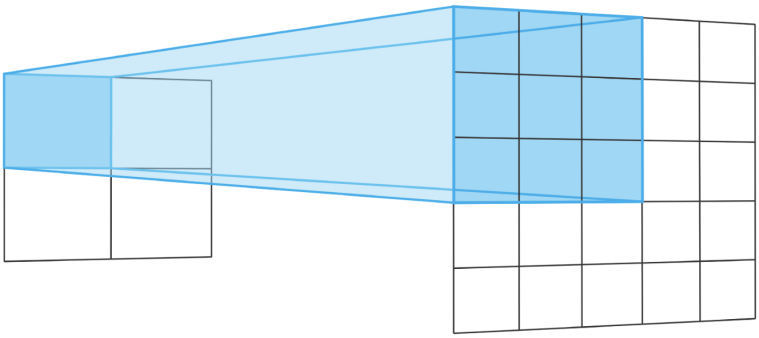

Figure 6.2: Transpose convolution, involving a 3x3 kernel over a 2x2 input with a stride 2, is equivalent to a convolution involving a 3x3 kernel over a 5x5 input with stride 2.

6.2.2 The Discriminator

Also, the discriminator is also a m_d all convolutional layer with batch normalisation after all layers except for the input layer. One characteristic very popular with the discriminator is the use of leaky ReLU (lReLU) activation layers. The lReLU function is defined as:

$$lReLU(x) = \begin{cases} x & \text{if } x > 0 \\ \alpha x & \text{if } x \leq 0 \end{cases} \tag{6.2}$$

where α is a real number, typically near zero. for ExoGAN the value has been set to 0.2.

The discriminator uses as input nxn images and returns as an output the probability that the input image is real. In this description, the discriminator performs as a binary classifier.

6.3 Generative Adversarial Networks in literature

Currently, GANs make impressive results in generating highly realistic images. In the future years, they will probably be able to generate high-quality images and videos[1]. In the next sections I show some possible applications for GANs.

6.3.1 Cross-domain transfer

CycleGAN ((Zhu et al., 2017)), is a GAN trained on several images with different domains. CycleGAN can transform images from one domain (for example, a real image) to another domain (for example a Van Gogh or a Cezanne painting), as shown in Figure 6.3

[1] `https://medium.com/@jonathan_hui/gan-some-cool-applications-of-gans-4c9ecca35900`

Figure 6.3: Example of cross-domain transfer. On the left there is the column of Input images. Starting from the second column, there are some example of artistic styles transferred to the input images. They are, in order, Monet, Van Gogh, Cezann and Ukiyo-e styles. (Image from Zhu et al. (2017))

6.3.2 Super resolution

GANs can also be used to increase the resolution of an input image. Ledig et al. (2016) Introduce SRGAN (Super Resolution Generative Adversarial Network). In Figure 6.4 I show the results of three different methods which try to return an output image with a higher resolution than the input. The bicubic interpolation gives poor results, SRResNet gives better results and SRGAN returns the best results (Ledig et al., 2016).

6.3.3 Image inpainting

Another useful application of GANs is image inpainting. This technique is used to repaire damaged picture and to reconstruct some possible missing part from an input image. In figure 6.5 I show the results from Context Encoders (Pathak et al., 2016), from the input images have been removed a central part. Besides the damaged image is shown the repaired image with Context Encoders.

In the next sections, I show how image inpainting can be used to retrieve the parameters space of an exoplanetary atmosphere.

6.4 Adversarial Training

As described in the previous section, both Generator and Discriminator networks are pitted against one another during training. The goal of the training phase is to reach a Nash Equilibrium, i.e. when neither player can improve by unilaterally changing one's strategy. Figure 6.6 shows a schematic of the ExoGAN setup.

In order to return the generator distribution p_g over the data $\mathbf{x}$ we start from a prior distribution of Gaussian distributed latent variables $p(\mathbf{z})$ and define $G(\mathbf{z};\boldsymbol{\theta}_G)$ as the mapping from latent variable space to generated data. Here $\boldsymbol{\theta}_G$ are the hyperparameters of the Generator network (see table B.1).

Let $D(\mathbf{x})$ be the probability that $\mathbf{x}$ came from the data rather than p_g. Hence, in the state of convergence, we have $p_g = p_{data}$ and $D(\mathbf{x}) = \frac{\mathbf{1}}{\mathbf{2}}$. In the training phase we need D to maximise the probability of assigning the correct label to both training examples and samples from G. At the same time we want G to minimize the probability $\log\left(1 - D(G(\mathbf{z}))\right)$. We can now define the cross-entropy cost-function of the Discriminator as:

$$J^{(D)} = -\left[\log D(\mathbf{x}) + \log\left(1 - D\left(G(\mathbf{z})\right)\right)\right] \tag{6.3}$$

During training, we employ batch training, with the cost function of a batch of n data samples

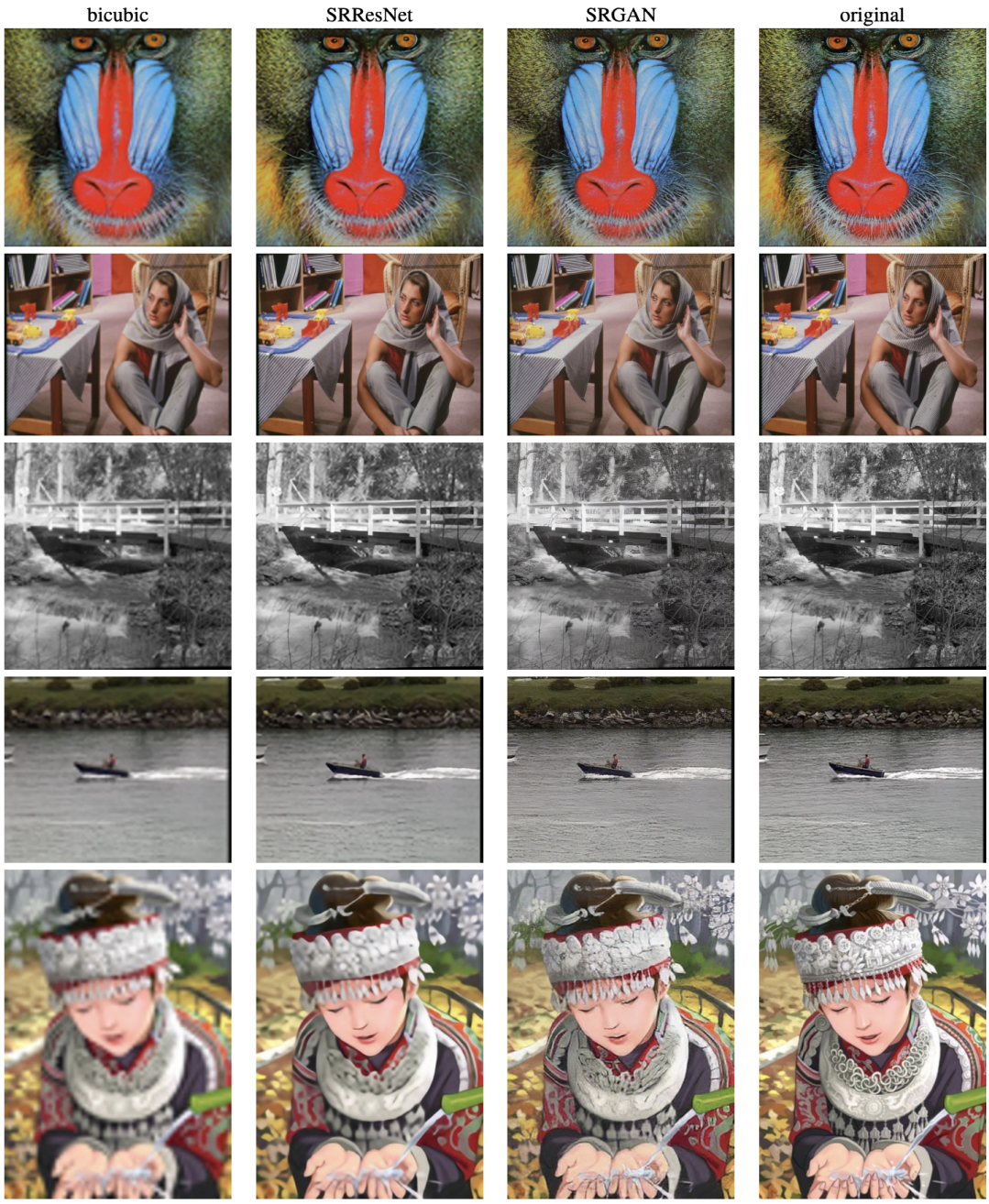

Figure 6.4: Result after reconstruction of a low resolution image with three different methods. From left to right, the super-resolution attempt using a bicubic interpolation, SRResNet, SRGAN and the original image (Image from Ledig et al. (2016)).

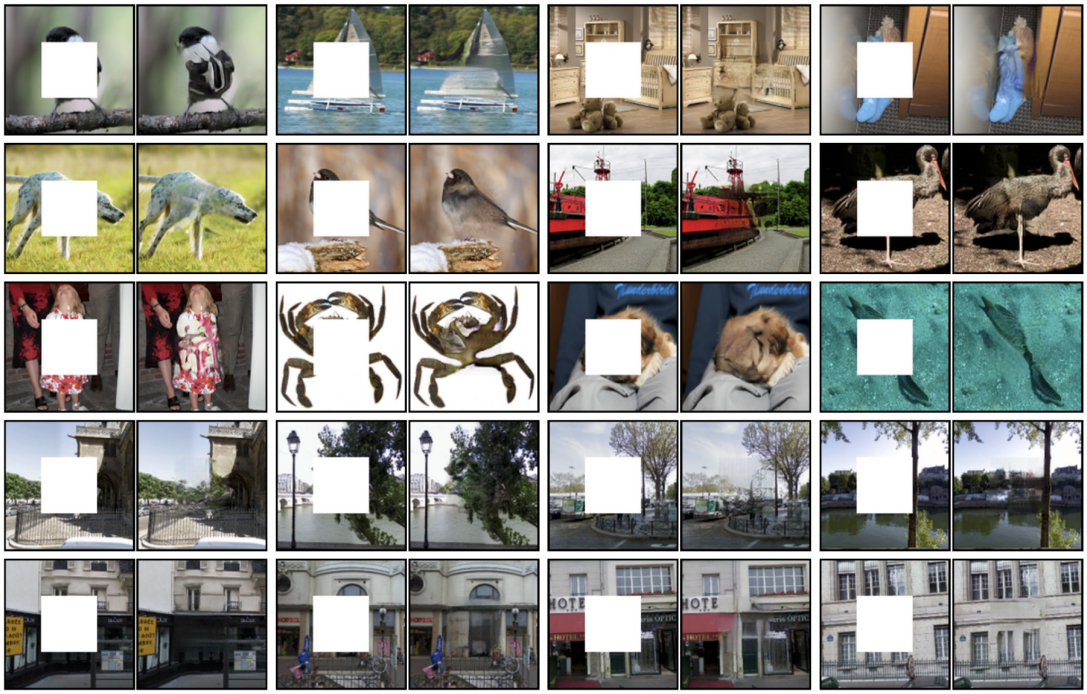

Figure 6.5: Reconstruction of a damaged image with inpainting techniques. Each input image has been modified by removing the central part. Besides each input image is shown the reconstructed image using Context Encoder (Image from Pathak et al. (2016)).

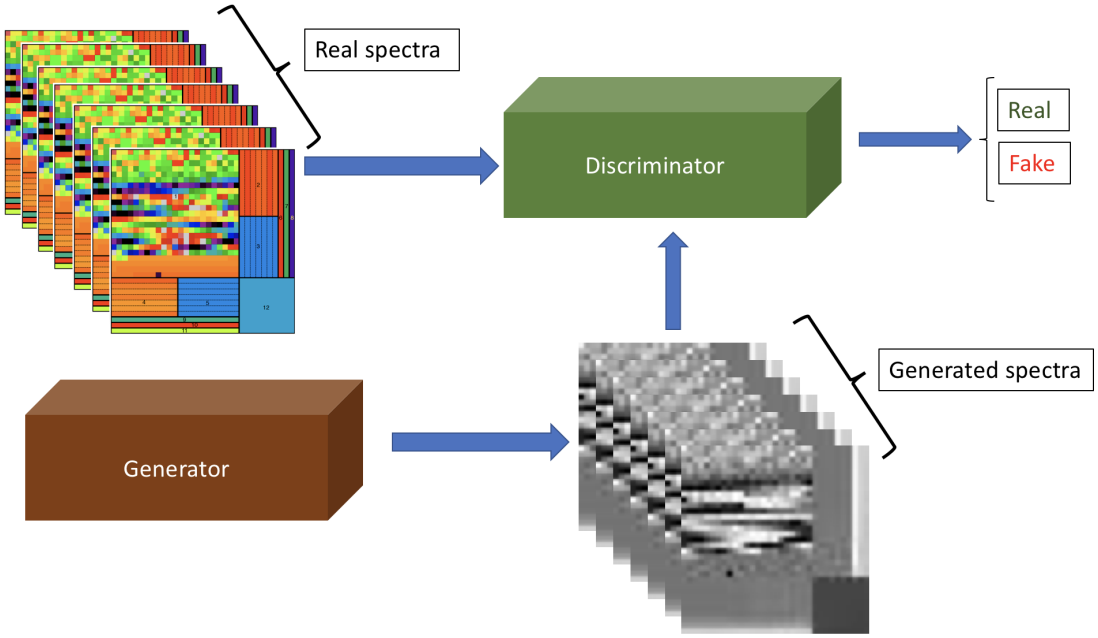

Figure 6.6: The ExoGAN scheme. The Generator produces datasets sampling from a latent variable space **z**. The Discriminator compares the generated dataset with data drawn from the training set (top left). The network has converged when the Discriminator cannot differentiate Real spectra from Generated spectra any longer.

being

$$J^{(D)} = -\left\{\sum_{i=1}^{n} \log D(x_i) + \right. \\ \left. + \sum_{i=1}^{n} \log\left(1 - D(G(z_i))\right)\right\} \tag{6.4}$$

which can be written as the expectation values over the data and generated samples:

$$J^{(D)} = -\{\mathbb{E}_{\mathbf{x}\sim p_{data}}[\log D(\mathbf{x})] \\ + \mathbb{E}_{\mathbf{z}\sim p_z}[\log\left(1 - D(G(\mathbf{z}))\right)]\}. \tag{6.5}$$

Since the discriminator wants to minimize the cost function and the generator wants to maximise it, we can summarise the training as a zero-sum game where the cost function for the generator is given by: $J^{(G)} = -J^{(D)}$. Hence, to capture the entire game, we only need to specify the loss-function of the Discriminator since it encompasses both $\boldsymbol{\theta}^{(D)}$ and $\boldsymbol{\theta}^{(G)}$ hyperparameters. We then optimise the value function $V(\boldsymbol{\theta}^{(D)}, \boldsymbol{\theta}^{(G)}) = -J^{(D)}(\boldsymbol{\theta}^{(D)}, \boldsymbol{\theta}^{(G)})$,

$$\min_G \max_D V(D, G) = \mathbb{E}_{\mathbf{x}\sim p_{data}}[\log D(\mathbf{x})] \\ + \mathbb{E}_{\mathbf{z}\sim p_z}[\log\left(1 - D(G(\mathbf{z}))\right)]. \tag{6.6}$$

As stated earlier, equation 6.6 constitutes a `minmax` game since it involves minimising over G in an outer loop and maximising over D in an inner loop.

6.5 Application to exoplanetary spectra

Here I explain the data format of the input and training data. In figure 6.7 I show an example a transmission spectrum of a cloud-free hot-Jupiter with water as the only trace-gas at $3 \cdot 10^{-4}$ volume mixing ratio at a constant resolution of $\frac{\Delta\lambda}{\lambda} = 100$. We train ExoGAN on a wavelength range of 0.3μm -50μm. For this work, we restrict the sampling resolution to be R = 100 for every spectrum. This choice, however, does not preclude training with higher resolution data in the future.

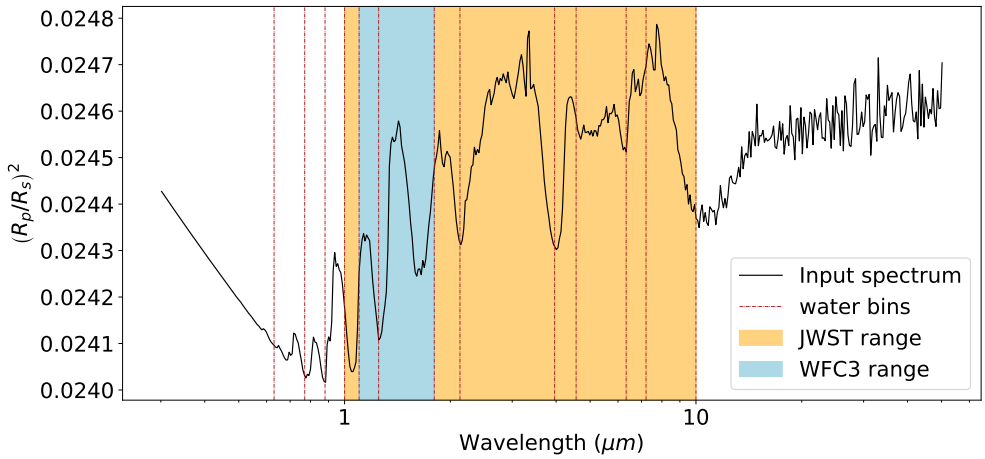

Figure 6.7: Spectral binning used in this work. The black line is a simulated spectrum of the hot-Jupiter HD 189733b. The red vertical lines represent the bin edges of prominent water bands. The blue and orange areas are the Hubble/WFC3 and JWST band-passes considered in this chapter, respectively.

6.5.1 Normalisation

For the neural network to learn efficiently, we must normalise the data to lie between zero and unity. We have experimented with various normalisation schemes. The most obvious scheme is a 'global' normalisation, where we normalise the full training set by its global maximum and minimum values. This approach proved problematic as spectral signatures for planets with low trace-gas abundances, and small atmospheric scale heights, would be too weak/flat to be recognisable by the neural network for reasonable training times. We have therefore opted to normalise each training spectrum to amplify the spectral features. Assuming that the most common broadband absorber is water in an exoplanetary atmosphere, we divide the spectral range along its major water bands in the IR, see dashed red lines in Fig 6.7. Note this does not mean that water-free atmospheres cannot be detected. Additionally, we divide the spectrum by the pass-bands of the JWST/NIRISS, NIRCam and MIRI instruments (Kalirai, 2018) and the Hubble/WFC3 instrument passband. In total, we have 14 spectral bands. We now normalise each spectral band between 0 and 1 and record the minimum and maximum normalisation factors for each. This normalisation scheme ensures a maximum amplification of the spectral features while allows a reconstruction of the spectrum in each spectral bin.

6.5.2 The Atmospheric Spectrum and Parameters Array (ASPA)

To store all aspects of an atmospheric transmission spectrum, I define the Atmospheric Spectrum and Parameters Array (ASPA). It is a 2D array encoding the 1D normalised spectral bands,

each band's minimum and maximum normalisation factors and the associated forward model parameter values. I parametrise each training spectrum with seven forward model parameters, $\boldsymbol{\phi}$, namely: H_2O, CO_2, CH_4 and CO volume mixing ratios, the mass of the planet M_p, the radius R_p and its isothermal temperature T_p at the terminator. Figure 6.8 shows a false-colour ASPA. For this work, the ASPA is a 33×33 matrix (or 2D image), with the main part (section 1) encoding the spectral information. Sections 2 - 5 encode the normalisation factors and 6 - 12 the atmospheric parameters. By design, the planet's water abundance takes a significantly large range area of the ASPA, reflecting the relative importance of water in forming the spectral continuum. The ASPA format is adaptable to other configurations in the future.

6.6 The training

To train ExoGAN on a wide range of possible exoplanetary atmospheres, I generated a very comprehensive training set of atmospheric forward models using the TauREx retrieval code (Waldmann et al., 2015a,b). I sampled each of the seven previously mentioned forward model parameters (H_2O, CO_2, CH_4 and CO abundances, the mass of the planet M_p, the radius R_p and the temperature T_p) 10 times within the parameter ranges denoted in table 6.1. This configuration yields 10^7 forward models, which are split into 90% training set and 10% test set. The test set is used to validate the accuracy of the network on previously unseen data. As discussed later on, I find this training set to be overcomplete and only require a smaller subset of the full training set for convergence.

During the training, I perform two training iterations of the discriminator to every training step of the generator. For the training phase, I used a minibatch sizes o 64 training ASPAs and a NVIDIA TESLA V100 GPU. We required $\sim$ 9 hours per epoch, i.e. until the algorithm could go through the whole training set, on the V100 GPU and comparatively about three days on 20 CPU cores in parallel. The convergences of the loss functions during the training phase are shown in figure 6.9. The full model setup can be found in the appendix (table B.2). We tested three different sizes of our latent variable space $\mathbf{z}$, with $z_{dim} = 50$, 100 and 200. We found $z_{dim} = 50$, to yield significantly noisier reconstructions at the end of one epoch of training, whereas no discernible differences between $z_{dim} = 100$ and $z_{dim} = 200$ could be observed. We hence settled on $z_{dim} = 100$. We have adopted a training minibatch size of 64 ASPAs and found no significant effect of larger training batch sizes on network convergence.

During minibatch training, the algorithm is presented with a sub-set of the full training data (in this case 64 ASPAs) rather than the full training set (or batch). This eases memory requirements of large training set, in particular for memory limited devices such as GPUs. By

Training set parameters		
Variable	lower bound	upper bound
H_2O	10^{-8}	10^{-1}
CO_2	10^{-8}	10^{-1}
CO	10^{-8}	10^{-1}
CH_4	10^{-8}	10^{-1}
M_p	0.8 M_J	2.0 M_J
R_p	0.8 R_J	1.5 R_J
T_p	1000 K	2000 K

Table 6.1: Parameters boundary condition used to generate the training set. Each parameter has been divided into 10 parts and used to model 10^7 different spectra.

only considering a sub-set of training data at a time, a gradient descent optimiser, such as ADAM, is still able to perform well, despite the increase in variance on the gradient estimated. In order to avoid biased estimations and convergence to local minima, minibatches must be selected randomly from the training set at each iteration.

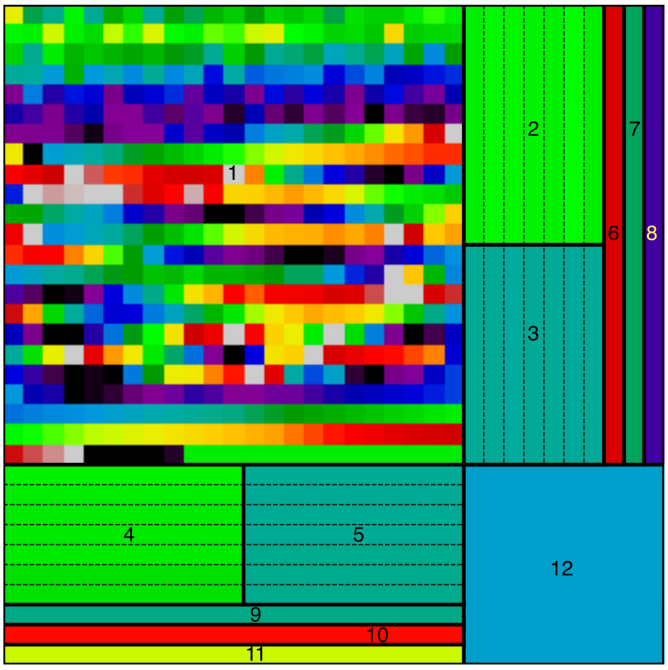

Figure 6.8: The Atmospheric Spectra and Parameters Array (ASPA). Each area is dedicated to a particular atmospheric characteristic: Area **1** is the spectrum between 1μm and 50μm at resolution 100 normalised between 0 and 1 in each spectral bin. Areas **2** to **5** give information about the normalisation factors used in the different section of the spectrum, clear and dark area give, respectively, information about the maximum values and the minimum values. In areas **6** to **8** we encode the atmospheric trace-gas volume mixing ratios of CO_2, CO and CH_4 respectively. Areas **9** to **11** are, respectively M_p, R_p and T_p. Area **12** gives information on the H_2O trace-gas volume mixing ratio.

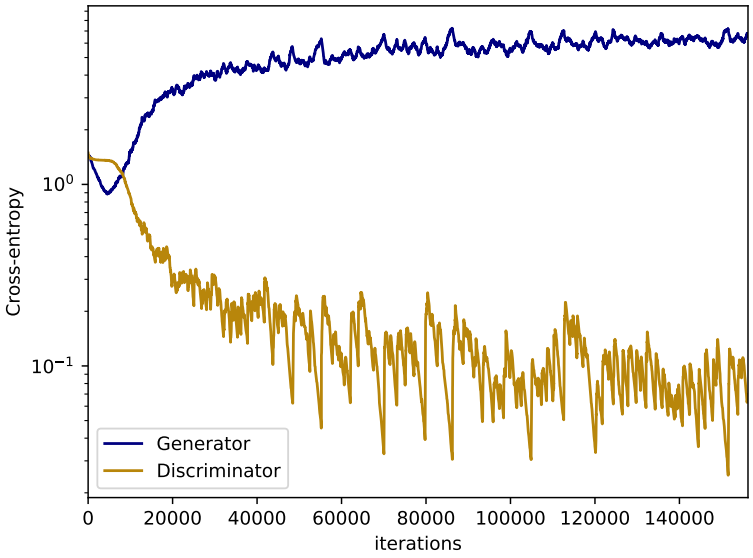

Figure 6.9: Discriminator (golden) and Generator (blue) cross-entropies as function of the iteration steps.

6.7 Data reconstruction

Once we have trained ExoGAN, we can now define our 'retrieval' model. As alluded to above, we use the inpainting properties of a GAN to complete the missing data, in this case, the forward model parameters, in the ASPA. In other words, we convert the observed spectrum into the ASPA format and keep unknown values (parameters and missing wavelength ranges) masked. Given the information available, the ExoGAN will then attempt to fill in the missing information to complete the full ASPA. Here we follow the semantic inpainting algorithm by Yeh et al. (2016).

We can define our reconstructed data, $\mathbf{x}_{recon}$, from the incomplete observed data, $\mathbf{y}$, using

$$\mathbf{x}_{recon} = M \odot \mathbf{y} + (1 - M) \odot G(\hat{\mathbf{z}}) \tag{6.7}$$

where M is a binary mask set to zero for missing values in $\mathbf{y}$, i.e. forward model parameter values and, possibly, missing wavelength ranges. Here, $\odot$ constitutes the Hadamard product and $G(\hat{\mathbf{z}})$ is the GAN generated data. We note that after the ExoGAN has been trained, $\mathbf{z}$ represents an encoding manifold of p_{data} and we denote the closest match of $(M \odot G(\mathbf{z}))$ to $(M \odot \mathbf{y})$ with $\hat{\mathbf{z}}$, where $\hat{\mathbf{z}} \subseteq \mathbf{z}$. The aim is now to obtain $\hat{\mathbf{z}}$ that accurately completes $\mathbf{x}_{recon}$.

Let us define the following optimisation.

$$\hat{\mathbf{z}} = \arg\min_{z} \mathcal{L}(\mathbf{z}). \tag{6.8}$$

where $\mathcal{L}$ is a loss function of $\mathbf{z}$ that finds its minimum when $\hat{\mathbf{z}}$ is reached. Following Yeh et al.

(2016), we define the loss function to be comprised of two parts, contextual loss and perceptual loss,

$$\mathcal{L} = \mathcal{L}_{cont}(\mathbf{z}) + \lambda \mathcal{L}_{perc}(\mathbf{z}). \tag{6.9}$$

The contextual loss, $\mathcal{L}_{cont}(\mathbf{z})$ is the difference between the observed data and the generated data. Here we follow the definition by Amos (2016):

$$\mathcal{L}_{cont}(\mathbf{z}) = \| \, M \odot G(\mathbf{z}) - M \odot y \, \|_1 \, . \tag{6.10}$$

Empirically, Yeh et al. (2016) find the l_1 norm to yield slightly better results, though the l_2 norm can equally be used. The l_p norm of a vector $\boldsymbol{v} = (v_1, ..., v_n)$, is defined as:

$$l_p = \| \, \boldsymbol{v} \, \|_p := \left(\sum_{i=1}^{n} |v_i|^p \right)^{\frac{1}{p}} \tag{6.11}$$

Whereas the conceptual loss compares the generated data with the observed data directly, the perceptual loss, $\mathcal{L}_{perc}(\mathbf{z})$, uses the discriminator network to verify the validity of the generated data given the training set.

$$\mathcal{L}_{perc}(\mathbf{z}) = \log\left(1 - D(G(\mathbf{z}))\right) \tag{6.12}$$

To solve equation 6.8 we use the ADAM optimiser (Kingma and Ba, 2014) with a learning rate of 0.1. For a deeper discussion about the ADAM optimiser, see Appendix B.1.

We investigated the ratio of perceptual loss (Eq 6.12) to contextual loss (Eq 6.10) and found $\lambda = 0.1$ to be optimal but note that $\lambda > 0.1$ gives too much emphasis to the perceptual loss term and yielded less reliable results.

In figures 6.10 & 6.11 we show the three phases associated to a prediction: Left, the ground truth; Middle: the masked spectrum/parameters; Right: the reconstructed ASPA. Figure 6.12 shows a water-dominated atmosphere of a test-set hot-Jupiter (black) and the ExoGAN reconstructed spectrum based on the Hubble/WFC3 bandpass only (red). We find a very good agreement between reconstructed and ground-truth spectra.

6.8 Atmospheric parameter retrieval

To retrieve the atmospheric forward model parameters, we assume the observational uncertainties on the spectrum to be Gaussian distributed. We then generate 1000 noisy instances of the

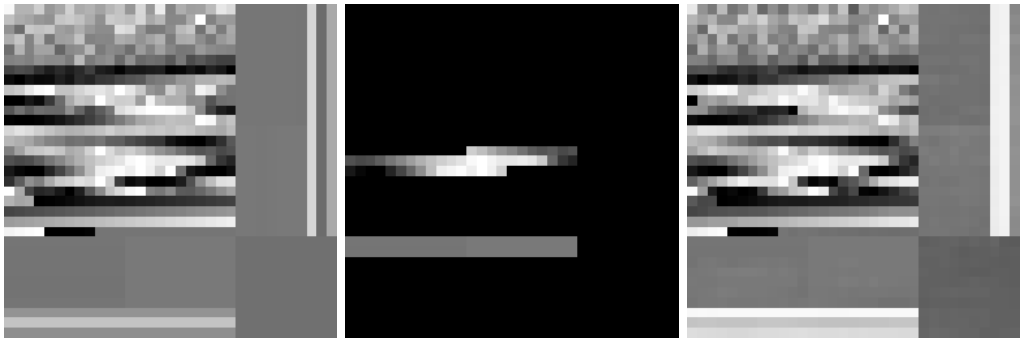

Figure 6.10: **Left**: input spectrum together with the parameters pixels. **Centre**: masked ASPA leaving Hubble/WFC3 wavelengths only. **Right**: ExoGAN completed ASPA given the middle ASPA.

Figure 6.11: Same as figure 6.10 but only masking the atmospheric forward model parameters.

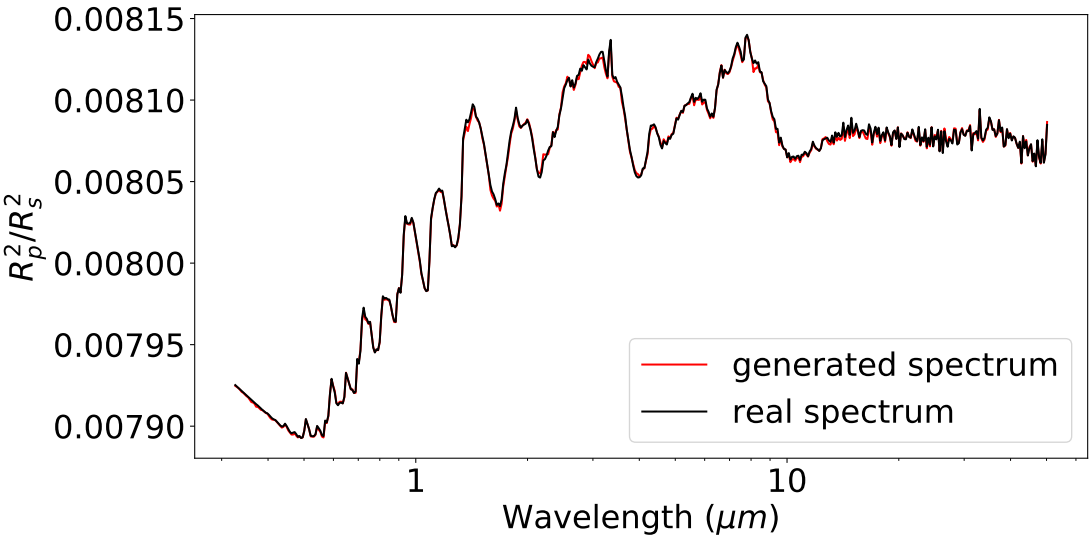

Figure 6.12: Spectral reconstruction of ExoGANof a water dominated Hubble/WFC3 spectrum. Black: the ground-truth spectrum; Red: the ExoGAN reconstructed spectrum across all wavelengths giving as input only the Hubble/WFC3 band-pass.

Training set parameters			
Variable	$A(0\,\sigma_\phi)$	$A(1\,\sigma_\phi)$	$A(2\,\sigma_\phi)$
CO	64.4%	74.9%	80.8%
CO_2	93.7%	96.4%	97.3%
H_2O	86.3%	92.9%	94.8%
CH_4	80.3%	88.4%	91.9%
R_p	99.8%	99.8%	99.8%
M_p	88.8%	90.5%	91.6%
T_p	89.4%	91.9%	93.1%

Table 6.2: ExoGAN prediction accuracies associated to each parameters for the training set. The $A(0\,\sigma_\phi)$ column represent the absolute accuracy of the prediction without taking into account the error bar of the retrieval. The 2^{nd} and 3^{rd} columns are taking into account the $1\,\sigma$ and $2\,\sigma$ retrieved errors following equation 6.13.

observed spectrum, $x_i(\lambda)$, by sampling from a normal distribution with a mean of $x(\lambda)$ and standard deviation σ_λ. From these noisy spectrum instances, we generate 1000 corresponding ASPAs with missing information (may they be parameters, spectral ranges or both) masked. We now let ExoGAN predict and inpaint these ASPAs. Finally, we collect all parameter predictions and calculate the mean and standard deviation of the resulting distribution. Hence, the resulting distributions are not posterior distributions derived from a Nested or MCMC sampling atmospheric retrieval, but are conceptually more similar to running a retrieval based on optimal-estimation multiple times and collecting the distribution of results.

6.9 Accuracy tests

We defined the accuracy of the retrieved parameter, A, as the function of the ground-truth parameter value, ϕ, the retrieved value, ϕ_{recon}, and its corresponding error σ_ϕ,

$$A(\phi, \sigma_\phi) = \frac{1}{N} \sum_{i}^{N} \frac{(\boldsymbol{\phi}_{i,recon} - \boldsymbol{\phi}_i)^2}{\boldsymbol{\phi}_i{}^2 + \sigma_{\phi_i}^2} \tag{6.13}$$

where N is the number of reconstructed ASPA instances.

We compute the reconstruction accuracies for 1000 randomly selected planets for each, the test and training sets. The accuracies are summarised in tables 6.2 & 6.3 for $0\,\sigma$ (an exact match), $1\,\sigma$ and $2\,\sigma$ confidence intervals. Figure 6.13 shows an example of the parameter distributions retrieved for a test-case planet.

6.9.1 Comparison with a classical retrieval model

In this section, we compare the ExoGAN results with a 'classical' retrieval result obtained with the TauREx retrieval code. For this comparison and tests in subsequent sections, we used as example the hot-Jupiter HD 189733b with planetary/orbital parameters taken from Torres et al.

Test set parameters			
Variable	$A(0\,\sigma_\phi)$	$A(1\,\sigma_\phi)$	$A(2\,\sigma_\phi)$
CO	62.8%	72.6%	78.2%
CO_2	94.2%	96.6%	97.4%
H_2O	89.6%	92.8%	93.9%
CH_4	80.3%	88.2%	91.6%
R_p	100.0%	100.0%	100.0%
M_p	88.0%	89.7%	90.8%
T_p	90.4%	92.2%	93.2%

Table 6.3: Same as table 6.2 but for the test set.

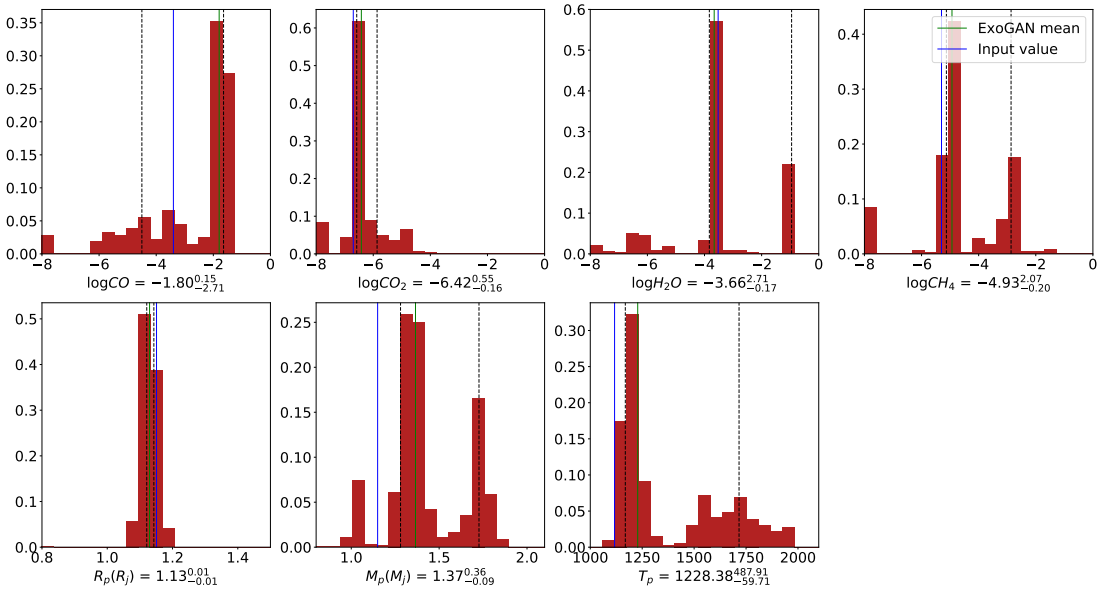

Figure 6.13: ExoGAN parameter distribution of the default test planet. In green we find the mean predicted value. The blue line represent the ground truth value. The vertical dotted lines show the $1\,\sigma$ bounds estimated by ExoGAN.

Test planet parameters	
Parameter	Value
R_*	$0.752\,R_\odot$
R_p	$1.151\,R_J$
M_p	$1.150\,M_J$
T_p	1117 K
H_2O	$3 \cdot 10^{-4}$
CO	$4 \cdot 10^{-4}$
CO_2	$2 \cdot 10^{-7}$
CH_4	$5 \cdot 10^{-6}$

Table 6.4: Test-case atmospheric and planetary parameters used based on HD 189733b. The molecular abundances are given in volume mixing ratios.

(2008a); Butler et al. (2006) and atmospheric chemistry based on Venot et al. (2012), see table 6.4.

We now retrieve the forward model parameters for both TauREx and ExoGAN for spectra across the Hubble/WFC3 only band and a broad (0.3 - 15 μm) wavelength band. Here the Hubble/WFC3 spectrum was taken from Tsiaras et al. (2018) and interpolated to the ExoGAN resolution using a quadratic interpolation (figure 6.14). The large wavelength range spectrum is synthetic, based on table 6.4.

The current ExoGAN version shows generally broader posterior distributions (see figure 6.15) and it can result in bimodal distributions for some parameters, leading to larger uncertainties for some retrieved parameters than those obtained with a Bayesian analysis. In figure 6.15 we compare both sets of results (TauREx and ExoGAN's results). The Hubble/WFC3 and large wavelength retrievals are shown with square and circular markers respectively. In both cases, the ExoGAN predictions are consistent with the TauREx retrievals within the error bars. We note that in the case of CO in the Hubble/WFC3 data, neither TauREx nor ExoGAN feature detections as expected.

We then generated a second synthetic spectrum of HD 189733 b between 0.3−15 μm, using the parameters of Venot et al. (2012) and overplotted the TauREx retrieved posterior distributions with those derived by ExoGAN, figure 6.16. Both algorithms converge to the same solution with the ExoGAN results showing a broader distribution. The only significant difference is the CO abundance, where the ExoGAN abundances are higher. Note that both, TauREx and ExoGAN show tails in their CO abundance posteriors indicating the difficulties of retrieving CO even for classical retrieval algorithms.

Comparisons of run-time are remarkable. Using the TauREx Retrieval code with seven free parameters a standard nested-sampling analysis takes $\sim$ 10 hours on 24 CPU cores using absorption cross-sections at a resolution of R = 15,000 and spanning a large (0.3 - 15 μm) wavelength range. The trained ExoGAN requires $\sim$ 2 minutes for the same analysis. This result constitutes a speed up of $\sim$ 300 times and is independent of the number of free parameters and of the resolution of the input spectrum. Similarly, training ExoGAN on higher resolution data, does not significantly impact its runtime after training as both the size and architecture of the underlying network remain unchanged.

6.10 Robustness tests

To test the limits of ExoGAN we simulate three conditions previously encountered by the network. We use the same example planet as in the previous section (table 6.4) and simulate the

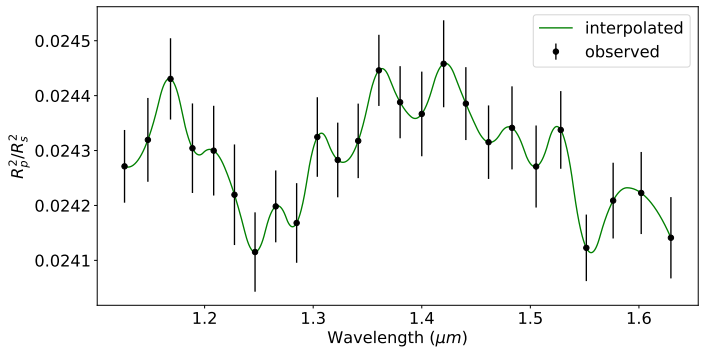

Figure 6.14: Real HD 189733b observation with the Hubble WFC3 camera (Tsiaras et al., 2018). The black points are the observed data and the green line is the interpolated spectrum to the ExoGAN resolution.

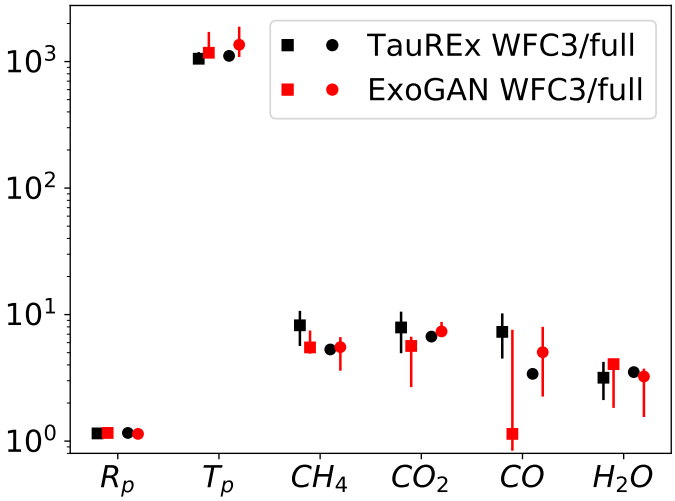

Figure 6.15: Comparison between the ExoGAN predictions (red points) and TauREx (black points). For the molecules we show the value $-log$(mixing-ratio). The squared points show the results for a real spectrum of HD 189733b using Hubble/WFC3. The round points are the results for a synthetic model of HD 189733b between 0.3 - 15 μm. The results from the two retrievals are in both cases consistent with each others within the error bars.

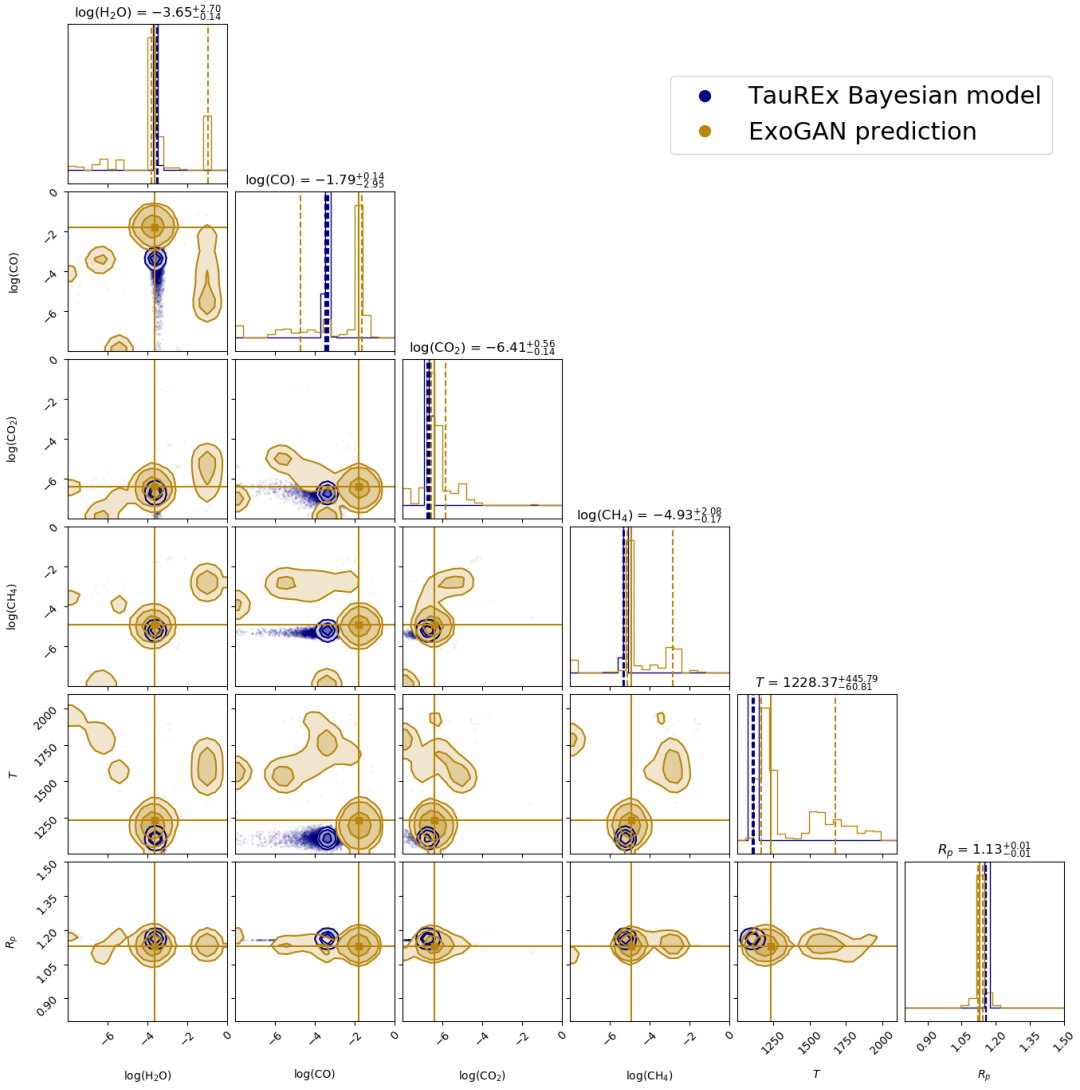

Figure 6.16: TauREx posterior distributions (in blue) compared to a ExoGAN prediction (in golden). As input spectrum, we used a synthetic spectrum of HD 189733 b with planetary and atmospheric parameters from Venot et al. (2012) and a wavelength range of 0.3 - 15 μm. The two results are in agreement with each other.

Robustness results						
Variable	clouds		unkwnown gases		T offscale	
	Input	ExoGAN	Input	ExoGAN	Input	ExoGAN
$\log(CO)$	-3.4	$-4.1^{3.1}_{2.5}$	< -8	$-5.7^{1.8}_{1.4}$	-3.4	$-3.1^{0.4}_{3.8}$
$\log(CO_2)$	-6.7	$-6.0^{2.3}_{1.7}$	< -8	$-5.5^{3.9}_{1.8}$	-6.7	$-5.6^{4.4}_{0.2}$
$\log(H_2O)$	-3.5	$-3.6^{1.1}_{3.0}$	-3.5	$-3.3^{0.7}_{3.5}$	-3.5	$-2.9^{0.2}_{4.1}$
$\log(CH_4)$	-5.3	$-6.7^{1.6}_{1.1}$	< -8	$-5.5^{2.0}_{1.9}$	-5.3	$-5.1^{2.1}_{1.1}$
R_p (R_J)	1.15	$1.18^{0.01}_{0.01}$	1.15	$1.14^{0.01}_{0.01}$	1.15	$1.16^{0.02}_{0.01}$
M_p (M_J)	1.15	$1.23^{0.59}_{0.42}$	1.15	$1.39^{0.43}_{0.49}$	1.15	$1.60^{0.2}_{0.7}$
T_p (K)	1117	1681^{153}_{208}	1117	1689^{179}_{506}	2500	$1744^{157}_{6.4}$

Table 6.5: Summary of all the robustness test results. For each value we show the input value used for the spectrum and the predicted result from ExoGAN. For the unknown gases test we used ammonia with a volume mixing ratio of 10^{-4}.

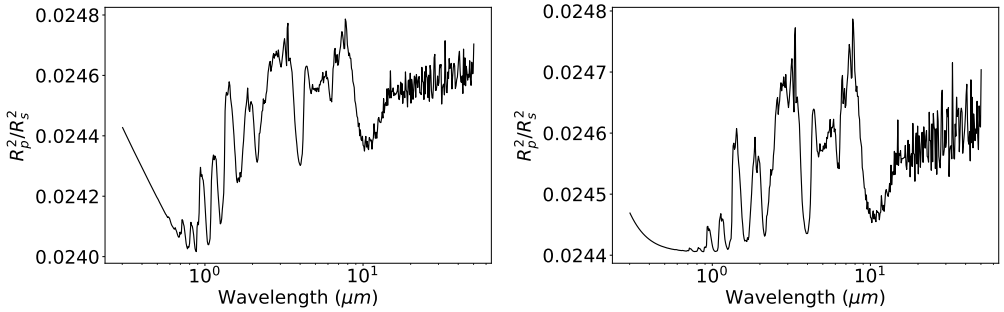

Figure 6.17: Simulated spectra of the default test planet HD 189733b without clouds (left) and with grey clouds at 10 mbar cloud top pressure. (right).

following three scenarios unseen by ExoGAN during training phase:

- the presence of clouds;
- the addition of a trace gas unknown to the network;
- atmospheric temperatures outside the training range.

Each test is discussed below, and the ExoGAN predicted abundances versus the ground-truth are summarised in table 6.5. Furthermore, we test the ExoGAN's robustness against varying signal-to-noise (S/N) levels of the observed spectrum.

6.10.1 Presence of clouds

Here we test the response of ExoGAN to the presence of clouds in the atmospheric spectrum. We simulate a grey cloud deck at 10 mbar pressure (figure 6.17) and let ExoGAN reconstruct the atmospheric parameters, see figure 6.18. The lack of information due to the clouds presence results in a wider distribution of parameters. However, ExoGAN is still able to retrieve all trace-gas abundances within $1\,\sigma$ confidence. We find that temperature estimates can be overestimated. This result is likely a consequence of the normalisation procedure used in the presence of clouds.

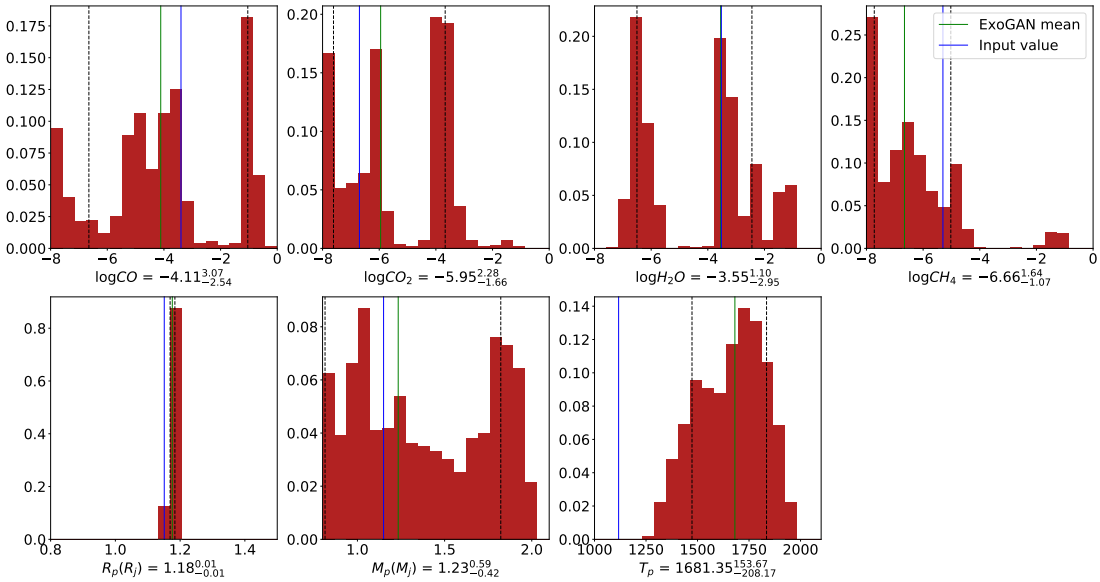

Figure 6.18: Same as figure 6.13 but for the clouds robustness test for the default test planet, section 6.10.1.

6.10.2 Presence of molecules outside of the training set

In this test, we simulate the impact of unknown features on the retrievability of known trace gases. We here consider a spectrum containing water at the default test value and NH_3 with a mixing ratio of 10^{-4}. Though Venot et al. (2012) estimated an NH_3 mixing ratio of 10^{-6}, we use an unrealistically high value as a worst-case scenario. By removing all other trained trace-gases but water, we also test for spurious detections in non-existing trace-gases. Figure 6.19 shows the ExoGAN parameter distributions. We find the network to recognise the absence of trace-gases and does not detect 'false positives', while still recovering the exact mixing ratio of H_2O.

6.10.3 Parameters outside the training range

In the third robustness test we simulated a default planetary atmosphere but an effective temperature of 2500 K, 500 K above the temperature training range. In this test, as shown in figure 6.20, all parameters converge toward the real solution within $1\,\sigma$, except for the planetary temperature. Here, the network does not retrieve the correct temperature but assigns a large error bar suggesting that the temperature value is unconstrained if the input value is not contained in the domain range of ExoGAN.

6.10.4 Impact of spectral signal-to-noise

We test ExoGAN for varying levels of observational noise. Here we take the default planet (table 6.4) and add noise in steps of 10ppm in the range $[0, 100]$ ppm. In figure 6.21 we show

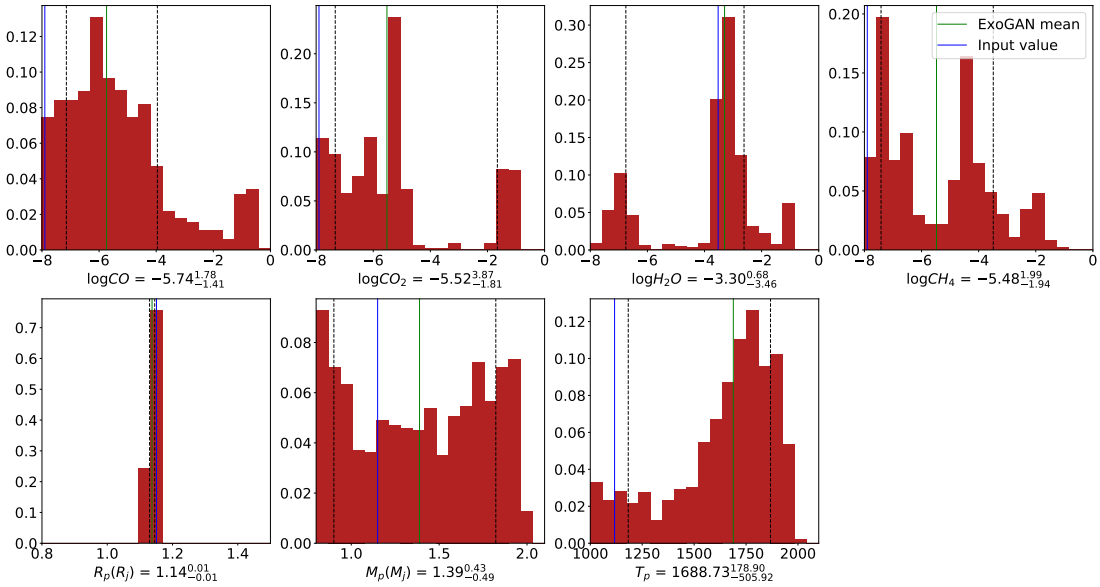

Figure 6.19: Same as figure 6.13 but for the ExoGAN analysis for a spectrum with only water and NH_3, section 6.10.2.

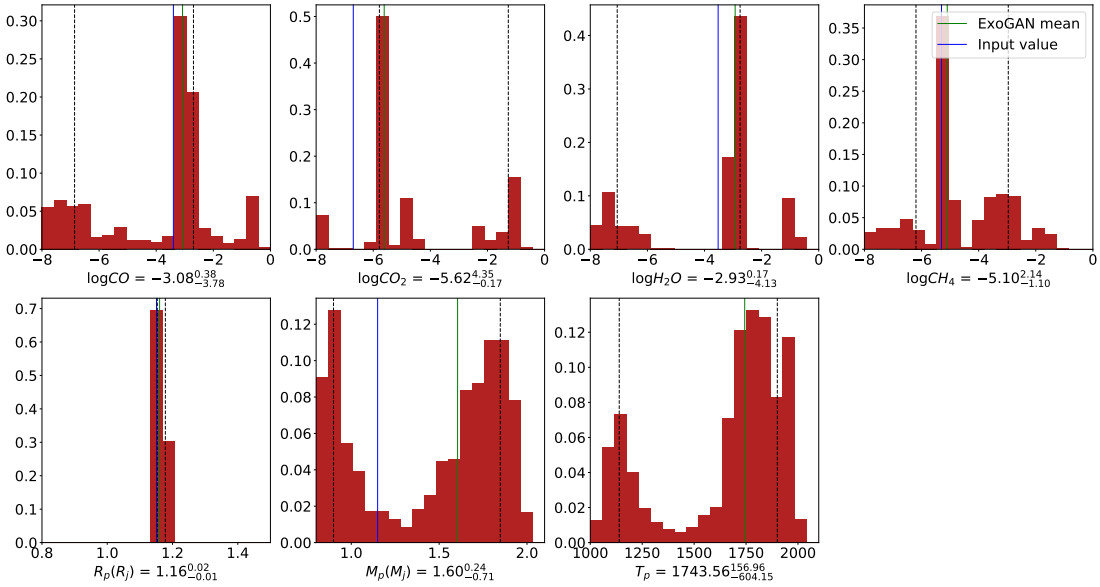

Figure 6.20: Same as figure 6.13 but for the ExoGAN analysis for a planetary temperature at 2500 K, 500 K outside the training range, see section 6.10.3.

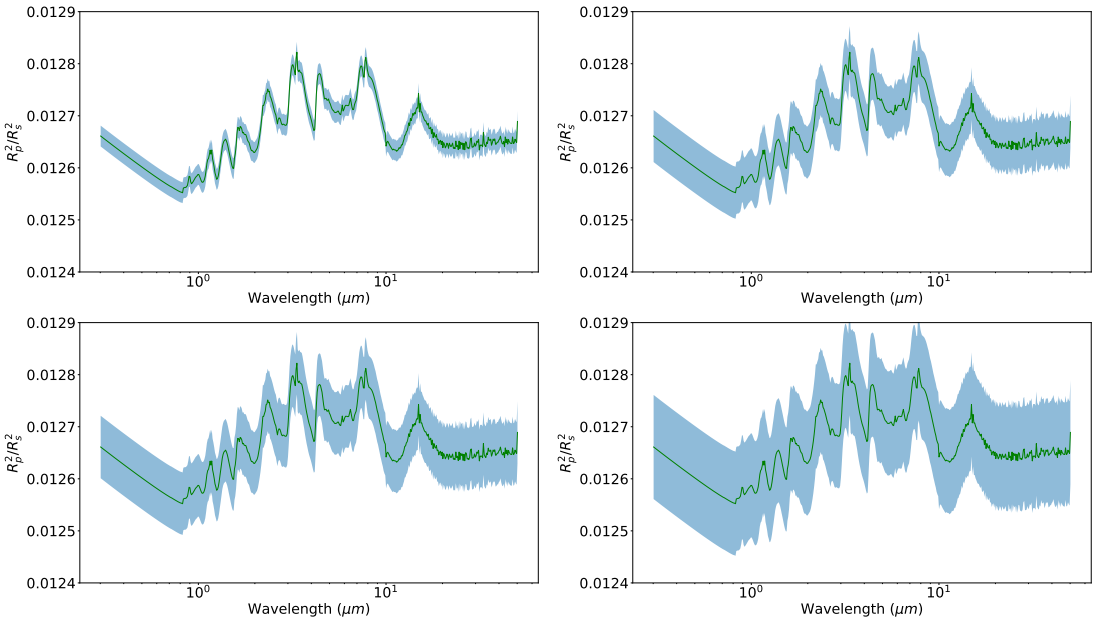

Figure 6.21: Four examples of spectra used to calculate the accuracy of the ExoGAN. The green line represents the input spectrum and the blue part is the area representing the error bars, σ_λ in which we varied the input signal to simulate a noisy spectrum. In the **top left** we show the 20ppm error bars, in the **top right** the 50ppm, in the **bottom left** the 60 ppm and the **bottom right** the 100ppm one.

examples of spectra at σ_λ: 20, 50, 60 and 100 ppm noise level.

For each noise level, we calculated the accuracy of the prediction following equation 6.13, but setting $A(\sigma_\phi = 0)$, figure 6.22. We note that figure 6.22 only shows the difference between the predicted value and an exact match and prediction accuracies increase when retrieval error bars are taken into account. Here we want to demonstrate the relative degradation of the prediction accuracy as a function of σ_λ.

As intuitively expected, the noisier the spectra, the less accurate the model. The Radius of the planet can be easily recognised by the ExoGAN in the entire error range tested. The most difficult parameter to identify is the CO abundance and the mass of the planet.

6.11 Discussion

6.11.1 Training phase and data

In this work, we used 10^7 forward models over seven atmospheric forward model parameters. We find that this training set is significantly over-complete and the ExoGAN training can be completed successfully with $\sim 50\,\%$ of the existing training set. Optimising training in future iterations will allow for the inclusion of more complex atmospheric forward models.

One of the main difficulties for training neural networks with transmission spectra is the

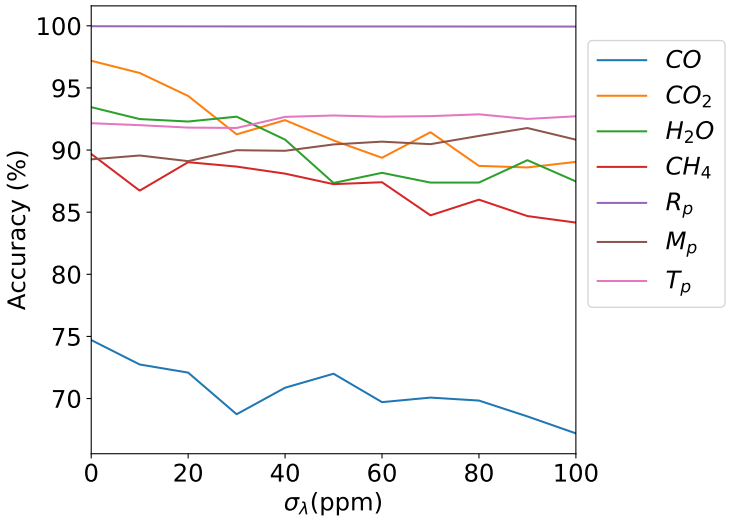

Figure 6.22: Accuracy as a function of spectral error bars, σ_λ. As discussed in the text, we note that this figure does not take into account the retrieval error bar, i.e. $A(\sigma_\phi = 0)$ following equation 6.13.

normalisation of the spectra in R_p/R_*. A consistent normalisation across a broad range of possible atmospheres is required during the training process, but difficult to achieve in reality given strongly varying atmospheric scale heights and trace-gas abundances. In this work, we adopted a normalisation based on instrument pass-bands as well as water bands. Though in practice this approach works for most scenarios, it can introduce biases when high-altitude clouds are present. In these cases, we find that the normalisation procedure stretches the observed spectrum too much, leading the network to identify higher atmospheric temperatures than it otherwise would. In future work, we plan to mitigate this effect by including grey clouds in the training set as well as further refining the normalisation scheme. We note that for emission spectroscopy a consistent normalisation is more readily achieved if the planetary and stellar equilibrium temperatures are assumed to be known (Waldmann, 2016).

ExoGAN has been trained on a large set of simulated forward models. By including ExoGAN as an integral part in the TauREx retrieval framework, we will be able to use forward models created during a standard retrieval run (of the order of 10^5 - 10^6 models per retrieval) to perform online learning and continuously improve the accuracy of ExoGAN over time.

6.11.2 Comparison with other machine learning architectures

In the previous sections, we have explored the use of DCGANs to retrieve atmospheric parameters from observations. GANs belong to the class of semi-supervised and unsupervised generative models and since their inception have been subject to significant research. In this work, my use

of DCGAN is unsupervised as we provide the parameters together with the data to be modelled. Such an approach allows for a high degree of flexibility in using ExoGAN, as we only need to re-define the ASPA array to train on new problem sets.

Most other generative models require the likelihood function of the data to be defined, something we do not intrinsically know for many exoplanet observations, whereas GAN based models are likelihood-free methods and $p_{\boldsymbol{\theta}}(\mathbf{x})$ does not need to be computed during training. This characteristic has obvious advantages over pure variational autoencoders which require a parametrised form of the probability space from which it draws its latent variables.

Whilst we have explored the use of GANs in the scope of this work, we note that other neural network architectures, such as simpler deep believe networks or VAEs, may yield comparable results. In fact, recent work by the 2018 NASA Frontier Development Lab[2] has explored various deep learning architecture in the context of atmospheric retrievals with promising results. Similarly, other machine learning frameworks may also be successfully used to model exoplanetary spectra. For example, Márquez-Neila et al. (2018) recently presented an atmospheric retrieval algorithm based on random forests regression (Breiman, 2001) and demonstrated the algorithm on Hubble/WFC3 observations.

6.11.3 Future work

In this work, we have used the 'vanilla' DCGAN as underlying algorithm. Since its inception, various interesting additions to the classical GAN have been proposed which we intend to explore in future work. Notable amongst them are the VAE-GAN hybrids, random forest and GAN hybrids and Bayesian-GAN models.

The VAE-GAN models (e.g. Rosca et al., 2017; Dosovitskiy and Brox, 2016; Ulyanov et al., 2017; Makhzani et al., 2015), allow direct inference using GANs. Something that is not possible using purely generative models. To further guard against model collapse, Zuo et al. (2018) have recently proposed a random forest and GAN hybrid algorithm, GAF, where the fully connected layer of the GAN's discriminator is replace by a random forest classifier. Saatchi and Wilson (2017) proposed a Bayesian-GAN by drawing probability distributions over $\boldsymbol{\theta}^{(D)}$ and $\boldsymbol{\theta}^{(G)}$, allowing for fully bayesian predictive models and further guarding against model collapse.

6.12 Summary and Conclusion

In the era of JWST and ARIEL observations, next-generation atmospheric retrieval algorithms must reflect the higher information content of the observation with an increase in atmospheric

[2] frontierdevelopmentlab.org

model complexity. Complex models are computationally heavy, creating potential bottlenecks given current state-of-the-art sampling schemes. Artificial intelligence approaches will provide essential tools to mitigate the increase in computational burden while maintaining retrieval accuracies.

In this work, I introduced the first deep learning approach to solving the inverse retrieval of exoplanetary atmospheres. I trained deep convolutional generative adversarial network on an extensive library of atmospheric forward models and their associated model parameters. The training set spans a broad range of atmospheric chemistries and planet types. Once trained, the ExoGAN algorithm achieves comparable performances to more traditional statistical sampling based retrievals, and the ExoGAN results can be used to constrain the prior ranges of subsequent retrievals (to significantly cut computation times) or be used as stand-alone results. I found ExoGAN to be up to 300 times faster than a standard retrieval for large spectral ranges. ExoGAN is designed to be universally applicable to a wide range of instruments and wavelength ranges without additional training.

Chapter 7

The ARIEL Mission Reference Sample

Target selection is the very first step towards exoplanetary characterisation. In this chapter, I show how to generate an optimal target list for a space mission dedicated to transit spectroscopy: the ARIEL (Atmospheric Remote-sensing Exoplanet Large-survey) space mission.

ARIEL is a space mission selected by the European Space Agency (ESA) for its next medium-class science mission due for launch in mid 2028. The goal of the ARIEL mission is to investigate the chemical composition of several hundred planets orbiting distant stars in order to address the fundamental questions on how planetary systems form and evolve. A key objective of the mission is to find out whether the chemical composition of exoplanetary atmospheres correlates with fundamental parameters such as the planetary size, density, temperature, and stellar type and metallicity. During its four-year mission, ARIEL aims at observing a statistically significant sample of exoplanets, ranging from Jupiter- and Neptune-size down to super-Earth and Earth-size in the visible and the infrared with its meter-class telescope. The analysis of ARIEL spectra and photometric data will allow extracting the chemical fingerprints of gases and condensates in the planets' atmospheres, including the elemental composition for the most favourable targets. It will also enable the study of thermal and scattering properties of the atmosphere as the planet orbit around the star.

The primary purpose of this chapter is to estimate an optimal list of targets observable by ARIEL and quantify a realistic mission scenario to be completed in 4 years nominal mission lifetime, including the commissioning phase.

In order to achieve the mission objectives, the sample should include gaseous and rocky planets with a range of temperatures around stars of different spectral type and metallicity. With this aim, it is necessary to consider both the already known exoplanets and the "expected" ones yet to be discovered. The data collected by Kepler allow estimating the occurrence rate of exoplanets according to their size and orbital periods. Using this planetary occurrence rate and the number density of stars in the Solar neighbourhood, we can estimate the number of exoplanets expected to exist with a particular size, orbital period range and orbiting a star of a particular spectral type and metallicity. Here I describe the assumptions made to estimate an optimal sample of exoplanets observable by ARIEL and define the Mission Reference Sample (MRS). It is clear that this nominal list of planets will change over the years depending on the new exoplanetary discoveries. The work presented in this paper is valid for all the missions dedicated to transit spectroscopy such as the CHEOPS (N. Rando, 2018) and the Twinkle space missions (Tessenyi et al., 2017).

In Section 7.2 I explain the method used to estimate the number and the parameters of the planetary systems yet to be discovered. All the potential ARIEL targets will be presented in Section 7.3, where I show all the planets that can be observed during the mission lifetime, and out of which it is possible to select the optimal sample. Section 7.4 is dedicated to the selection and description of an ARIEL MRS fulfilling the mission requirements. I compare the proposed ARIEL MRS to the sample expected to be discovered by TESS, confirming that TESS could provide a significant fraction of the ARIEL targets. In Section 7.5 I show a possible MRS which maximises the coverage of the planetary and stellar physical parameters.

In the following I show part of my work on the ARIEL target list published in Zingales et al. (2018).

7.1 Description of the models

I used the ESA Radiometric Model (Puig et al., 2015) to estimate the performances of the ARIEL mission given the planetary, stellar and orbital characteristics: namely the stellar type and brightness, the planetary size, mass, equilibrium temperature and atmospheric composition, the orbital period and eccentricity. This tool takes into account the mission instrumental parameters and planetary system characteristics to calculate:

- The SNR (Signal to Noise Ratio) that can be achieved in a single transit;
- The SNR that can be achieved in a single occultation;
- The number of transit/occultation revisits necessary to achieve a specified SNR;

- The total number and types of targets that can be included in the mission lifetime.

In this work, the list of planets considered as input to the radiometric model includes known and simulated exoplanets, as detailed in the following sections. I used the instrument parameters of the ARIEL payload as designed during the phase A study. To increase the efficiency of my simulations I used a Python tool as a wrapper of the ESA Radiometric Model, so I could test different mission configurations that fulfil the mission science objectives. The results were validated with ExoSim, a time domain simulator used for the ARIEL space mission, but thanks to its modularity it can be used to study any transit spectroscopy instrument from space or ground. ExoSim has been developed by Sarkar et al. (2016); Sarkar and Pascale (2015); Pascale et al. (2015) (see App C.1).

7.2 Simulations of planetary systems expected to be discovered in the next decade

7.2.1 Star count estimate

I used the stellar mass function as obtained from the 10-pc RECONS (REsearch Consortium On Nearby Stars) to estimate the number of stars as a function of the K magnitude. I assume mass-luminosity-K magnitude conversions from Baraffe et al. (1998). Ribas and Lovis (2013) adopted the same procedure. The number of main sequence stars with limit K-mag $m_K = 7$ used to infer the number density of stars in the Solar neighbourhood is shown in Tab 7.1.

Mass ($M_\odot$)	**Spectral type**	**N_* ($K < 7$)**
1.25 - 1.09	F6 - F9	5646
1.09 - 0.87	G0 - G8	3356
0.87 - 0.65	K0 - K5	1167
0.65 - 0.41	K7 - M1	386
0.41 - 0.22	M2 - M3	81
0.22 - 0.10	M4 - late M	28

Table 7.1: Star counts considering different spectral types with limiting magnitude $m_K = 7$.

The number density and the number of stars are related through Eq 7.1:

$$\rho_* = \frac{N_*(K < 7)}{\frac{4}{3}\pi d^3} \tag{7.1}$$

where the distance d derives from the relation between K magnitude m_K and the distance d:

$$m_K = -2.5 \log \frac{R_*^2 S_s(\Delta\lambda)}{d^2 S_0^K(\Delta\lambda)} \tag{7.2}$$

In Eq 7.2, R_* is the stellar radius, $S_0^K(\Delta\lambda)$ is the zero point flux for the standard K-band filter profile, $\Delta\lambda$ is the filter band pass given in Cohen et al. (2003) and $S_s(\Delta\lambda)$ the stellar flux density evaluated over the same bandwidth. I neglect the interstellar absorption since my stars are at a relatively short distance. Equation 7.2 is implemented in the ARIEL Radiometric Model (Puig et al., 2015).

Density	
	Star / pc^3
ρ(**F6-F9**)	0.0039
ρ(**G0-G8**)	0.0044
ρ(**K0-K5**)	0.0049
ρ(**K7-M1**)	0.0074
ρ(**M2-M3**)	0.0059
ρ(**M4 - late M**)	0.0118

Table 7.2: Main sequence star densities considering different spectral types with limiting magnitude $m_K = 7$

7.2.2 Planetary population and occurrence rate

In this section, I briefly review the current knowledge about the occurrence rate of planets, i.e. the average expected number of planets per star. Fressin et al. (2013) used the Kepler statistics to publish the planetary occurrence rates around F, G, K main sequence stars ordered by orbital periods and planetary types. An accurate planetary occurrence rate is pivotal to the reliability of the estimate of the existing planets in the Solar neighbourhood. I used the planetary occurrence rate values for F, G, K stars from Fressin et al. (2013), being the most complete, i.e. covering all planetary types and stars. I have extended the same occurrence rates to M stars but, by doing that, I am effectively underestimating the number of planets with a short period around M dwarfs in my sample.

Mulders et al. (2016) updated the planetary occurrence rate for planets between $0.5R_\oplus$ and $4R_\oplus$ and orbital period < 50 days, using a more recent list of planets discovered by the Kepler satellite. Fig 7.2 shows the comparison between Mulders et al. (2016) and Fressin et al. (2013). The differences between the two occurrence rates can be up to an order of magnitude. Mulders et al. (2015) show that M stars have 3.5 times more small planets ($1.0 - 2.8R_\oplus$) than F, G, K stars, but two times fewer Neptune-sized and larger ($> 2.8R_\oplus$) planets. The fraction of M-stars considered in our work is only $\sim 7\%$ of the total stellar sample, so it has significantly underestimated the number of small planets around M-dwarfs, which are optimal targets for transit spectroscopy. More recent and complete occurrence rates are expected to be published in the next months. Given the discrepancy between Mulders and Fressin's statistics, it is expected

a substantial improvement in our estimates when the most recent Kepler statistics will become available. The recent papers by Fulton et al. (2017) and Mayo et al. (2018) confirm results from Fressin et al. (2013).

Fressin et al. (2013) provided the following statistics for different planetary classes:

- Jupiters: $6R_\oplus < R_p \leq 22R_\oplus$
- Neptunes: $4R_\oplus < R_p \leq 6R_\oplus$
- Small Neptunes: $2R_\oplus < R_p \leq 4R_\oplus$
- Super Earths: $1.25R_\oplus < R_p \leq 2R_\oplus$
- Earths: $0.8R_\oplus < R_p \leq 1.25R_\oplus$

I adopted a size resolution of $1R_\oplus$ in each of these classes.

The number of planets can be estimated as:

$$N_p = \frac{4}{3}\pi d^3 \rho_* P_{t,p} P_{geom} \tag{7.3}$$

where d is the radius of a sphere with the Sun at the centre, ρ_* is the number density of the stars, $P_{t,p}$ is the probability of having a t-type planet orbiting with an orbital period p (See Fig 7.1). $P_{geom} = R_*/a$ is the geometrical probability of a transit.

I simulated all the transiting planets in the solar neighbourhood up to $m_K = 14$: all these planets described by N_p constitute the "Mission Reference Population".

The equilibrium temperature (Eq 7.4) of the planet can be estimated assuming the incoming and outgoing radiation at the planetary surface are in equilibrium:

$$T_p = T_* \left(\frac{R_*}{2a}\right)^{\frac{1}{2}} \left(\frac{1-A}{\varepsilon}\right)^{\frac{1}{4}} \tag{7.4}$$

Here T_* and R_* are the stellar temperature and radius, a the semi-major axis of the orbit, A is the planetary albedo and ε is the atmospheric emissivity.

The ARIEL space mission will focus on planets with an orbital period shorter than 50 days. As expected, shorter periods mean shorter semi-major axis and, therefore, from Eq 7.4, typically warmer temperature.

To avoid duplications, every time a planet/star system is detected with the same physical properties of a simulated one, it is replaced with the known one. In Sec 7.3 I show that in the solar system neighbourhood there are ~ 9500 planets for which the ARIEL science requirements can be achieved in less than six transits or eclipses.

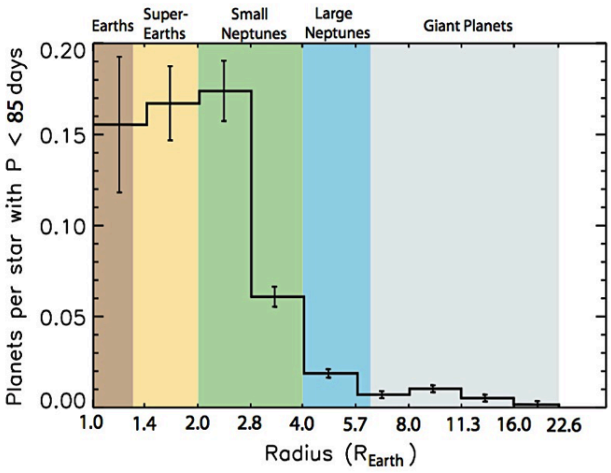

Figure 7.1: Average number of planets per star and per size bin with an orbital period shorter than 85 days orbiting around F, G, K stars. The statistics was extracted from the Q1 - Q6 Kepler data (Fressin et al., 2013).

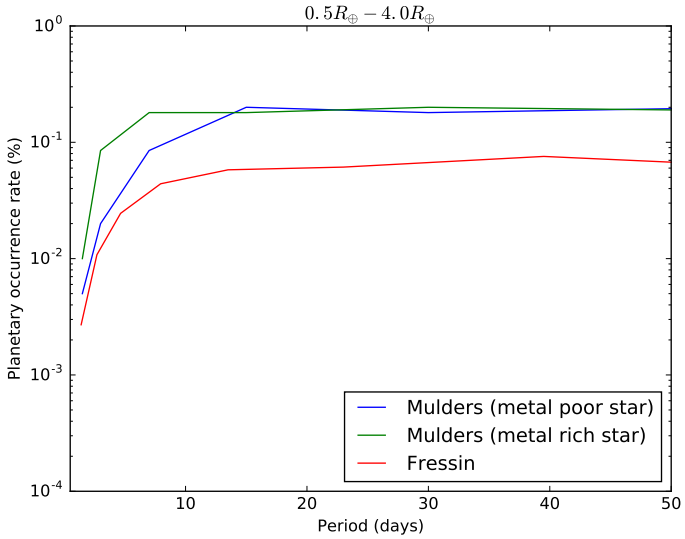

Figure 7.2: Comparison of three different distributions estimating the planetary occurrence rate as a function of orbital period for planets between $0.5R_\oplus$ and $4R_\oplus$. Blue and green lines: results from Mulders et al. (2016) for two metallicity classes. Red line: results from Fressin et al. (2013). The Fressin et al. (2013) statistics strongly underestimates the occurence of sub Neptune size planets compared to Mulders et al. (2016) and other more recent estimates. The reason is the large number of small planets discovered after 2013.

7.2.3 Planetary masses and densities

To simulate a realistic planetary population it is necessary to consider a distribution of plausible masses given a planetary radius. The planetary mass controls the surface gravity and therefore the scale height (H) of the atmosphere:

$$H = \frac{k\,T}{\mu_{atm}\,g} \tag{7.5}$$

Estimating the planetary mass is not a trivial task, given the range of planetary densities observed today. I used a Python tool written by Chen and Kipping (2016) to estimate the mass of all the planets in our simulated sample. Chen and Kipping (2016) use the currently known planets to derive the statistical distribution of the mass of a given planet when its radius is known. Thus, except for known systems, for each planet in our simulated sample, the mass is randomly drawn following that distribution. In Fig 7.3 I show the mass distribution for all the planets in our simulations. Moreover, as a very few planets have a radius larger than $20R_{\oplus}$, I use that radius as an upper limit. There is already a well-known degeneracy in the $7 - 20R_{\oplus}$ range: objects with a radius within that range can be planets as well as very cool stars. However, this should not be too concerning, as observations have shown that very short-period, low-mass stellar companions are much less frequent than hot giant planets (Piskorz et al., 2015).

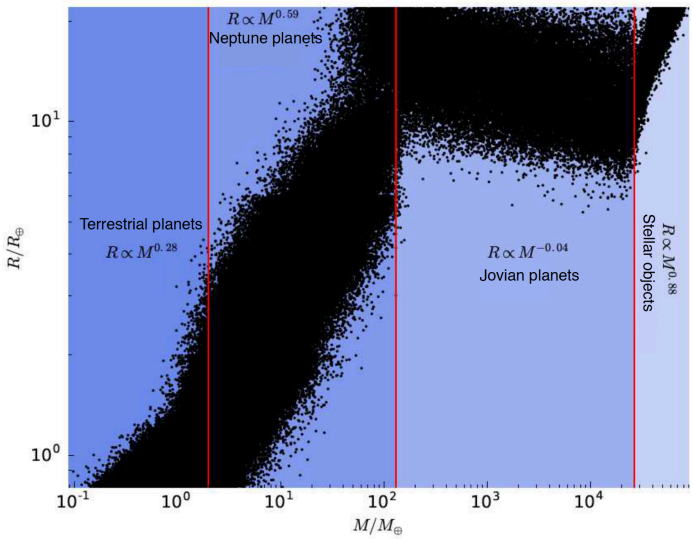

Figure 7.3: Mass-Radius distribution for all the simulated planets. The mass-radius relationship has been calculated with the Chen and Kipping (2016) tool.

7.3 ARIEL science goals and Mission Reference Population

7.3.1 The 3 tier approach

The ARIEL primary science objectives call for atmospheric spectra or photometric lightcurves of a large and diverse sample of known exoplanets covering a wide range of masses, densities, equilibrium temperatures, orbital properties and host-stars (Tinetti et al., 2018). Other science objectives require, by contrast, the profound knowledge of a select sub-sample of objects. In order to maximise the science return of ARIEL and take full advantage of its unique characteristics, a three-tiered approach has been considered, where three different samples are observed at optimised spectral resolutions, wavelength intervals and signal-to-noise ratios. A summary of the three-tiers and observational methods is given below in table 7.3.

In this section, I present the pool of potential targets that could reach the specifications for each tier. The number of targets for the various tiers are shown as a function of planetary radius in Fig 7.4, 7.6 and 7.8 and as a function of effective temperature in 7.5, 7.7 and 7.9. Note that the planets shown in these figures do not represent the final sample, as it would take too long to observe all of them. They are the pool from which the MRS can be selected to best address the scientific questions summarised below. The fact that the number of potential targets is much larger than the number that can be observed illustrates that ARIEL can choose the final sample among a great variety of observable planets, providing much flexibility.

ARIEL 3-tiers	
Survey (∼37%)	Low spectral resolution observations ($R \geq 10$ across all channels) of a large sample of planets in the Vis-IR, with SNR ≥7.
Deep (∼60%)	Intermediate spectral resolution observations ($R > 50$ in AIRS channel 0 and $R > 15$ in AIRS channel 1) of a subsample in the VIS-IR.
Benchmark (∼3%)	Very best planets, re-observed multiple time with all techniques. Full spectral resolution.

Table 7.3: Summary of the survey tiers and the observational strategy required to accomplish them. Each tier will use a % of the nominal mission lifetime, as indicated in the left column.

In Table 7.4 I show the spectral coverage and the resolving power of the ARIEL photometric and spectroscopic sensors. In Table 7.3 I report a summary of the three tiers and the observational strategy.

ARIEL spectral coverage		
Channel Name	**Wavelength (μm)**	**Resolving Power**
VisPhot	0.5 - 0.55	Photometer
FGS-1	0.8 - 1.0	Photometer
FGS-2	1.05 - 1.2	Photometer
NIRSpec	1.25 - 1.95	R$\geq$10
AIRS-Channel #0	1.95 - 3.9	R$\geq$100
AIRS-Channel #1	3.9 - 7.8	R$\geq$30

Table 7.4: Spectral range and spectral resolving power required for the ARIEL photometric and spectroscopic channels.

7.3.2 Key science questions

The key questions and objectives of each tier can be summarised as follows (see Tinetti et al., submitted for further details):

Survey - Tier 1:

- *What fraction of planets is covered by clouds?* – tier 1 mode is particularly useful for discriminating between planets that are likely to have clear atmospheres, versus those that are so cloudy that no molecular absorption features are visible in transmission. Extremely cloudy planets may be identified simply from low-resolution observations over a broad wavelength range. This preliminary information will, therefore, allow us to take an informed decision about whether to continue the spectral characterisation of the planet at a higher spectral resolution and therefore include or not the planet in the tier 2 sample.

- *What fraction of small planets have still hydrogen and helium retained from the protoplanetary disk?* – Primordial (primary atmosphere) atmospheres are expected to be mainly made of hydrogen and helium, i.e. the gaseous composition of the protoplanetary nebula. If an atmosphere is made of heavier elements, then the atmosphere has probably evolved (secondary atmosphere). An easy way to distinguish between primordial (hydrogen-rich) and evolved atmospheres (metal-rich), is to examine the transit spectra of the planet: the main atmospheric component will influence the atmospheric scale height, thus changing the amplitude of the spectral features noticeably. This question is essential to understand how super-Earths formed and evolved.

- *Can we classify planets through colour-colour diagrams or colour-magnitude diagrams?* – Colour-colour or colour-magnitude diagrams are a traditional way of comparing and categorising luminous objects in astronomy. Similarly to the Herzsprung-Russell diagram, which led to a breakthrough in understanding stellar formation and evolution, the compilation of similar diagrams for exoplanets might lead to similar developments (Triaud et al., 2014).

- *What is the bulk composition of the terrestrial exoplanets?* – The planetary density may constrain the composition of the planet interior. However, this measurement alone may lead to non-unique interpretations (Valencia et al., 2007). A robust determination of the composition of the upper atmosphere of transiting planets will reveal the extent of compositional segregation between the atmosphere and the interior, removing the degeneracy originating from the uncertainty in the presence and mass of their (inflated?) atmospheres.

- *What is the energy balance of the planet?* – Eclipse measurements in the optical and infrared can provide the bulk temperature and albedo of the planet, thereby allowing the estimation of the planetary energy balance and whether the planet has an internal heat source or not.

Deep - Tier 2:

A key objective of ARIEL is to understand whether there is a correlation between the chemistry of the planet and basic parameters such as planetary size, density, temperature and stellar type and metallicity. Spectroscopic measurements at a higher resolution compared to tier 1 and it will allow in particular to measure:

- The main atmospheric component for small planets;

- The chemical abundances of trace gases, which is pivotal to understand the type of chemistry (equilibrium/ non-equilibrium).

- The atmospheric thermal structure, both vertical and horizontal;

- The cloud properties, i.e. cloud particles size and distribution,

- The elemental composition in gaseous planets. This information can be used to constrain formation scenarios (Öberg et al., 2011).

Benchmark - Tier 3:

A fraction of planets around very bright stars will repeatedly be observed through time to obtain:

- A very detailed knowledge of the planetary chemistry and dynamics;

- An understanding of the weather, and the spatial and temporal variability of the atmosphere.

Benchmark planets are the best candidates for phase-curve spectroscopic measurements.

7.3.3 Target samples

In this section I discuss some lists of potential targets for ARIEL: these are expected to evolve until launch and will be updated regularly to include new planet discoveries.

ARIEL tier 1 (Survey) will analyse a large sample of exoplanets to address science questions where a statistically significant population of objects needs to be observed. ARIEL tier 1 will also allow a rapid, broad characterisation of planets is permitting a more informed selection of tier 2 and tier 3 planetary candidates. For most planetary candidates, tier 1 performances can be reached between one and two transits/eclipses. In Fig 7.4 and 7.5 I show that in the solar system neighbourhood there are $\sim$ 9500 targets observable by ARIEL for which the science requirements can be reached in less than six transits or eclipses.

ARIEL tier 2 (Deep, the core of the mission) will analyse a sub-sample of tier 1 planets with a higher spectral resolution, allowing an optimal characterisation of the atmospheres, including information on the thermal structure, abundance of trace gases, clouds and elemental composition.

In Fig 7.6 and 7.7 I show the properties of all the planetary candidates that could be studied by ARIEL in the Deep mode with a number of transit or eclipse events between 1 and 100.

The third ARIEL tier (Benchmark, the reference planets) will study the brightest planets (section 7.4.3), i.e. the ones orbiting very bright stars which can be studied in full spectral resolution with a relatively small number of transits/eclipses. For the planets observed in benchmark mode in 1 or 2 events, it is possible to study the spatial and temporal variability (i.e. study the weather and evaluate its impact when observations are averaged over time). In Fig 7.8 and 7.9 I show the properties of the tier 3 planetary candidates.

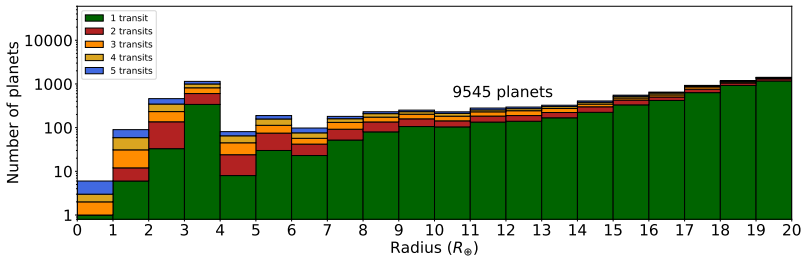

Figure 7.4: Complete set of tier 1 planets from the ARIEL mission reference population. The final list of tier 1 planets will include an optimal sub-sample. Different colours indicate the number of transits/eclipses needed to reach tier 1 performances. The planets shown here can achieve the tier 1 requirements combining the signal of ≤ 5 transits/eclipses.

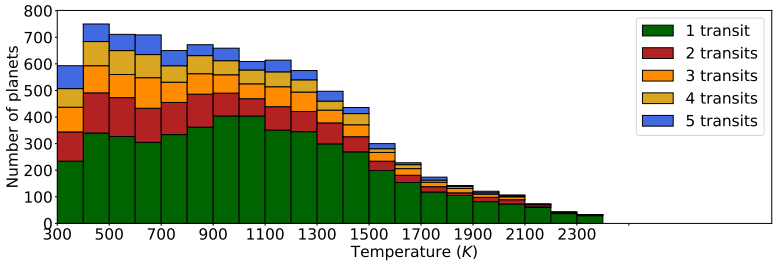

Figure 7.5: Temperature distribution for the planets illustrated in fig. 7.4.

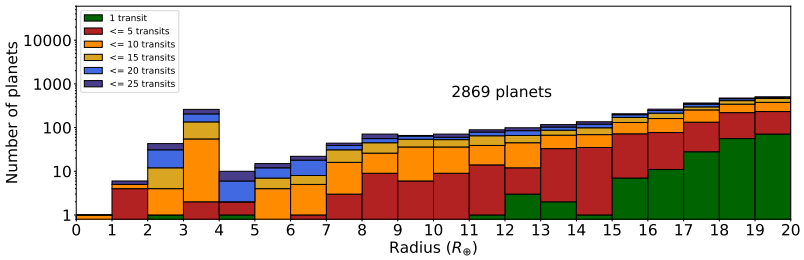

Figure 7.6: Planets from the ARIEL mission reference population in the Deep mode (Tier 2) with a small/moderate number of transits/eclipses, divided in size bins. The final list of tier 2 planets will include an optimal sub-sample. Different colours indicate the number of transits/eclipses needed to reach tier 2 performances.

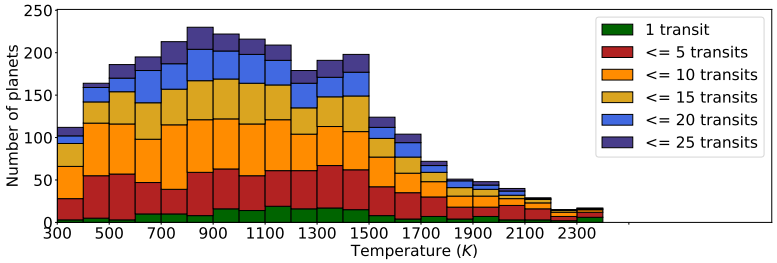

Figure 7.7: Temperature distribution for the planets illustrated in fig. 7.6.

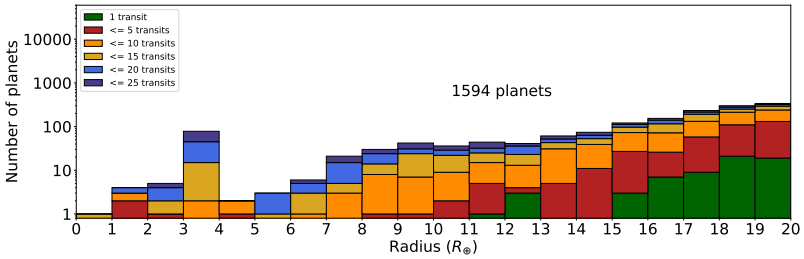

Figure 7.8: Number of planets from the mission reference population observable by ARIEL in the Benchmark mode with a < 25 number of transits/eclipses, divided in size bins. Different colours indicate the number of transits/eclipses needed to reach tier 3 performances.

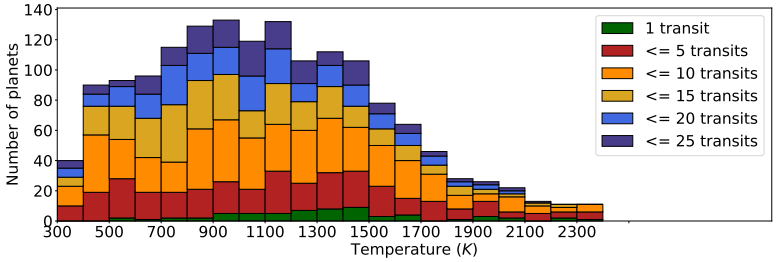

Figure 7.9: Temperature distribution for the planets illustrated in fig. 7.8.

7.4 A possible scenario for the ARIEL space mission

In Section 7.3 I presented the rationale behind a comprehensive list of planet candidates which could be observed with the ARIEL space mission. Here I discuss possible optimisations of the Mission Reference Sample, which ideally should include a large and diverse sample of planets, have the right balance among the three tiers and, most importantly, must be completed during the nominal mission lifetime (4 years including the commissioning phase).

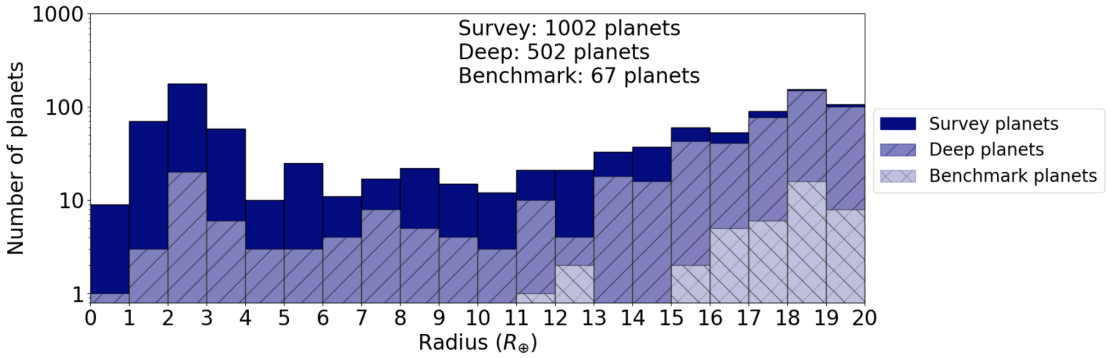

Figure 7.10: Overview of the ARIEL MRS, comparing the number of planets observable in the three tiers during the mission lifetime.

In Fig 7.10 I show a possible MRS with all the three tiers nested together. This MRS is optimised to yield the maximum number of targets, taking into account the nominal mission lifetime. It has been built starting from all the targets feasible within one transit/eclipse and adding all the targets that can be done within 2, 3, 4 and so on transits/eclipses in ascending order. The mentioned target list is just one of the possible configurations for the MRS, and one would expect the ARIEL MRS to evolve in the response of new exoplanetary discoveries in the next decade.

7.4.1 MRS tier 1: Survey

Our simulations indicate that the current ARIEL design as presented at the end of the Phase A study allows to observe 1002 planets in tier 1. All the planets can be observed during 37% of

the scientific mission time. Most giant planets and Neptunes fulfil the tier 1 science objectives in 1 transit/eclipse, the smaller planets require up to 6 events (fig. 7.11 and 7.12). Fig. 7.13 and 7.14 illustrate how the 1002 planets are distributed in terms of planetary size, temperature, density and stellar type.

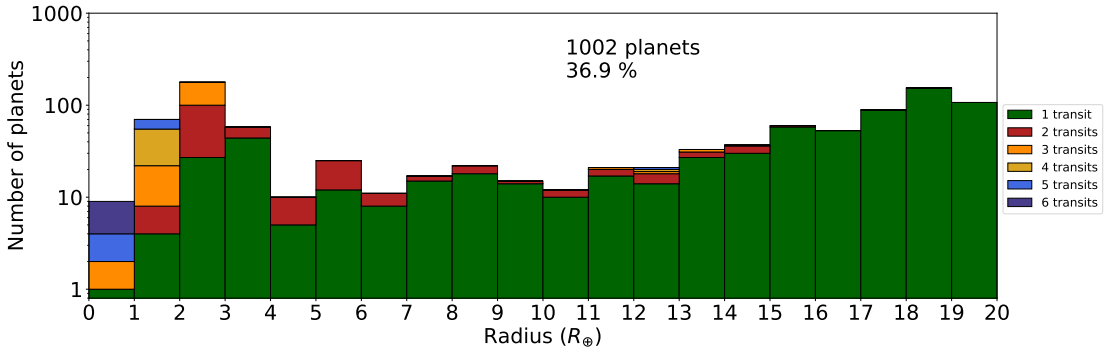

Figure 7.11: ARIEL MRS tier 1 planets organised in size-bins. Different colours indicate the number of transits/eclipses needed to reach tier 1 performances.

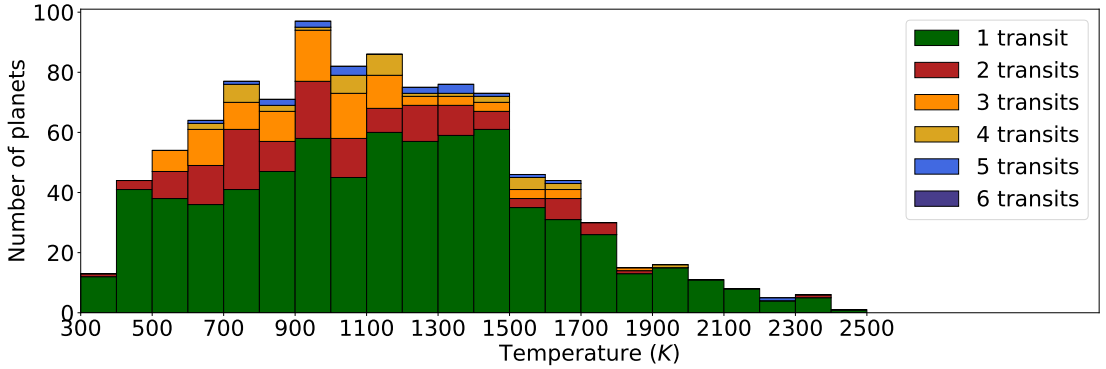

Figure 7.12: ARIEL MRS tier 1 planets organised in temperature-bins. Different colours indicate the number of transits/eclipses needed to reach tier 1 performances.

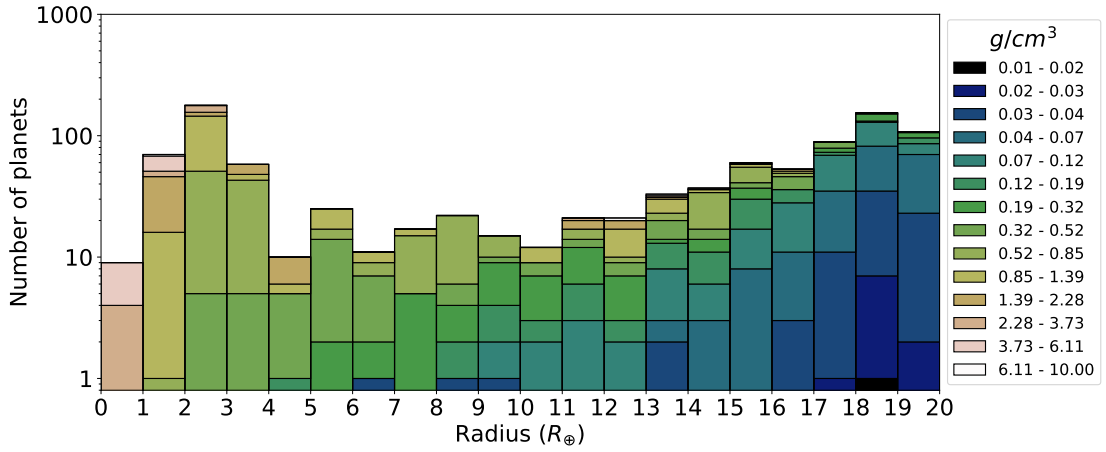

Figure 7.13: ARIEL MRS tier 1 planets organised in size-bins. Different colours indicate differences in the simulated planetary densities.

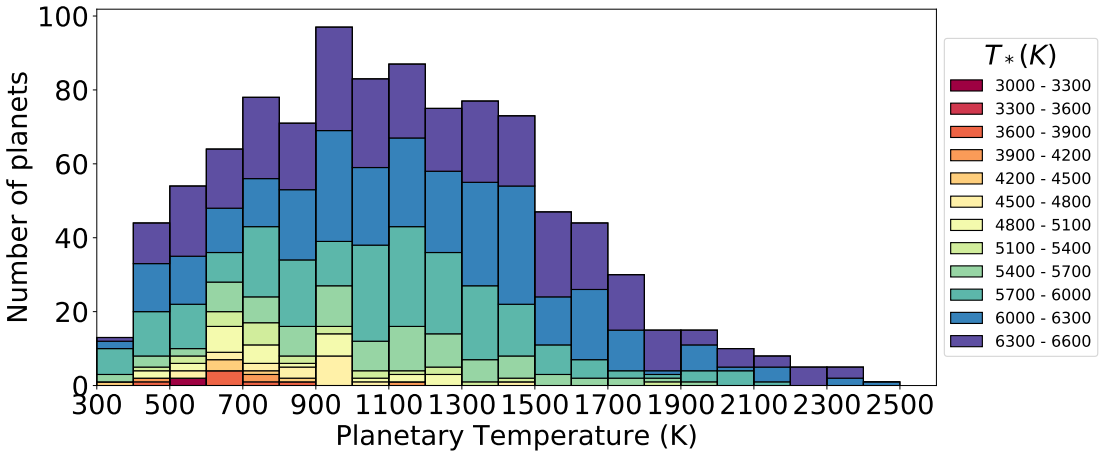

Figure 7.14: ARIEL MRS tier 1 planets organised in temperature-bins. Different colours indicate differences in the simulated stellar temperatures.

7.4.2 MRS tier 2: Deep

The Deep is the core of the mission. Our simulations indicate that the current ARIEL design as presented at the end of the Phase A study allows to observe $\sim$ 500 planets in tier 2 assuming 60% of the mission lifetime. Fig. 7.17 and 7.18 illustrate how the 500 planets are distributed in terms of planetary size, temperature, density and stellar type.

Most gaseous planets fulfil the tier 2 science objectives in less than five transits/eclipses, the smaller planets require up to twenty events (fig. 7.15 and 7.16). I included a variety of planets from cold (300 K) to very hot (2500 K) as shown in Fig 7.16. I also scheduled $\sim$ 50 planets that will be studied with both transit and eclipse methods, indicated by stripes in Fig 7.15). These are the best candidates for phase-curves observations, which inclusion in the observational schedule can be decided depending on the scientific relevance on the target.

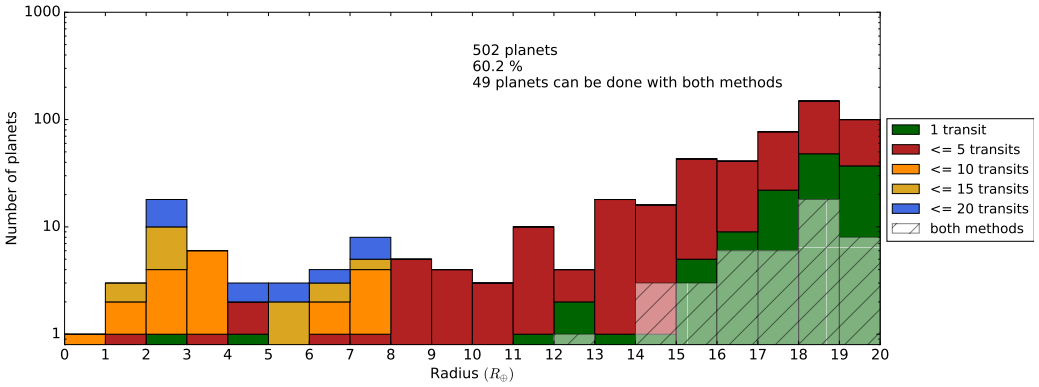

Figure 7.15: ARIEL MRS tier 2 planets organised in size-bins. Different colours indicate the number of transits/eclipses needed to reach tier 2 performances. Stripes indicate planets that will be studied with both transit and eclipse methods

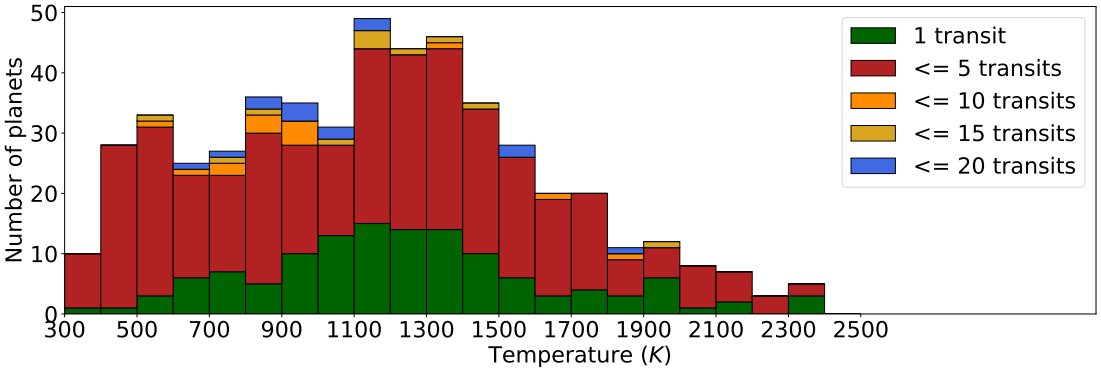

Figure 7.16: ARIEL MRS tier 2 planets organised in temperature-bins. Different colours indicate the number of transits/eclipses needed to reach tier 2 performances.

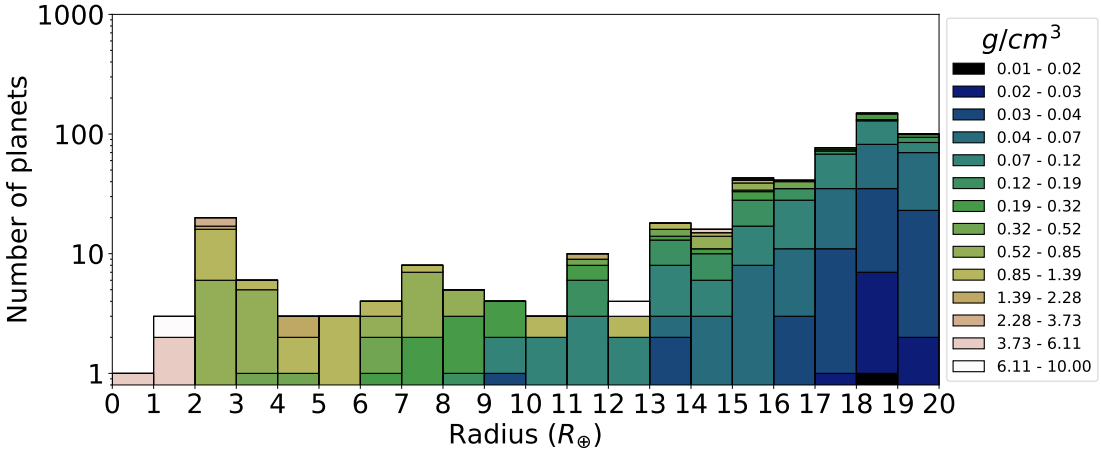

Figure 7.17: ARIEL MRS tier 2 planets organised in size-bins. Different colours indicate differences in the simulated planetary densities.

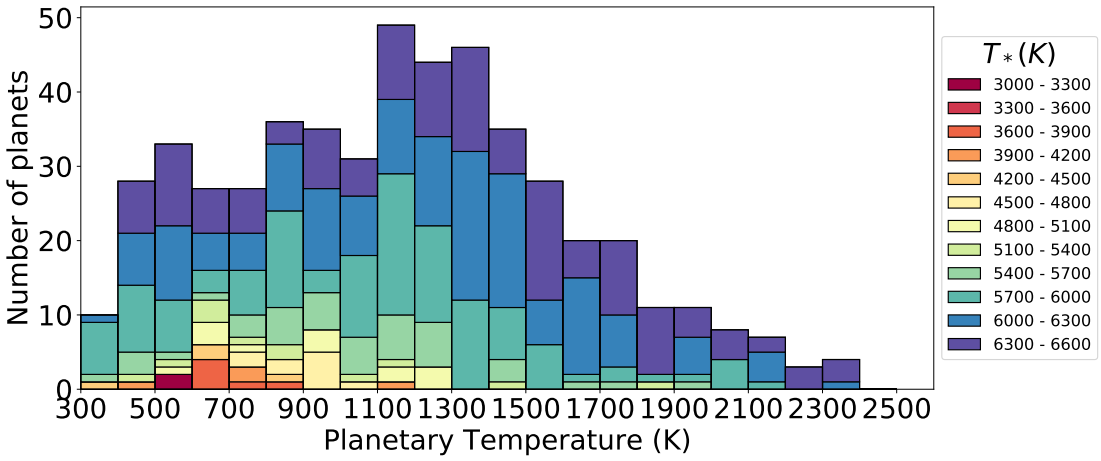

Figure 7.18: ARIEL MRS tier 2 planets organised in temperature-bins. Different colours indicate differences in the simulated stellar temperatures.

7.4.3 MRS tier 3: Benchmark

In the current MRS, I have selected as tier 3, 67 gaseous planets for weather studies. Fig. (7.19) shows the temperature distribution covered by the tier 3 sample. Only 3% of the mission lifetime is required to achieve the tier 3 science objectives for this sample.

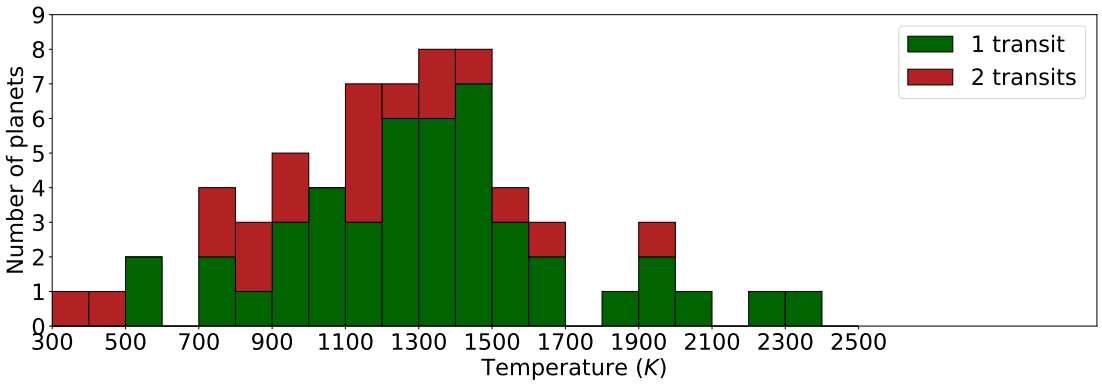

Figure 7.19: Temperature distribution of the planets observable by ARIEL in the Benchmark.

7.4.4 Compliance with TESS expected yields

The Transiting Exoplanet Survey Satellite (TESS) is expected to provide a large fraction of the targets observable by ARIEL. The numbers of targets envisioned in the sample presented here are perfectly in line with the expected yield from the Transiting Exoplanet Survey Satellite (TESS), as shown in Fig 7.20 where I compare the expected TESS discoveries and the ARIEL MRS. It is noticeable that the ARIEL MRS is well within the TESS sample (Sullivan et al., 2015). The success of the TESS mission will allow the characterisation of hundreds of planets by ARIEL.

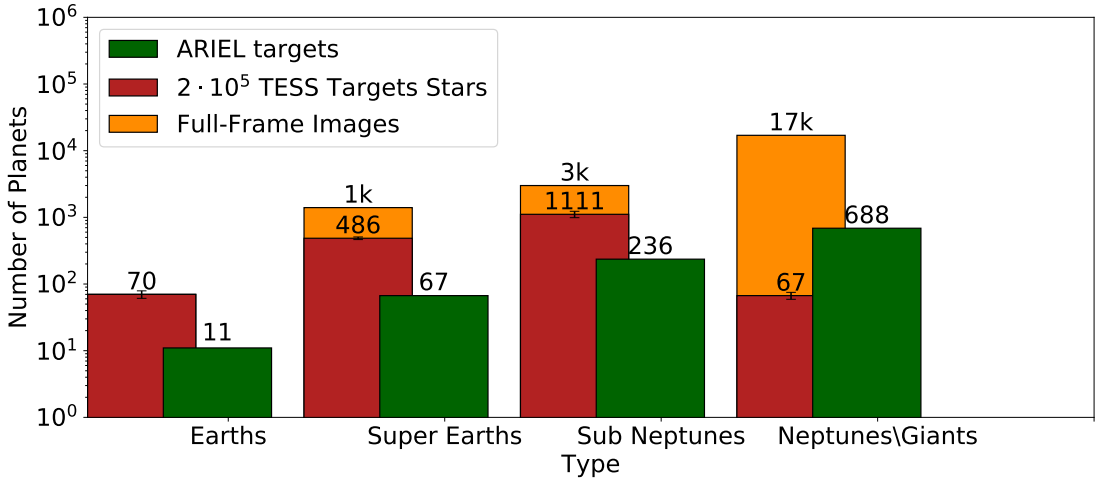

Figure 7.20: Comparison between the TESS targets (Sullivan et al., 2015) and the ARIEL MRS (green bars).

7.4.5 ARIEL MRS with currently known targets

In February 2018 ∼210 transiting planets fulfil the ARIEL previous criteria. It means that, even if ARIEL were launched tomorrow, it would observe at least 210 relevant targets. Given the number of planets known today, the MRS can be organised into the following three tiers:

- Survey: 210 planets using 30% of the mission lifetime (Fig 7.21);
- Deep: 158 planets using 60% of the mission lifetime (Fig 7.26);
- Benchmark: 67 planets using 10% of the mission lifetime (Fig 7.27).

In Fig 7.21, 7.22 and 7.23 I show the key physical parameters of the known planets defining the current observable MRS current MRS. In Fig 7.24 and 7.25 I show the properties of the stellar hosts. As mentioned previously, the number of known planets is expected to increase dramatically in the future.

Pictorial representation (M. Ollivier, private comm.) of the known planets sky coordinates and their sky visibility all over the year is given in Fig 7.28. It shows that objects far away from the ecliptic plane will be visible longer than the planet close to this plane.

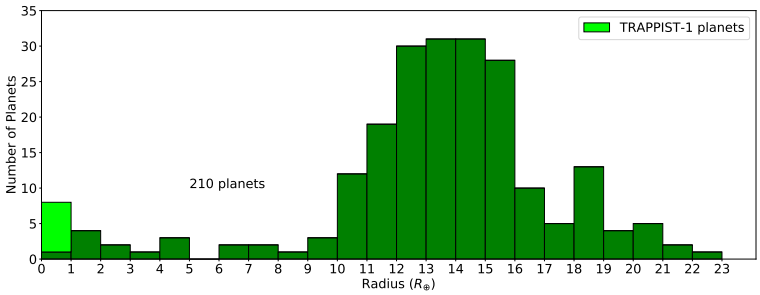

Figure 7.21: ARIEL MRS with currently available planets radius distribution.

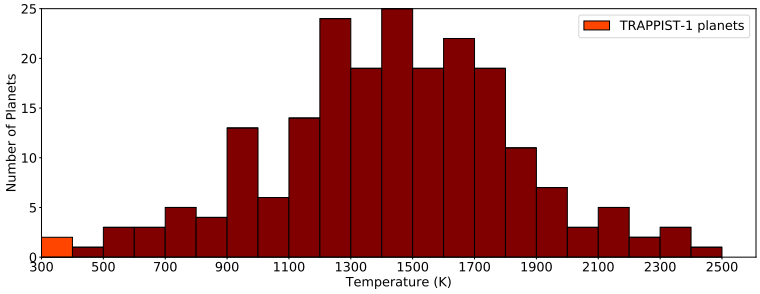

Figure 7.22: ARIEL MRS with currently available planets temperature distribution.

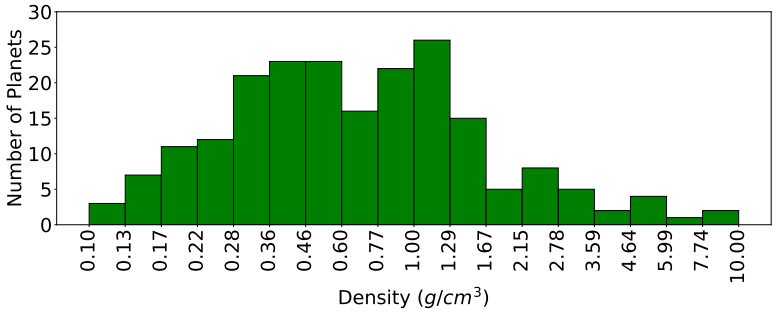

Figure 7.23: ARIEL MRS with currently available planets density distribution.

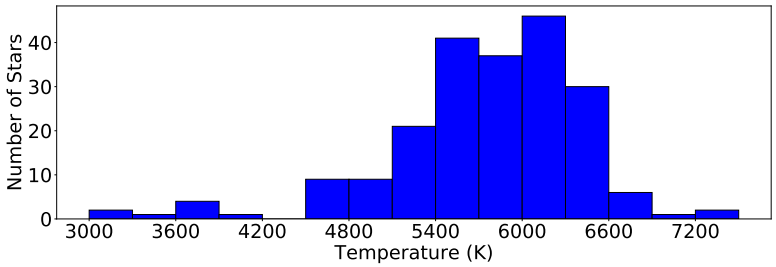

Figure 7.24: Temperature distribution of the stellar hosts for the planets shown in fig. 7.21

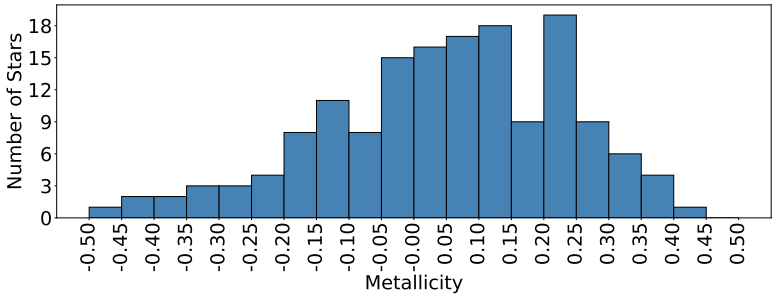

Figure 7.25: Metallicity distribution of the stellar hosts for the planets shown in fig. 7.21

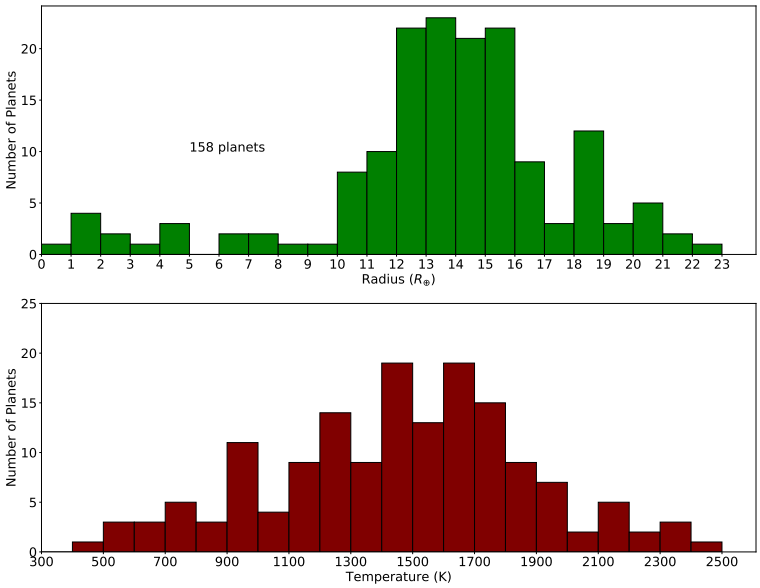

Figure 7.26: Planets known today and observable by ARIEL in Deep mode, distributed in size-bins (**top**) and temperature bins (**bottom**) – 158 planets.

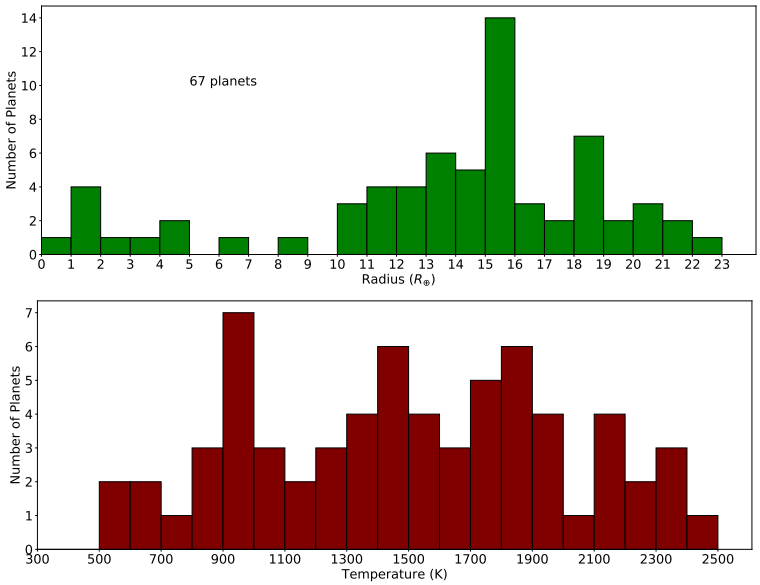

Figure 7.27: Planets known today and observable by ARIEL in Benchmark mode, distributed size-bins (**top**) and temperature bins (**bottom**) – 67 planets.

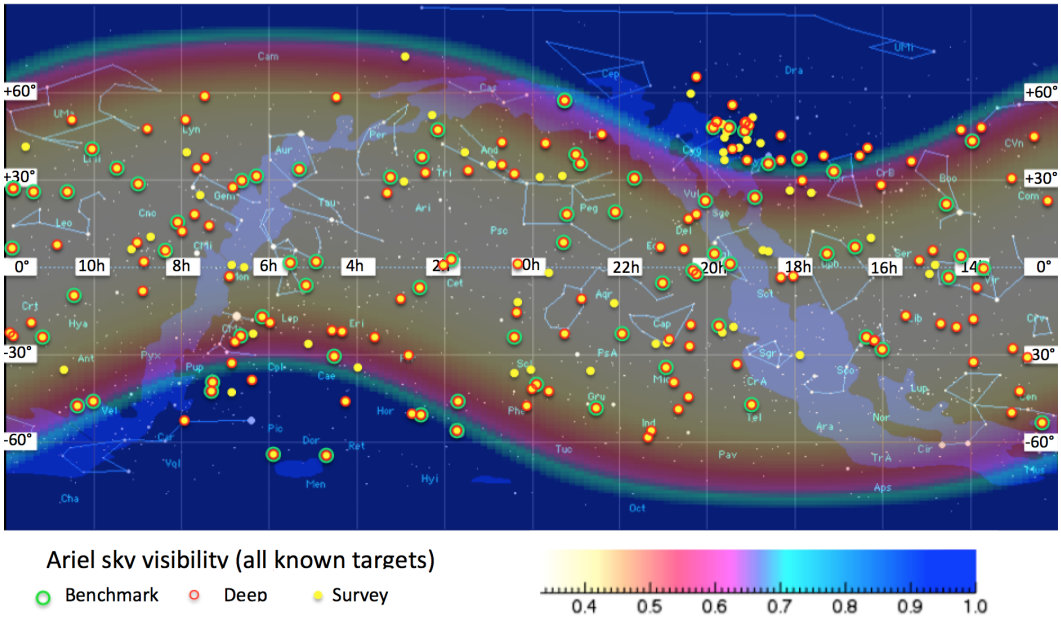

Figure 7.28: A plot illustrating the fraction of the year for which a given location in the sky (in equatorial coordinates) is visible to ARIEL, as seen from a representative operational orbit of ARIEL at L2. Yellow dots: planets observed in tier 1. Red dots: planets observed in tier 2. Green dots: planets observed in tier 3. (Marc Ollivier, private communication)

Table 7.5: Bins of T_{eff}, [Fe/H], R_{pl}, T_{pl} defining the 4D parameter space.

Stellar Temp.: T_{eff}	$3000 < T(K) < 4100$	$4100 < T(K) < 5800$	$T > 5800K$
Labels	M-Late K	Early K-G	F-G
Metallicity: [Fe/H]	[Fe/H] < -0.15	$-0.15 <$[Fe/H]< 0.15	[Fe/H]> 0.15
Labels	Low [Fe/H]	Solar	High [Fe/H]
Planet Radius: R_{pl}	$R_{pl} < 3R_{\oplus}$	$3 < R_{\oplus} < 8$	$R_{pl} > 8R_{\oplus}$
Labels	Earths/ Super Earths	Neptunes	Jupiters
Planet Temp.: T_{pl}	contiguous bins: [250, 500, 800, 1200, 1600, 2600] K		

7.5 MRS optimisation for star/planet properties

In this section, I show another possible selection of the tier 1 sample that maximises the diversity of stellar hosts, additionally to other planet parameters.

7.5.1 Method

I will limit our analysis to those systems which can be studied in up to six visits for each planet (either transit or an occultation).

I chose four physical quantities that define a 4D space to distribute the ARIEL targets. The quantities are: stellar effective temperature (T_{eff}), metallicity ([Fe/H]), planetary radius (R_{pl}) and planetary theoretical equilibrium temperature (T_{pl}). For the metallicity, I use the values observed in the solar neighbourhood and reported by Casagrande et al. (2011). I adopt three bins for stellar T_{eff}, [Fe/H] and planetary R_{pl}, while for the T_{pl} I use five bins, as detailed in Table 7.5. The three T_{eff} bins correspond approximately to the ranges of spectral types M-Late / K stars, Early K-G stars and F-G stars, respectively, as indicated in the labels in Fig 7.30 to 7.32. Analogously, I separated the sample in low metallicity, solar metallicity and high metallicity. I inferred from Casagrande et al. (2011) that the metallicities of stars in the solar neighbourhood are consistent with a normal distribution with mean -0.1 and standard deviation sd=0.2. Using such model distribution, I simulated the values of [Fe/H] for each star in the ARIEL sample.

The binning into three intervals of T_{eff}, [Fe/H] and R_{pl} is a reasonable trade-off between a detailed representation of the sample and a simple visualisation of the richness and diversity of the physical configurations of the sample.

The 4D space of T_{eff} , [Fe/H], R_{pl} and T_{pl} is composed by a total of $3 \times 3 \times 3 \times 5 = 135$ cells. I assume that ten systems are sufficiently reliable to determine the properties of the atmospheres of planets in each cell.

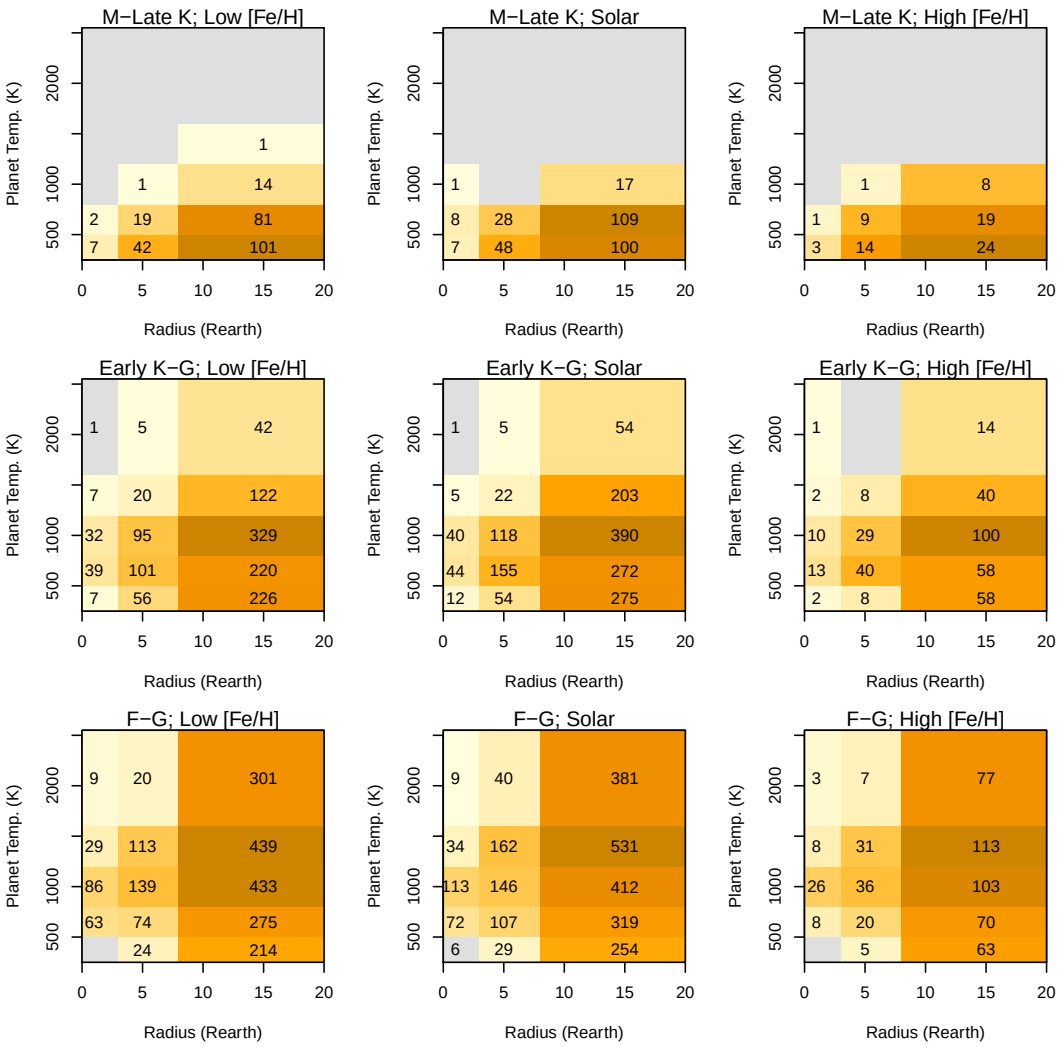

Figure 7.29: Distribution of the 9545 planets in the 4D space of T_{eff}, [Fe/H], R_{pl}, T_{pl}. Above each panels I indicate the spectral type and metallicity. The numbers in each cell are the numbers of planets with the corresponding properties. The colour scale indicates more populated cells (darker orange/brown). Grey cells without any number indicate no objects.

7.5.2 Results

The population of 9545 planets is distributed in the 4-D bins as in Fig 7.29.

From this distribution I selected 1002 exoplanets, requiring 1538 satellite visits altogether. These 1002 planets are distributed in the 4D space as shown in Fig. 7.30. The 3×3 panel grid distributes the sample along the three spectral types and the metallicity ranges reported in Table 7.5. Each panel is a matrix with planetary radii along the x-axis and (calculated) equilibrium temperatures along the y-axis, as specified in Table 7.5 and discussed above. The numbers in each box identify the numbers of systems with the corresponding R_{pl}, T_{pl}, spectral type, and [Fe/H] values.

The 1002 systems in Fig. 7.30 tend to populate the cells corresponding to F-G-early and K

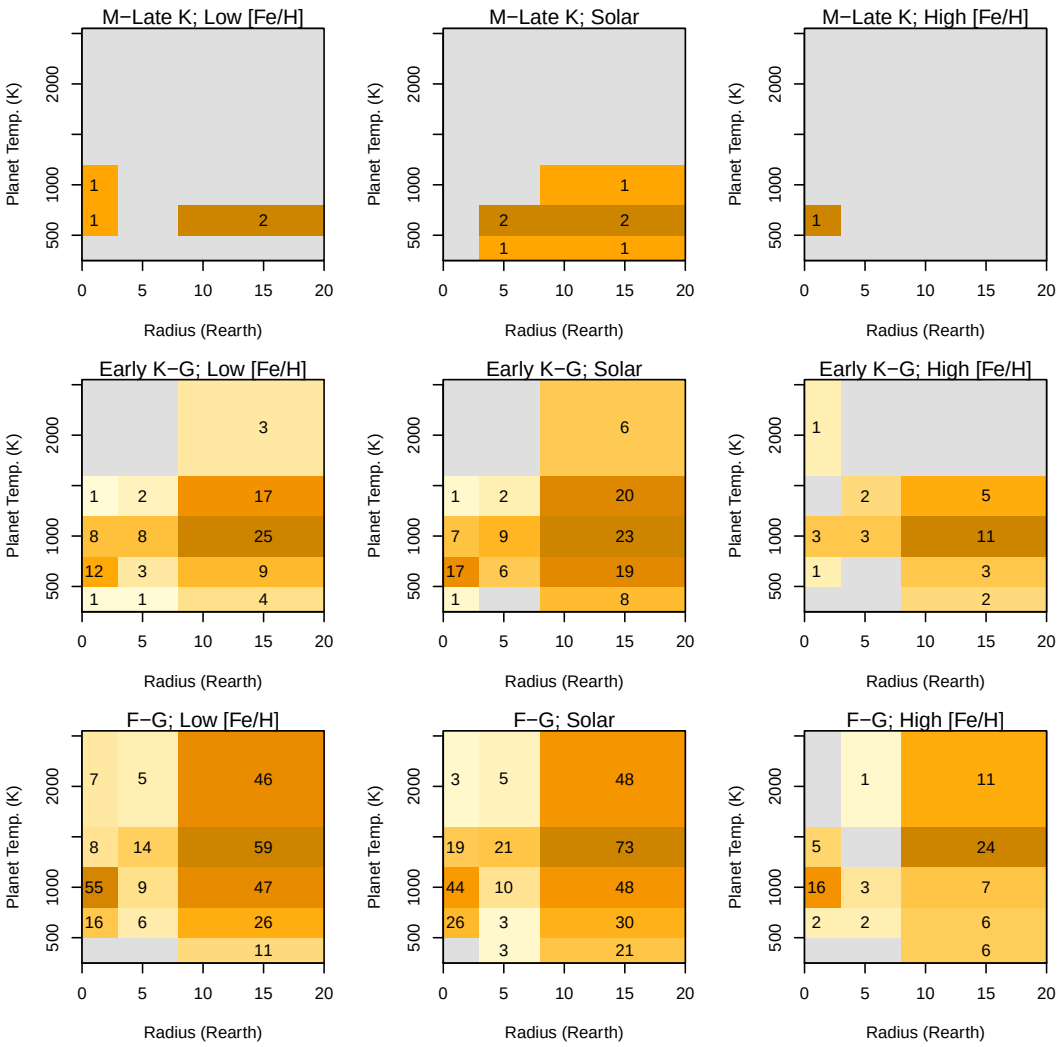

Figure 7.30: Same as Fig. 7.29 1002 planets of the Mission Reference Sample.

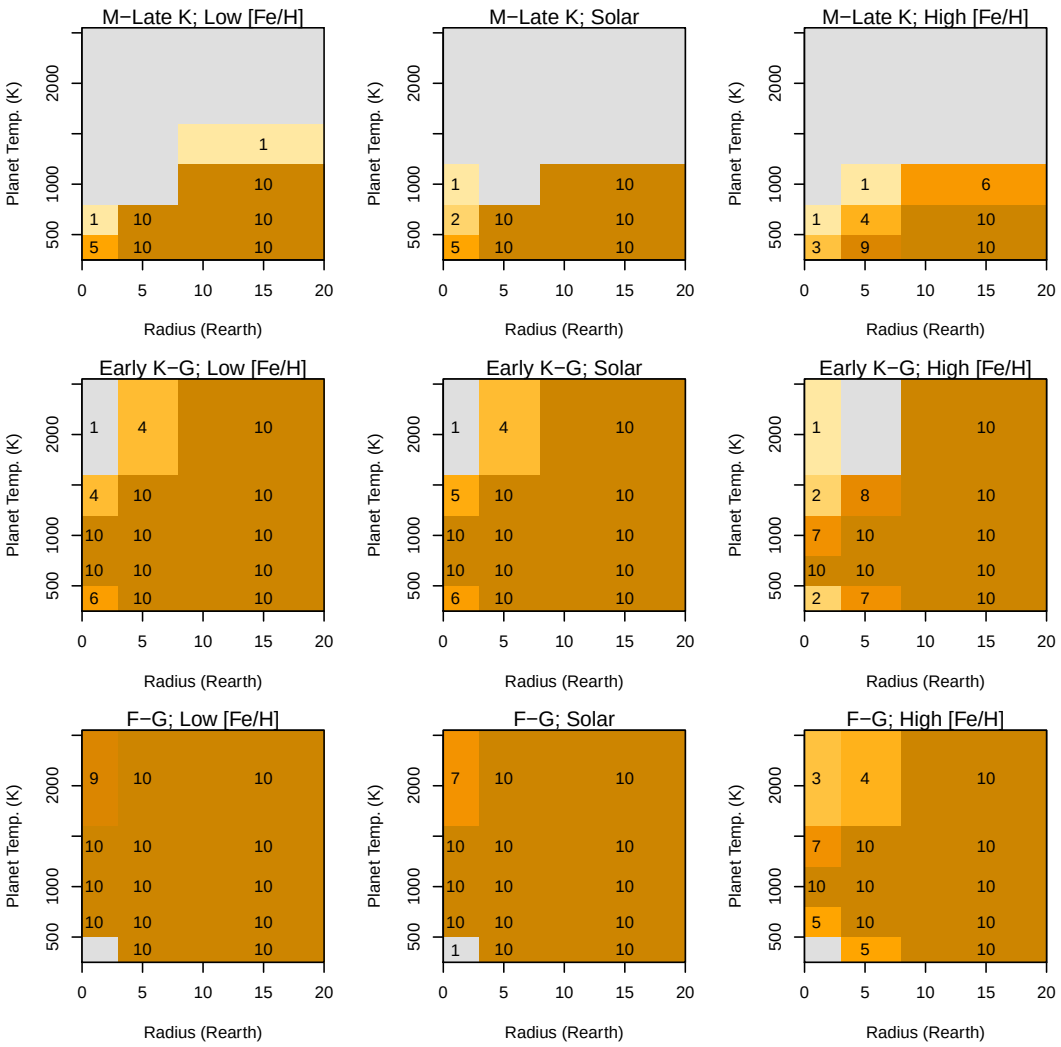

Figure 7.31: Same as Fig. 7.30 for the selected sample of 908 known and simulated planetary systems. They have been selected by filling each cell with up to 10 objects and for a budget of total satellite visits of about 1500.

stars orbited by Neptunes/Jupiters size planets (with a number of planets per cell $N > 20$), as these systems are the easiest to be observed with high signal to noise and, on average, with one or two visits. At the same time, planets around M or late K stars are much less represented in this distribution, especially planets smaller than Neptunes. This issue was identified in the previous sections as a result of extending the occurrence rate for F, G, K to M stars and it can be addressed by prioritising these targets over the rest of the population. I selected 908 planets and, in particular, 594 of them require only 1 visit (65.4%), 151 planets require 2 visits (16.6%), 83 planets require 3 visits (9.1%), 41 planets require 4 visits (4.5%), and 39 planets require 5 visits (4.4%). The final sample is shown in Fig 7.31, where now $\sim$ 19% of the population are Earths/Super Earth or Neptunes around M, or K stars observable with less than six visits.

Assuming a total number of visits as in the 1002 planets configuration (approximately 1500

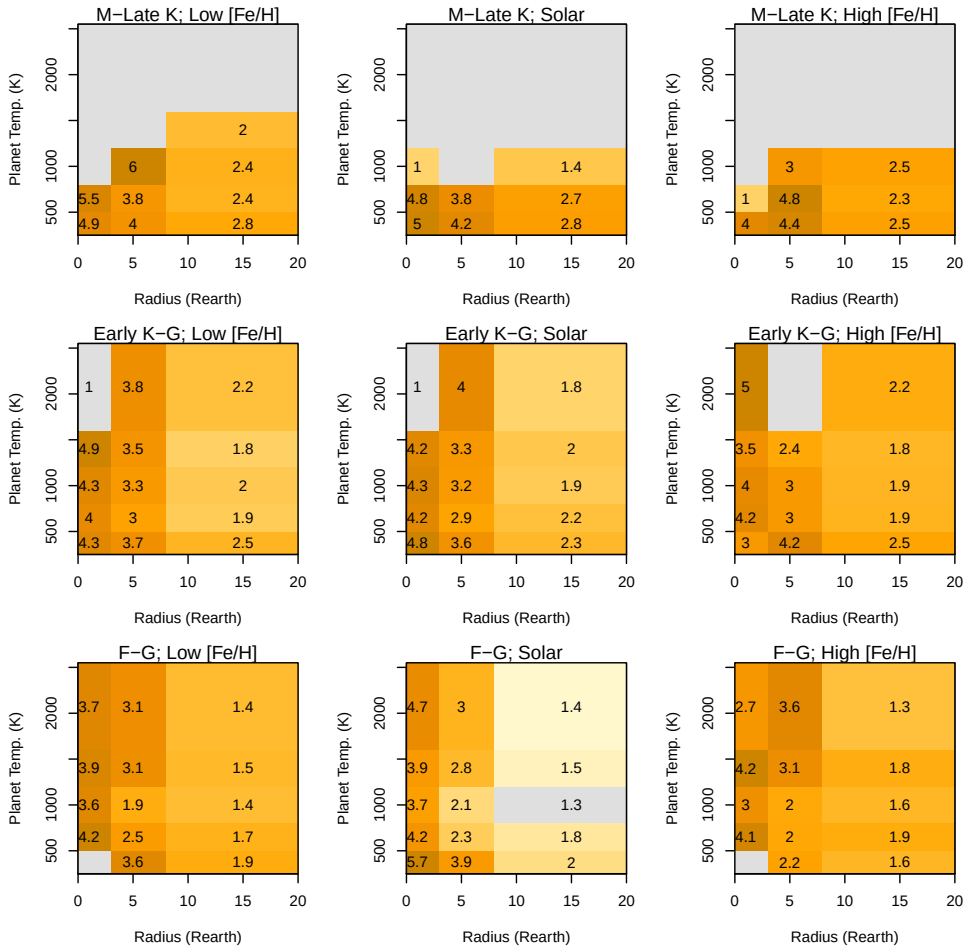

Figure 7.32: Average number of visits required for the sample selected in Fig. 7.31. The binning is as in Figs. 7.30 to 7.31.

visits), I fixed the maximum number of systems (10 planets in our choice) in each 4D space cell. This choice implies that any additional targets in an “already full" cell will be discarded. In this way, I can include planets in the empty or poorly populated parts of the parameter space. The goal is to verify that I can cover with enough statistics most of the 4D parameter space. The distribution of systems selected with such criteria is shown in Fig. 7.31. Compared to Fig. 7.30, I see that I can efficiently cover most of the 4D space in planetary sizes, planetary temperatures, host temperatures and metallicities, apart from those combinations of parameters corresponding to not physical or rare systems (e.g., very hot planets around very cool stars), not present in the reference population of Figure 7.29. Our selection is composed of 908 unique planets requiring a total of 1504 visits. Among already known systems, 92 of the initial 211 systems are in this new list. This selection is not unique and depends on our choices, but our exercise shows that we have great freedom on the final choice on how to spend ARIEL observing time, as it can be easily tuned on specific needs. Fig. 7.32 shows the average number of visits required to cover each cell of the 4D space. The number of visits needed for Jupiters and Neptunes is, typically, one or two,

while Earths/Super Earths require from 3 to 5 visits each. To summarise, out of the 908 planets in our selection there are 594 planets requiring only 1 visit (65.4%), 151 planets requiring 2 visits (16.6%), 83 planets requiring 3 visits (9.1%), 41 planets requiring 4 visits (4.5%), and 39 planets requiring 5 visits (4.4%).

As a final comment, I have verified that, by increasing the maximum number of systems per 4D cell while keeping fixed the total number of visits to $\sim$ 1500, I obtain that the number of observed planets increases (for example assuming N=15 as maximum systems per cell, I can observe up to 1000 systems), but at the same time the 4D cells of systems with cold/warm Earths/Super Earths would tend to be left empty and thus unexplored. This exercise shows the degree of flexibility offered by ARIEL in the choice of the target sample.

7.6 Summary and conclusions

In this chapter I demonstrated that the current ARIEL design enables the observation of 900-1000 planets during its four-year lifetime, depending on the physical parameters of the planet/star systems which one wants to optimise. The optimal sample of targets fulfils all the science objectives of the mission. While we currently know $\sim$200 transiting exoplanets which could be part of the mission reference sample, new space missions and ground-based observatories are expected to discover thousands of new planets in the next decade. NASA-TESS alone is expected to deliver most ARIEL targets. Since the publication of Zingales et al. (2018) work other surveys related to other space missions came out. In particular it is remarkable the work of Barclay et al. (2018) about the TESS sample which is still compatible with the current MRS and confirms that the TESS space mission will provide valuable candidates for the final ARIEL mission reference sample.

Chapter 8

Conclusion

At the centre of exoplanetary research lies the data and techniques necessary to analyse them. In this thesis I described the "classic" methodology to study exoplanets, focusing on the physics of their atmosphere and the importance of transit spectroscopy to infer exoplanetary atmospheric properties.

In the future, many ground-based surveys and space missions (e.g. JWST, ARIEL and Twinkle) will provide more accurate observations of thousands of exoplanetary atmospheres. The high number of exoplanets observed will enable population studies on a more statistically consistent sample of targets than those available today. For this reason, it is necessary to improve our techniques to study consistently a large sample of exoplanetary atmospheres.

With this thesis, I offered a new tool to analyse quickly complex atmospheres, ExoGAN. I described the traditional techniques which make use of computationally-intensive Bayesian analysis, and I showed how neural network algorithms could increase the computational efficiency during an atmospheric retrieval. At the current stage, ExoGAN can be used to generate informative prior distributions for a subsequent Bayesian analysis. In the future, it could potentially substitute the current analysis method, allowing to include computationally-intensive models which are, otherwise, prohibitive to include in a standard retrieval code.

I started this thesis by explaining the atmospheric models used in a retrieval tool such as TauREx and illustrated the rationale behind Bayesian analysis. After explaining the state-of-art techniques and models to study exoplanetary atmospheres, I applied a fully-Bayesian retrieval tool, TauREx, to the atmosphere of 30 exoplanets, demonstrating the existence of, at least, water vapour, in all the detectable exoplanetary atmospheres of the sample considered.

After explaining the traditional analysis techniques, I described the theory behind some

deep learning algorithms, focusing on the basics of artificial neural networks and convolutional neural networks. Then, I introduced ExoGAN, a Deep Convolutional Generative Adversarial Network, trained on a set of 10 million exoplanetary atmospheres, and able to understand how exoplanetary spectra are related to the chemical and physical parameters of the atmospheres.

After explaining all the possible techniques used to study exoplanetary atmospheres, I suggested how to generate a list of potential candidates for a space mission dedicated to transit spectroscopy: the ARIEL space mission. I demonstrated how, using the instruments mount on board of the ARIEL space mission, it will be possible to characterise at least 1000 exoplanetary atmospheres after the year 2028.

My thesis explains how the use of artificial intelligent algorithms can be used to accelerate the resolution of many complex physical problems. It introduces ExoGAN to the scientific community, and explains how it can be used to analyse exoplanetary atmospheres. Even though my application was focused to atmospheric analysis, due to its versatility, ExoGAN can be shaped to solve many different problems in all the scientific fields.

Appendix A

Additional material for Chapter 4

In this Appendix I show all the posterior distributions computed for all the 30 planet and their best fit spectrum. I also include the contribution graphs, which show the main components of a the final retrieved transmission model. The number of free parameters computed with the $\mathcal{T}$-REx retrieval code is 10 for each planet (12 TiO and VO are included, just for those planets with an equilibrium temperature above 1400 K). In the following are shown the low resolution retrievals. Retrievals for input spectra with a higher resolution do not show significant differences so I decided to show just the analysis of low resolution spectra. Posterior distributions are useful in order to see any correlation between the parameters and the convergence around a solution. For some cases there is more than one statistically significant solution, in these cases I show the posterior of all the possible solutions, the best fitted spectra in different colours and the contribution graph of the first possible models. For each of the following retrieval, $\mathcal{T}$-REx needs $\sim$7 hours on 24 CPU cores using cross sections between 0.3μm and 50μm at resolution $R = 15000$.

WASP-121 b

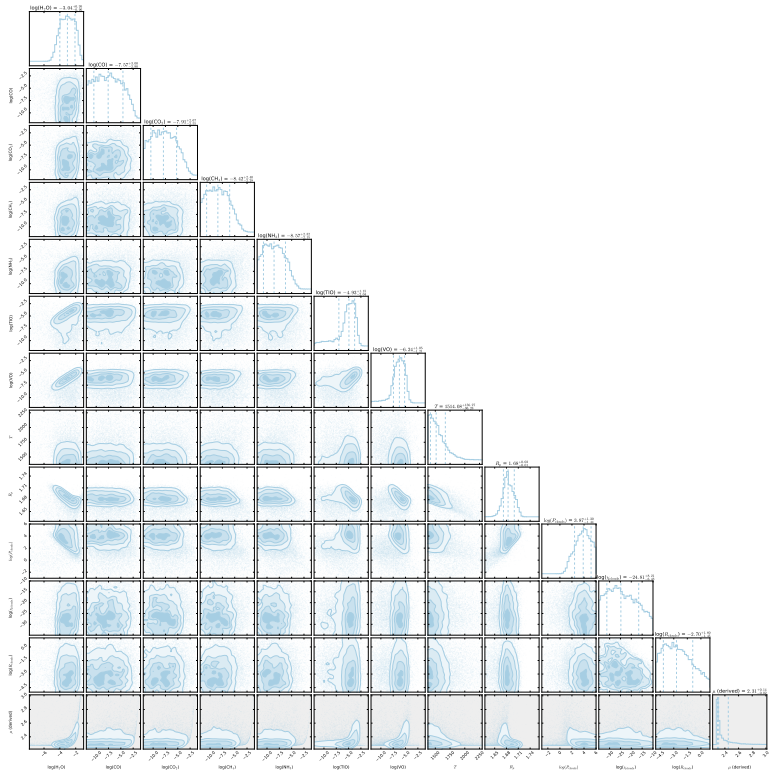

Figure A.1: The posterior distribution of the Bayesian retrieval for WASP-121 b.

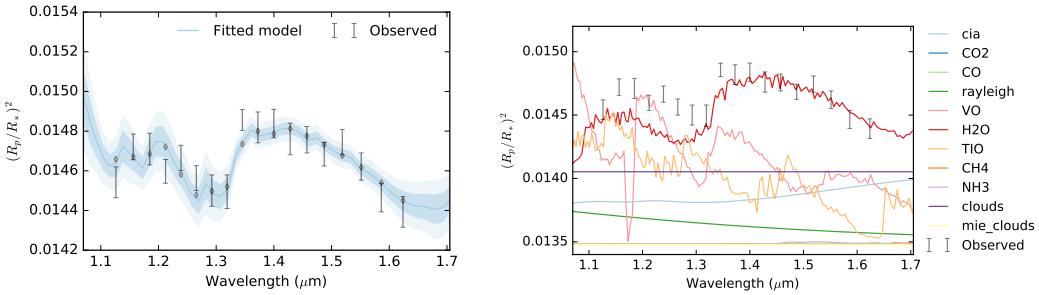

Figure A.2: Best fit spectrum for WASP-121 b transmission spectrum in low resolution (**right**) and contribution from each parameter in the model (**left**).

GJ-436 b

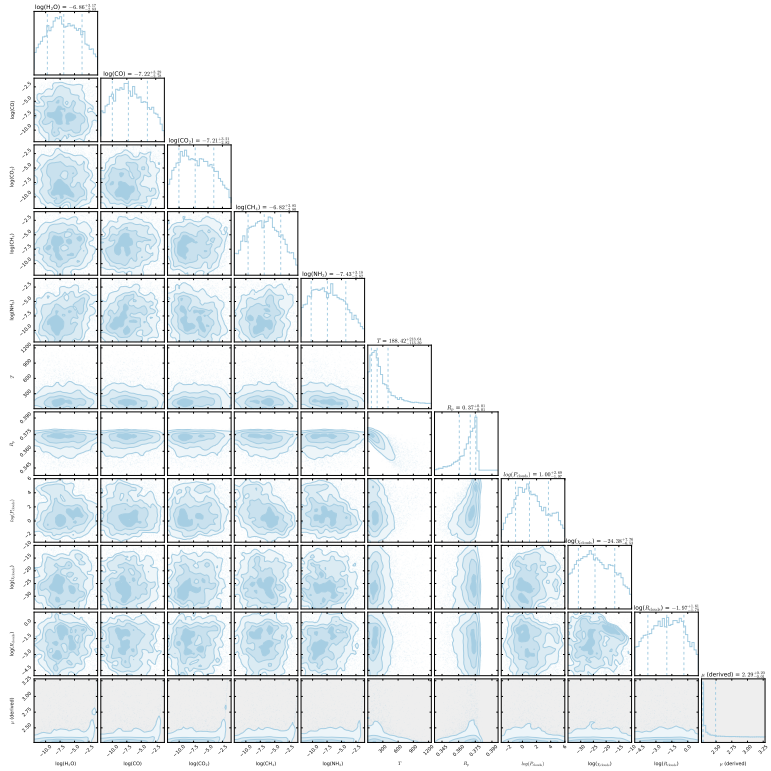

Figure A.3: The posterior distribution of the Bayesian retrieval for GJ-436 b.

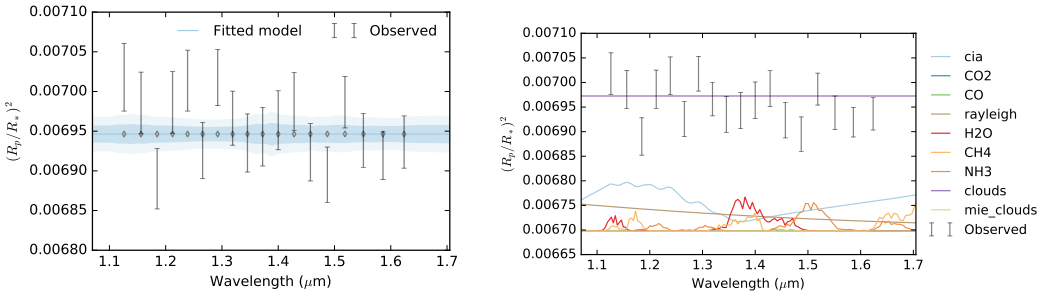

Figure A.4: Best fit spectrum for GJ-436 b transmission spectrum in low resolution (**right**) and contribution from each parameter in the model (**left**).

WASP-43 b

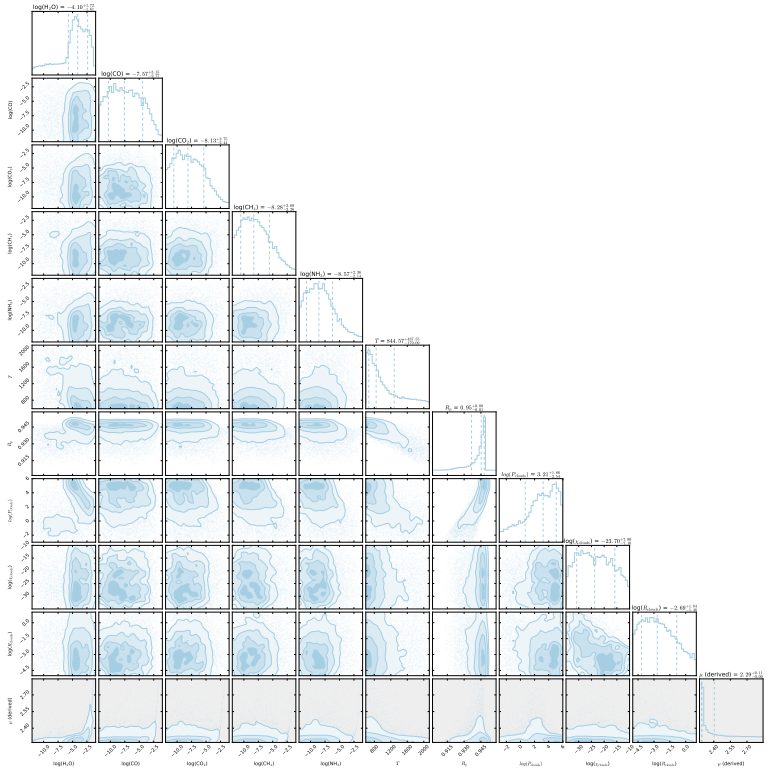

Figure A.5: The posterior distribution of the Bayesian retrieval for WASP-43 b.

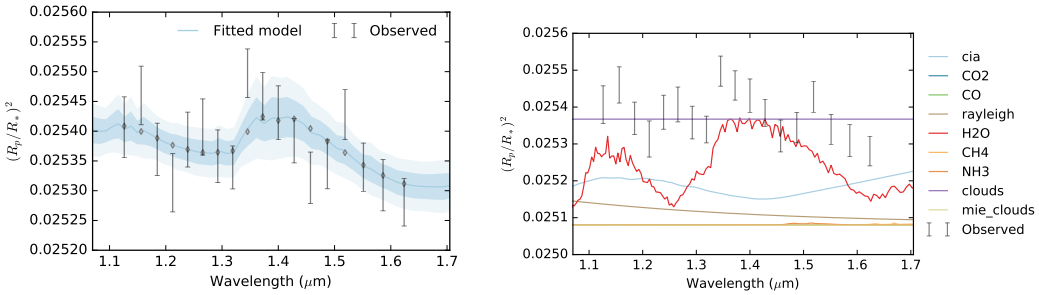

Figure A.6: Best fit spectrum for WASP-43 b transmission spectrum in low resolution (**right**) and contribution from each parameter in the model (**left**).

HATP-26 b

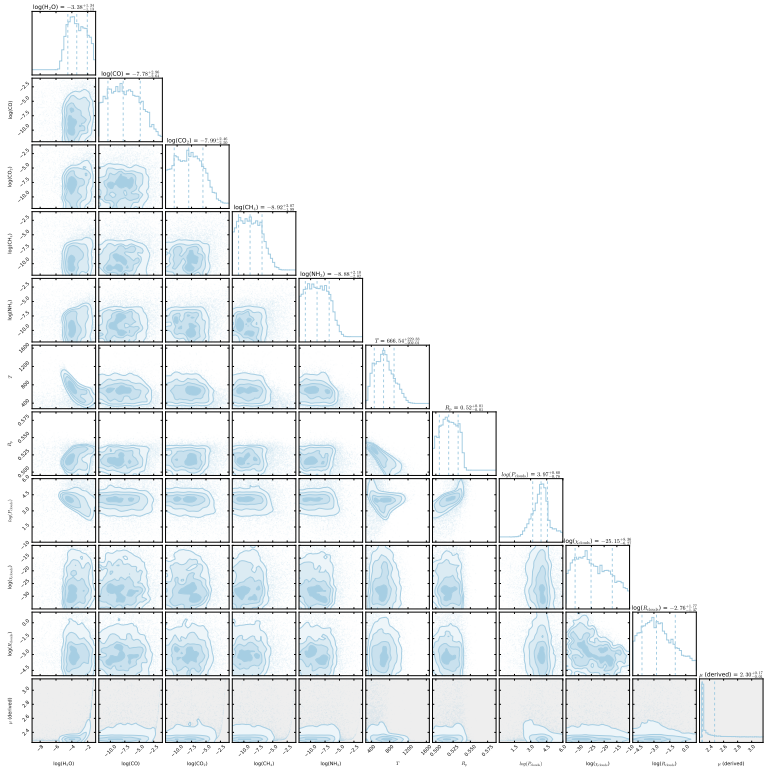

Figure A.7: The posterior distribution of the Bayesian retrieval for HATP-26 b.

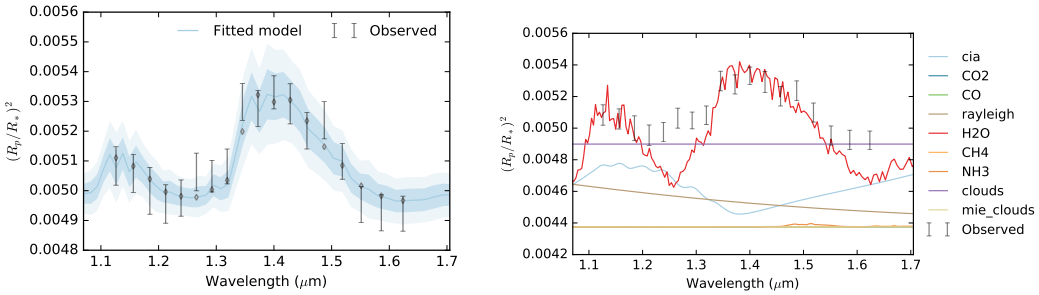

Figure A.8: Best fit spectrum for HATP-26 b transmission spectrum in low resolution (**right**) and contribution from each parameter in the model (**left**).

HATP-3 b

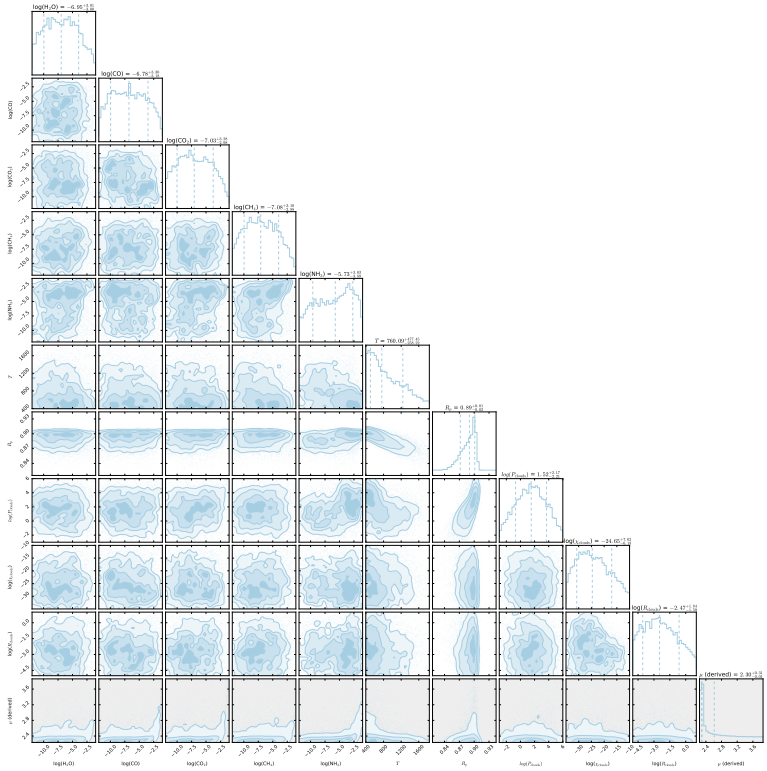

Figure A.9: The posterior distribution of the Bayesian retrieval for HATP-3 b.

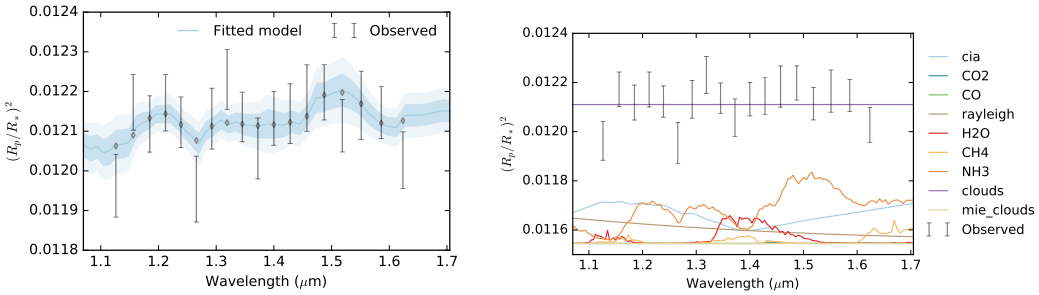

Figure A.10: Best fit spectrum for HATP-3 b transmission spectrum in low resolution (**right**) and contribution from each parameter in the model (**left**).

HD-189733 b

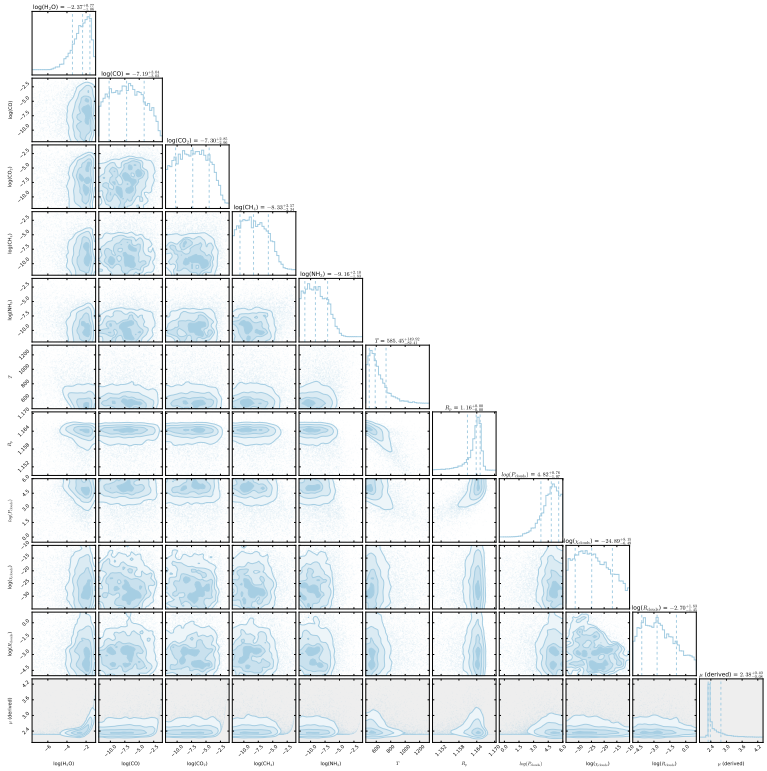

Figure A.11: The posterior distribution of the Bayesian retrieval for HD-189733 b.

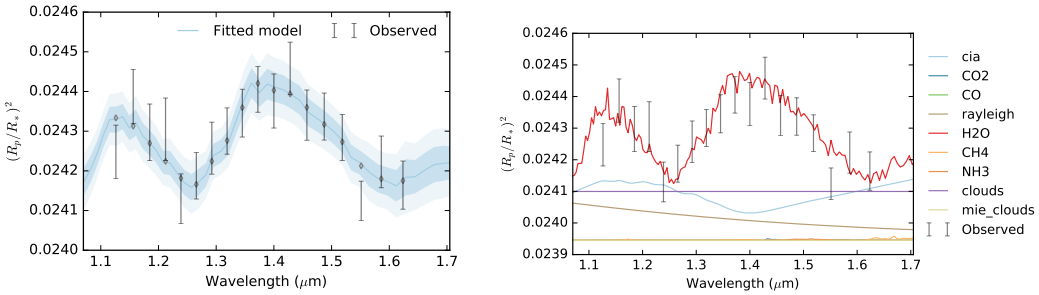

Figure A.12: Best fit spectrum for HD-189733 b transmission spectrum in low resolution (**right**) and contribution from each parameter in the model (**left**).

WASP-12 b

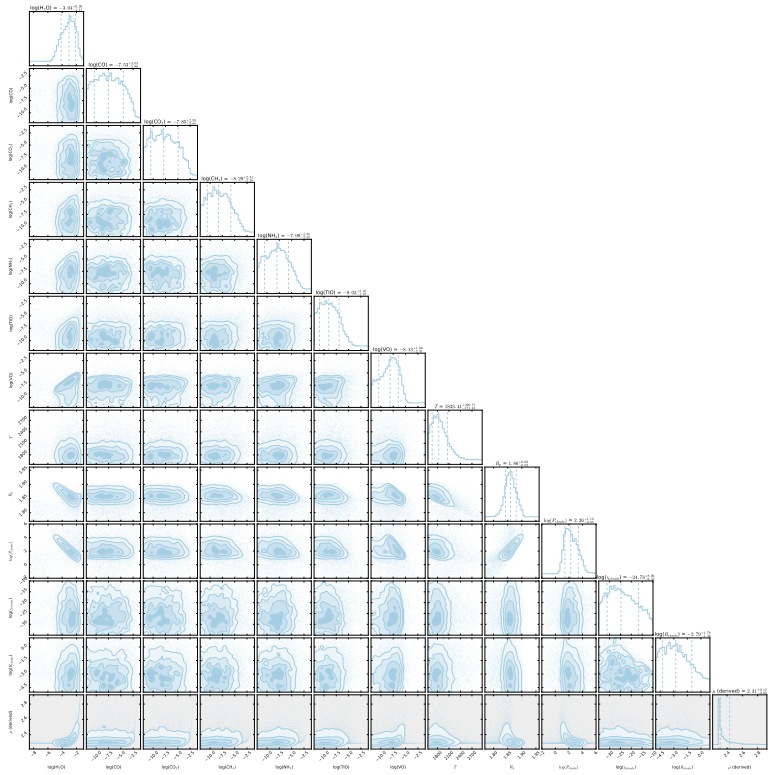

Figure A.13: The posterior distribution of the Bayesian retrieval for WASP-12 b.

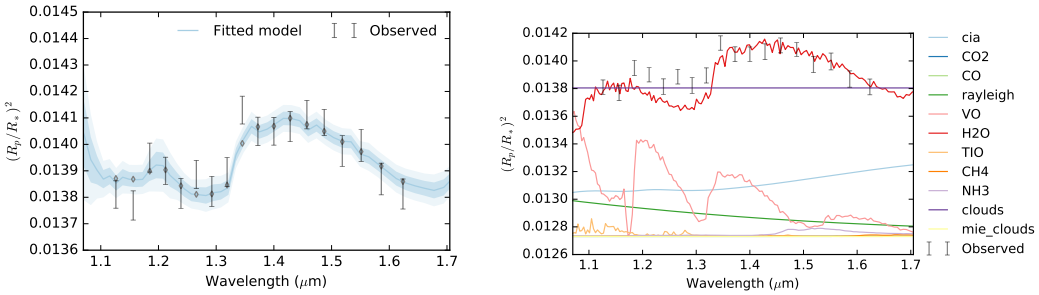

Figure A.14: Best fit spectrum for WASP-12 b transmission spectrum in low resolution (**right**) and contribution from each parameter in the model (**left**).

WASP-74 b

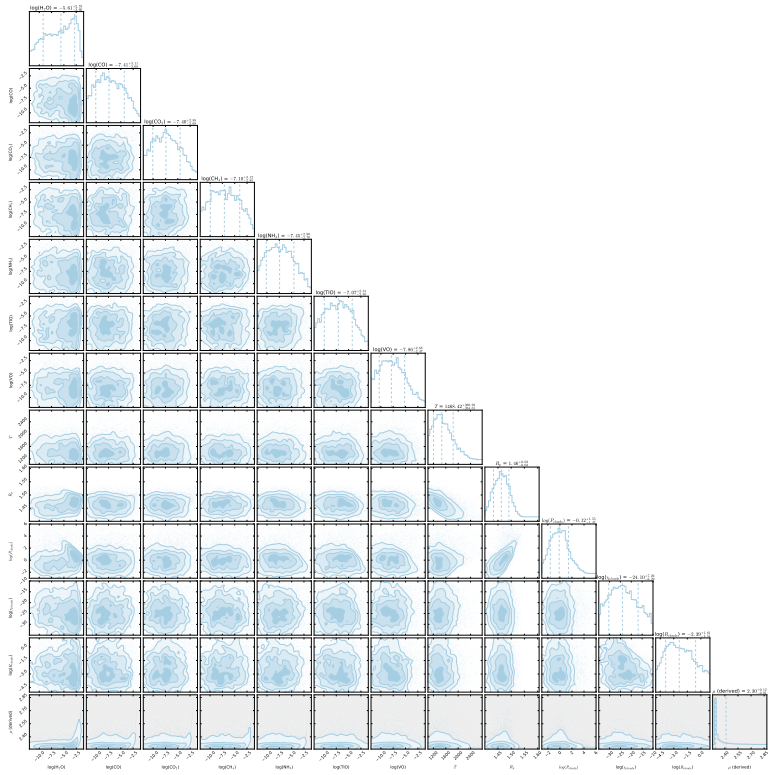

Figure A.15: The posterior distribution of the Bayesian retrieval for WASP-74 b.

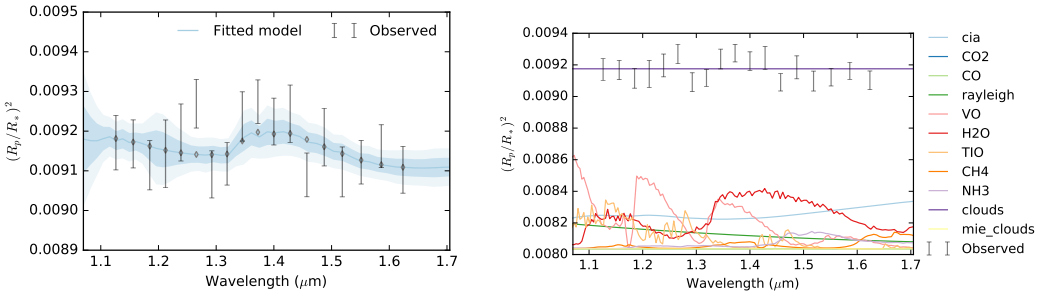

Figure A.16: Best fit spectrum for WASP-74 b transmission spectrum in low resolution (**right**) and contribution from each parameter in the model (**left**).

HATP-11 b

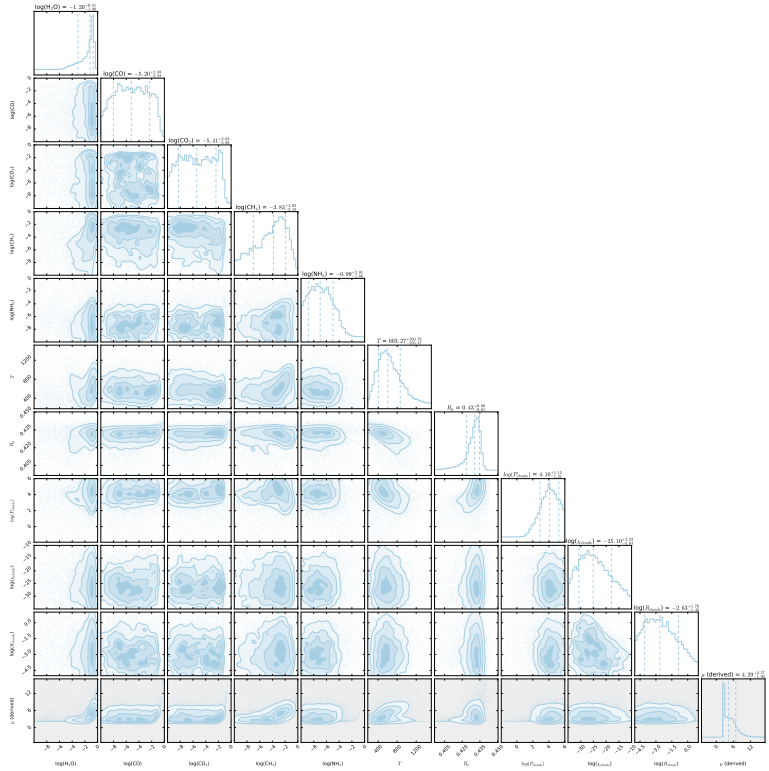

Figure A.17: The posterior distribution of the Bayesian retrieval for HATP-11 b.

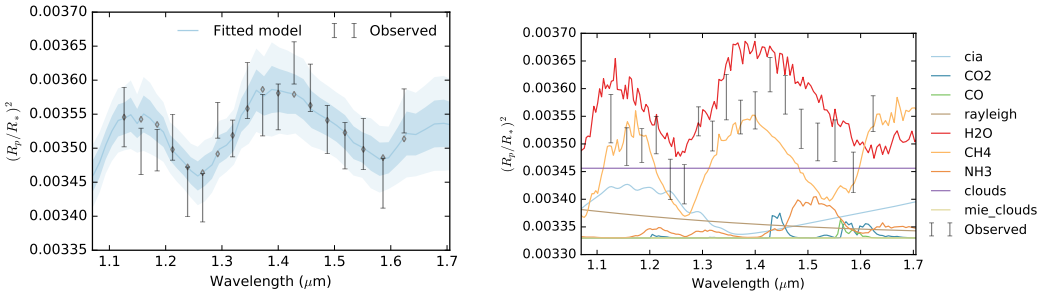

Figure A.18: Best fit spectrum for HATP-11 b transmission spectrum in low resolution (**right**) and contribution from each parameter in the model (**left**).

HATP-12 b

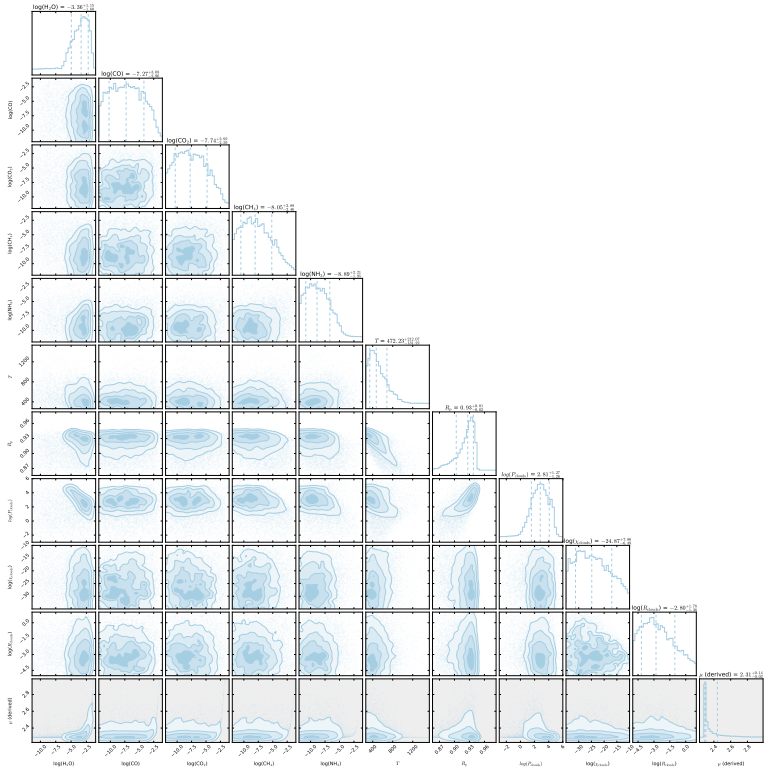

Figure A.19: The posterior distribution of the Bayesian retrieval for HATP-12 b.

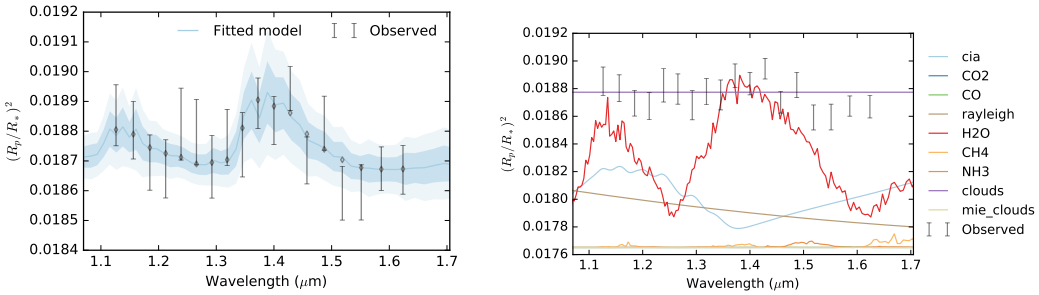

Figure A.20: Best fit spectrum for HATP-12 b transmission spectrum in low resolution (**right**) and contribution from each parameter in the model (**left**).

HATP-18 b

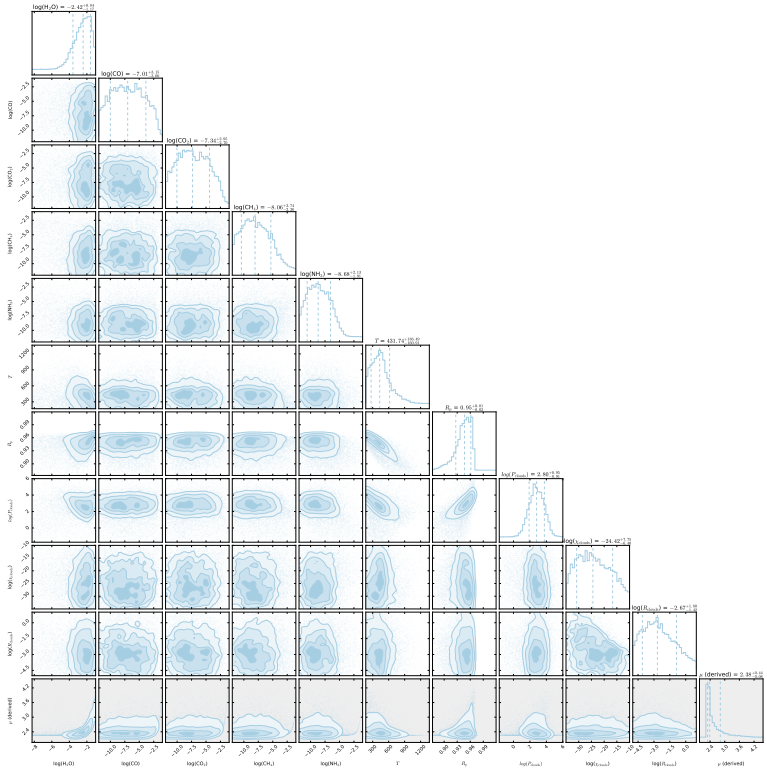

Figure A.21: The posterior distribution of the Bayesian retrieval for HATP-18 b.

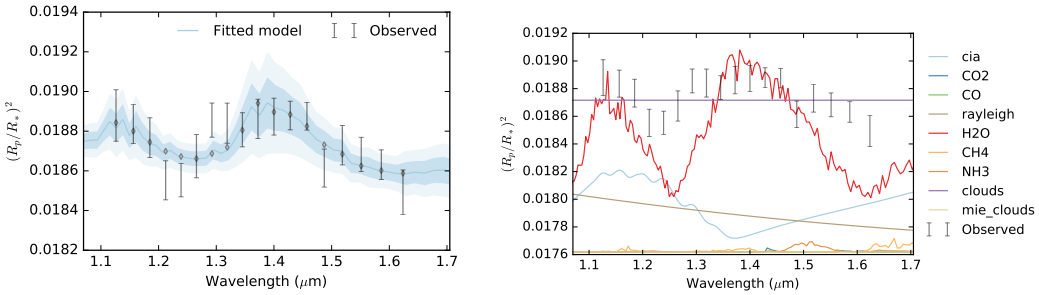

Figure A.22: Best fit spectrum for HATP-18 b transmission spectrum in low resolution (**right**) and contribution from each parameter in the model (**left**).

WASP-52 b

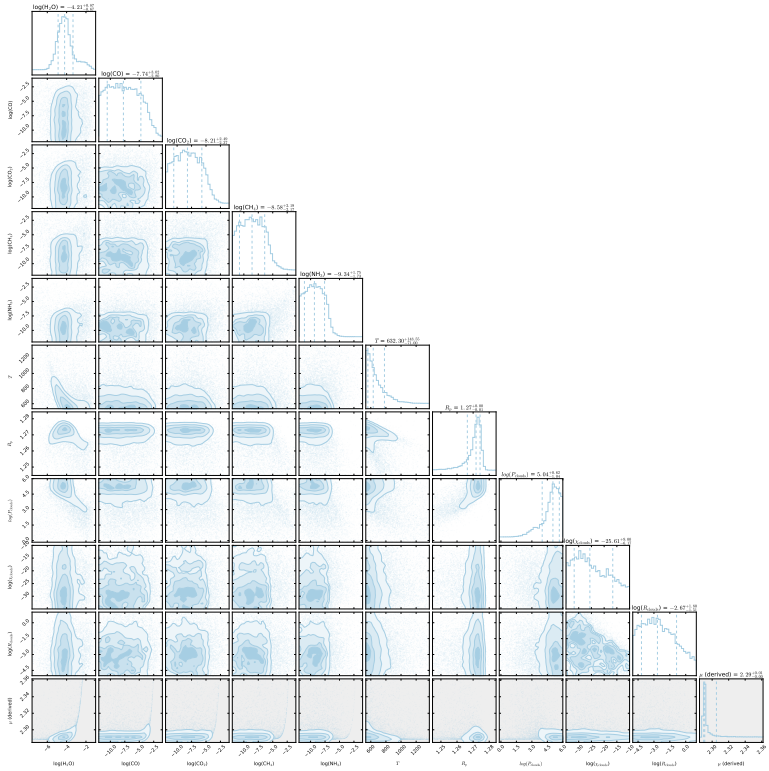

Figure A.23: The posterior distribution of the Bayesian retrieval for WASP-52 b.

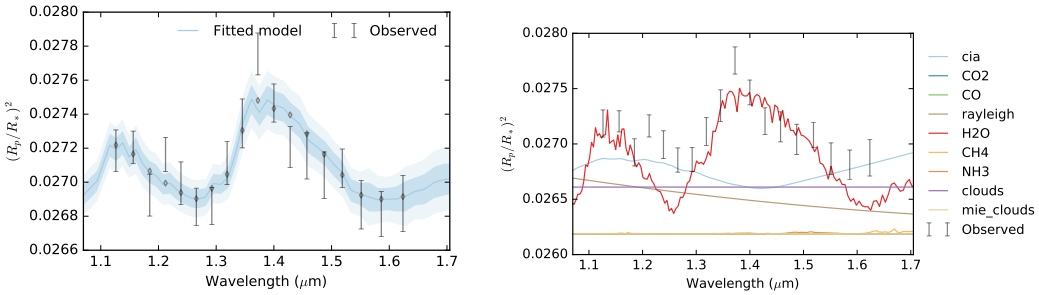

Figure A.24: Best fit spectrum for WASP-52 b transmission spectrum in low resolution (**right**) and contribution from each parameter in the model (**left**).

HD-209458 b

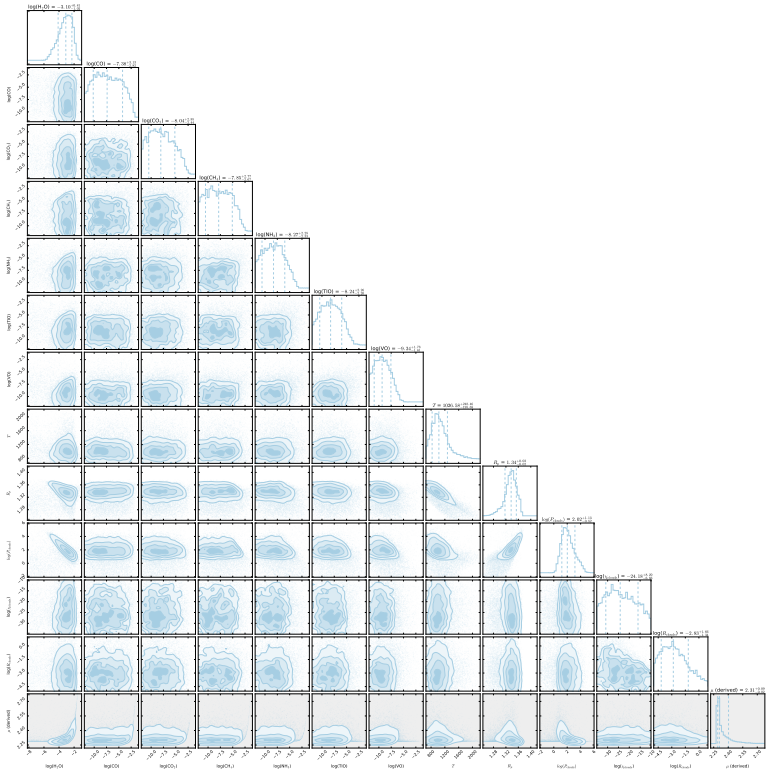

Figure A.25: The posterior distribution of the Bayesian retrieval for HD-209458 b.

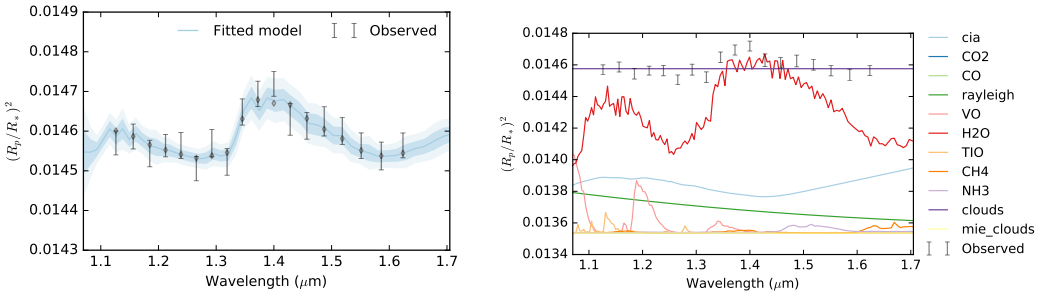

Figure A.26: Best fit spectrum for HD-209458 b transmission spectrum in low resolution (**right**) and contribution from each parameter in the model (**left**).

WASP-39 b

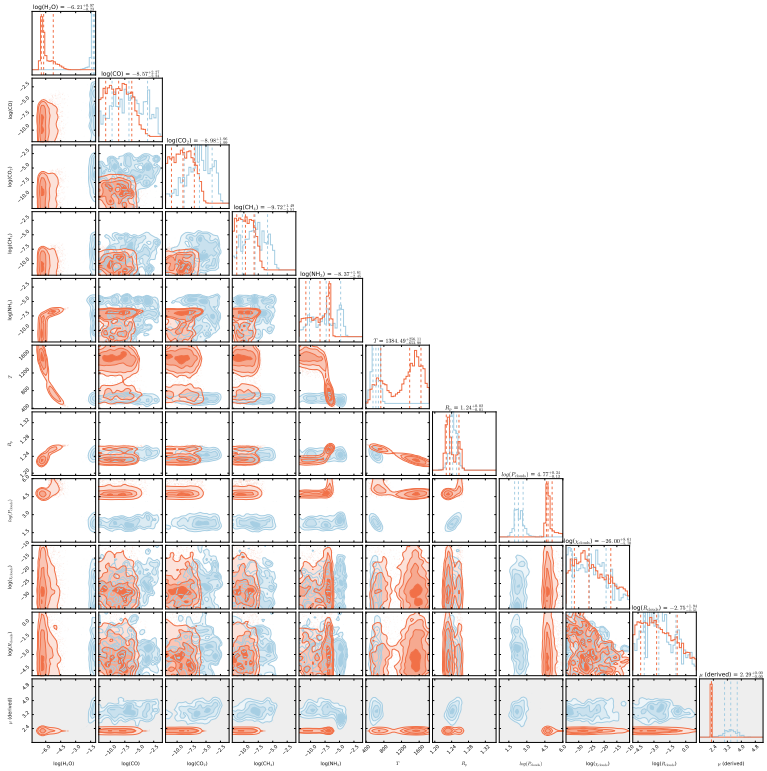

Figure A.27: The posterior distribution of the Bayesian retrieval for WASP-39 b.

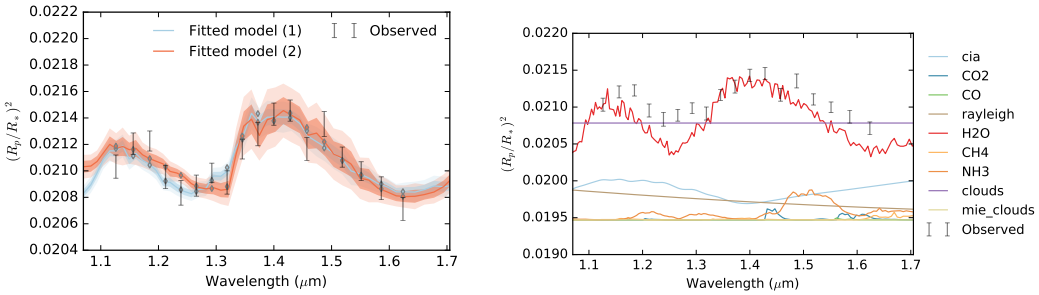

Figure A.28: Best fit spectrum for WASP-39 b transmission spectrum in low resolution (**right**) and contribution from each parameter in the model (**left**).

WASP-63 b

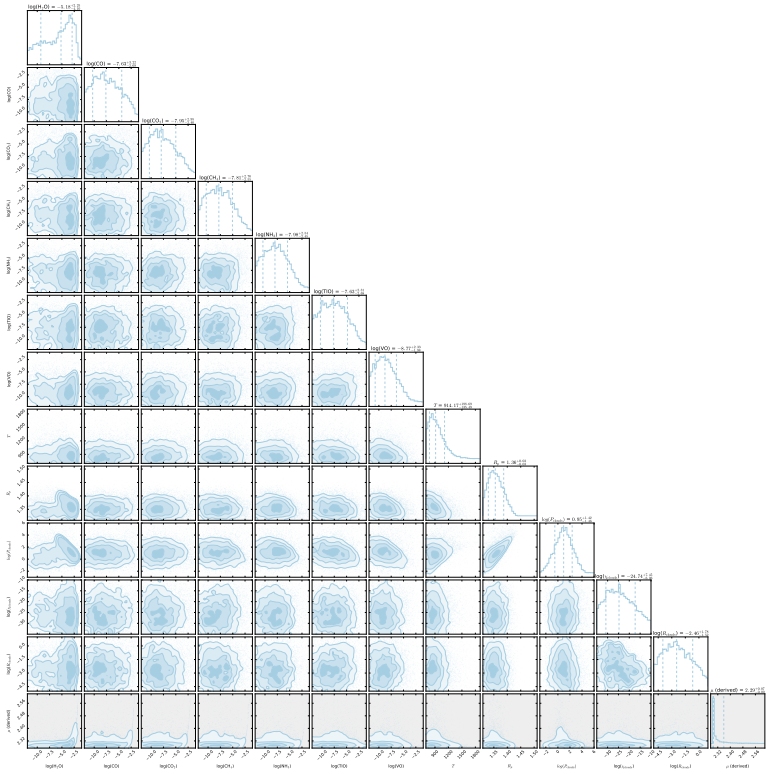

Figure A.29: The posterior distribution of the Bayesian retrieval for WASP-63 b.

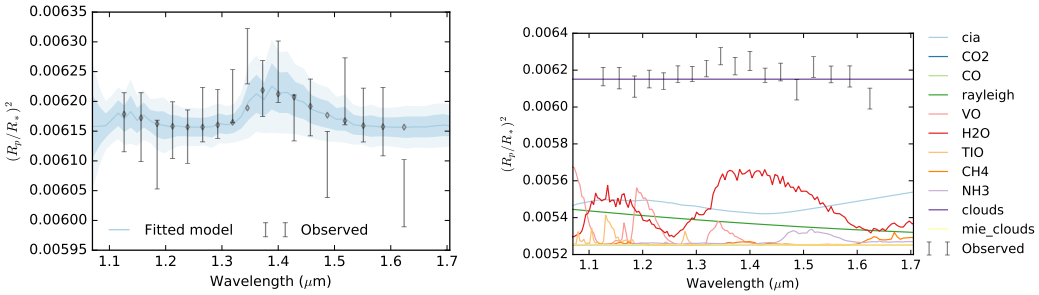

Figure A.30: Best fit spectrum for WASP-63 b transmission spectrum in low resolution (**right**) and contribution from each parameter in the model (**left**).

WASP-69 b

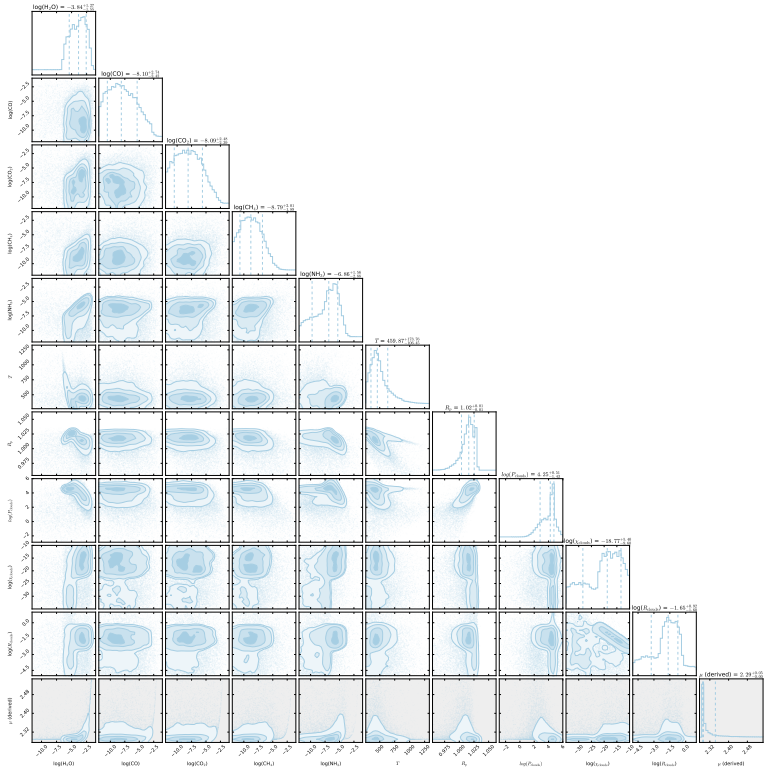

Figure A.31: The posterior distribution of the Bayesian retrieval for WASP-69 b.

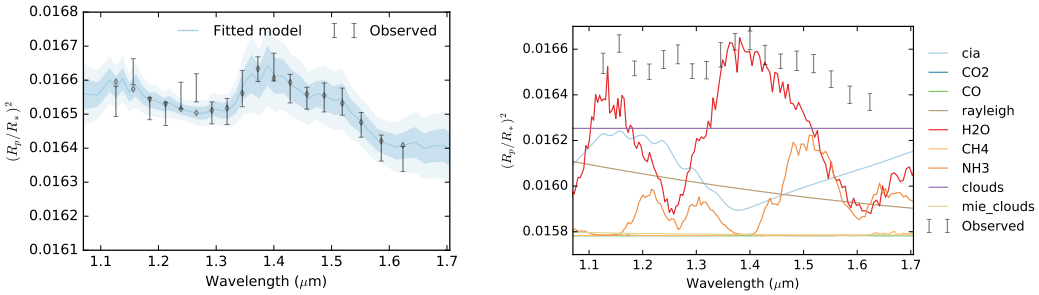

Figure A.32: Best fit spectrum for WASP-69 b transmission spectrum in low resolution (**right**) and contribution from each parameter in the model (**left**).

WASP-101 b

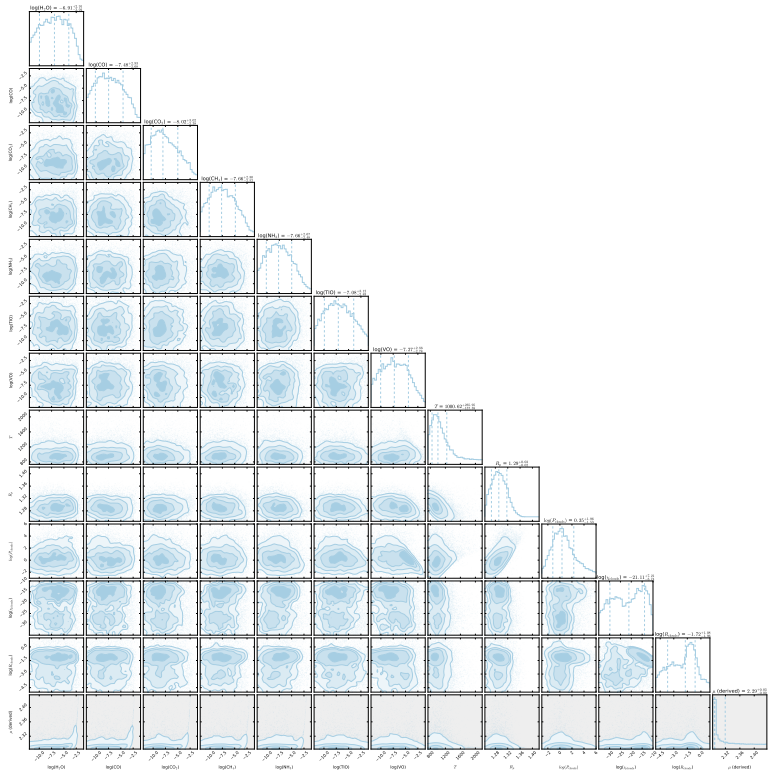

Figure A.33: The posterior distribution of the Bayesian retrieval for WASP-101 b.

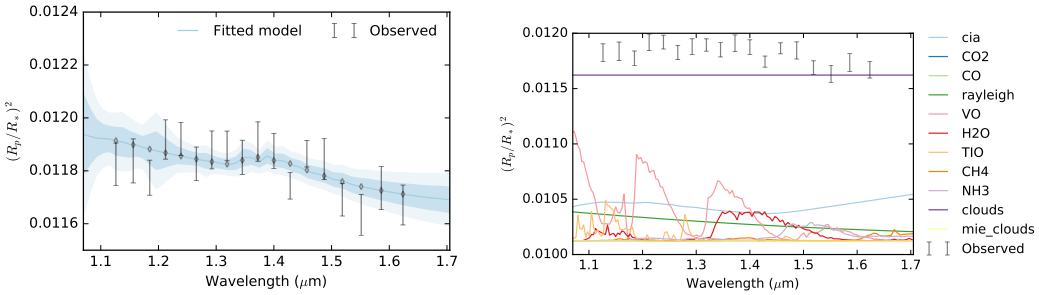

Figure A.34: Best fit spectrum for WASP-101 b transmission spectrum in low resolution (**right**) and contribution from each parameter in the model (**left**).

WASP-80 b

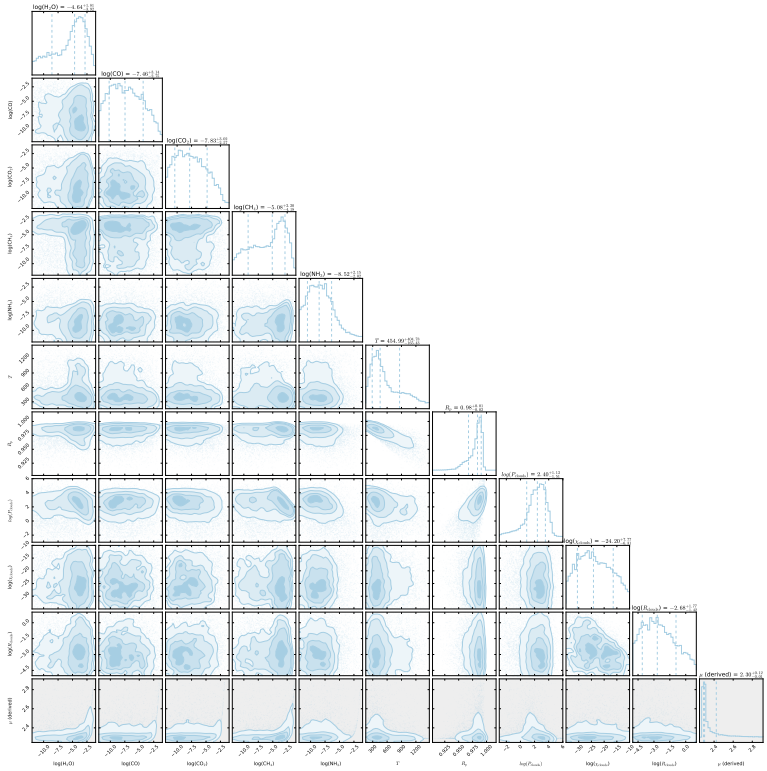

Figure A.35: The posterior distribution of the Bayesian retrieval for WASP-80 b.

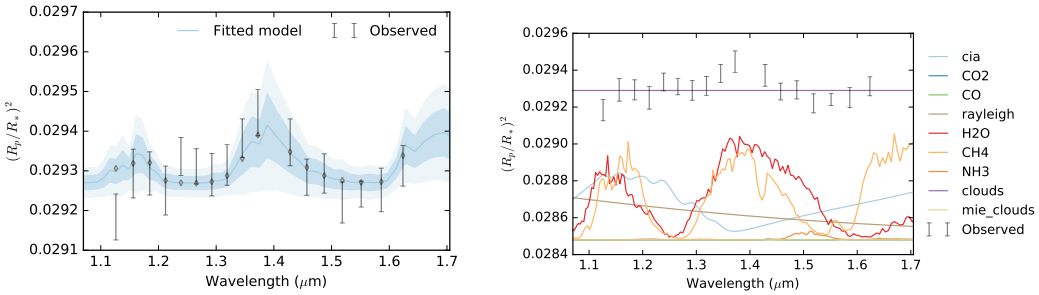

Figure A.36: Best fit spectrum for WASP-80 b transmission spectrum in low resolution (**right**) and contribution from each parameter in the model (**left**).

WASP-29 b

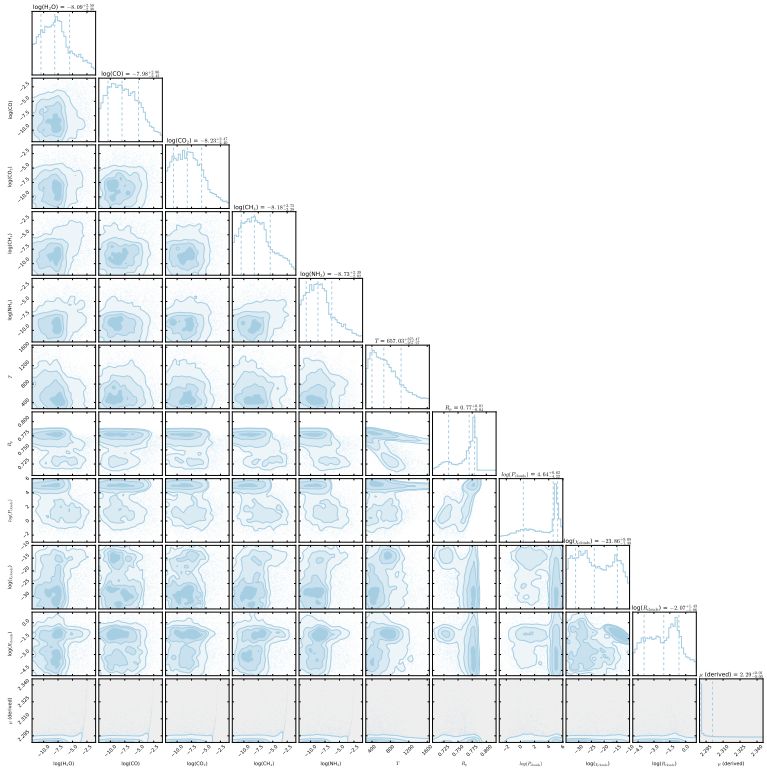

Figure A.37: The posterior distribution of the Bayesian retrieval for WASP-29 b.

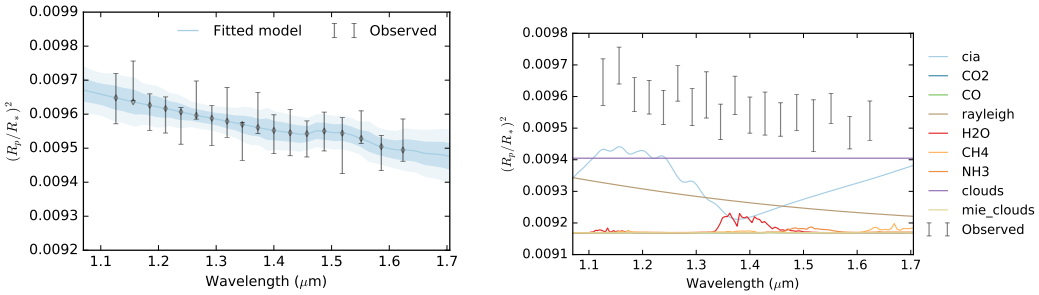

Figure A.38: Best fit spectrum for WASP-29 b transmission spectrum in low resolution (**right**) and contribution from each parameter in the model (**left**).

HD-149026 b

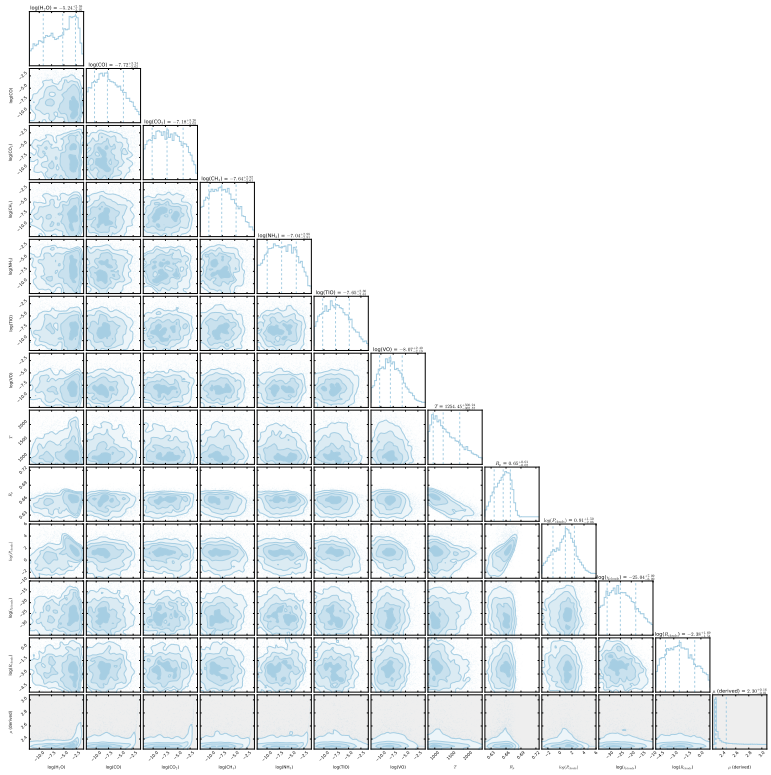

Figure A.39: The posterior distribution of the Bayesian retrieval for HD-149026 b.

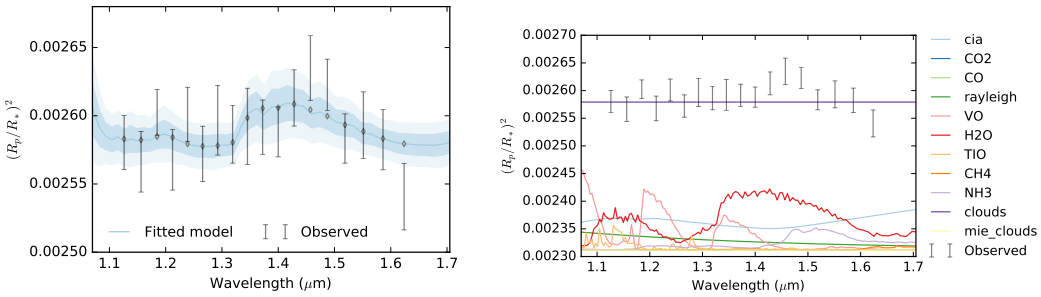

Figure A.40: Best fit spectrum for HD-149026 b transmission spectrum in low resolution (**right**) and contribution from each parameter in the model (**left**).

HATP-17 b

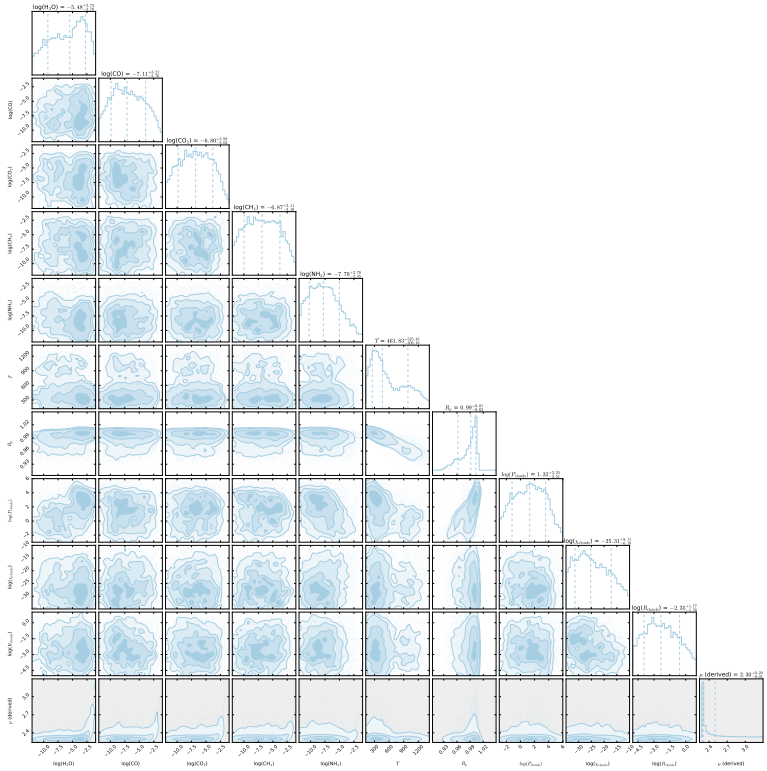

Figure A.41: The posterior distribution of the Bayesian retrieval for HATP-17 b.

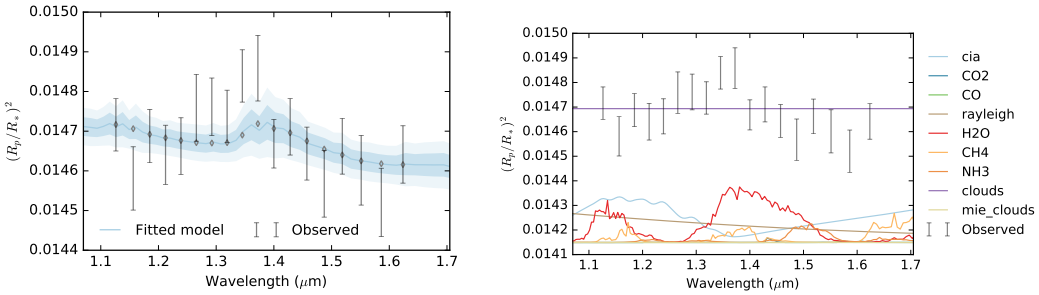

Figure A.42: Best fit spectrum for HATP-17 b transmission spectrum in low resolution (**right**) and contribution from each parameter in the model (**left**).

HATP-38 b

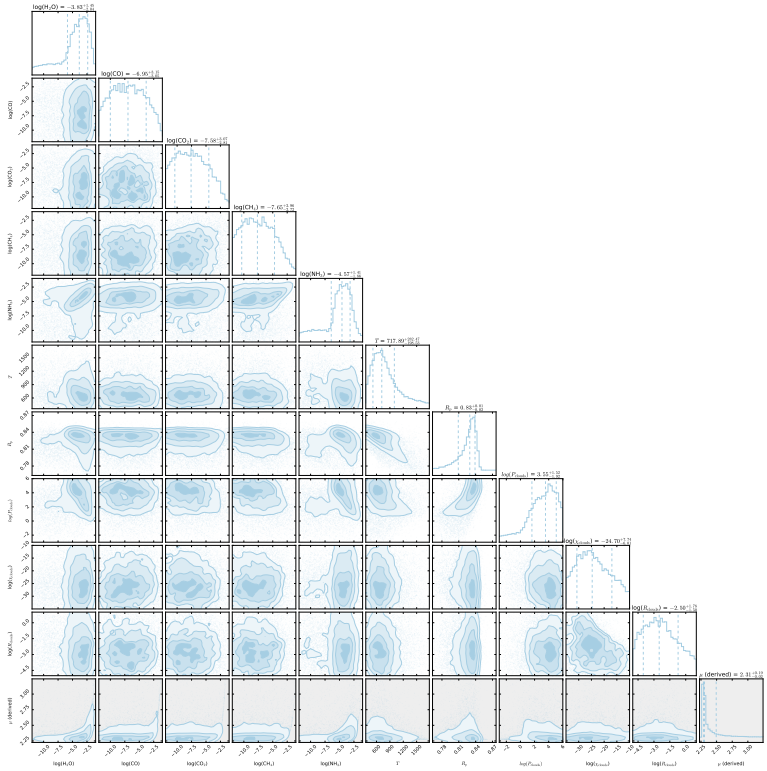

Figure A.43: The posterior distribution of the Bayesian retrieval for HATP-38 b.

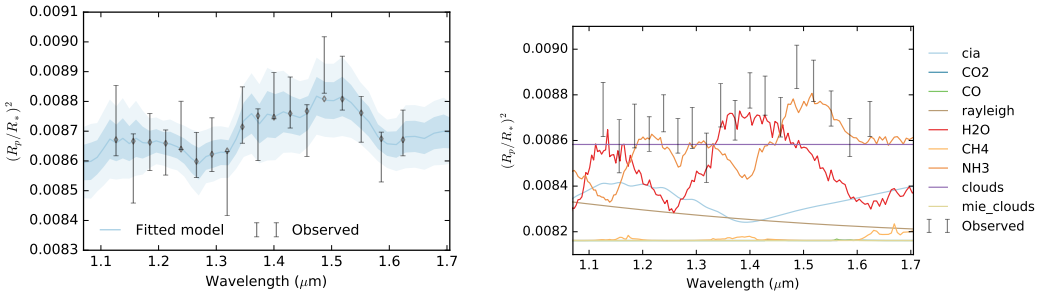

Figure A.44: Best fit spectrum for HATP-38 b transmission spectrum in low resolution (**right**) and contribution from each parameter in the model (**left**).

HATP-32 b

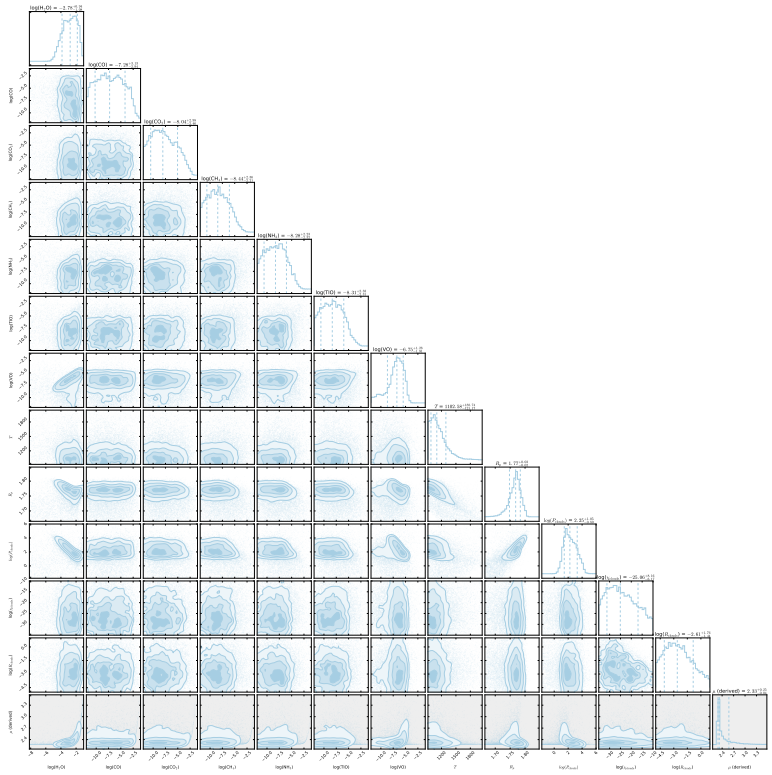

Figure A.45: The posterior distribution of the Bayesian retrieval for HATP-32 b.

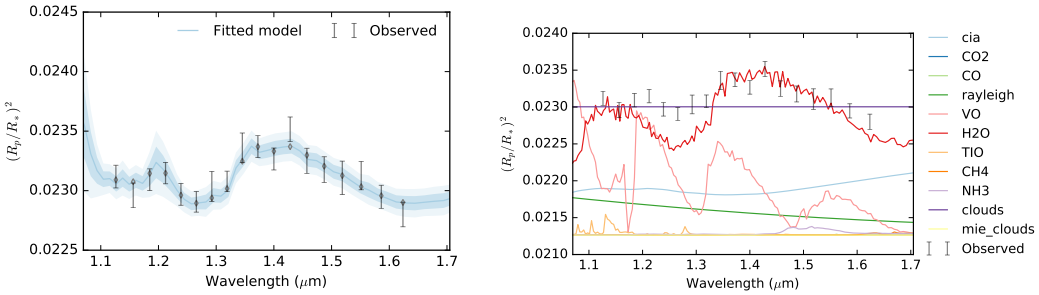

Figure A.46: Best fit spectrum for HATP-32 b transmission spectrum in low resolution (**right**) and contribution from each parameter in the model (**left**).

WASP-31 b

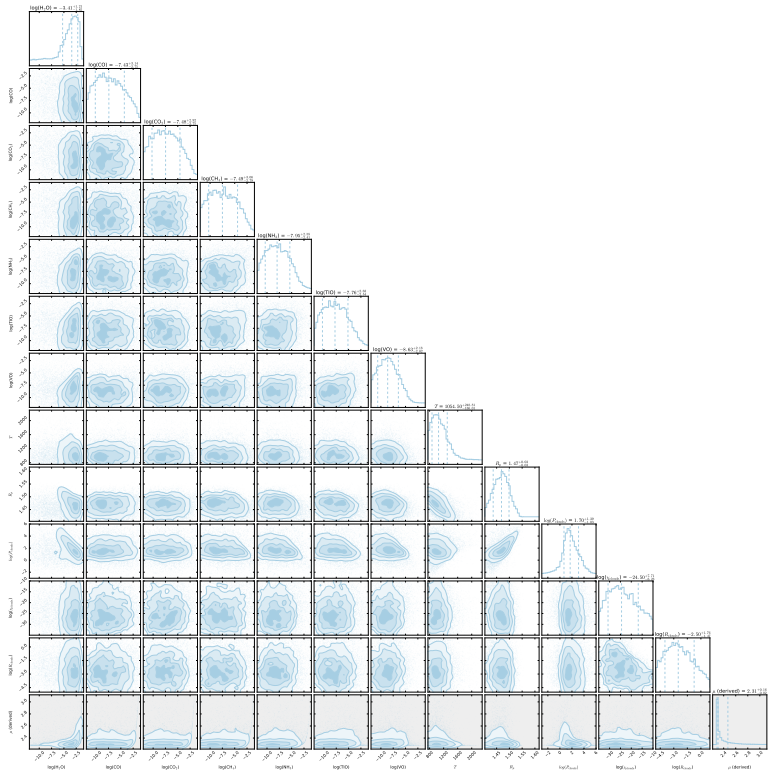

Figure A.47: The posterior distribution of the Bayesian retrieval for WASP-31 b.

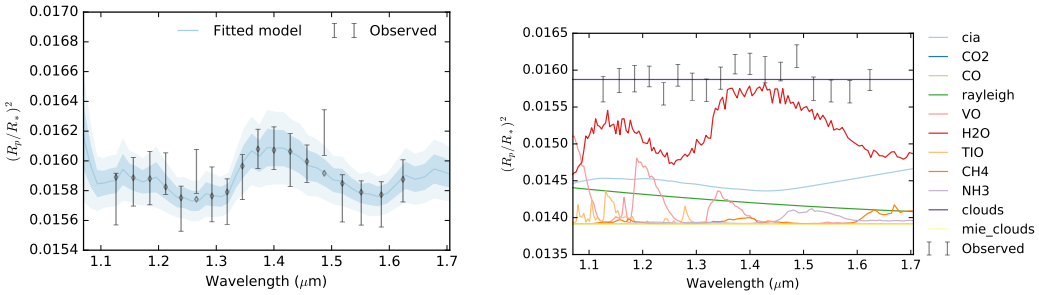

Figure A.48: Best fit spectrum for WASP-31 b transmission spectrum in low resolution (**right**) and contribution from each parameter in the model (**left**).

WASP-76 b

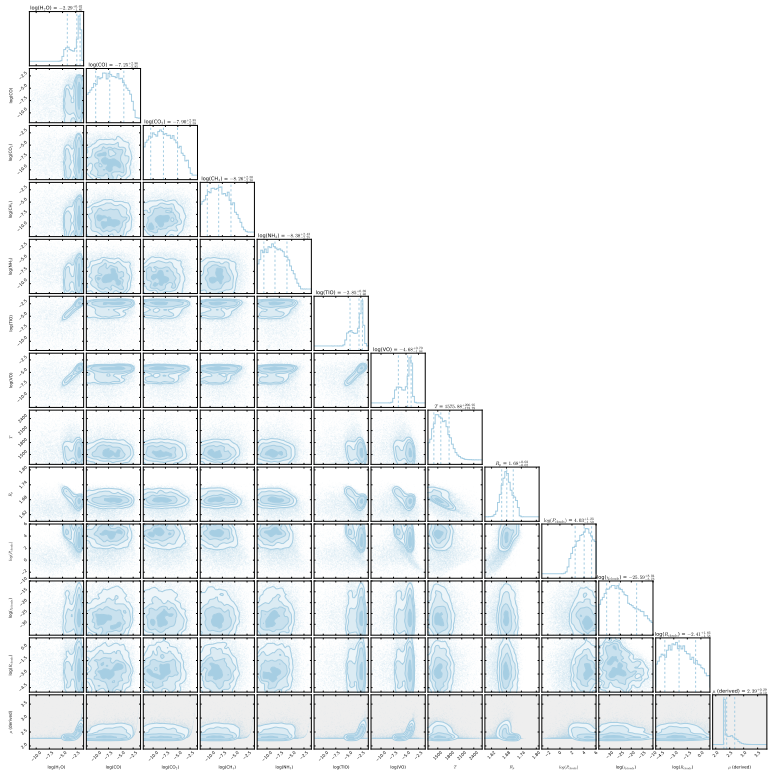

Figure A.49: The posterior distribution of the Bayesian retrieval for WASP-76 b.

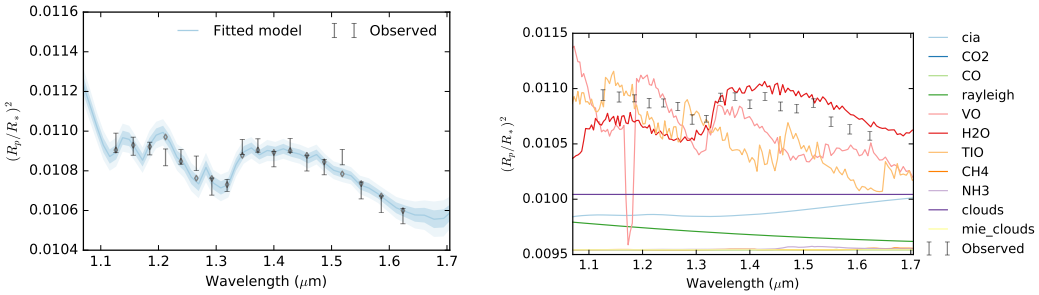

Figure A.50: Best fit spectrum for WASP-76 b transmission spectrum in low resolution (**right**) and contribution from each parameter in the model (**left**).

XO-1 b

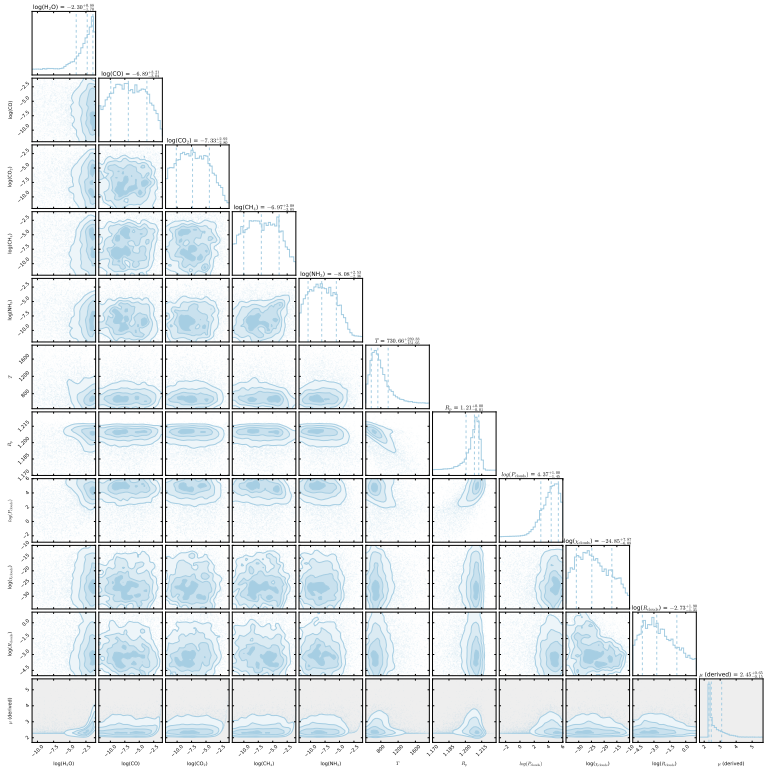

Figure A.51: The posterior distribution of the Bayesian retrieval for XO-1 b.

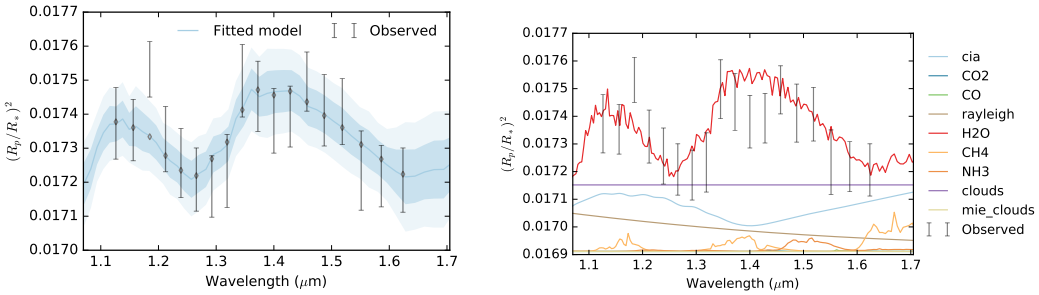

Figure A.52: Best fit spectrum for XO-1 b transmission spectrum in low resolution (**right**) and contribution from each parameter in the model (**left**).

GJ-3470 b

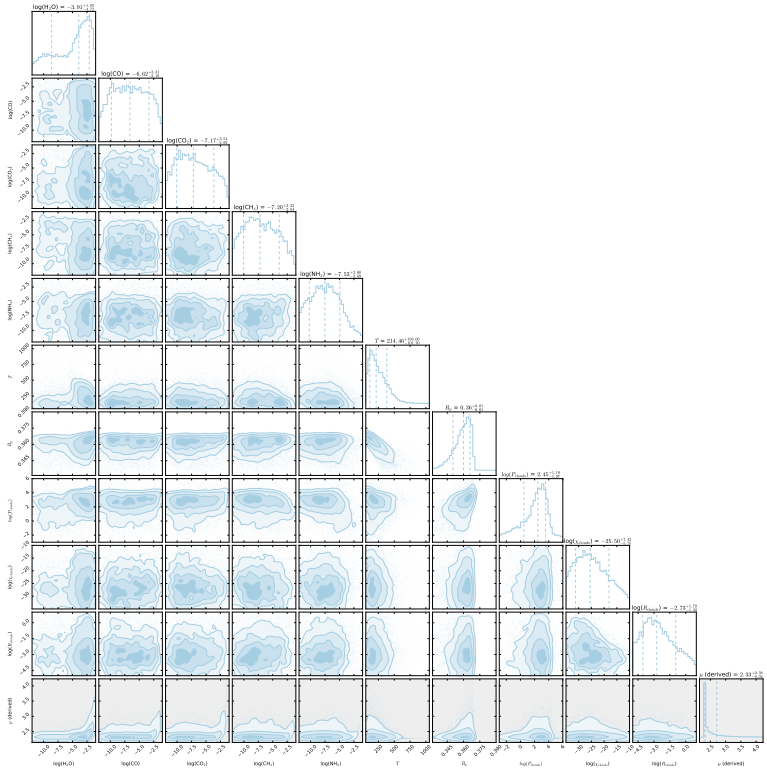

Figure A.53: The posterior distribution of the Bayesian retrieval for GJ-3470 b.

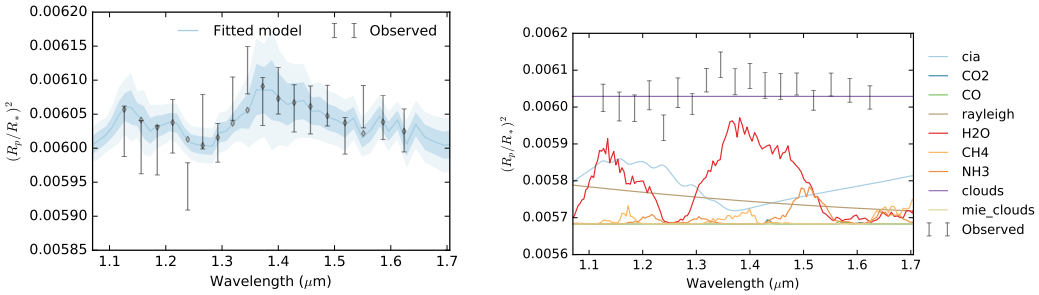

Figure A.54: Best fit spectrum for GJ-3470 b transmission spectrum in low resolution (**right**) and contribution from each parameter in the model (**left**).

HATP-1 b

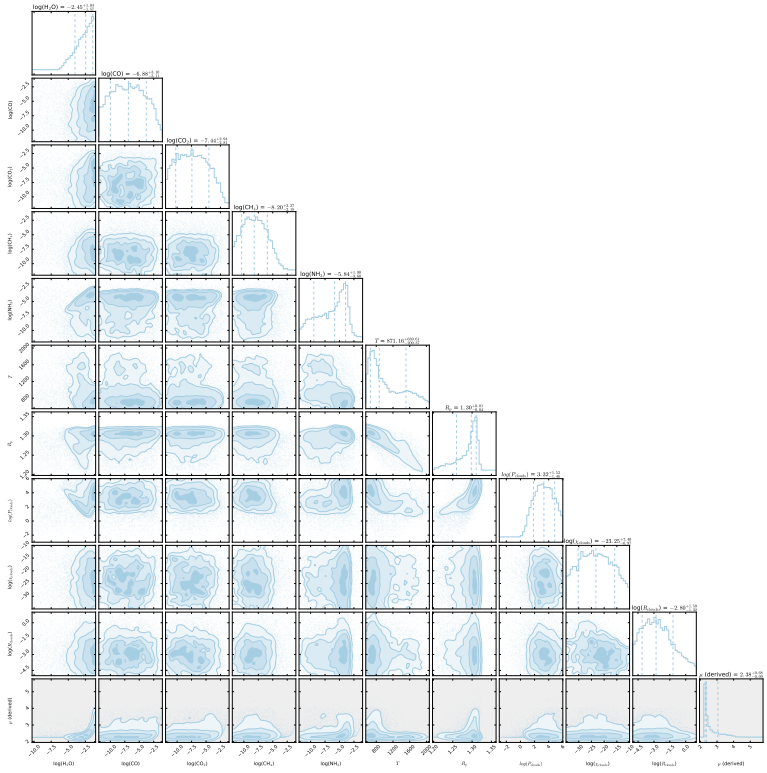

Figure A.55: The posterior distribution of the Bayesian retrieval for HATP-1 b.

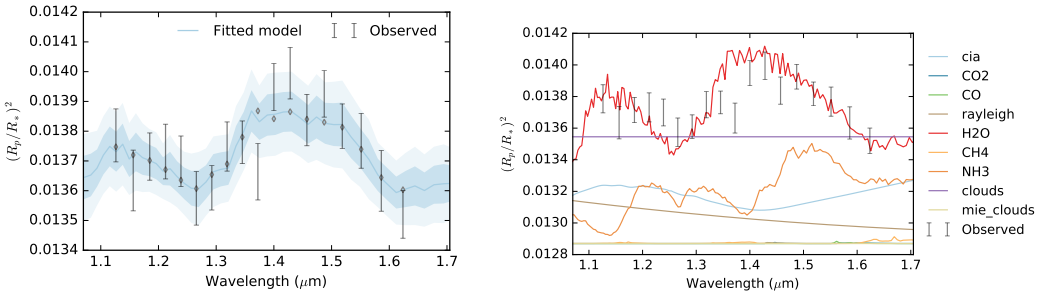

Figure A.56: Best fit spectrum for HATP-1 b transmission spectrum in low resolution (**right**) and contribution from each parameter in the model (**left**).

WASP-67 b

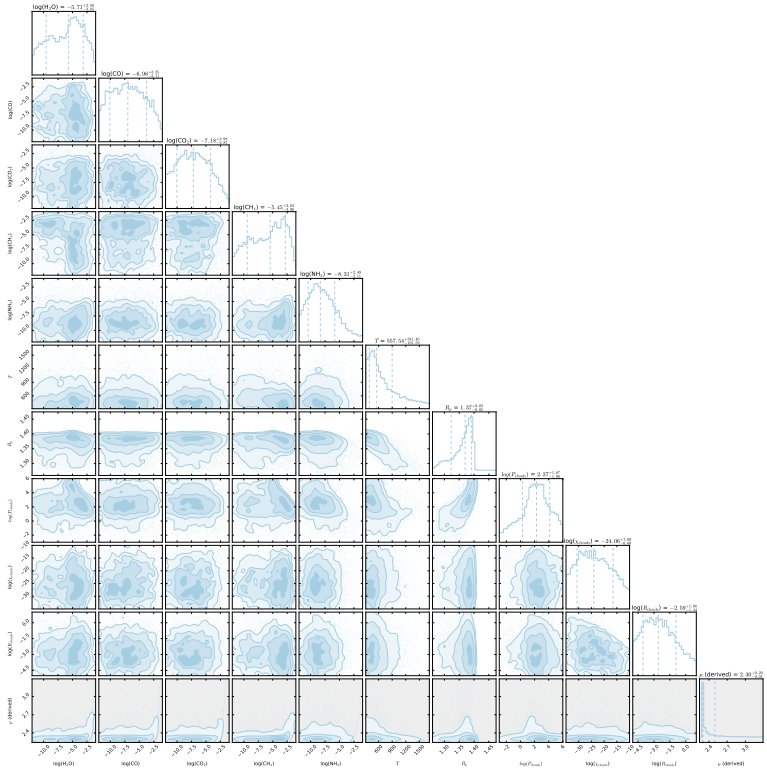

Figure A.57: The posterior distribution of the Bayesian retrieval for WASP-67 b.

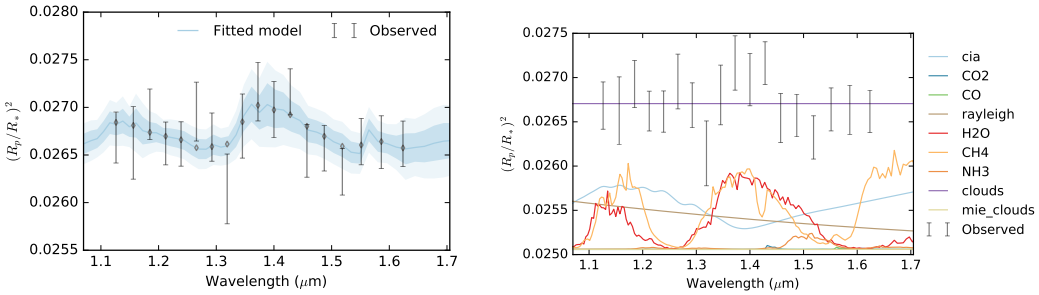

Figure A.58: Best fit spectrum for WASP-67 b transmission spectrum in low resolution (**right**) and contribution from each parameter in the model (**left**).

HATP-41 b

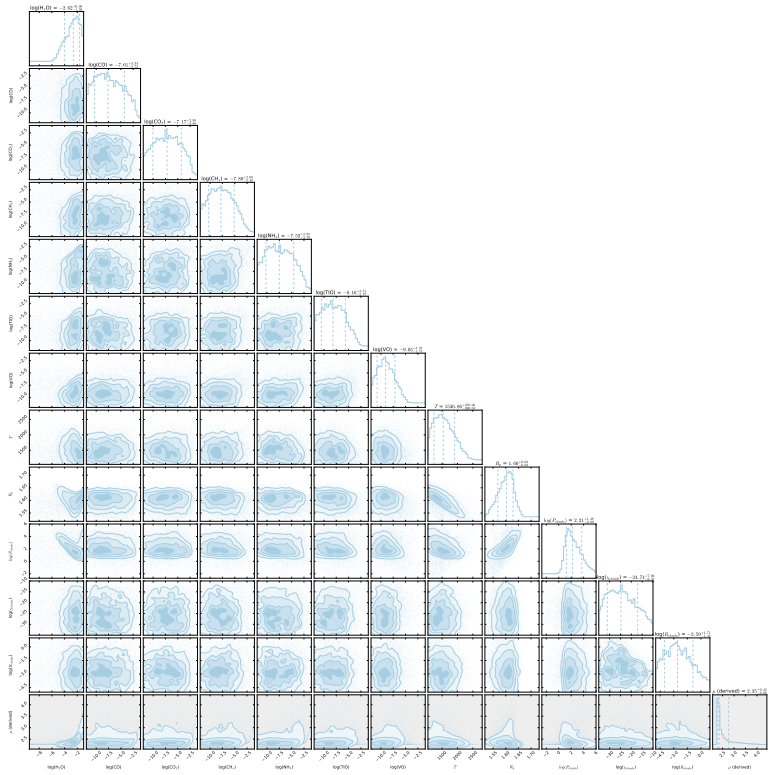

Figure A.59: The posterior distribution of the Bayesian retrieval for HATP-41 b.

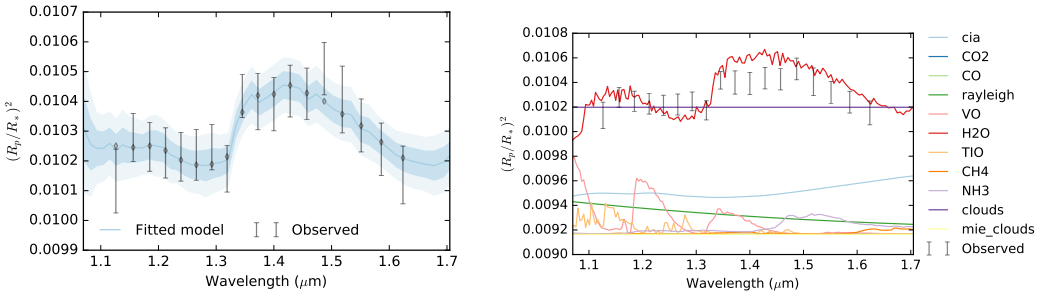

Figure A.60: Best fit spectrum for HATP-41 b transmission spectrum in low resolution (**right**) and contribution from each parameter in the model (**left**).

Appendix B

Additional material for Chapter 6

B.1 The ADAM optimiser

The Adaptive Moment Estimation (ADAM) is a very popular algorithm in deep learning and it computes adaptive learning rate for the parameters of a neural network. It stores the exponentially decaying average of past squared gradients v_t together with the exponentially decaying average of the past gradients m_t. Keeping the notation of Ruder (2016), the past and the squared past gradients, m_t and v_t are defined as:

$$m_t = \beta_1 m_{t-1} + (1 - \beta_1) g_t \tag{B.1}$$

and,

$$v_t = \beta_2 v_{t-1} + (1 - \beta_2) g_t^2, \tag{B.2}$$

with β_1 and β_2 being the decay rates, and $g_t = \nabla_{\mathbf{z}} \mathcal{L}(\mathbf{z_t})$ the gradient of the $\mathcal{L}$ function defined in Equation 6.9

Equations B.1 and B.2 estimates, respectively, the mean (or first moment) and the variance (or second moment) of the gradients. Since the two moments are initialised as vectors of 0's, they are biased towards zero, particularly during the first time steps or when the decay rates β_1 and β_2 are small. To correct the biases Kingma and Ba (2014) defined the bias-corrected moments as:

$$\hat{m}_t = \frac{m_t}{1 - \beta_1^t} \tag{B.3}$$

and,

$$\hat{v}_t = \frac{v_t}{1 - \beta_2^t}. \tag{B.4}$$

At this point it is possible to update the $\mathbf{z}$ variable using the Adam update rule:

$$\mathbf{z}_{t+1} = \mathbf{z}_t - \frac{\eta}{\sqrt{\hat{v}_t} + \varepsilon} \hat{m}_t \tag{B.5}$$

We used the values suggested by Kingma and Ba (2014) for the hyperparameters, shown in Table B.2.

B.2 Batch Normalisation

A characteristics of DCGANs is the use of batch normalisation (BN) (Ioffe and Szegedy, 2015; Xiang and Li, 2017). BN is now a common technique in deep learning applications to accelerate the training of neural networks. DCGAN networks (Radford et al., 2015) use BN for both the Discriminator and the Generator nets. Nevertheless, GAN architectures started using BN just for the generator net with the LAPGAN networks (Denton et al., 2015). Nowadays, many GAN architectures use BN. The idea behind BN is using a batch of samples $\{x_1, x_2, ..., x_m\}$ and computing, keeping the notation of Xiang and Li (2017), the following:

$$y_i = \frac{x_i - \mu_B}{\sigma_B} \cdot \gamma + \beta, \tag{B.6}$$

with μ_B, σ_B, respectively, the mean and the standard deviation of the batch and γ and β the learned parameters. BN allows to have an output with a mean μ and a standard deviation σ independently on the input distribution.

B.3 ExoGAN architecture and parameters

ExoGAN is made up of two neural networks, the generator and the discriminator, whose parameters are shown in Tab B.1.

Layer	Operation	Output	Dimension
Discriminator ($\boldsymbol{\theta}^{(D)}$)			
$\mathbf{X}$			$m \cdot 33 \cdot 33 \cdot 1$
h_0	conv	leaky relu - batch norm	$m \cdot 17 \cdot 17 \cdot 64$
h_1	conv	leaky relu - batch norm	$m \cdot 9 \cdot 9 \cdot 128$
h_2	conv	leaky relu - batch norm	$m \cdot 5 \cdot 5 \cdot 256$
h_3	conv	leaky relu - batch norm	$m \cdot 3 \cdot 3 \cdot 512$
h_4	linear	sigmoid	$m \cdot 1$
Generator ($\boldsymbol{\theta}^{(G)}$)			
$\mathbf{z}$			$m \cdot 100$
h_0	linear	relu - batch norm	$m \cdot 3 \cdot 3 \cdot 512$
h_1	deconv	relu - batch norm	$m \cdot 5 \cdot 5 \cdot 256$
h_2	deconv	relu - batch norm	$m \cdot 9 \cdot 9 \cdot 128$
h_3	deconv	relu - batch norm	$m \cdot 17 \cdot 17 \cdot 64$
h_4	deconv	sigmoid	$m \cdot 33 \cdot 33 \cdot 1$

Table B.1: Architecture of ExoGAN listing the hyperparameters $\boldsymbol{\theta}^{(D)}$ and $\boldsymbol{\theta}^{(G)}$. We used 5 layer deep networks for both Generator and Discriminators. m is the batch size fixed to 64 during training.

Hyper-parameter	*Stage*		Description
	Training	Prediction	
batch size	64	1024	Number of spectral samples used at each training/prediction iteration for both networks
$\mathbf{z}$	100	100	Generator gaussian prior distribution
η	$2 \cdot 10^{-4}$	$1 \cdot 10^{-1}$	Learning rate for the Adam optimizer
β_1	0.5	0.9	Exponential decay rate for the first moment estimates in the Adam optimizer.
β_2	-	0.999	Exponential decay rate for the second moment estimates in the Adam optimizer.
λ	-	0.1	Hyper-parameter that controls the importance of the contextual loss compared to the perceptual loss
ε	-	10^{-8}	Constant which prevents the denominator in Equation B.5 to be zero

Table B.2: Hyperparameters used in ExoGAN.

Appendix C

Additional material for Chapter 7

C.1 ESA Radiometric Model validation with ExoSim

I compare the out-of-transit signal and noise from ESA Radiometric Model (ERM) with that from ExoSim. An early version of ARIEL with a grating design was used for the instrument model in each. I model 55 Cancri and GJ 1214 with the same PHOENIX spectra in each simulator and include only photon noise and the noise floor, $N_{min}(\lambda)$, which is dominated by dark current noise. All the calculations are done per unit time and spectral bin ($R = 30$ in Ch1 and $R = 100$ in Ch0). The noise variance was compared assuming an aperture mask on the final images, and the noiseless signal per unit time was compared assuming no aperture. In the ERM, I use the following expression for N_{min} giving the noise variance:

$$N_{min}(\lambda) = \frac{2.44 f \lambda^2}{m R {\Delta_{pix}}^2} I_{dc} \tag{C.1}$$

where I_{dc} is the dark current per pixel, m is the reciprocal linear dispersion of the spectrum in μm wavelength per μm distance, R is the spectral resolving power and Δ_{pix} is the pixel pitch. The ExoSim noise variance results are the mean results from 50 simulations, with the standard deviations shown as error bars in the following figures. For 55 Cancri e case (Fig C.1), overall wavelength bins, the ERM signal is always within 2% of ExoSim, and the averaged noise variance within 5% of the ERM. In 94% of the bins, the ERM noise variance is within the standard deviation from ExoSim.

For GJ 1214 (Fig C.2), the ERM signal is within 4% of ExoSim over all bins, and the averaged noise variance within 6% of ExoSim over all bins. The ERM noise variance is always within the

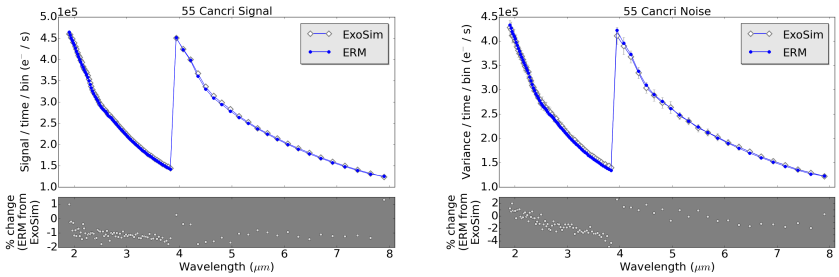

Figure C.1: Comparison between the out-of-transit signal (left) and noise (right) simulated by ExoSim (white points) and the ESA Radiometric Model (blue points) for the star 55 Cancri. Subplots show the percent difference of the ERM from ExoSim.

standard deviation from ExoSim over all bins.

There is, therefore, a good agreement between the two simulators.

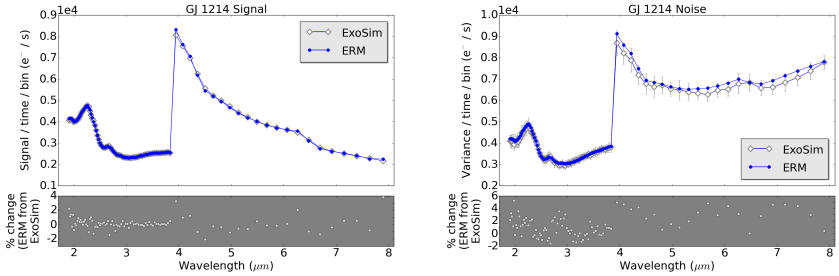

Figure C.2: Comparison between the out-of-transit signal (left) and noise (right) simulated by ExoSim (white points) and the ESA Radiometric Model (blue points) for the star GJ 1214. Subplots show the percent difference of the ERM from ExoSim.

C.2 Known planets observable by ARIEL

#	Planet	planetary properties				stellar properties		Observation	
		R ($R_\oplus$)	M ($M_\oplus$)	P (days)	T (K)	R ($R_\odot$)	T (K)	#	type
1	55 Cnc e	1.88	8.07	0.74	1891	0.95	5196	1	transit
2	EPIC 204129699 b	15.47	563.97	1.26	1473	0.91	5280	1	transit
3	WASP-52 b	13.94	146.24	1.75	1267	0.87	5000	1	transit
4	HD 189733 A b	12.49	361.78	2.22	1180	0.80	4980	1	transit
5	WASP-77 A b	13.28	559.52	1.36	1762	1.00	5500	1	transit
6	WASP-85 A b	16.24	387.85	2.66	1341	1.04	5685	1	transit
7	WASP-33 b	15.78	1459.19	1.22	2541	1.50	7200	1	occultation
8	WASP-19 b	15.21	371.32	0.79	1998	0.97	5500	1	occultation
9	WASP-95 b	13.28	359.23	2.18	1521	1.11	5630	1	transit
10	WASP-121 b	19.83	376.08	1.27	2295	1.35	6459	1	transit
11	WASP-12 b	19.05	446.34	1.09	2399	1.35	6118	1	occultation
12	WASP-35 b	14.48	228.89	3.16	1414	1.07	5990	1	transit
13	HAT-P-30 b	14.70	226.03	2.81	1594	1.24	6304	1	transit
14	WASP-108 b	14.09	283.57	2.68	1558	1.17	6000	2	transit
15	HD 209458 b	15.14	226.99	3.52	1401	1.15	6075	1	transit
16	WASP-122 b	21.64	436.17	1.71	1900	1.40	5720	1	transit
17	WASP-2 A b	12.26	290.57	2.15	1276	0.89	5255	2	transit
18	HAT-P-32 b	22.35	299.15	2.15	1850	1.18	6207	1	transit
19	WASP-43 b	11.37	646.62	0.81	1403	0.72	4520	1	occultation
20	WASP-123 b	14.56	292.47	2.98	1477	1.21	5740	1	transit
21	WASP-101 b	15.47	158.95	3.59	1518	1.34	6400	1	transit
22	WASP-74 b	17.12	302.01	2.14	1872	1.48	5990	1	transit
23	WASP-76 b	20.08	292.47	1.81	2125	1.46	6250	1	transit
24	WASP-1 b	16.27	271.49	2.52	1777	1.24	6160	1	occultation
25	KELT-10 b	15.35	215.86	4.17	1340	1.11	5948	1	transit
26	KELT-3 b	14.90	464.78	2.70	1774	1.28	6304	1	transit
27	WASP-62 b	15.25	181.21	4.41	1389	1.25	6230	1	transit
28	HD 149026 b	7.88	113.17	2.88	1699	1.30	6147	1	transit
29	WASP-97 b	12.40	419.64	2.07	1500	1.12	5640	2	occultation
30	WASP-94 A b	18.87	143.69	3.95	1464	1.29	6170	1	transit
31	HAT-P-8 b	14.50	405.33	3.08	1687	1.19	6200	1	occultation
32	WASP-54 b	18.14	202.19	3.69	1531	1.15	6100	1	transit
33	WASP-109 b	15.83	289.30	3.32	1729	0.91	6520	1	transit
34	HAT-P-41 b	18.49	254.33	2.69	1886	1.42	6390	1	transit
35	HAT-P-13 b	14.05	270.22	2.92	1600	1.22	5638	1	transit
36	KELT-15 b	15.83	289.30	3.33	1500	1.18	6003	2	transit
37	KELT-7 b	16.82	406.92	2.73	1996	1.53	6789	1	transit
38	HAT-P-6 b	14.59	336.03	3.85	1629	1.29	6570	2	transit
39	WASP-49 b	12.24	120.17	2.78	1334	0.94	5600	1	transit
40	WASP-15 b	15.67	172.31	3.75	1609	1.18	6300	1	transit
41	WASP-79 b	18.65	286.12	3.66	1709	1.56	6600	1	transit
42	KELT-4A b	18.64	286.75	2.99	1779	1.20	6206	1	transit
43	WASP-17 b	21.85	154.50	3.74	1725	1.31	6650	1	transit
44	WASP-3 b	15.96	654.89	1.85	1933	1.24	6400	1	occultation
45	WASP-7 b	14.59	305.19	4.95	1448	1.28	6400	1	transit
46	KELT-8 b	20.41	275.63	3.24	1633	1.21	5754	1	transit
47	HAT-P-22 b	11.85	682.55	3.21	1248	0.92	5302	3	transit
48	WASP-13 b	15.44	158.95	4.35	1494	1.19	5989	1	transit
49	HAT-P-33 b	20.05	242.56	3.47	1799	1.40	6446	1	transit
50	TrES-4 A b	20.17	157.05	3.55	1644	1.45	6295	1	transit

#	Planet	planetary properties				stellar properties		Observation	
		R ($R_\oplus$)	M ($M_\oplus$)	P (days)	T (K)	R ($R_\odot$)	T (K)	#	type
51	WASP-82 b	18.33	394.20	2.71	2127	1.63	6490	1	transit
52	WASP-31 b	16.87	151.96	3.41	1502	1.16	6200	1	transit
53	HAT-P-45 b	15.65	283.57	3.13	1605	1.26	6330	2	transit
54	KELT-2A b	14.33	472.41	4.11	1671	1.31	6148	1	transit
55	WASP-26 b	14.06	326.81	2.76	1618	1.12	5950	2	occultation
56	TrES-2	12.83	398.34	2.47	1458	0.98	5850	4	transit
57	WASP-50 b	12.62	467.32	1.96	1354	0.89	5400	5	transit
58	WASP-63 b	15.69	120.80	4.38	1496	1.32	5570	1	transit
59	XO-2N b	10.68	189.79	2.62	1312	0.97	5332	2	transit
60	WASP-104 b	12.48	404.38	1.76	1476	1.08	5475	3	occultation
61	WASP-41 b	13.28	292.47	3.05	1278	0.95	5450	2	transit
62	HAT-P-40 b	18.98	195.51	4.46	1719	1.51	6080	1	transit
63	WASP-48 b	18.33	311.55	2.14	1980	1.19	5920	1	occultation
64	HAT-P-4 b	13.94	216.18	3.06	1653	1.26	5890	2	transit
65	WASP-4 b	14.96	356.53	1.34	1818	0.93	5500	1	occultation
66	WASP-103 b	17.59	467.32	0.93	2430	1.20	6110	1	occultation
67	WASP-75 b	13.94	340.16	2.48	1660	1.14	6100	2	occultation
68	Qatar-1 b	12.77	422.82	1.42	1347	0.85	4910	5	occultation
69	WASP-20 b	16.00	99.50	4.90	1345	1.20	5950	1	transit
70	TrES-3 b	14.32	607.20	1.31	1654	0.88	5720	1	occultation
71	PTFO 8-8695 b	20.96	953.72	0.45	1884	0.34	3470	1	occultation
72	HAT-P-1 b	13.35	166.58	4.47	1259	1.13	5975	1	transit
73	WASP-90 b	17.89	200.28	3.92	1791	1.55	6430	2	transit
74	HAT-P-46 b	14.09	156.73	4.47	1413	1.28	6120	1	transit
75	WASP-111 b	15.82	581.77	2.31	2065	1.50	6400	1	occultation
76	XO-1 b	12.99	286.12	3.94	1216	1.00	5940	1	transit
77	WASP-34 b	13.39	187.57	4.32	1131	1.01	5700	1	transit
78	WASP-88 b	18.65	178.03	4.95	1716	1.45	6431	1	transit
79	HATS-3 b	18.62	361.78	3.55	1757	1.30	6351	2	occultation
80	WASP-100 b	18.54	645.35	2.85	2143	1.57	6900	1	occultation
81	WASP-68 b	13.61	302.01	5.08	1447	1.24	5911	2	transit
82	CoRoT-2 b	16.08	1052.27	1.74	1484	0.97	5575	1	occultation
83	HAT-P-49 b	15.51	549.98	2.69	2072	1.54	6820	1	occultation
84	HAT-P-56 b	16.09	693.04	2.79	1791	1.30	6566	1	occultation
85	HAT-P-7 b	16.01	543.30	2.20	2141	1.59	6310	1	occultation
86	WASP-21 b	12.75	87.74	4.32	1298	0.89	5800	1	transit
87	WASP-22 b	12.71	186.93	3.53	1383	1.10	6000	2	transit
88	WASP-24 b	12.11	328.08	2.34	1611	1.13	6075	4	occultation
89	WASP-25 b	13.83	184.39	3.76	1209	1.00	5750	1	transit
90	HAT-P-5 b	13.74	336.98	2.79	1477	1.16	5960	6	transit
91	WASP-69 b	11.60	82.66	3.87	938	0.83	4715	1	transit
92	WASP-87 b	15.20	693.04	1.68	2251	1.20	6450	1	occultation
93	HAT-P-24 b	13.63	217.77	3.36	1581	1.19	6329	4	transit
94	HAT-P-39 b	17.24	190.43	3.54	1705	1.40	6430	3	transit
95	WASP-16 b	11.06	271.81	3.12	1235	1.02	5550	4	transit
96	TrES-1 b	12.06	241.93	3.03	1147	0.88	5250	2	transit
97	WASP-64 b	13.95	404.06	1.57	1587	0.98	5400	3	occultation
98	WASP-6 b	13.43	159.91	3.36	1161	0.89	5450	1	transit
99	WASP-55 b	14.27	181.21	4.47	1236	1.01	5900	1	transit
100	HAT-P-36 b	13.87	582.41	1.33	1778	1.02	5580	1	occultation

#	Planet	planetary properties				stellar properties		Observation	
		R ($R_\oplus$)	M ($M_\oplus$)	P (days)	T (K)	R ($R_\odot$)	T (K)	#	type
101	HAT-P-9 b	15.36	213.00	3.92	1490	1.28	6350	4	transit
102	HAT-P-14 b	13.17	699.40	4.63	1525	1.39	6600	3	occultation
103	WASP-28 b	13.31	288.34	3.41	1429	1.02	6150	6	transit
104	XO-4 b	14.70	546.80	4.13	1418	1.32	5700	6	occultation
105	WASP-58 b	15.03	282.94	5.02	1242	0.94	5800	2	transit
106	HAT-P-23 b	15.01	664.43	1.21	1997	1.13	5905	1	occultation
107	Qatar-2 b	12.55	790.63	1.34	1256	0.74	4645	9	occultation
108	WASP-5 b	12.85	520.41	1.63	1693	1.00	5700	2	occultation
109	WASP-65 b	12.20	492.76	2.31	1446	0.93	5600	7	occultation
110	CoRoT-1 b	16.35	327.44	1.51	1839	0.95	6298	1	occultation
111	HAT-P-27 b	11.19	197.10	3.04	1161	0.92	5300	3	transit
112	KELT-6 b	12.95	140.51	7.85	1284	1.13	6272	1	transit
113	WASP-45 b	12.73	320.13	3.13	1165	0.91	5140	6	transit
114	WASP-72 b	11.08	448.25	2.22	1819	1.23	6250	2	occultation
115	HATS-1 b	14.29	589.72	3.45	1332	0.99	5870	14	transit
116	WASP-78 b	19.20	368.77	2.18	2136	2.02	6100	1	occultation
117	WASP-96 b	13.17	152.60	3.43	1251	1.06	5540	3	transit
118	HAT-P-28 b	13.30	199.01	3.26	1345	1.02	5680	6	transit
119	WASP-39 b	13.94	89.01	4.06	1088	0.93	5400	1	transit
120	WASP-80 b	10.45	176.12	3.07	794	0.57	4145	1	transit
121	HATS-2 b	12.82	427.58	1.35	1528	0.88	5227	5	occultation
122	WASP-71 b	16.02	712.75	2.90	1987	1.56	6050	1	occultation
123	WASP-38 b	11.96	861.53	6.87	1218	1.23	6150	10	transit
124	WASP-110 b	13.58	162.13	3.78	1113	0.89	5400	1	transit
125	HAT-P-3 b	9.07	187.88	2.90	1115	0.92	5224	4	transit
126	WASP-47 b	12.84	336.98	4.16	1240	1.04	5576	8	transit
127	WASP-98 b	12.07	263.86	2.96	1149	0.69	5525	8	transit
128	WASP-46 b	14.38	667.92	1.43	1615	0.96	5620	3	occultation
129	HAT-P-25 b	13.06	180.22	3.65	1172	1.01	5500	3	transit
130	WASP-18 b	12.78	3315.77	0.94	2345	1.24	6400	1	occultation
131	WASP-67 b	15.36	133.52	4.61	1000	0.87	5200	1	transit
132	WASP-14 b	14.06	2333.75	2.24	1834	1.21	6462	1	occultation
133	WASP-60 b	9.44	163.40	4.31	1261	0.51	5900	6	transit
134	WASP-11 b	11.47	146.24	3.72	1002	0.82	4974	1	transit
135	HAT-P-35 b	14.62	335.07	3.65	1537	1.24	6096	12	occultation
136	WASP-36 b	13.93	724.51	1.54	1655	1.02	5881	3	occultation
137	HAT-P-50 b	14.13	429.17	3.12	1805	1.27	6280	3	occultation
138	WASP-99 b	12.07	883.78	5.75	1438	1.48	6180	6	occultation
139	HAT-P-42 b	14.01	309.96	4.64	1389	1.18	5743	13	transit
140	WASP-73 b	12.73	597.66	4.09	1736	1.34	6036	3	occultation
141	WASP-135 b	14.27	604.02	1.40	1673	0.98	5675	3	occultation
142	WASP-23 b	10.56	281.03	2.94	1099	0.78	5150	10	transit
143	TrES-5 b	13.27	565.24	1.48	1433	0.88	5171	10	occultation
144	HAT-P-16 b	13.06	1332.98	2.78	1527	1.22	6140	3	occultation
145	Kepler-12 b	19.20	136.70	4.44	1341	1.09	5953	2	transit
146	Kepler-7 b	17.71	137.65	4.89	1584	1.36	5933	4	transit
147	WASP-44 b	11.00	276.26	2.42	1275	0.92	5410	28	transit
148	XO-5 b	11.30	342.39	4.19	1206	0.88	5510	16	transit
149	HAT-P-43 b	14.08	209.82	3.33	1322	1.05	5645	12	transit
150	HAT-P-55 b	12.97	185.02	3.58	1278	1.01	5808	10	transit

#	Planet	planetary properties				stellar properties		Observation	
		R ($R_\oplus$)	M ($M_\oplus$)	P (days)	T (K)	R ($R_\odot$)	T (K)	#	type
151	WASP-32 b	13.06	1144.46	2.72	1507	1.10	6100	5	occultation
152	HAT-P-29 b	12.15	247.33	5.72	1224	1.21	6087	8	transit
153	WASP-10 b	11.85	972.79	3.09	1009	0.71	4675	37	transit
154	Kepler-6 b	14.27	213.00	3.23	1354	1.05	5640	15	transit
155	HD219134b	1.61	4.47	3.09	934	0.78	4699	1	transit
156	HATS-13 b	13.30	172.62	3.04	1212	0.96	5523	10	transit
157	HAT-P-51 b	14.19	98.23	4.22	1159	0.98	5449	2	transit
158	HAT-P-34 b	13.14	1057.99	5.45	1440	1.39	6442	10	occultation
159	WASP-37 b	12.47	539.17	3.58	1293	0.85	5800	43	transit
160	WASP-56 b	11.98	181.52	4.62	1117	1.03	5600	4	transit
161	WASP-66 b	15.25	737.54	4.09	1754	1.30	6600	3	occultation
162	WASP-112 b	13.07	279.76	3.04	1349	0.81	5610	28	transit
163	HAT-P-44 b	14.05	124.62	4.30	1092	0.94	5295	2	transit
164	HAT-P-37 b	12.93	371.63	2.80	1166	0.93	5500	37	transit
165	Gliese 436 b	4.13	23.11	2.64	695	0.45	3684	1	transit
166	WASP-29 b	8.69	77.57	3.92	970	0.82	4800	1	transit
167	HD 219134 b	1.57	3.81	3.09	931	0.79	4699	1	transit
168	HAT-P-12 b	10.52	67.08	3.21	932	0.73	4650	1	transit
169	Kepler-13 A b	15.43	2571.87	1.76	2389	1.72	7200	1	occultation
170	HAT-P-19 b	12.17	92.83	4.01	982	0.84	4990	1	transit
171	CoRoT-11 b	15.25	791.59	2.99	1686	1.27	6440	5	occultation
172	Kepler-8 b	15.58	187.57	3.52	1528	1.13	6251	20	transit
173	HATS-10 b	10.63	167.22	3.31	1369	1.10	5880	28	transit
174	WTS-2 b	14.96	356.06	1.02	1495	0.82	5000	16	occultation
175	HAT-P-52 b	11.07	260.05	2.75	1184	0.89	5131	43	transit
176	HAT-P-20 b	9.51	2303.55	2.88	946	0.76	4595	97	occultation
177	WASP-120 b	16.62	1592.71	3.61	1842	1.45	6450	1	occultation
178	HATS-9 b	11.69	266.09	1.92	1769	1.03	5366	9	occultation
179	CoRoT-19 b	15.91	352.88	3.90	1616	1.21	6090	16	occultation
180	OGLE-TR-10 b	18.87	216.18	3.10	1554	1.28	6075	16	occultation
181	WASP-42 b	11.85	158.95	4.98	969	0.88	5200	1	transit
182	WASP-61 b	13.61	654.89	3.86	1509	1.22	6250	17	occultation
183	HAT-P-31 b	11.74	690.18	5.01	1343	1.22	6065	43	occultation
184	HAT-P-53 b	14.46	471.77	1.96	1624	1.09	5956	7	occultation
185	WASP-8 b	11.39	713.38	8.16	906	1.03	5600	6	transit
186	HATS-4 b	11.19	420.59	2.52	1282	1.00	5403	97	occultation
187	Kepler-447 b	18.11	435.53	7.79	908	0.76	5493	2	transit
188	Kepler-76 b	14.92	638.99	1.54	2074	1.20	6409	2	occultation
189	WASP-57 b	10.05	213.63	2.84	1430	1.01	5600	43	occultation
190	CoRoT-5 b	15.23	148.46	4.04	1315	1.00	6100	15	transit
191	HD 17156 b	12.02	1014.44	21.22	816	1.27	6079	9	transit
192	Kepler-412 b	14.54	298.51	1.72	1780	1.17	5750	12	occultation
193	XO-3 b	13.35	3748.12	3.19	1665	1.21	6429	1	occultation
194	WASP-117 b	11.20	87.58	10.02	997	1.13	6040	1	transit
195	Gliese 1214 b	2.77	6.20	1.58	552	0.18	3250	1	transit
196	Gliese 3470 b	3.80	13.73	3.34	635	0.51	3652	1	transit
197	HAT-P-11 b	4.96	25.75	4.89	848	0.81	4780	1	transit
198	GJ 1132 b	1.16	1.62	1.63	529	0.18	3270	1	transit
199	Gliese 436 c	0.66	0.28	1.37	813	0.45	3684	1	transit
200	HAT-P-26 b	6.20	18.76	4.23	967	0.82	5079	1	transit
201	HAT-P-18 b	10.39	62.31	5.51	818	0.77	4870	1	transit
202	HD 97658 b	2.34	7.55	9.49	729	0.77	5119	1	transit
203	HAT-P-17 b	11.08	169.76	10.34	758	0.86	5246	1	transit
204	WASP-84 b	10.70	222.53	8.52	780	0.85	5280	1	transit
205	HATS-6 b	10.95	101.41	3.33	693	0.57	3724	1	transit
206	EPIC 203771098 c	7.93	27.02	42.36	596	1.12	5743	1	transit
207	KOI-142 b	4.13	1.76	10.95	764	1.02	5513	1	transit
208	HATS-5 b	10.01	75.34	4.76	998	0.94	5304	1	transit
209	Kepler-51 b	6.95	2.10	45.15	496	1.04	6018	1	transit
210	HAT-P-2 b	10.44	2778.51	5.63	1443	1.36	6290	1	occultation

Table C.1: List of known planets observable by ARIEL. The former to last column represents the number of transits/eclipses necessary to fulfil the ARIEL Tier 1 goals.

Bibliography

E. R. Adams, S. Seager, and L. Elkins-Tanton. Ocean Planet or Thick Atmosphere: On the Mass-Radius Relationship for Solid Exoplanets with Massive Atmospheres. *ApJ*, 673:1160–1164, February 2008. doi: 10.1086/524925.

R. L. Akeson, X. Chen, D. Ciardi, M. Crane, J. Good, M. Harbut, E. Jackson, S. R. Kane, A. C. Laity, S. Leifer, M. Lynn, D. L. McElroy, M. Papin, P. Plavchan, S. V. Ramírez, R. Rey, K. von Braun, M. Wittman, M. Abajian, B. Ali, C. Beichman, A. Beekley, G. B. Berriman, S. Berukoff, G. Bryden, B. Chan, S. Groom, C. Lau, A. N. Payne, M. Regelson, M. Saucedo, M. Schmitz, J. Stauffer, P. Wyatt, and A. Zhang. The NASA Exoplanet Archive: Data and Tools for Exoplanet Research. *Publications of the ASP*, 125:989, August 2013. doi: 10.1086/672273.

Saleh Albelwi and Ausif Mahmood. A framework for designing the architectures of deep convolutional neural networks. *Entropy*, 19(6), 2017.

Michael E Alfaro, Stefan Zoller, and François Lutzoni. Bayes or bootstrap? a simulation study comparing the performance of bayesian markov chain monte carlo sampling and bootstrapping in assessing phylogenetic confidence. *Molecular Biology and Evolution*, 20(2):255–266, 2003.

J. M. Almenara, F. Bouchy, P. Gaulme, M. Deleuil, M. Havel, D. Gandolfi, H. J. Deeg, G. Wuchterl, T. Guillot, B. Gardes, T. Pasternacki, S. Aigrain, R. Alonso, M. Auvergne, A. Baglin, A. S. Bonomo, P. Borde, J. Cabrera, S. Carpano, W. D. Cochran, Sz. Csizmadia, C. Damiani, R. F. Diaz, R. Dvorak, M. Endl, A. Erikson, S. Ferraz-Mello, M. Fridlund, G. Hébrard, M. Gillon, E. Guenther, A. Hatzes, A. Léger, H. Lammer, P. J. MacQueen, T. Mazeh, C. Moutou, M. Ollivier, A. Ofir, M. Paetzold, H. Parviainen, D. Queloz, H. Rauer, D. Rouan, A. Santerne, B. Samuel, J. Schneider, L. Tal-Or, B. Tingley, and J. Weingrill. Transiting exoplanets from the corot space mission. *Astronomy and Astrophysics - A&A*, 555, July 2013. doi: 10.1051/0004-6361/201321462. URL `https://hal.archives-ouvertes.fr/hal-01441496`.

Brandon Amos. Image Completion with Deep Learning in TensorFlow. `http://bamos.github.io/2016/08/09/deep-completion`, 2016. Accessed: 12/05/2018.

D. R. Anderson, A. Collier Cameron, C. Hellier, M. Lendl, T. A. Lister, P. F. L. Maxted, D. Queloz, B. Smalley, A. M. S. Smith, A. H. M. J. Triaud, R. G. West, D. J. A. Brown, M. Gillon, F. Pepe, D. Pollacco, D. Ségransan, R. A. Street, and S. Udry. WASP-31b: a low-density planet transiting a metal-poor, late-F-type dwarf star. *A&A*, 531:A60, July 2011. doi: 10.1051/0004-6361/201016208.

D. R. Anderson, A. Collier Cameron, L. Delrez, A. P. Doyle, F. Faedi, A. Fumel, M. Gillon, Y. Gómez Maqueo Chew, C. Hellier, E. Jehin, M. Lendl, P. F. L. Maxted, F. Pepe, D. Pollacco, D. Queloz, D. Ségransan, I. Skillen, B. Smalley, A. M. S. Smith, J. Southworth, A. H. M. J. Triaud, O. D. Turner, S. Udry, and R. G. West. Three newly discovered sub-Jupiter-mass planets: WASP-69b and WASP-84b transit active K dwarfs and WASP-70Ab transits the evolved primary of a G4+K3 binary. *MNRAS*, 445:1114–1129, December 2014. doi: 10.1093/mnras/stu1737.

James A. Anderson. *An Introduction to Neural Networks*. MIT Press, Cambridge, MA, USA, 1st edition, 1995.

M. Arjovsky and L. Bottou. Towards Principled Methods for Training Generative Adversarial Networks. *ArXiv e-prints*, January 2017.

É. Artigau, J. F. Donati, and X. Delfosse. Planet Detection, Magnetic Field of Protostars and Brown Dwarfs Meteorology with SPIRou. In Christopher Johns-Krull, Matthew K. Browning, and Andrew A. West, editors, *16th Cambridge Workshop on Cool Stars, Stellar Systems, and the Sun*, volume 448, page 771, December 2011.

G. Á. Bakos, R. W. Noyes, G. Kovács, D. W. Latham, D. D. Sasselov, G. Torres, D. A. Fischer, R. P. Stefanik, B. Sato, J. A. Johnson, A. Pál, G. W. Marcy, R. P. Butler, G. A. Esquerdo, K. Z. Stanek, J. Lázár, I. Papp, P. Sári, and B. Sipőcz. HAT-P-1b: A Large-Radius, Low-Density Exoplanet Transiting One Member of a Stellar Binary. *ApJ*, 656:552–559, February 2007. doi: 10.1086/509874.

G. Á. Bakos, G. Torres, A. Pál, J. Hartman, G. Kovács, R. W. Noyes, D. W. Latham, D. D. Sasselov, B. Sipőcz, G. A. Esquerdo, D. A. Fischer, J. A. Johnson, G. W. Marcy, R. P. Butler, H. Isaacson, A. Howard, S. Vogt, G. Kovács, J. Fernandez, A. Moór, R. P. Stefanik, J. Lázár, I. Papp, and P. Sári. HAT-P-11b: A Super-Neptune Planet Transiting a Bright K Star in the Kepler Field. *ApJ*, 710:1724–1745, February 2010. doi: 10.1088/0004-637X/710/2/1724.

Pierre Baldi and Peter Sadowski. The dropout learning algorithm. *Artif. Intell.*, 210:78–122, May 2014. ISSN 0004-3702. doi: 10.1016/j.artint.2014.02.004. URL `http://dx.doi.org/10.1016/j.artint.2014.02.004`.

I. Baraffe, G. Chabrier, F. Allard, and P. H. Hauschildt. Evolutionary models for solar metallicity low-mass stars: mass-magnitude relationships and color-magnitude diagrams. *A&A*, 337:403–412, September 1998.

R. J. Barber, J. Tennyson, G. J. Harris, and R. N. Tolchenov. A high-accuracy computed water line list. *MNRAS*, 368:1087–1094, May 2006. doi: 10.1111/j.1365-2966.2006.10184.x.

T. Barclay, J. Pepper, and E. V. Quintana. A Revised Exoplanet Yield from the Transiting Exoplanet Survey Satellite (TESS). *ArXiv e-prints*, April 2018.

J. K. Barstow and P. G. J. Irwin. Habitable worlds with JWST: transit spectroscopy of the TRAPPIST-1 system? *MNRAS*, 461:L92–L96, September 2016. doi: 10.1093/mnrasl/slw109.

J. K. Barstow, S. Aigrain, P. G. J. Irwin, L. N. Fletcher, and J.-M. Lee. Constraining the atmosphere of GJ 1214b using an optimal estimation technique. *MNRAS*, 434:2616–2628, September 2013. doi: 10.1093/mnras/stt1204.

J. K. Barstow, S. Aigrain, P. G. J. Irwin, S. Kendrew, and L. N. Fletcher. Erratum: Transit spectroscopy with JWST: systematics, star-spots and stitching. *MNRAS*, 451:1306–1306, August 2015. doi: 10.1093/mnras/stv1041.

J. K. Barstow, S. Aigrain, P. G. J. Irwin, and D. K. Sing. A Consistent Retrieval Analysis of 10 Hot Jupiters Observed in Transmission. *ApJ*, 834:50, January 2017. doi: 10.3847/1538-4357/834/1/50.

N. Batalha, J. Kalirai, J. Lunine, M. Clampin, and D. Lindler. Transiting Exoplanet Simulations with the James Webb Space Telescope. *ArXiv e-prints*, July 2015.

J L Bean, Eliza Miller-Ricci Kempton, and D Homeier. A ground-based transmission spectrum of the super-Earth exoplanet GJ 1214b. *Nature*, 468(7):669–672, December 2010.

C. Beichman, B. Benneke, H. Knutson, R. Smith, P.-O. Lagage, C. Dressing, D. Latham, J. Lunine, S. Birkmann, P. Ferruit, G. Giardino, E. Kempton, S. Carey, J. Krick, P. D. Deroo, A. Mandell, M. E. Ressler, A. Shporer, M. Swain, G. Vasisht, G. Ricker, J. Bouwman, I. Crossfield, T. Greene, S. Howell, J. Christiansen, D. Ciardi, M. Clampin, M. Greenhouse, A. Sozzetti, P. Goudfrooij, D. Hines, T. Keyes, J. Lee, P. McCullough, M. Robberto, J. Stansberry, J. Valenti, M. Rieke, G. Rieke, J. Fortney, J. Bean, L. Kreidberg, D. Ehrenreich,

D. Deming, L. Albert, R. Doyon, and D. Sing. Observations of Transiting Exoplanets with the James Webb Space Telescope (JWST). *Publications of the ASP*, 126:1134, December 2014. doi: 10.1086/679566.

Yoshua Bengio. *Learning Deep Architectures for AI*, volume 2. Now Publishers Inc, 2009.

B. Benneke and S. Seager. Atmospheric Retrieval for Super-Earths: Uniquely Constraining the Atmospheric Composition with Transmission Spectroscopy. *ApJ*, 753:100, July 2012a. doi: 10.1088/0004-637X/753/2/100.

B. Benneke and S. Seager. Atmospheric Retrieval for Super-Earths: Uniquely Constraining the Atmospheric Composition with Transmission Spectroscopy. *ApJ*, 753:100, July 2012b. doi: 10.1088/0004-637X/753/2/100.

B. Benneke and S. Seager. How to Distinguish between Cloudy Mini-Neptunes and Water/Volatile-dominated Super-Earths. *ApJ*, 778:153, December 2013. doi: 10.1088/0004-637X/778/2/153.

Björn Benneke and Sara Seager. How to Distinguish between Cloudy Mini-Neptunes and Water/Volatile-dominated Super-Earths. *APJ*, 778(2):153, December 2013.

A Berg, J Deng, and L Fei-Fei. Large scale visual recognition challenge (ilsvrc), 2010. *URL http://www. image-net. org/challenges/LSVRC*, 3, 2010.

Zachory K Berta, D Charbonneau, Jean-Michel Desert, E Miller-Ricci Kempton, Peter R McCullough, Christopher J Burke, J Fortney, Jonathan Irwin, Philip Nutzman, and D Homeier. The Flat Transmission Spectrum of the Super-Earth GJ1214b from Wide Field Camera 3 on the Hubble Space Telescope. *Nature*, 747(1):35, March 2012.

J.-L. Beuzit, M. Feldt, K. Dohlen, D. Mouillet, P. Puget, F. Wildi, L. Abe, J. Antichi, A. Baruffolo, P. Baudoz, A. Boccaletti, M. Carbillet, J. Charton, R. Claudi, M. Downing, C. Fabron, P. Feautrier, E. Fedrigo, T. Fusco, J.-L. Gach, R. Gratton, T. Henning, N. Hubin, F. Joos, M. Kasper, M. Langlois, R. Lenzen, C. Moutou, A. Pavlov, C. Petit, J. Pragt, P. Rabou, F. Rigal, R. Roelfsema, G. Rousset, M. Saisse, H.-M. Schmid, E. Stadler, C. Thalmann, M. Turatto, S. Udry, F. Vakili, and R. Waters. SPHERE: a 'Planet Finder' instrument for the VLT. In *Ground-based and Airborne Instrumentation for Astronomy II*, volume 7014 of *Proc. SPIE*, page 701418, July 2008. doi: 10.1117/12.790120.

L. I. Biddle, K. A. Pearson, I. J. M. Crossfield, B. J. Fulton, S. Ciceri, J. Eastman, T. Barman, A. W. Mann, G. W. Henry, A. W. Howard, M. H. Williamson, E. Sinukoff, D. Dragomir,

L. Vican, L. Mancini, J. Southworth, A. Greenberg, J. D. Turner, R. Thompson, B. W. Taylor, S. E. Levine, and M. W. Webber. Warm ice giant GJ 3470b - II. Revised planetary and stellar parameters from optical to near-infrared transit photometry. *MNRAS*, 443:1810–1820, September 2014. doi: 10.1093/mnras/stu1199.

J. L. Birkby, R. J. de Kok, M. Brogi, E. J. W. de Mooij, H. Schwarz, S. Albrecht, and I. A. G. Snellen. Detection of water absorption in the day side atmosphere of HD 189733 b using ground-based high-resolution spectroscopy at 3.2μm. *MNRAS*, 436:L35–L39, November 2013. doi: 10.1093/mnrasl/slt107.

J. L. Birkby, R. J. de Kok, M. Brogi, H. Schwarz, and I. A. G. Snellen. Discovery of Water at High Spectral Resolution in the Atmosphere of 51 Peg b. *AJ*, 153:138, March 2017. doi: 10.3847/1538-3881/aa5c87.

Stephan M. Birkmann, Pierre Ferruit, Tim Rawle, Marco Sirianni, Catarina Alves de Oliveira, Torsten Böker, Giovanna Giardino, Nora Lützgendorf, Anthony Marston, Martin Stuhlinger, Maurice B. J. te Plate, Peter Jensen, Peter Rumler, Bernhard Dorner, Hermann Karl, Peter Mosner, Raymond H. Wright, and Robert Rapp. The JWST/NIRSpec instrument: update on status and performances. In *Space Telescopes and Instrumentation 2016: Optical, Infrared, and Millimeter Wave*, volume 9904, page 99040B, July 2016. doi: 10.1117/12.2231837.

W.M. Bolstad. *Introduction to Bayesian Statistics (Wiley-Interscience)*. 2007.

W. J. Borucki, D. Koch, G. Basri, N. Batalha, T. Brown, D. Caldwell, J. Caldwell, J. Christensen-Dalsgaard, W. D. Cochran, E. DeVore, E. W. Dunham, A. K. Dupree, T. N. Gautier, J. C. Geary, R. Gilliland, A. Gould, S. B. Howell, J. M. Jenkins, Y. Kondo, D. W. Latham, G. W. Marcy, S. Meibom, H. Kjeldsen, J. J. Lissauer, D. G. Monet, D. Morrison, D. Sasselov, J. Tarter, A. Boss, D. Brownlee, T. Owen, D. Buzasi, D. Charbonneau, L. Doyle, J. Fortney, E. B. Ford, M. J. Holman, S. Seager, J. H. Steffen, W. F. Welsh, J. Rowe, H. Anderson, L. Buchhave, D. Ciardi, L. Walkowicz, W. Sherry, E. Horch, H. Isaacson, M. E. Everett, D. Fischer, G. Torres, J. A. Johnson, M. Endl, P. MacQueen, S. T. Bryson, J. Dotson, M. Haas, J. Kolodziejczak, J. Van Cleve, H. Chandrasekaran, J. D. Twicken, E. V. Quintana, B. D. Clarke, C. Allen, J. Li, H. Wu, P. Tenenbaum, E. Verner, F. Bruhweiler, J. Barnes, and A. Prsa. Kepler Planet-Detection Mission: Introduction and First Results. *Science*, 327:977, February 2010. doi: 10.1126/science.1185402.

A. Borysow. Collision-induced absorption coefficients of H_2 pairs at temperatures from 60 K to 1000 K. *A&A*, 390:779–782, August 2002. doi: 10.1051/0004-6361:20020555.

A. Borysow, U. G. Jorgensen, and Y. Fu. High-temperature (1000-7000 K) collision-induced absorption of H“2 pairs computed from the first principles, with application to cool and dense stellar atmospheres. *J. Quant. Spec. Radiat. Transf.*, 68:235–255, February 2001. doi: 10.1016/S0022-4073(00)00023-6.

Leo Breiman. Random forests. *Machine Learning*, 45(1):5–32, Oct 2001. ISSN 1573-0565. doi: 10.1023/A:1010933404324. URL `https://doi.org/10.1023/A:1010933404324`.

M. Bridges, F. Feroz, M. P. Hobson, and A. N. Lasenby. Bayesian optimal reconstruction of the primordial power spectrum. *MNRAS*, 400:1075–1084, December 2009. doi: 10.1111/j.1365-2966.2009.15525.x.

M. Brogi, I. A. G. Snellen, R. J. de Kok, S. Albrecht, J. L. Birkby, and E. J. W. de Mooij. Detection of Molecular Absorption in the Dayside of Exoplanet 51 Pegasi b? *ApJ*, 767:27, April 2013. doi: 10.1088/0004-637X/767/1/27.

M Brogi, I A G Snellen, R J de Kok, S Albrecht, J L Birkby, and E J W de Mooij. Detection of Molecular Absorption in the Dayside of Exoplanet 51 Pegasi b? *ApJ*, 767(1):27, April 2013.

M. Brogi, R. J. de Kok, J. L. Birkby, H. Schwarz, and I. A. G. Snellen. Carbon monoxide and water vapor in the atmosphere of the non-transiting exoplanet HD 179949 b. *A&A*, 565:A124, May 2014. doi: 10.1051/0004-6361/201423537.

M. Brogi, R. J. de Kok, S. Albrecht, I. A. G. Snellen, J. L. Birkby, and H. Schwarz. Rotation and Winds of Exoplanet HD 189733 b Measured with High- dispersion Transmission Spectroscopy. *ApJ*, 817:106, February 2016. doi: 10.3847/0004-637X/817/2/106.

Matteo Brogi, Ignas A. G. Snellen, Remco J. de Kok, Simon Albrecht, Jayne Birkby, and Ernst J. W. de Mooij. The signature of orbital motion from the dayside of the planet τ Boötis b. *Nature*, 486:502–504, June 2012. doi: 10.1038/nature11161.

G. Bruno, N. K. Lewis, K. B. Stevenson, J. Filippazzo, M. Hill, J. D. Fraine, H. R. Wakeford, D. Deming, B. Kilpatrick, M. R. Line, C. V. Morley, K. A. Collins, D. M. Conti, J. Garlitz, and J. E. Rodriguez. A Comparative Study of WASP-67 b and HAT-P-38 b from WFC3 Data. *AJ*, 155:55, February 2018. doi: 10.3847/1538-3881/aaa0c7.

N. I. Burangulov. Model of penetrative convection and its application to the atmosphere, oceans, and laboratory experiments. *Akademiia Nauk SSSR Fizika Atmosfery i Okeana*, 13:1248–1256, December 1977.

A. Burrows, W. B. Hubbard, J. I. Lunine, M. Marley, T. Guillot, D. Saumon, and R. S. Freedman. Extra-Solar Giant Planet and Brown Dwarf Models. In David Soderblom, editor, *Planets Beyond the Solar System and the Next Generation of Space Missions*, volume 119, page 9, January 1997.

Adam Burrows. Scientific Return of Coronagraphic Exoplanet Imaging and Spectroscopy Using WFIRST. *ArXiv e-prints*, art. arXiv:1412.6097, December 2014.

Adam Burrows and Jonathan Lunine. Astronomical questions of origin and survival. *Nature*, 378:333, November 1995. doi: 10.1038/378333a0.

Adam Burrows, David Sudarsky, and Ivan Hubeny. Spectra and Diagnostics for the Direct Detection of Wide-Separation Extrasolar Giant Planets. *ApJ*, 609:407–416, July 2004. doi: 10.1086/420974.

R. P. Butler, J. T. Wright, G. W. Marcy, D. A. Fischer, S. S. Vogt, C. G. Tinney, H. R. A. Jones, B. D. Carter, J. A. Johnson, C. McCarthy, and A. J. Penny. Catalog of Nearby Exoplanets. *ApJ*, 646:505–522, July 2006. doi: 10.1086/504701.

Kerri L. Cahoy, Mark S. Marley, and Jonathan J. Fortney. Exoplanet Albedo Spectra and Colors as a Function of Planet Phase, Separation, and Metallicity. *ApJ*, 724:189–214, November 2010. doi: 10.1088/0004-637X/724/1/189.

L. Casagrande, R. Schönrich, M. Asplund, S. Cassisi, I. Ramírez, J. Meléndez, T. Bensby, and S. Feltzing. New constraints on the chemical evolution of the solar neighbourhood and Galactic disc(s). Improved astrophysical parameters for the Geneva-Copenhagen Survey. *A&A*, 530: A138, June 2011. doi: 10.1051/0004-6361/201016276.

M. T. Chahine. Generalization of the relaxation method for the inverse solution of nonlinear and linear transfer equations. Technical report, 1977a.

M. T. Chahine. Temperature and Humidity Sounding in the Presence of Clouds. In H.-J. Bolla, editor, *Radiation in the Atmosphere*, page 319, 1977b.

David Charbonneau, Timothy M Brown, Robert W Noyes, and Ronald L Gilliland. Detection of an Extrasolar Planet Atmosphere. *APJ*, 568(1):377–384, March 2002.

David Charbonneau, Lori Allen, Travis Barman, Francois Bouchy, Timothy Brown, Michel Mayor, Tom Megeath, Claire Moutou, Didier Queloz, and Stephane Udry. Thermal Emission from the Newest, Closest, and Brightest Transiting Planet. Spitzer Proposal, October 2005a.

David Charbonneau, Lori E. Allen, S. Thomas Megeath, Guillermo Torres, Roi Alonso, Timothy M. Brown, Ronald L. Gilliland, David W. Latham, Georgi Mandushev, Francis T. O'Donovan, and Alessandro Sozzetti. Detection of Thermal Emission from an Extrasolar Planet. *ApJ*, 626:523–529, June 2005b. doi: 10.1086/429991.

J. Chen and D. M. Kipping. Probabilistic Forecasting of the Masses and Radii of Other Worlds. *ArXiv e-prints*, March 2016.

R. N. Clark and T. B. McCord. The Galilean satellites - New near-infrared spectral reflectance measurements /0.65-2.5 microns/ and a 0.325-5 micron summary. *Icarus*, 41:323–339, March 1980a. doi: 10.1016/0019-1035(80)90217-1.

R. N. Clark and T. B. McCord. The rings of Saturn - New near-infrared reflectance measurements and a 0.326-4.08 micron summary. *Icarus*, 43:161–168, August 1980b. doi: 10.1016/0019-1035(80)90116-5.

R. Claudi, S. Benatti, I. Carleo, A. Ghedina, G. Micela, E. Molinari, E. Oliva, A. Tozzi, and Giarps Team. GIARPS: the VIS-NIR high precision radial velocity facility TNG. In *Frontier Research in Astrophysics II*, page 70, May 2016.

D. Clery. New missions aim to make a short list of exo-Earths. *Science*, 359:1453–1453, March 2018. doi: 10.1126/science.359.6383.1453.

W. D. Cochran and A. P. Hatzes. Radial Velocity Variability of mid-F Dwarf Stars. In *American Astronomical Society Meeting Abstracts #184*, volume 26 of *Bulletin of the American Astronomical Society*, page 868, May 1994.

M. Cohen, W. A. Wheaton, and S. T. Megeath. Spectral Irradiance Calibration in the Infrared. XIV. The Absolute Calibration of 2MASS. *AJ*, 126:1090–1096, August 2003. doi: 10.1086/376474.

K. A. Collins, J. F. Kielkopf, and K. G. Stassun. Transit Timing Variation Measurements of WASP-12b and Qatar-1b: No Evidence Of Additional Planets. *AJ*, 153:78, February 2017. doi: 10.3847/1538-3881/153/2/78.

B. J. Conrath and R. A. Hanel. Infrared Interferometry from Satellites. In V. Manno and P. 337 J. S. S. L. Ring, Vol. 30, editors, *Infrared Detection Techniques for Space Research*, volume 30 of *Astrophysics and Space Science Library*, page 84, 1972. doi: 10.1007/978-94-010-2885-1_10.

B. J. Conrath, R. A. Hanel, V. G. Kunde, and C. Prabhakara. The Infrared Interferometer Experiment on Nimbus 3. *Journal of Geophysics Research*, 75:5831, 1970. doi: 10.1029/JC075i030p05831.

N. B. Cowan, T. Greene, D. Angerhausen, N. E. Batalha, M. Clampin, K. Colón, I. J. M. Crossfield, J. J. Fortney, B. S. Gaudi, J. Harrington, N. Iro, C. F. Lillie, J. L. Linsky, M. Lopez-Morales, A. M. Mandell, and K. B. Stevenson. Characterizing Transiting Planet Atmospheres through 2025. *Publications of the ASP*, 127:311, March 2015. doi: 10.1086/680855.

Patricio Cubillos, Jasmina Blecic, Joseph Harrington, Patricio Rojo, Nate Lust, Oliver Bowman, Madison Stemm, Andrew Foster, Thomas J. Loredo, Jonathan Fortney, and Nikku Madhusudhan. BART: Bayesian Atmospheric Radiative Transfer fitting code. Astrophysics Source Code Library, August 2016.

M. Damiano, G. Morello, A. Tsiaras, T. Zingales, and G. Tinetti. Near-IR Transmission Spectrum of HAT-P-32b using HST/WFC3. *AJ*, 154:39, July 2017. doi: 10.3847/1538-3881/aa738b.

C. Danielski, P. Deroo, I. P. Waldmann, M. D. J. Hollis, G. Tinetti, and M. R. Swain. 0.94-2.42 μm Ground-based Transmission Spectra of the Hot Jupiter HD-189733b. *ApJ*, 785:35, April 2014. doi: 10.1088/0004-637X/785/1/35.

R. J. de Kok and D. M. Stam. The influence of forward-scattered light in transmission measurements of (exo)planetary atmospheres. *Icarus*, 221:517–524, November 2012. doi: 10.1016/j.icarus.2012.08.020.

R. J. de Kok, C. Helling, D. M. Stam, P. Woitke, and S. Witte. The influence of non-isotropic scattering of thermal radiation on spectra of brown dwarfs and hot exoplanets. *A&A*, 531: A67, July 2011a. doi: 10.1051/0004-6361/201117015.

R. J. de Kok, D. M. Stam, and T. Karalidi. Characterizing Exoplanetary Atmospheres through Infrared Polarimetry. *ApJ*, 741:59, November 2011b. doi: 10.1088/0004-637X/741/1/59.

Remco de Kok, J. Birkby, M. Brogi, I. Snellen, S. Albrecht, E. de Mooij, and H. Schwarz. Exploring the atmosphere of HD 189733b at high spectral resolution. In *AAS/Division for Planetary Sciences Meeting Abstracts #45*, page 105.02, October 2013.

J. de Wit, M. Gillon, B. O. Demory, and S. Seager. Towards consistent mapping of distant worlds: secondary-eclipse scanning of the exoplanet HD 189733b. *A&A*, 548:A128, December 2012. doi: 10.1051/0004-6361/201219060.

L. Delrez, A. Santerne, J.-M. Almenara, D. R. Anderson, A. Collier-Cameron, R. F. Díaz, M. Gillon, C. Hellier, E. Jehin, M. Lendl, P. F. L. Maxted, M. Neveu-VanMalle, F. Pepe, D. Pollacco, D. Queloz, D. Ségransan, B. Smalley, A. M. S. Smith, A. H. M. J. Triaud, S. Udry, V. Van Grootel, and R. G. West. WASP-121 b: a hot Jupiter close to tidal disruption transiting an active F star. *MNRAS*, 458:4025–4043, June 2016. doi: 10.1093/mnras/stw522.

D. Deming, A. Wilkins, P. McCullough, A. Burrows, J. J. Fortney, E. Agol, I. Dobbs-Dixon, N. Madhusudhan, N. Crouzet, J.-M. Desert, R. L. Gilliland, K. Haynes, H. A. Knutson, M. Line, Z. Magic, A. M. Mandell, S. Ranjan, D. Charbonneau, M. Clampin, S. Seager, and A. P. Showman. Infrared Transmission Spectroscopy of the Exoplanets HD 209458b and XO-1b Using the Wide Field Camera-3 on the Hubble Space Telescope. *ApJ*, 774:95, September 2013. doi: 10.1088/0004-637X/774/2/95.

Drake Deming, Sara Seager, Joseph Harrington, and L. Jeremy Richardson. Infrared Photometry of the Very Hot Jupiter Orbiting HD 189733. Spitzer Proposal, October 2005.

Brice-Olivier Demory, M Gillon, Julien de Wit, Nikku Madhusudhan, Emeline Bolmont, Kevin Heng, Tiffany Kataria, Nikole Lewis, Renyu Hu, Jessica Krick, Vlada Stamenković, B Benneke, Stephen Kane, and Didier Queloz. A map of the large day-night temperature gradient of a super-Earth exoplanet. *Nature*, 532(7):207–209, April 2016.

Li Deng and Dong Yu. *Deep Learning: Methods and Applications*. Now Publishers Inc., Hanover, MA, USA, 2014. ISBN 1601988141, 9781601988140.

E. Denton, S. Chintala, A. Szlam, and R. Fergus. Deep Generative Image Models using a Laplacian Pyramid of Adversarial Networks. *ArXiv e-prints*, June 2015.

J.-M. Désert, A. Lecavelier des Etangs, G. Hébrard, D. K. Sing, D. Ehrenreich, R. Ferlet, and A. Vidal-Madjar. Search for Carbon Monoxide in the Atmosphere of the Transiting Exoplanet HD 189733b. *ApJ*, 699:478–485, July 2009. doi: 10.1088/0004-637X/699/1/478.

C. Dorn, A. Khan, K. Heng, J. A. D. Connolly, Y. Alibert, W. Benz, and P. Tackley. Can we constrain the interior structure of rocky exoplanets from mass and radius measurements? *A&A*, 577:A83, May 2015. doi: 10.1051/0004-6361/201424915.

Alexey Dosovitskiy and Thomas Brox. Generating images with perceptual similarity metrics based on deep networks. In D. D. Lee, M. Sugiyama, U. V. Luxburg, I. Guyon, and R. Garnett, editors, *Advances in Neural Information Processing Systems 29*, pages 658–666. Curran Associates, Inc., 2016. URL `http://papers.nips.cc/paper/`

6158-generating-images-with-perceptual-similarity-metrics-based-on-deep-networks.pdf.

Erik Edwards, Wael Salloum, Greg P Finley, James Fone, Greg Cardiff, Mark Miller, and David Suendermann-Oeft. Medical speech recognition: reaching parity with humans. In *International Conference on Speech and Computer*, pages 512–524. Springer, 2017.

D. Ehrenreich, X. Bonfils, C. Lovis, X. Delfosse, T. Forveille, M. Mayor, V. Neves, N. C. Santos, S. Udry, and D. Ségransan. Near-infrared transmission spectrum of the warm-Uranus GJ 3470b with the Wide Field Camera-3 on the Hubble Space Telescope. *A&A*, 570:A89, October 2014. doi: 10.1051/0004-6361/201423809.

D Ehrenreich, X Bonfils, C Lovis, X Delfosse, T Forveille, M Mayor, V Neves, N C Santos, Stéphane Udry, and D Ségransan. Near-infrared transmission spectrum of the warm-Uranus GJ 3470b with the Wide Field Camera-3 on the Hubble Space Telescope. *A&A*, 570:A89, October 2014.

M. Esposito, E. Covino, L. Mancini, A. Harutyunyan, J. Southworth, K. Biazzo, D. Gandolfi, A. F. Lanza, M. Barbieri, A. S. Bonomo, F. Borsa, R. Claudi, R. Cosentino, S. Desidera, R. Gratton, I. Pagano, A. Sozzetti, C. Boccato, A. Maggio, G. Micela, E. Molinari, V. Nascimbeni, G. Piotto, E. Poretti, and R. Smareglia. The GAPS Programme with HARPS-N at TNG. III: The retrograde orbit of HAT-P-18b. *A&A*, 564:L13, April 2014. doi: 10.1051/0004-6361/201423735.

Lisa J. Esteves, Ray Jayawardhana, and Ernst de Mooij. Making the Most of Kepler Photometry: Characterizing Exoplanets through Phase Curve Analysis. In *European Physical Journal Web of Conferences*, volume 101, page 02003, September 2015. doi: 10.1051/epjconf/201510102003.

T. M. Evans, D. K. Sing, H. R. Wakeford, N. Nikolov, G. E. Ballester, B. Drummond, T. Kataria, N. P. Gibson, D. S. Amundsen, and J. Spake. Detection of H_2O and Evidence for TiO/VO in an Ultra-hot Exoplanet Atmosphere. *ApJ*, 822:L4, May 2016. doi: 10.3847/2041-8205/822/1/L4.

F. Faedi, S. C. C. Barros, D. R. Anderson, D. J. A. Brown, A. Collier Cameron, D. Pollacco, I. Boisse, G. Hébrard, M. Lendl, T. A. Lister, B. Smalley, R. A. Street, A. H. M. J. Triaud, J. Bento, F. Bouchy, O. W. Butters, B. Enoch, C. A. Haswell, C. Hellier, F. P. Keenan, G. R. M. Miller, V. Moulds, C. Moutou, A. J. Norton, D. Queloz, A. Santerne, E. K. Simpson, I. Skillen, A. M. S. Smith, S. Udry, C. A. Watson, R. G. West, and P. J. Wheatley. WASP-39b: a highly inflated Saturn-mass planet orbiting a late G-type star. *A&A*, 531:A40, July 2011. doi: 10.1051/0004-6361/201116671.

Scott E. Fahlman. Faster-learning variations on back-propagation: An empirical study. In David S. Touretzky, Geoffrey E. Hinton, and Terrence J. Sejnowski, editors, *Proceedings of the 1988 Connectionist Models Summer School*, pages 38–51. San Francisco, CA: Morgan Kaufmann, 1989.

F Feroz and M P Hobson. Multimodal nested sampling: an efficient and robust alternative to Markov Chain Monte Carlo methods for astronomical data analyses. *Monthly Notices of the Royal Astronomical Society*, 384(2):449–463, February 2008a.

F. Feroz, M. P. Hobson, and M. Bridges. MULTINEST: an efficient and robust Bayesian inference tool for cosmology and particle physics. *MNRAS*, 398:1601–1614, October 2009a. doi: 10.1111/j.1365-2966.2009.14548.x.

F. Feroz, M. P. Hobson, and M. Bridges. MULTINEST: an efficient and robust Bayesian inference tool for cosmology and particle physics. *MNRAS*, 398:1601–1614, October 2009b. doi: 10.1111/j.1365-2966.2009.14548.x.

F. Feroz, J. R. Gair, P. Graff, M. P. Hobson, and A. Lasenby. Classifying LISA gravitational wave burst signals using Bayesian evidence. *Classical and Quantum Gravity*, 27(7):075010, April 2010. doi: 10.1088/0264-9381/27/7/075010.

F. Feroz, S. T. Balan, and M. P. Hobson. Detecting extrasolar planets from stellar radial velocities using Bayesian evidence. *MNRAS*, 415:3462–3472, August 2011a. doi: 10.1111/j.1365-2966.2011.18962.x.

F. Feroz, S. T. Balan, and M. P. Hobson. Bayesian evidence for two companions orbiting HIP 5158. *MNRAS*, 416:L104–L108, September 2011b. doi: 10.1111/j.1745-3933.2011.01109.x.

Farhan Feroz and MP Hobson. Multimodal nested sampling: an efficient and robust alternative to markov chain monte carlo methods for astronomical data analyses. *Monthly Notices of the Royal Astronomical Society*, 384(2):449–463, 2008b.

Farhan Feroz, Jonathan R Gair, Michael P Hobson, and Edward K Porter. Use of the MULTINEST algorithm for gravitational wave data analysis. *Classical and Quantum Gravity*, 26(21): 215003, October 2009.

J. Fraine, D. Deming, B. Benneke, H. Knutson, A. Jordán, N. Espinoza, N. Madhusudhan, A. Wilkins, and K. Todorov. Water vapour absorption in the clear atmosphere of a Neptune-sized exoplanet. *Nature*, 513:526–529, September 2014. doi: 10.1038/nature13785.

Jonathan Fraine, D Deming, B Benneke, H A Knutson, Andrés Jordán, Néstor Espinoza, Nikku Madhusudhan, Ashlee Wilkins, and Kamen Todorov. Water vapour absorption in the clear atmosphere of a Neptune-sized exoplanet. *Nature*, 513(7):526–529, September 2014.

F. Fressin, G. Torres, D. Charbonneau, S. T. Bryson, J. Christiansen, C. D. Dressing, J. M. Jenkins, L. M. Walkowicz, and N. M. Batalha. The False Positive Rate of Kepler and the Occurrence of Planets. *ApJ*, 766:81, April 2013. doi: 10.1088/0004-637X/766/2/81.

A. Fukui, N. Narita, K. Kurosaki, M. Ikoma, K. Yanagisawa, D. Kuroda, Y. Shimizu, Y. H. Takahashi, H. Ohnuki, M. Onitsuka, T. Hirano, T. Suenaga, K. Kawauchi, S. Nagayama, K. Ohta, M. Yoshida, N. Kawai, and H. Izumiura. Optical-to-near-infrared Simultaneous Observations for the Hot Uranus GJ3470b: A Hint of a Cloud-free Atmosphere. *ApJ*, 770:95, June 2013. doi: 10.1088/0004-637X/770/2/95.

Akihiko Fukui, Norio Narita, Kenji Kurosaki, Masahiro Ikoma, Kenshi Yanagisawa, Daisuke Kuroda, Yasuhiro Shimizu, Yasuhiro H Takahashi, Hiroshi Ohnuki, Masahiro Onitsuka, Teruyuki Hirano, Takuya Suenaga, Kiyoe Kawauchi, Shogo Nagayama, Kouji Ohta, Michitoshi Yoshida, Nobuyuki Kawai, and Hideyuki Izumiura. Optical-to-near-infrared Simultaneous Observations for the Hot Uranus GJ3470b: A Hint of a Cloud-free Atmosphere. *ApJ*, 770(2):95, June 2013.

B. J. Fulton, E. A. Petigura, A. W. Howard, H. Isaacson, G. W. Marcy, P. A. Cargile, L. Hebb, L. M. Weiss, J. A. Johnson, T. D. Morton, E. Sinukoff, I. J. M. Crossfield, and L. A. Hirsch. The California-Kepler Survey. III. A Gap in the Radius Distribution of Small Planets. *AJ*, 154:109, September 2017. doi: 10.3847/1538-3881/aa80eb.

Siddharth Gandhi and Nikku Madhusudhan. Retrieval of exoplanet emission spectra with hydra. *Monthly Notices of the Royal Astronomical Society*, 474(1):271–288, 2018. doi: 10.1093/mnras/stx2748. URL `http://dx.doi.org/10.1093/mnras/stx2748`.

Jonathan P. Gardner, John C. Mather, Mark Clampin, Rene Doyon, Matthew A. Greenhouse, Heidi B. Hammel, John B. Hutchings, Peter Jakobsen, Simon J. Lilly, Knox S. Long, Jonathan I. Lunine, Mark J. Mccaughrean, Matt Mountain, John Nella, George H. Rieke, Marcia J. Rieke, Hans-Walter Rix, Eric P. Smith, George Sonneborn, Massimo Stiavelli, H. S. Stockman, Rogier A. Windhorst, and Gillian S. Wright. The james webb space telescope. *Space Science Reviews*, 123(4):485–606, Apr 2006. ISSN 1572-9672. doi: 10.1007/s11214-006-8315-7. URL `https://doi.org/10.1007/s11214-006-8315-7`.

A. Gelman, J.B. Carlin, and H.S. et al. Stern. *Bayesian Data analysis, Third Edition, (CRC Press)*. 2013.

W.R Gilks, S. Richardson, and D.J. Spiegelhalter. *Markov Chain Monte Carlo in Practice, (Chapman & Hall/CRC)*. 1996.

I. J. Goodfellow, J. Pouget-Abadie, M. Mirza, B. Xu, D. Warde-Farley, S. Ozair, A. Courville, and Y. Bengio. Generative Adversarial Networks. *ArXiv e-prints*, June 2014.

Ian Goodfellow, Yoshua Bengio, and Aaron Courville. *Deep Learning*. MIT Press, 2016. `http://www.deeplearningbook.org`.

P. Graff, F. Feroz, M. P. Hobson, and A. Lasenby. BAMBI: blind accelerated multimodal Bayesian inference. *MNRAS*, 421:169–180, March 2012. doi: 10.1111/j.1365-2966.2011.20288.x.

Johnny P. Greco and Adam Burrows. The Direct Detectability of Giant Exoplanets in the Optical. *ApJ*, 808:172, August 2015. doi: 10.1088/0004-637X/808/2/172.

T. P. Greene, L. Chu, E. Egami, K. W. Hodapp, D. M. Kelly, J. Leisenring, M. Rieke, M. Robberto, E. Schlawin, and J. Stansberry. Slitless spectroscopy with the James Webb Space Telescope Near-Infrared Camera (JWST NIRCam). In *Space Telescopes and Instrumentation 2016: Optical, Infrared, and Millimeter Wave*, volume 9904 of *Proc. SPIE*, page 99040E, July 2016. doi: 10.1117/12.2231347.

P C Gregory. Bayesian exoplanet tests of a new method for MCMC sampling in highly correlated model parameter spaces. *MNRAS*, 410:94–110, 2011.

C. A. Griffith. Disentangling degenerate solutions from primary transit and secondary eclipse spectroscopy of exoplanets. *Philosophical Transactions of the Royal Society of London Series A*, 372:20130086–20130086, March 2014. doi: 10.1098/rsta.2013.0086.

C. J. Grillmair, A. Burrows, D. Charbonneau, L. Armus, J. Stauffer, V. Meadows, J. van Cleve, K. von Braun, and D. Levine. Strong water absorption in the dayside emission spectrum of the planet HD189733b. *Nature*, 456:767–769, December 2008. doi: 10.1038/nature07574.

Carl J. Grillmair, S. Carey, G. Helou, R. Hurt, L. Rebull, T. Soifer, G. K. Squires, and L. Storrie-Lombardi. Hot Science with a "Warm" Telescope: Observations of Extrasolar Planets During the Spitzer Warm Mission. In *American Astronomical Society Meeting Abstracts*, volume 211, page 134.07, December 2007.

R. A. Hanel and B. J. Conrath. Thermal Emission Spectra of the Earth and Atmosphere from the Nimbus 4 Michelson Interferometer Experiment. *Nature*, 228:143–145, October 1970. doi: 10.1038/228143a0.

J. D. Hartman, G. Á. Bakos, G. Torres, G. Kovács, R. W. Noyes, A. Pál, D. W. Latham, B. Sipőcz, D. A. Fischer, J. A. Johnson, G. W. Marcy, R. P. Butler, A. W. Howard, G. A. Esquerdo, D. D. Sasselov, G. Kovács, R. P. Stefanik, J. M. Fernandez, J. Lázár, I. Papp, and P. Sári. HAT-P-12b: A Low-Density Sub-Saturn Mass Planet Transiting a Metal-Poor K Dwarf. *ApJ*, 706:785–796, November 2009. doi: 10.1088/0004-637X/706/1/785.

J. D. Hartman, G. Á. Bakos, D. M. Kipping, G. Torres, G. Kovács, R. W. Noyes, D. W. Latham, A. W. Howard, D. A. Fischer, J. A. Johnson, G. W. Marcy, H. Isaacson, S. N. Quinn, L. A. Buchhave, B. Béky, D. D. Sasselov, R. P. Stefanik, G. A. Esquerdo, M. Everett, G. Perumpilly, J. Lázár, I. Papp, and P. Sári. HAT-P-26b: A Low-density Neptune-mass Planet Transiting a K Star. *ApJ*, 728:138, February 2011a. doi: 10.1088/0004-637X/728/2/138.

J. D. Hartman, G. Á. Bakos, G. Torres, D. W. Latham, G. Kovács, B. Béky, S. N. Quinn, T. Mazeh, A. Shporer, G. W. Marcy, A. W. Howard, D. A. Fischer, J. A. Johnson, G. A. Esquerdo, R. W. Noyes, D. D. Sasselov, R. P. Stefanik, J. M. Fernandez, T. Szklenár, J. Lázár, I. Papp, and P. Sári. HAT-P-32b and HAT-P-33b: Two Highly Inflated Hot Jupiters Transiting High-jitter Stars. *ApJ*, 742:59, November 2011b. doi: 10.1088/0004-637X/742/1/59.

J. D. Hartman, G. Á. Bakos, B. Béky, G. Torres, D. W. Latham, Z. Csubry, K. Penev, A. Shporer, B. J. Fulton, L. A. Buchhave, J. A. Johnson, A. W. Howard, G. W. Marcy, D. A. Fischer, G. Kovács, R. W. Noyes, G. A. Esquerdo, M. Everett, T. Szklenár, S. N. Quinn, A. Bieryla, R. P. Knox, P. Hinz, D. D. Sasselov, G. Fűrész, R. P. Stefanik, J. Lázár, I. Papp, and P. Sári. HAT-P-39b-HAT-P-41b: Three Highly Inflated Transiting Hot Jupiters. *AJ*, 144: 139, November 2012. doi: 10.1088/0004-6256/144/5/139.

Mohamad H. Hassoun. *Fundamentals of Artificial Neural Networks*. MIT Press, Cambridge, MA, USA, 1st edition, 1995. ISBN 026208239X.

W. K. Hastings. Monte Carlo sampling methods using Markov chains and their applications. 57(1):97–109, April 1970. ISSN 0006-3444 (print), 1464-3510 (electronic). doi: https://doi.org/10.2307/2334940. URL `http://www.jstor.org/stable/2334940;http://www.probability.ca/hastings/`. This paper introduces what is now known as the Metropolis–Hastings algorithm, a generalization of the work in Metropolis et al. (1953). See (**?**, page 255).

G. Hébrard, A. Collier Cameron, D. J. A. Brown, R. F. Díaz, F. Faedi, B. Smalley, D. R. Anderson, D. Armstrong, S. C. C. Barros, J. Bento, F. Bouchy, A. P. Doyle, B. Enoch, Y. Gómez Maqueo Chew, É. M. Hébrard, C. Hellier, M. Lendl, T. A. Lister, P. F. L. Maxted, J. McCormac, C. Moutou, D. Pollacco, D. Queloz, A. Santerne, I. Skillen, J. Southworth, J. Tregloan-Reed, A. H. M. J. Triaud, S. Udry, M. Vanhuysse, C. A. Watson, R. G. West, and P. J. Wheatley. WASP-52b, WASP-58b, WASP-59b, and WASP-60b: Four new transiting close-in giant planets. *A&A*, 549:A134, January 2013. doi: 10.1051/0004-6361/201220363.

C. Hellier, D. R. Anderson, A. Collier Cameron, M. Gillon, M. Lendl, P. F. L. Maxted, D. Queloz, B. Smalley, A. H. M. J. Triaud, R. G. West, D. J. A. Brown, B. Enoch, T. A. Lister, F. Pepe, D. Pollacco, D. Ségransan, and S. Udry. WASP-29b: A Saturn-sized Transiting Exoplanet. *ApJ*, 723:L60–L63, November 2010. doi: 10.1088/2041-8205/723/1/L60.

C. Hellier, D. R. Anderson, A. Collier Cameron, M. Gillon, E. Jehin, M. Lendl, P. F. L. Maxted, F. Pepe, D. Pollacco, D. Queloz, D. Ségransan, B. Smalley, A. M. S. Smith, J. Southworth, A. H. M. J. Triaud, S. Udry, and R. G. West. WASP-43b: the closest-orbiting hot Jupiter. *A&A*, 535:L7, November 2011. doi: 10.1051/0004-6361/201117081.

C. Hellier, D. R. Anderson, A. Collier Cameron, A. P. Doyle, A. Fumel, M. Gillon, E. Jehin, M. Lendl, P. F. L. Maxted, F. Pepe, D. Pollacco, D. Queloz, D. Ségransan, B. Smalley, A. M. S. Smith, J. Southworth, A. H. M. J. Triaud, S. Udry, and R. G. West. Seven transiting hot Jupiters from WASP-South, Euler and TRAPPIST: WASP-47b, WASP-55b, WASP-61b, WASP-62b, WASP-63b, WASP-66b and WASP-67b. *MNRAS*, 426:739–750, October 2012. doi: 10.1111/j.1365-2966.2012.21780.x.

C. Hellier, D. R. Anderson, A. C. Cameron, L. Delrez, M. Gillon, E. Jehin, M. Lendl, P. F. L. Maxted, F. Pepe, D. Pollacco, D. Queloz, D. Ségransan, B. Smalley, A. M. S. Smith, J. Southworth, A. H. M. J. Triaud, S. Udry, and R. G. West. Transiting hot Jupiters from WASP-South, Euler and TRAPPIST: WASP-95b to WASP-101b. *MNRAS*, 440:1982–1992, May 2014. doi: 10.1093/mnras/stu410.

C. Hellier, D. R. Anderson, A. Collier Cameron, L. Delrez, M. Gillon, E. Jehin, M. Lendl, P. F. L. Maxted, F. Pepe, D. Pollacco, D. Queloz, D. Ségransan, B. Smalley, A. M. S. Smith, J. Southworth, A. H. M. J. Triaud, O. D. Turner, S. Udry, and R. G. West. Three WASP-South Transiting Exoplanets: WASP-74b, WASP-83b, and WASP-89b. *AJ*, 150:18, July 2015. doi: 10.1088/0004-6256/150/1/18.

Bertrand Higy, Alessio Mereta, Giorgio Metta, and Leonardo Badino. Speech recognition for the icub platform. *Frontiers in Robotics and AI*, 5:10, 2018.

Geoffrey E. Hinton. Boltzmann machine. *Scholarpedia*, 2(5):1668, 2007. doi: 10.4249/scholarpedia.1668. URL `https://doi.org/10.4249/scholarpedia.1668`.

Geoffrey E. Hinton, Peter Dayan, Brendan J. Frey, and Radford M. Neal. The wake-sleep algorithm for unsupervised neural networks. *Science*, 268:1158–1161, 1995.

Geoffrey E. Hinton, Simon Osindero, and Yee Whye Teh. A fast learning algorithm for deep belief nets. *Neural Computation*, 18(7):1527–1554, 2006. doi: 10.1162/neco.2006.18.7.1527. URL `https://doi.org/10.1162/neco.2006.18.7.1527`.

A. W. Howard, G. Á. Bakos, J. Hartman, G. Torres, A. Shporer, T. Mazeh, G. Kovács, D. W. Latham, R. W. Noyes, D. A. Fischer, J. A. Johnson, G. W. Marcy, G. A. Esquerdo, B. Béky, R. P. Butler, D. D. Sasselov, R. P. Stefanik, G. Perumpilly, J. Lázár, I. Papp, and P. Sári. HAT-P-17b,c: A Transiting, Eccentric, Hot Saturn and a Long-period, Cold Jupiter. *ApJ*, 749:134, April 2012. doi: 10.1088/0004-637X/749/2/134.

Feng-Hsiung Hsu. *Behind Deep Blue: Building the Computer That Defeated the World Chess Champion*. Princeton University Press, Princeton, NJ, USA, 2002. ISBN 0691090653.

S. Ioffe and C. Szegedy. Batch Normalization: Accelerating Deep Network Training by Reducing Internal Covariate Shift. *ArXiv e-prints*, February 2015.

W. M. Irvine and J. Lenoble. Solving multiple scattering problems in planetary atmospheres. In J. G. Kuriyan, editor, *Radiation and Remote Probing of the Atmosphere*, 1974.

J. Irwin, D. Charbonneau, P. Nutzman, W. F. Welsh, A. Rajan, M. Hidas, T. M. Brown, T. A. Lister, D. Davies, G. Laughlin, and J. Langton. Parameters and Predictions for the Long-Period Transiting Planet HD 17156b. *ApJ*, 681:636–643, July 2008. doi: 10.1086/588461.

P G J Irwin, N A Teanby, R De Kok, L N Fletcher, C J A Howett, C C C Tsang, C F Wilson, S B Calcutt, C A Nixon, and P D Parrish. The NEMESIS planetary atmosphere radiative transfer and retrieval tool. *Journal of Quantitative Spectroscopy & Radiative Transfer*, 109 (6):1136–1150, April 2008.

A. R. Iyer, M. R. Swain, R. T. Zellem, M. R. Line, G. Roudier, G. Rocha, and J. H. Livingston. A Characteristic Transmission Spectrum Dominated by H_2O Applies to the Majority of HST/WFC3 Exoplanet Observations. *ApJ*, 823:109, June 2016. doi: 10.3847/0004-637X/823/2/109.

Aishwarya R Iyer, Mark Swain, Robert T Zellem, Michael R Line, Gael Roudier, Graça Rocha, and John H Livingston. A Characteristic Transmission Spectrum Dominated by H2O Applies to the Majority of HST/WFC3 Exoplanet Observations. *ApJ*, 823(2):109, June 2016.

Taiki Izumi, Ryo Aihara, Toshiyuki Hanazawa, Yohei Okato, Takanobu Uramoto, Shingo Uenohara, and KenâĂŹichi Furuya. Reducing computational complexity of multichannel nonnegative matrix factorization using initial value setting for speech recognition. In *Conference on Complex, Intelligent, and Software Intensive Systems*, pages 893–900. Springer, 2018.

H. Jeffreys. *Theory of Probability*. Oxford, Oxford, England, third edition, 2008.

Wei Jiang, Yu Li, Hua Shu, Linjun Zhang, and Yang Zhang. Use of semantic context and f 0 contours by older listeners during mandarin speech recognition in quiet and single-talker interference conditions. *The Journal of the Acoustical Society of America*, 141(4):EL338–EL344, 2017.

D. Jimenez Rezende, S. Mohamed, and D. Wierstra. Stochastic Backpropagation and Approximate Inference in Deep Generative Models. *ArXiv e-prints*, January 2014.

Hans-Ulrich Kaeufl, Pascal Ballester, Peter Biereichel, Bernard Delabre, Rob Donaldson, Reinhold Dorn, Enrico Fedrigo, Gert Finger, Gerhard Fischer, Francis Franza, Domingo Gojak, Gotthard Huster, Yves Jung, Jean-Louis Lizon, Leander Mehrgan, Manfred Meyer, Alan Moorwood, Jean-Francois Pirard, Jerome Paufique, Esther Pozna, Ralf Siebenmorgen, Armin Silber, Joerg Stegmeier, and Stefan Wegerer. CRIRES: a high-resolution infrared spectrograph for ESO's VLT. In Alan F. M. Moorwood and Masanori Iye, editors, *Ground-based Instrumentation for Astronomy*, volume 5492, pages 1218–1227, September 2004. doi: 10.1117/12.551480.

Jason Kalirai. Scientific discovery with the james webb space telescope. *Contemporary Physics*, 59(3):251–290, 2018. doi: 10.1080/00107514.2018.1467648. URL `https://doi.org/10.1080/00107514.2018.1467648`.

L. Kaltenegger. How to Characterize Habitable Worlds and Signs of Life. *Annual Review of Astron and Astrophys*, 55:433–485, August 2017. doi: 10.1146/annurev-astro-082214-122238.

L. D. Kaplan. Some Comments on L. Elterman's "The Measurement of Stratospheric Density Distribution with the Searchlight Technique". *Journal of Geophysics Research*, 57:423, September 1952.

N. V. Karpenka, M. C. March, F. Feroz, and M. P. Hobson. Bayesian constraints on dark matter halo properties using gravitationally lensed supernovae. *MNRAS*, 433:2693–2705, August 2013. doi: 10.1093/mnras/sts700.

E. R. Kass and E. A. Raftery. Bayes Factor. *Journal of the American Statistical Association*, 90:773, 1995. doi: 10.1080/01621459.1995.10476572.

Dylan Keating and Nicolas B. Cowan. Revisiting the Energy Budget of WASP-43b: Enhanced Day-Night Heat Transport. *ApJ*, 849:L5, November 2017. doi: 10.3847/2041-8213/aa8b6b.

W. W. Kellogg. *Meteorological soundings in the upper atmosphere*. 1964.

E. M.-R. Kempton, J. L. Bean, and V. Parmentier. An Observational Diagnostic for Distinguishing between Clouds and Haze in Hot Exoplanet Atmospheres. *ApJL*, 845:L20, August 2017. doi: 10.3847/2041-8213/aa84ac.

J. I. F. King. The Source Function for an Equilibrium Gray Atmosphere. *ApJ*, 124:406, September 1956. doi: 10.1086/146235.

D. P. Kingma and J. Ba. Adam: A Method for Stochastic Optimization. *ArXiv e-prints*, December 2014.

D. P Kingma and M. Welling. Auto-Encoding Variational Bayes. *ArXiv e-prints*, December 2013.

David M. Kipping and Christopher Lam. Transit clairvoyance: enhancing TESS follow-up using artificial neural networks. *MNRAS*, 465:3495–3505, March 2017. doi: 10.1093/mnras/stw2974.

W. Bastiaan Kleijn, Felicia S. C. Lim, Alejandro Luebs, Jan Skoglund, Florian Stimberg, Quan Wang, and Thomas C. Walters. Wavenet based low rate speech coding. *arXiv preprint arXiv:1712.01120*, 2017. URL `https://arxiv.org/abs/1712.01120`.

H A Knutson, D Charbonneau, Lori E Allen, A Burrows, and S Thomas Megeath. The 3.6-8.0 μm Broadband Emission Spectrum of HD 209458b: Evidence for an Atmospheric Temperature Inversion. *ApJ*, 673(1):526–531, January 2008.

H. A. Knutson, N. Madhusudhan, N. B. Cowan, J. L. Christiansen, E. Agol, D. Deming, J.-M. Désert, D. Charbonneau, G. W. Henry, D. Homeier, J. Langton, G. Laughlin, and S. Seager. A Spitzer Transmission Spectrum for the Exoplanet GJ 436b, Evidence for Stellar Variability, and Constraints on Dayside Flux Variations. *ApJ*, 735:27, July 2011. doi: 10.1088/0004-637X/735/1/27.

H. A. Knutson, B. Benneke, D. Deming, and D. Homeier. A featureless transmission spectrum for the Neptune-mass exoplanet GJ436b. *Nature*, 505:66–68, January 2014. doi: 10.1038/nature12887.

H A Knutson, B Benneke, D Deming, and D Homeier. A featureless transmission spectrum for the Neptune-mass exoplanet GJ436b. *Nature*, 505(7):66–68, January 2014.

H. A. Knutson, D. Dragomir, L. Kreidberg, E. M.-R. Kempton, P. R. McCullough, J. J. Fortney, J. L. Bean, M. Gillon, D. Homeier, and A. W. Howard. Hubble Space Telescope Near-IR Transmission Spectroscopy of the Super-Earth HD 97658b. *ApJ*, 794:155, October 2014. doi: 10.1088/0004-637X/794/2/155.

Heather A. Knutson. Extrasolar planets: Water on distant worlds. *Nature*, 448:143–145, July 2007. doi: 10.1038/448143a.

Heather A. Knutson, David Charbonneau, Lori E. Allen, Jonathan J. Fortney, Eric Agol, Nicolas B. Cowan, Adam P. Showman, Curtis S. Cooper, and S. Thomas Megeath. A map of the day-night contrast of the extrasolar planet HD 189733b. *Nature*, 447:183–186, May 2007. doi: 10.1038/nature05782.

D. G. Koch, W. J. Borucki, G. Basri, N. M. Batalha, T. M. Brown, D. Caldwell, J. Christensen-Dalsgaard, W. D. Cochran, E. DeVore, E. W. Dunham, T. N. Gautier, III, J. C. Geary, R. L. Gilliland, A. Gould, J. Jenkins, Y. Kondo, D. W. Latham, J. J. Lissauer, G. Marcy, D. Monet, D. Sasselov, A. Boss, D. Brownlee, J. Caldwell, A. K. Dupree, S. B. Howell, H. Kjeldsen, S. Meibom, D. Morrison, T. Owen, H. Reitsema, J. Tarter, S. T. Bryson, J. L. Dotson, P. Gazis, M. R. Haas, J. Kolodziejczak, J. F. Rowe, J. E. Van Cleve, C. Allen, H. Chandrasekaran, B. D. Clarke, J. Li, E. V. Quintana, P. Tenenbaum, J. D. Twicken, and H. Wu. Kepler Mission Design, Realized Photometric Performance, and Early Science. *ApJ*, 713:L79–L86, April 2010. doi: 10.1088/2041-8205/713/2/L79.

Q M Konopacky, T S Barman, Bruce A Macintosh, and Christian Marois. Detection of Carbon Monoxide and Water Absorption Lines in an Exoplanet Atmosphere. *Science*, 339(6):1398–1401, March 2013.

R. k. Kopparapu, J. F. Kasting, and K. J. Zahnle. A Photochemical Model for the Carbon-rich Planet WASP-12b. *ApJ*, 745:77, January 2012. doi: 10.1088/0004-637X/745/1/77.

L. Kreidberg. *Exoplanet Atmosphere Measurements from Transmission Spectroscopy and Other Planet Star Combined Light Observations*, page 100. 2017. doi: 10.1007/978-3-319-30648-3_100-1.

L Kreidberg, J L Bean, B Deke, D Deming, Kevin B Stevenson, Sara Seager, Z Berta-Thompson, Andreas Seifahrt, and D Homeier. Clouds in the atmosphere of the super-Earth exoplanet GJ1214b. *Nature*, 505(7):69–72, January 2014.

L. Kreidberg, J. L. Bean, J.-M. Désert, M. R. Line, J. J. Fortney, N. Madhusudhan, K. B. Stevenson, A. P. Showman, D. Charbonneau, P. R. McCullough, S. Seager, A. Burrows, G. W. Henry, M. Williamson, T. Kataria, and D. Homeier. A Precise Water Abundance Measurement for the Hot Jupiter WASP-43b. *ApJ*, 793:L27, October 2014. doi: 10.1088/2041-8205/793/2/L27.

L. Kreidberg, M. R. Line, J. L. Bean, K. B. Stevenson, J.-M. Désert, N. Madhusudhan, J. J. Fortney, J. K. Barstow, G. W. Henry, M. H. Williamson, and A. P. Showman. A Detection of Water in the Transmission Spectrum of the Hot Jupiter WASP-12b and Implications for Its Atmospheric Composition. *ApJ*, 814:66, November 2015. doi: 10.1088/0004-637X/814/1/66.

L Kreidberg, Michael R Line, J L Bean, K B Stevenson, Jean-Michel Desert, Nikku Madhusudhan, J Fortney, Joanna K Barstow, Gregory W Henry, Michael H Williamson, and Adam P Showman. A Detection of Water in the Transmission Spectrum of the Hot Jupiter WASP-12b and Implications for Its Atmospheric Composition. *ApJ*, 814(1):66, November 2015.

L. Kreidberg, M. R. Line, V. Parmentier, K. B. Stevenson, T. Louden, M. Bonnefoy, J. K. Faherty, G. W. Henry, M. H. Williamson, K. Stassun, J. L. Bean, J. J. Fortney, A. P. Showman, J.-M. Désert, and J. Arcangeli. Global Climate and Atmospheric Composition of the Ultra-Hot Jupiter WASP-103b from HST and Spitzer Phase Curve Observations. *ArXiv e-prints*, April 2018.

A Krizhevsky, I Sutskever, and GE Hinton. Imagenet classification with deep convolutional neural networks. advances in neural information processing 25, 2012.

A. Lamb, V. Dumoulin, and A. Courville. Discriminative Regularization for Generative Models. *ArXiv e-prints*, February 2016.

A. A. Lanotte, M. Gillon, B.-O. Demory, J. J. Fortney, N. Astudillo, X. Bonfils, P. Magain, X. Delfosse, T. Forveille, C. Lovis, M. Mayor, V. Neves, F. Pepe, D. Queloz, N. Santos, and S. Udry. A global analysis of Spitzer and new HARPS data confirms the loneliness and metal-richness of GJ 436 b. *A&A*, 572:A73, December 2014. doi: 10.1051/0004-6361/201424373.

G. Laughlin, M. Crismani, and F. C. Adams. On the Anomalous Radii of the Transiting Extrasolar Planets. *ApJ*, 729:L7, March 2011. doi: 10.1088/2041-8205/729/1/L7.

B. Lavie, J. M. Mendonça, C. Mordasini, M. Malik, M. Bonnefoy, B.-O. Demory, M. Oreshenko, S. L. Grimm, D. Ehrenreich, and K. Heng. HELIOS-Retrieval: An Open-source, Nested Sampling Atmospheric Retrieval Code, Application to the HR 8799 Exoplanets and Inferred Constraints for Planet Formation. *ArXiv e-prints*, October 2016.

Baptiste Lavie, João M. Mendonça, Christoph Mordasini, Matej Malik, Mickaël Bonnefoy, Brice-Olivier Demory, Maria Oreshenko, Simon L. Grimm, David Ehrenreich, and Kevin Heng. HELIOS-RETRIEVAL: An Open-source, Nested Sampling Atmospheric Retrieval Code; Application to the HR 8799 Exoplanets and Inferred Constraints for Planet Formation. *AJ*, 154: 91, September 2017. doi: 10.3847/1538-3881/aa7ed8.

Yann LeCun, Bernhard E. Boser, John S. Denker, Donnie Henderson, Richard E. Howard, Wayne E. Hubbard, and Lawrence D. Jackel. Backpropagation applied to handwritten zip code recognition. *Neural Computation*, 1(4):541–551, 1989. doi: 10.1162/neco.1989.1.4.541. URL `https://doi.org/10.1162/neco.1989.1.4.541`.

C. Ledig, L. Theis, F. Huszar, J. Caballero, A. Cunningham, A. Acosta, A. Aitken, A. Tejani, J. Totz, Z. Wang, and W. Shi. Photo-Realistic Single Image Super-Resolution Using a Generative Adversarial Network. *ArXiv e-prints*, September 2016.

J.-M. Lee, K. Heng, and P. G. J. Irwin. Atmospheric Retrieval Analysis of the Directly Imaged Exoplanet HR 8799b. *ApJ*, 778:97, December 2013a. doi: 10.1088/0004-637X/778/2/97.

J.-M. Lee, K. Heng, and P. G. J. Irwin. Atmospheric Retrieval Analysis of the Directly Imaged Exoplanet HR 8799b. *ApJ*, 778:97, December 2013b. doi: 10.1088/0004-637X/778/2/97.

M. R. Line and V. Parmentier. The Influence of Nonuniform Cloud Cover on Transit Transmission Spectra. *ApJ*, 820:78, March 2016a. doi: 10.3847/0004-637X/820/1/78.

M. R. Line and V. Parmentier. The Influence of Nonuniform Cloud Cover on Transit Transmission Spectra. *ApJ*, 820:78, March 2016b. doi: 10.3847/0004-637X/820/1/78.

M. R. Line, A. Wolf, X. Zhang, and Y. Yung. Characteriztion of Exoplanet Atmospheres: Spectral Retrieval and Chemistry. In *American Astronomical Society Meeting Abstracts #221*, volume 221 of *American Astronomical Society Meeting Abstracts*, page 224.02, January 2013.

M. R. Line, K. B. Stevenson, J. Bean, J.-M. Desert, J. J. Fortney, L. Kreidberg, N. Madhusudhan, A. P. Showman, and H. Diamond-Lowe. No Thermal Inversion and a Solar Water Abundance for the Hot Jupiter HD 209458b from HST/WFC3 Spectroscopy. *AJ*, 152:203, December 2016. doi: 10.3847/0004-6256/152/6/203.

Michael R Line, Aaron S Wolf, Xi Zhang, Heather Knutson, Joshua A Kammer, Elias Ellison, Pieter Deroo, Dave Crisp, and Yuk L Yung. A Systematic Retrieval Analysis of Secondary Eclipse Spectra. I. A Comparison of Atmospheric Retrieval Techniques. *The Astrophysical Journal*, 775(2):137, October 2013.

K.N. Liou. *An Introduction to Atmospheric Radiation*. International Geophysics. Elsevier Science, 2002. ISBN 9780080491677. URL `https://books.google.it/books?id=mQ1DiDpX34UC`.

Alexandra C. Lockwood, John A. Johnson, Chad F. Bender, John S. Carr, Travis Barman, Alexander J. W. Richert, and Geoffrey A. Blake. Near-IR Direct Detection of Water Vapor in Tau Boötis b. *ApJ*, 783:L29, March 2014. doi: 10.1088/2041-8205/783/2/L29.

L.V. Lorenz. *Lysbevaegelsen i og uden for en af plane Lysbølger belyst kugle*. 8Det- Kongelige Danske Videnskabernes Selskabs skrifter: Naturvidenskabelig og Mathematisk Afdeling. Luno, 1890. URL `https://books.google.it/books?id=loKFAQAACAAJ`.

Roxana E. Lupu, Mark S. Marley, Nikole Lewis, Michael Line, Wesley A. Traub, and Kevin Zahnle. Developing Atmospheric Retrieval Methods for Direct Imaging Spectroscopy of Gas Giants in Reflected Light. I. Methane Abundances and Basic Cloud Properties. *AJ*, 152:217, December 2016. doi: 10.3847/0004-6256/152/6/217.

R. J. MacDonald and N. Madhusudhan. HD 209458b in new light: evidence of nitrogen chemistry, patchy clouds and sub-solar water. *MNRAS*, 469:1979–1996, August 2017. doi: 10.1093/mnras/stx804.

B. Macintosh, Gemini Planet Imager instrument Team, G. Planet Imager Exoplanet Survey, and G. Observatory. The Gemini Planet Imager. In *American Astronomical Society Meeting Abstracts #223*, volume 223 of *American Astronomical Society Meeting Abstracts*, page 229.02, January 2014.

B. Macintosh, J. R. Graham, T. Barman, R. J. De Rosa, Q. Konopacky, M. S. Marley, C. Marois, E. L. Nielsen, L. Pueyo, A. Rajan, J. Rameau, D. Saumon, J. J. Wang, J. Patience, M. Ammons, P. Arriaga, E. Artigau, S. Beckwith, J. Brewster, S. Bruzzone, J. Bulger, B. Burningham, A. S. Burrows, C. Chen, E. Chiang, J. K. Chilcote, R. I. Dawson, R. Dong, R. Doyon, Z. H. Draper, G. Duchêne, T. M. Esposito, D. Fabrycky, M. P. Fitzgerald, K. B. Follette, J. J. Fortney, B. Gerard, S. Goodsell, A. Z. Greenbaum, P. Hibon, S. Hinkley, T. H. Cotten, L. W. Hung, P. Ingraham, M. Johnson-Groh, P. Kalas, D. Lafreniere, J. E. Larkin, J. Lee, M. Line, D. Long, J. Maire, F. Marchis, B. C. Matthews, C. E. Max, S. Metchev,

M. A. Millar-Blanchaer, T. Mittal, C. V. Morley, K. M. Morzinski, R. Murray-Clay, R. Oppenheimer, D. W. Palmer, R. Patel, M. D. Perrin, L. A. Poyneer, R. R. Rafikov, F. T. Rantakyrö, E. L. Rice, P. Rojo, A. R. Rudy, J. B. Ruffio, M. T. Ruiz, N. Sadakuni, L. Saddlemyer, M. Salama, D. Savransky, A. C. Schneider, A. Sivaramakrishnan, I. Song, R. Soummer, S. Thomas, G. Vasisht, J. K. Wallace, K. Ward- Duong, S. J. Wiktorowicz, S. G. Wolff, and B. Zuckerman. Discovery and spectroscopy of the young jovian planet 51 Eri b with the Gemini Planet Imager. *Science*, 350:64–67, October 2015. doi: 10.1126/science.aac5891.

Bruce A Macintosh, J R Graham, T S Barman, R J De Rosa, Q Konopacky, M S Marley, C Marois, E L Nielsen, L Pueyo, A Rajan, J Rameau, D Saumon, J J Wang, J Patience, M Ammons, P Arriaga, E Artigau, S Beckwith, J Brewster, S Bruzzone, J Bulger, B Burningham, A S Burrows, C Chen, E Chiang, J K Chilcote, R I Dawson, R Dong, R Doyon, Z H Draper, G Duchêne, T M Esposito, D Fabrycky, M P Fitzgerald, K B Follette, J Fortney, B Gerard, S Goodsell, A Z Greenbaum, P Hibon, S Hinkley, T H Cotten, L W Hung, P Ingraham, M Johnson-Groh, P Kalas, D Lafrenière, J E Larkin, J Lee, M Line, D Long, J Maire, F Marchis, B C Matthews, C E Max, S Metchev, M A Millar-Blanchaer, T Mittal, C V Morley, K M Morzinski, R Murray-Clay, R Oppenheimer, D W Palmer, R Patel, M D Perrin, L A Poyneer, R R Rafikov, F T Rantakyrö, E L Rice, P Rojo, A R Rudy, J B Ruffio, M T Ruiz, N Sadakuni, L Saddlemyer, M Salama, D Savransky, A C Schneider, A Sivaramakrishnan, I Song, R Soummer, S Thomas, G Vasisht, J K Wallace, K Ward-Duong, S J Wiktorowicz, S G Wolff, and B Zuckerman. Discovery and spectroscopy of the young jovian planet 51 Eri b with the Gemini Planet Imager. *Science*, 350(6):64–67, October 2015.

N. Madhusudhan and A. Burrows. Analytic Models for Albedos, Phase Curves, and Polarization of Reflected Light from Exoplanets. *ApJ*, 747:25, March 2012. doi: 10.1088/0004-637X/747/1/25.

N Madhusudhan and S Seager. A Temperature and Abundance Retrieval Method for Exoplanet Atmospheres. *The Astrophysical Journal*, 707(1):24–39, December 2009.

A. Makhzani, J. Shlens, N. Jaitly, I. Goodfellow, and B. Frey. Adversarial Autoencoders. *ArXiv e-prints*, November 2015.

Avi M Mandell, Avi M Mandell, K Haynes, Evan Sinukoff, Nikku Madhusudhan, A Burrows, and D Deming. Exoplanet Transit Spectroscopy Using WFC3: WASP-12 b, WASP-17 b, and WASP-19 b. *ApJ*, 779(2):128, December 2013.

M. Mansfield, J. L. Bean, M. R. Line, V. Parmentier, L. Kreidberg, J.-M. Desert, J. J. Fortney,

K. B. Stevenson, J. Arcangeli, and D. Dragomir. A HST/WFC3 Thermal Emission Spectrum of the Hot Jupiter HAT-P-7b. *ArXiv e-prints*, May 2018.

G. W. Marcy and R. P. Butler. Precision radial velocities with an iodine absorption cell. *Publications of the ASP*, 104:270–277, April 1992. doi: 10.1086/132989.

M. S. Marley, R. Freedman, and J. I. Lunine. The Cloudy Atmospheres of Brown Dwarfs: Lessons for Direct Detection of Extrasolar Giant Planets. In *AAS/Division for Planetary Sciences Meeting Abstracts #31*, page 02.03, September 1999.

Mark S. Marley and Sujan Sengupta. Probing the physical properties of directly imaged gas giant exoplanets through polarization. *MNRAS*, 417:2874–2881, November 2011. doi: 10.1111/j.1365-2966.2011.19448.x.

P. Márquez-Neila, C. Fisher, R. Sznitman, and K. Heng. Supervised machine learning for analysing spectra of exoplanetary atmospheres. *Nature Astronomy*, June 2018. doi: 10.1038/s41550-018-0504-2.

A. W. Mayo, A. Vanderburg, D. W. Latham, A. Bieryla, T. D. Morton, L. A. Buchhave, C. D. Dressing, C. Beichman, P. Berlind, M. L. Calkins, D. R. Ciardi, I. J. M. Crossfield, G. A. Esquerdo, M. E. Everett, E. J. Gonzales, L. A. Hirsch, E. P. Horch, A. W. Howard, S. B. Howell, J. Livingston, R. Patel, E. A. Petigura, J. E. Schlieder, N. J. Scott, C. F. Schumer, E. Sinukoff, J. Teske, and J. G. Winters. 275 Candidates and 149 Validated Planets Orbiting Bright Stars in K2 Campaigns 0-10. *AJ*, 155:136, March 2018. doi: 10.3847/1538-3881/aaadff.

M. Mayor and D. Queloz. A Jupiter-mass companion to a solar-type star. *Nature*, 378:355–359, November 1995. doi: 10.1038/378355a0.

P. R. McCullough, N. Crouzet, D. Deming, and N. Madhusudhan. Water Vapor in the Spectrum of the Extrasolar Planet HD 189733b. I. The Transit. *ApJ*, 791:55, August 2014. doi: 10.1088/0004-637X/791/1/55.

L. K. McKemmish, S. N. Yurchenko, and J. Tennyson. ExoMol line lists - XVIII. The high-temperature spectrum of VO. *MNRAS*, 463:771–793, November 2016. doi: 10.1093/mnras/stw1969.

R. S. McMillan, T. L. Moore, M. L. Perry, and P. H. Smith. Long, accurate time series measurements of radial velocities of solar-type stars. *Astrophysics and Space Science*, 212:271–280, February 1994. doi: 10.1007/BF00984531.

Nicholas Metropolis, Arianna W. Rosenbluth, Marshall N. Rosenbluth, Augusta H. Teller, and Edward Teller. Equation of state calculations by fast computing machines. 21(6): 1087–1092, June 1953. ISSN 0021-9606 (print), 1089-7690 (electronic). doi: https://doi.org/10.1063/1.1699114. URL http://link.aip.org/link/doi/10.1063/1.1699114;http://pubs.acs.org/cgi-bin/chemport/version=1.0&coi=1:CAS:528:DyaG3sXltlKhsw%253D%253D&pissn=0095-2338&pyear=2005&&md5=2eba6ee7d50b361b924c3ff8efeda4b1. This article introduces the Metropolis algorithm, which the journal *Computing in Science and Engineering* cited in the top 10 algorithms having the "greatest influence on the development and practice of science and engineering in the 20th Century." See **??**, and the Hasting–Metropolis generalization in Hastings (1970). See also **???**. According to (**?**, page 263), this paper has been cited more than 10,000 times.

L. Metz, B. Poole, D. Pfau, and J. Sohl-Dickstein. Unrolled Generative Adversarial Networks. *ArXiv e-prints*, November 2016.

Assaf Michaely, Carolina Parada, Frank Zhang, Gabor Simko, and Petar Aleksic. Keyword spotting for google assistant using contextual speech recognition. In *ASRU 2017*, 2017.

Gustav Mie. BeitrÃďge zur optik trÃijber medien, speziell kolloidaler metallÃűsungen. *Annalen der Physik*, 330(3):377–445, 1908. doi: 10.1002/andp.19083300302. URL https://onlinelibrary.wiley.com/doi/abs/10.1002/andp.19083300302.

E. Miller-Ricci Kempton, K. Zahnle, and J. J. Fortney. The Atmospheric Chemistry of GJ 1214b: Photochemistry and Clouds. *ApJ*, 745:3, January 2012. doi: 10.1088/0004-637X/745/1/3.

G. Morello, I. P. Waldmann, G. Tinetti, I. D. Howarth, G. Micela, and F. Allard. Revisiting Spitzer Transit Observations with Independent Component Analysis: New Results for the GJ 436 System. *ApJ*, 802:117, April 2015. doi: 10.1088/0004-637X/802/2/117.

G. D. Mulders, I. Pascucci, and D. Apai. An Increase in the Mass of Planetary Systems around Lower-mass Stars. *ApJ*, 814:130, December 2015. doi: 10.1088/0004-637X/814/2/130.

G. D. Mulders, I. Pascucci, D. Apai, A. Frasca, and J. Molenda-Zakowicz. A Super-Solar Metallicity For Stars With Hot Rocky Exoplanets. *ArXiv e-prints*, September 2016.

C. Corral Van Damme K. Isaak F. Ratti P. Verhoeve F. Safa R. Southworth C. Broeg W. Benz N. Rando, J. Asquier. Cheops: the esa mission for exo-planets characterization, 2018. URL https://doi.org/10.1117/12.2311300.

K. I. Öberg, A. C. A. Boogert, K. M. Pontoppidan, S. van den Broek, E. F. van Dishoeck, S. Bottinelli, G. A. Blake, and N. J. Evans, II. The Spitzer Ice Legacy: Ice Evolution from Cores to Protostars. *ApJ*, 740:109, October 2011. doi: 10.1088/0004-637X/740/2/109.

Heeyoung Oh, S. Pak, I. Yuk, D. T. Jaffe, C. Park, S. Lee, S. Lee, M. Chun, H. Lee, J. Strubhar, K. Kim, T. Pyo, H. Seo, and S. I. Barnes. The Calibration System for IGRINS, a High Resolution Near-IR Spectrograph. In *American Astronomical Society Meeting Abstracts #216*, volume 216, page 415.10, May 2010.

J. Olivero. Empirical fits to the Voigt line width: A brief review. *J. Quant. Spec. Radiat. Transf.*, 17:233–236, February 1977. doi: 10.1016/0022-4073(77)90161-3.

Wanli Ouyang, Xiaogang Wang, Xingyu Zeng, Shi Qiu, Ping Luo, Yonglong Tian, Hongsheng Li, Shuo Yang, Zhe Wang, Chen-Change Loy, et al. Deepid-net: Deformable deep convolutional neural networks for object detection. In *Proceedings of the IEEE Conference on Computer Vision and Pattern Recognition*, pages 2403–2412, 2015.

Ovid and Martin. *Metamorphoses*. 2004.

E. Pascale, I. P. Waldmann, C. J. MacTavish, A. Papageorgiou, A. Amaral-Rogers, R. Varley, V. Coudé du Foresto, M. J. Griffin, M. Ollivier, S. Sarkar, L. Spencer, B. M. Swinyard, M. Tessenyi, and G. Tinetti. EChOSim: The Exoplanet Characterisation Observatory software simulator. *Experimental Astronomy*, 40:601–619, December 2015. doi: 10.1007/s10686-015-9471-0.

Enzo Pascale, Naidu Bezawada, Joanna Barstow, Jean-Philippe Beaulieu, Neil Bowles, Vincent Coudé du Foresto, Athena Coustenis, Leen Decin, Pierre Drossart, Paul Eccleston, Therese Encrenaz, Francois Forget, Matt Griffin, Manuel Güdel, Paul Hartogh, Astrid Heske, Pierre-Olivier Lagage, Jeremy Leconte, Pino Malaguti, Giusi Micela, Kevin Middleton, Michiel Min, Andrea Moneti, Juan Carlos Morales, Lorenzo Mugnai, Marc Ollivier, Emanuele Pace, Andreas Papageorgiou, Goran Pilbratt, Ludovic Puig, Miroslaw Rataj, Tom Ray, Ignasi Ribas, Marco Rocchetto, Subhajit Sarkar, Franck Selsis, William Taylor, Jonathan Tennyson, Giovanna Tinetti, Diego Turrini, Bart Vandenbussche, Olivia Venot, Ingo P. Waldmann, Paulina Wolkenberg, Gillian Wright, Maria-Rosa Zapatero Osorio, and Tiziano Zingales. The ARIEL space mission. In *Society of Photo-Optical Instrumentation Engineers (SPIE) Conference Series*, volume 10698, page 106980H, July 2018. doi: 10.1117/12.2311838.

Deepak Pathak, Philipp Krähenbühl, Jeff Donahue, Trevor Darrell, and Alexei Efros. Con-

text encoders: Feature learning by inpainting. In *Computer Vision and Pattern Recognition (CVPR)*, 2016.

A. G. Pavelev. Concerning the solution of the inverse problem of refraction. *Radiotekhnika i Elektronika*, 25:2504–2509, December 1980.

Kyle A. Pearson, Leon Palafox, and Caitlin A. Griffith. Searching for exoplanets using artificial intelligence. *MNRAS*, 474:478–491, February 2018. doi: 10.1093/mnras/stx2761.

A. S. Pine. Self-, N2, O2, H2, Ar, and He broadening in the nu3 band Q branch of CH4. *J. Chem. Phys.*, 97:773–785, July 1992. doi: 10.1063/1.463943.

D. Piskorz, H. A. Knutson, H. Ngo, P. S. Muirhead, K. Batygin, J. R. Crepp, S. Hinkley, and T. D. Morton. Friends of Hot Jupiters. III. An Infrared Spectroscopic Search for Low-mass Stellar Companions. *ApJ*, 814:148, December 2015. doi: 10.1088/0004-637X/814/2/148.

David Poole, Alan Mackworth, and Randy Goebel. *Computational Intelligence: A Logical Approach*. Oxford University Press, Inc., New York, NY, USA, 1997. ISBN 0-19-510270-3.

L. Y. Pratt. Non-literal transfer among neural network learners. pages 92–04. Chapman and Hall, 1993.

L. Puig, K. Isaak, M. Linder, I. Escudero, P.-E. Crouzet, R. Walker, M. Ehle, J. Hübner, R. Timm, B. de Vogeleer, P. Drossart, P. Hartogh, C. Lovis, G. Micela, M. Ollivier, I. Ribas, I. Snellen, B. Swinyard, G. Tinetti, and P. Eccleston. The phase 0/A study of the ESA M3 mission candidate EChO. *Experimental Astronomy*, 40:393–425, December 2015. doi: 10.1007/s10686-014-9419-9.

E. Racah, C. Beckham, T. Maharaj, S. Ebrahimi Kahou, Prabhat, and C. Pal. ExtremeWeather: A large-scale climate dataset for semi-supervised detection, localization, and understanding of extreme weather events. *ArXiv e-prints*, December 2016.

A. Radford, L. Metz, and S. Chintala. Unsupervised Representation Learning with Deep Convolutional Generative Adversarial Networks. *ArXiv e-prints*, November 2015.

H. Rauer, C. Catala, C. Aerts, T. Appourchaux, W. Benz, A. Brandeker, J. Christensen-Dalsgaard, M. Deleuil, L. Gizon, M. J. Goupil, M. Güdel, E. Janot-Pacheco, M. Mas-Hesse, I. Pagano, G. Piotto, D. Pollacco, Ċ. Santos, A. Smith, J. C. Suárez, R. Szabó, S. Udry, V. Adibekyan, Y. Alibert, J. M. Almenara, P. Amaro-Seoane, M. Ammler-von Eiff, M. Asplund, E. Antonello, S. Barnes, F. Baudin, K. Belkacem, M. Bergemann, G. Bihain, A. C. Birch, X. Bonfils, I. Boisse, A. S. Bonomo, F. Borsa, I. M. Brandão, E. Brocato, S. Brun,

M. Burleigh, R. Burston, J. Cabrera, S. Cassisi, W. Chaplin, S. Charpinet, C. Chiappini, R. P. Church, Sz. Csizmadia, M. Cunha, M. Damasso, M. B. Davies, H. J. Deeg, R. F. Díaz, S. Dreizler, C. Dreyer, P. Eggenberger, D. Ehrenreich, P. Eigmüller, A. Erikson, R. Farmer, S. Feltzing, F. de Oliveira Fialho, P. Figueira, T. Forveille, M. Fridlund, R. A. García, P. Giommi, G. Giuffrida, M. Godolt, J. Gomes da Silva, T. Granzer, J. L. Grenfell, A. Grotsch-Noels, E. Günther, C. A. Haswell, A. P. Hatzes, G. Hébrard, S. Hekker, R. Helled, K. Heng, J. M. Jenkins, A. Johansen, M. L. Khodachenko, K. G. Kislyakova, W. Kley, U. Kolb, N. Krivova, F. Kupka, H. Lammer, A. F. Lanza, Y. Lebreton, D. Magrin, P. Marcos-Arenal, P. M. Marrese, J. P. Marques, J. Martins, S. Mathis, S. Mathur, S. Messina, A. Miglio, J. Montalban, M. Montalto, M. J. P. F. G. Monteiro, H. Moradi, E. Moravveji, C. Mordasini, T. Morel, A. Mortier, V. Nascimbeni, R. P. Nelson, M. B. Nielsen, L. Noack, A. J. Norton, A. Ofir, M. Oshagh, R. M. Ouazzani, P. Pápics, V. C. Parro, P. Petit, B. Plez, E. Poretti, A. Quirrenbach, R. Ragazzoni, G. Raimondo, M. Rainer, D. R. Reese, R. Redmer, S. Reffert, B. Rojas-Ayala, I. W. Roxburgh, S. Salmon, A. Santerne, J. Schneider, J. Schou, S. Schuh, H. Schunker, A. Silva-Valio, R. Silvotti, I. Skillen, I. Snellen, F. Sohl, S. G. Sousa, A. Sozzetti, D. Stello, K. G. Strassmeier, M. Švanda, Gy. M. Szabó, A. Tkachenko, D. Valencia, V. Van Grootel, S. D. Vauclair, P. Ventura, F. W. Wagner, N. A. Walton, J. Weingrill, S. C. Werner, P. J. Wheatley, and K. Zwintz. The PLATO 2.0 mission. *Experimental Astronomy*, 38:249–330, November 2014. doi: 10.1007/s10686-014-9383-4.

S. Ravanbakhsh, F. Lanusse, R. Mandelbaum, J. Schneider, and B. Poczos. Enabling Dark Energy Science with Deep Generative Models of Galaxy Images. *ArXiv e-prints*, September 2016.

John Rayner, Tim Bond, Morgan Bonnet, Dan Jaffe, Gary Muller, and Alan Tokunaga. iSHELL: a 1-5 micron cross-dispersed R=70,000 immersion grating spectrograph for IRTF. In *Ground-based and Airborne Instrumentation for Astronomy IV*, volume 8446, page 84462C, September 2012. doi: 10.1117/12.925511.

S. Redfield, M. Endl, W. D. Cochran, and L. Koesterke. Sodium Absorption from the Exoplanetary Atmosphere of HD 189733b Detected in the Optical Transmission Spectrum. *ApJl*, 673: L87–L90, January 2008. doi: 10.1086/527475.

Shaoqing Ren, Kaiming He, R Girshick, and Jian Sun. Faster r-cnn: Towards real-time object detection with region proposal networks,(2015). *arXiv preprint arXiv:1506.01497*, 2015.

I. Ribas and C. Lovis. Echo targets: the mission reference sample and beyond [echo-sre-saphasea-001_mrsv2.4], european space agency, 2013.

C. Richard, I. E. Gordon, L. S. Rothman, M. Abel, L. Frommhold, M. Gustafsson, J.-M. Hartmann, C. Hermans, W. J. Lafferty, G. S. Orton, K. M. Smith, and H. Tran. New section of the HITRAN database: Collision-induced absorption (CIA). *J. Quant. Spec. Radiat. Transf.*, 113:1276–1285, July 2012. doi: 10.1016/j.jqsrt.2011.11.004.

L Jeremy Richardson, D Deming, K Horning, Sara Seager, and J Harrington. A spectrum of an extrasolar planet. *Nature*, 445(7):892–895, February 2007.

Lee J. Richardson, D. Deming, K. Horning, S. Seager, and J. Harrington. Emission Spectra of Transiting Extrasolar Planets with Spitzer. In *American Astronomical Society Meeting Abstracts #210*, volume 210, page 102.04, May 2007.

G. R. Ricker. The Transiting Exoplanet Survey Satellite Mission. *Journal of the American Association of Variable Star Observers (JAAVSO)*, 42:234, June 2014.

G. R. Ricker, J. N. Winn, R. Vanderspek, D. W. Latham, G. Á. Bakos, J. L. Bean, Z. K. Berta-Thompson, T. M. Brown, L. Buchhave, N. R. Butler, R. P. Butler, W. J. Chaplin, D. Charbonneau, J. Christensen-Dalsgaard, M. Clampin, D. Deming, J. Doty, N. De Lee, C. Dressing, E. W. Dunham, M. Endl, F. Fressin, J. Ge, T. Henning, M. J. Holman, A. W. Howard, S. Ida, J. M. Jenkins, G. Jernigan, J. A. Johnson, L. Kaltenegger, N. Kawai, H. Kjeldsen, G. Laughlin, A. M. Levine, D. Lin, J. J. Lissauer, P. MacQueen, G. Marcy, P. R. McCullough, T. D. Morton, N. Narita, M. Paegert, E. Palle, F. Pepe, J. Pepper, A. Quirrenbach, S. A. Rinehart, D. Sasselov, B. Sato, S. Seager, A. Sozzetti, K. G. Stassun, P. Sullivan, A. Szentgyorgyi, G. Torres, S. Udry, and J. Villasenor. Transiting Exoplanet Survey Satellite (TESS). *Journal of Astronomical Telescopes, Instruments, and Systems*, 1(1):014003, January 2015. doi: 10.1117/1.JATIS.1.1.014003.

G. R. Ricker, R. Vanderspek, J. Winn, S. Seager, Z. Berta-Thompson, A. Levine, J. Villasenor, D. Latham, D. Charbonneau, M. Holman, J. Johnson, D. Sasselov, A. Szentgyorgyi, G. Torres, G. Bakos, T. Brown, J. Christensen-Dalsgaard, H. Kjeldsen, M. Clampin, S. Rinehart, D. Deming, J. Doty, E. Dunham, S. Ida, N. Kawai, B. Sato, J. Jenkins, J. Lissauer, G. Jernigan, L. Kaltenegger, G. Laughlin, D. Lin, P. McCullough, N. Narita, J. Pepper, K. Stassun, and S. Udry. The Transiting Exoplanet Survey Satellite. In *Space Telescopes and Instrumentation 2016: Optical, Infrared, and Millimeter Wave*, volume 9904 of *Proc. SPIE*, page 99042B, July 2016. doi: 10.1117/12.2232071.

Martin Riedmiller and Heinrich Braun. A direct adaptive method for faster backpropagation

learning: The rprop algorithm. In *IEEE INTERNATIONAL CONFERENCE ON NEURAL NETWORKS*, pages 586–591, 1993.

M. Rocchetto, I. P. Waldmann, O. Venot, P. O. Lagage, and G. Tinetti. Exploring Biases of Atmospheric Retrievals in Simulated JWST Transmission Spectra of Hot Jupiters. *ApJ*, 833: 120, December 2016a. doi: 10.3847/1538-4357/833/1/120.

M. Rocchetto, I. P. Waldmann, O. Venot, P.-O. Lagage, and G. Tinetti. Exploring Biases of Atmospheric Retrievals in Simulated JWST Transmission Spectra of Hot Jupiters. *ApJ*, 833: 120, December 2016b. doi: 10.3847/1538-4357/833/1/120.

F. Rodler, M. Lopez-Morales, and I. Ribas. Weighing the Non-transiting Hot Jupiter τ Boo b. *ApJ*, 753:L25, July 2012. doi: 10.1088/2041-8205/753/1/L25.

F. Rodler, M. Kürster, and J. R. Barnes. Detection of CO absorption in the atmosphere of the hot Jupiter HD 189733b. *MNRAS*, 432:1980–1988, July 2013. doi: 10.1093/mnras/stt462.

A. C Rodriguez, T. Kacprzak, A. Lucchi, A. Amara, R. Sgier, J. Fluri, T. Hofmann, and A. Réfrégier. Fast Cosmic Web Simulations with Generative Adversarial Networks. *ArXiv e-prints*, January 2018.

M. Rosca, B. Lakshminarayanan, D. Warde-Farley, and S. Mohamed. Variational Approaches for Auto-Encoding Generative Adversarial Networks. *ArXiv e-prints*, June 2017.

L. S. Rothman, I. E. Gordon, R. J. Barber, H. Dothe, R. R. Gamache, A. Goldman, V. I. Perevalov, S. A. Tashkun, and J. Tennyson. HITEMP, the high-temperature molecular spectroscopic database. *J. Quant. Spec. Radiat. Transf.*, 111:2139–2150, October 2010. doi: 10.1016/j.jqsrt.2010.05.001.

L. S. Rothman, I. E. Gordon, Y. Babikov, A. Barbe, D. Chris Benner, P. F. Bernath, M. Birk, L. Bizzocchi, V. Boudon, L. R. Brown, A. Campargue, K. Chance, E. A. Cohen, L. H. Coudert, V. M. Devi, B. J. Drouin, A. Fayt, J.-M. Flaud, R. R. Gamache, J. J. Harrison, J.-M. Hartmann, C. Hill, J. T. Hodges, D. Jacquemart, A. Jolly, J. Lamouroux, R. J. Le Roy, G. Li, D. A. Long, O. M. Lyulin, C. J. Mackie, S. T. Massie, S. Mikhailenko, H. S. P. Müller, O. V. Naumenko, A. V. Nikitin, J. Orphal, V. Perevalov, A. Perrin, E. R. Polovtseva, C. Richard, M. A. H. Smith, E. Starikova, K. Sung, S. Tashkun, J. Tennyson, G. C. Toon, V. G. Tyuterev, and G. Wagner. The HITRAN2012 molecular spectroscopic database. *J. Quant. Spec. Radiat. Transf.*, 130:4–50, November 2013. doi: 10.1016/j.jqsrt.2013.07.002.

S. Ruder. An overview of gradient descent optimization algorithms. *ArXiv e-prints*, September 2016.

D. E. Rumelhart, G. E. Hinton, and R. J. Williams. Parallel distributed processing: Explorations in the microstructure of cognition, vol. 1. chapter Learning Internal Representations by Error Propagation, pages 318–362. MIT Press, Cambridge, MA, USA, 1986. ISBN 0-262-68053-X. URL http://dl.acm.org/citation.cfm?id=104279.104293.

Olga Russakovsky, Jia Deng, Hao Su, Jonathan Krause, Sanjeev Satheesh, Sean Ma, Zhiheng Huang, Andrej Karpathy, Aditya Khosla, Michael Bernstein, Alexander C. Berg, and Li Fei-Fei. Imagenet large scale visual recognition challenge. *International Journal of Computer Vision*, 115(3):211–252, Dec 2015. ISSN 1573-1405. doi: 10.1007/s11263-015-0816-y. URL https://doi.org/10.1007/s11263-015-0816-y.

Y. Saatchi and A. G. Wilson. Bayesian GAN. *ArXiv e-prints*, May 2017.

T. Salimans, I. Goodfellow, W. Zaremba, V. Cheung, A. Radford, and X. Chen. Improved Techniques for Training GANs. *ArXiv e-prints*, June 2016.

A. L. Samuel. Some studies in machine learning using the game of checkers. *IBM J. Res. Dev.*, 3(3):210–229, July 1959. ISSN 0018-8646. doi: 10.1147/rd.33.0210. URL http://dx.doi.org/10.1147/rd.33.0210.

S. Sarkar and E. Pascale. ExoSim: a novel simulator of exoplanet spectroscopic observations. *European Planetary Science Congress 2015, held 27 September - 2 October, 2015 in Nantes, France, Online at <A href="http://meetingorganizer.copernicus.org/EPSC2015/EPSC2015"> http://meetingorganizer.copernicus.org/EPSC2015</A>, id.EPSC2015-187*, 10:EPSC2015-187, October 2015.

S. Sarkar, A. Papageorgiou, and E. Pascale. Exploring the potential of the ExoSim simulator for transit spectroscopy noise estimation. In *Space Telescopes and Instrumentation 2016: Optical, Infrared, and Millimeter Wave*, volume 9904, page 99043R, July 2016. doi: 10.1117/12.2234216.

B. Sato, J. D. Hartman, G. Á. Bakos, B. Béky, G. Torres, D. W. Latham, G. Kovács, Z. Csubry, K. Penev, R. W. Noyes, L. A. Buchhave, S. N. Quinn, M. Everett, G. A. Esquerdo, D. A. Fischer, A. W. Howard, J. A. Johnson, G. W. Marcy, D. D. Sasselov, T. Szklenár, J. Lázár, I. Papp, and P. Sári. HAT-P-38b: A Saturn-Mass Planet Transiting a Late G Star. *PASJ*, 64: 97, October 2012. doi: 10.1093/pasj/64.5.97.

Thomas Schatz, Francis Bach, and Emmanuel Dupoux. Evaluating automatic speech recognition

systems as quantitative models of cross-lingual phonetic category perception. *The Journal of the Acoustical Society of America*, 143(5):EL372–EL378, 2018.

Kevin Schawinski, Ce Zhang, Hantian Zhang, Lucas Fowler, and Gokula Krishnan Santhanam. Generative adversarial networks recover features in astrophysical images of galaxies beyond the deconvolution limit. *Monthly Notices of the Royal Astronomical Society: Letters*, 467(1): L110–L114, 2017. doi: 10.1093/mnrasl/slx008. URL `http://dx.doi.org/10.1093/mnrasl/slx008`.

S. Seager, B. A. Whitney, and D. D. Sasselov. Photometric Light Curves and Polarization of Close-in Extrasolar Giant Planets. *ApJ*, 540:504–520, September 2000. doi: 10.1086/309292.

Thomas Sellke, M. J. Bayarri, and James O. Berger. Calibration of p values for testing precise null hypotheses. *The American Statistician*, 55(1):62–71, 2001. ISSN 00031305. URL `http://www.jstor.org/stable/2685531`.

C. J. Shallue and A. Vanderburg. Identifying Exoplanets with Deep Learning: A Five-planet Resonant Chain around Kepler-80 and an Eighth Planet around Kepler-90. *AJ*, 155:94, February 2018. doi: 10.3847/1538-3881/aa9e09.

Kyle B. Sheppard, Avi M. Mandell, Patrick Tamburo, Siddharth Gandhi, Arazi Pinhas, Nikku Madhusudhan, and Drake Deming. Evidence for a dayside thermal inversion and high metallicity for the hot jupiter wasp-18b. *The Astrophysical Journal Letters*, 850(2):L32, 2017. URL `http://stacks.iop.org/2041-8205/850/i=2/a=L32`.

Mor-Yosef Shlomo, Zeevi Dan, Samueloff Arnon, Donhin Milka, Frankfurter Hadassah, and Schenker Joseph G. Vaginal delivery following one previous cesarean birth: Nation wide survey. *Asia-Oceania Journal of Obstetrics and Gynaecology*, 16(1):33–37, 1990. doi: 10.1111/j.1447-0756.1990.tb00212.x. URL `https://obgyn.onlinelibrary.wiley.com/doi/abs/10.1111/j.1447-0756.1990.tb00212.x`.

Adam P. Showman and Lorenzo M. Polvani. Equatorial Superrotation on Tidally Locked Exoplanets. *ApJ*, 738:71, September 2011. doi: 10.1088/0004-637X/738/1/71.

David Silver, Julian Schrittwieser, Karen Simonyan, Ioannis Antonoglou, Aja Huang, Arthur Guez, Thomas Hubert, Lucas Baker, Matthew Lai, Adrian Bolton, Yutian Chen, Timothy Lillicrap, Fan Hui, Laurent Sifre, George van den Driessche, Thore Graepel, and Demis Hassabis. Mastering the game of go without human knowledge. *Nature*, 550:354–, October 2017. URL `http://dx.doi.org/10.1038/nature24270`.

D. K. Sing, H. R. Wakeford, A. P. Showman, N. Nikolov, J. J. Fortney, A. S. Burrows, G. E. Ballester, D. Deming, S. Aigrain, J.-M. Désert, N. P. Gibson, G. W. Henry, H. Knutson, A. Lecavelier des Etangs, F. Pont, A. Vidal-Madjar, M. W. Williamson, and P. A. Wilson. HST hot-Jupiter transmission spectral survey: detection of potassium in WASP-31b along with a cloud deck and Rayleigh scattering. *MNRAS*, 446:2428–2443, January 2015. doi: 10.1093/mnras/stu2279.

D. K. Sing, J. J. Fortney, N. Nikolov, H. R. Wakeford, T. Kataria, T. M. Evans, S. Aigrain, G. E. Ballester, A. S. Burrows, D. Deming, J.-M. Désert, N. P. Gibson, G. W. Henry, C. M. Huitson, H. A. Knutson, A. Lecavelier Des Etangs, F. Pont, A. P. Showman, A. Vidal-Madjar, M. H. Williamson, and P. A. Wilson. A continuum from clear to cloudy hot-Jupiter exoplanets without primordial water depletion. *Nature*, 529:59–62, January 2016a. doi: 10.1038/nature16068.

D. K. Sing, J. J. Fortney, N. Nikolov, H. R. Wakeford, T. Kataria, T. M. Evans, S. Aigrain, G. E. Ballester, A. S. Burrows, D. Deming, J.-M. Désert, N. P. Gibson, G. W. Henry, C. M. Huitson, H. A. Knutson, A. Lecavelier Des Etangs, F. Pont, A. P. Showman, A. Vidal-Madjar, M. H. Williamson, and P. A. Wilson. A continuum from clear to cloudy hot-Jupiter exoplanets without primordial water depletion. *Nature*, 529:59–62, January 2016b. doi: 10.1038/nature16068.

J. Skilling. Nested sampling for general Bayesian computation. *Bayesian Analysis*, 1(4):833–860, 2006. doi: 10.1214/06-BA127.

John Skilling. Nested Sampling. *Bayesian Inference and Maximum Entropy Methods in Science and Engineering: 24th International Workshop on Bayesian Inference and Maximum Entropy Methods in Science and Engineering held 25-30 July*, 735:395–405, November 2004.

P. H. Smith and L. R. Doose. Observing Saturn from Pioneer 11. *Sky and Telescope*, 58:405, November 1979.

I. A. G. Snellen, R. J. de Kok, E. J. W. de Mooij, and S. Albrecht. The orbital motion, absolute mass and high-altitude winds of exoplanet HD209458b. *Nature*, 465:1049–1051, June 2010. doi: 10.1038/nature09111.

I A G Snellen, Bernhard R Brandl, R J de Kok, Matteo Brogi, Jayne Birkby, and Henriette Schwarz. Fast spin of the young extrasolar planet β Pictoris b. *Nature*, 509(7):63–65, May 2014.

Ignas A. G. Snellen, Bernhard R. Brandl, Remco J. de Kok, Matteo Brogi, Jayne Birkby, and Henriette Schwarz. Fast spin of the young extrasolar planet β Pictoris b. *Nature*, 509:63–65, May 2014. doi: 10.1038/nature13253.

J. J. Spake, D. K. Sing, T. M. Evans, A. Oklopčić, V. Bourrier, L. Kreidberg, B. V. Rackham, J. Irwin, D. Ehrenreich, A. Wyttenbach, H. R. Wakeford, Y. Zhou, K. L. Chubb, N. Nikolov, J. M. Goyal, G. W. Henry, M. H. Williamson, S. Blumenthal, D. R. Anderson, C. Hellier, D. Charbonneau, S. Udry, and N. Madhusudhan. Helium in the eroding atmosphere of an exoplanet. *Nature*, 557:68–70, May 2018. doi: 10.1038/s41586-018-0067-5.

B.A. Sparkes. *The Red and the Black: Studies in Greek Pottery*. Routledge, 1996. ISBN 9780415126618. URL `https://books.google.it/books?id=3QOhvreYQMIC`.

D. S. Spiegel and A. Burrows. Thermal Processes Governing Hot-Jupiter Radii. *ApJ*, 772:76, July 2013. doi: 10.1088/0004-637X/772/1/76.

D. M. Stam, W. A. de Rooij, G. Cornet, and J. W. Hovenier. Integrating polarized light over a planetary disk applied to starlight reflected by extrasolar planets. *A&A*, 452:669–683, June 2006. doi: 10.1051/0004-6361:20054364.

D. Stark, B. Launet, K. Schawinski, C. Zhang, M. Koss, M. D. Turp, L. F. Sartori, H. Zhang, Y. Chen, and A. K. Weigel. PSFGAN: a generative adversarial network system for separating quasar point sources and host galaxy light. *MNRAS*, 477:2513–2527, June 2018. doi: 10.1093/mnras/sty764.

K. B. Stevenson, J. Harrington, S. Nymeyer, N. Madhusudhan, S. Seager, W. C. Bowman, R. A. Hardy, D. Deming, E. Rauscher, and N. B. Lust. Possible thermochemical disequilibrium in the atmosphere of the exoplanet GJ 436b. *Nature*, 464:1161–1164, April 2010. doi: 10.1038/nature09013.

K. B. Stevenson, J. L. Bean, A. Seifahrt, J.-M. Désert, N. Madhusudhan, M. Bergmann, L. Kreidberg, and D. Homeier. Transmission Spectroscopy of the Hot Jupiter WASP-12b from 0.7 to 5 μm. *AJ*, 147:161, June 2014a. doi: 10.1088/0004-6256/147/6/161.

K. B. Stevenson, J.-M. Désert, M. R. Line, J. L. Bean, J. J. Fortney, A. P. Showman, T. Kataria, L. Kreidberg, P. R. McCullough, G. W. Henry, D. Charbonneau, A. Burrows, S. Seager, N. Madhusudhan, M. H. Williamson, and D. Homeier. Thermal structure of an exoplanet atmosphere from phase-resolved emission spectroscopy. *Science*, 346:838–841, November 2014b. doi: 10.1126/science.1256758.

Kevin B. Stevenson, Jacob L. Bean, Nikku Madhusudhan, and Joseph Harrington. Deciphering the Atmospheric Composition of WASP-12b: A Comprehensive Analysis of its Dayside Emission. *ApJ*, 791:36, August 2014c. doi: 10.1088/0004-637X/791/1/36.

M. Stiavelli and M. Robberto. Performance of the WFC3-IR channel with FPA#64. Technical report, May 2003.

C. Strege, G. Bertone, F. Feroz, M. Fornasa, R. Ruiz de Austri, and R. Trotta. Global fits of the cMSSM and NUHM including the LHC Higgs discovery and new XENON100 constraints. *Journal of Cosmology and Astroparticle Physics*, 4:013, April 2013. doi: 10.1088/1475-7516/2013/04/013.

David Sudarsky, Adam Burrows, and Philip Pinto. Albedo and Reflection Spectra of Extrasolar Giant Planets. *ApJ*, 538:885–903, August 2000. doi: 10.1086/309160.

David Sudarsky, Adam Burrows, and Ivan Hubeny. Theoretical Spectra and Atmospheres of Extrasolar Giant Planets. *ApJ*, 588:1121–1148, May 2003. doi: 10.1086/374331.

G. Suissa, J. Chen, and D. Kipping. A HARDCORE model for constraining an exoplanet's core size. *MNRAS*, 476:2613–2620, May 2018. doi: 10.1093/mnras/sty381.

P. W. Sullivan, J. N. Winn, Z. K. Berta-Thompson, D. Charbonneau, D. Deming, C. D. Dressing, D. W. Latham, A. M. Levine, P. R. McCullough, T. Morton, G. R. Ricker, R. Vanderspek, and D. Woods. The Transiting Exoplanet Survey Satellite: Simulations of Planet Detections and Astrophysical False Positives. *ApJ*, 809:77, August 2015. doi: 10.1088/0004-637X/809/1/77.

M. R. Swain, G. Vasisht, and G. Tinetti. The presence of methane in the atmosphere of an extrasolar planet. *Nature*, 452:329–331, March 2008a. doi: 10.1038/nature06823.

M. R. Swain, G. Vasisht, and G. Tinetti. The presence of methane in the atmosphere of an extrasolar planet. *Nature*, 452:329–331, March 2008b. doi: 10.1038/nature06823.

M. R. Swain, G. Tinetti, G. Vasisht, P. Deroo, C. Griffith, J. Bouwman, P. Chen, Y. Yung, A. Burrows, L. R. Brown, J. Matthews, J. F. Rowe, R. Kuschnig, and D. Angerhausen. Water, Methane, and Carbon Dioxide Present in the Dayside Spectrum of the Exoplanet HD 209458b. *ApJ*, 704:1616–1621, October 2009. doi: 10.1088/0004-637X/704/2/1616.

Christian Szegedy, Alexander Toshev, and Dumitru Erhan. Deep neural networks for object detection. In C. J. C. Burges, L. Bottou, M. Welling, Z. Ghahramani, and K. Q. Weinberger, editors, *Advances in Neural Information Processing Systems 26*, pages 2553–2561. Curran Associates, Inc., 2013. URL `http://papers.nips.cc/paper/5207-deep-neural-networks-for-object-detection.pdf`.

D.W. Tandy. *Works and Days: A Translation and Commentary for the Social Sciences*. University of California Press, 1997. ISBN 9780520917354. URL https://books.google.it/books?id=sHkgON1Gr1wC.

J. Tennyson, S. N. Yurchenko, A. F. Al-Refaie, E. J. Barton, K. L. Chubb, P. A. Coles, S. Diamantopoulou, M. N. Gorman, C. Hill, A. Z. Lam, L. Lodi, L. K. McKemmish, Y. Na, A. Owens, O. L. Polyansky, T. Rivlin, C. Sousa-Silva, D. S. Underwood, A. Yachmenev, and E. Zak. The ExoMol database: Molecular line lists for exoplanet and other hot atmospheres. *Journal of Molecular Spectroscopy*, 327:73–94, September 2016. doi: 10.1016/j.jms.2016.05.002.

R. J. Terrile, W. Fink, T. Huntsberger, S. Lee, E. R. Tisdale, G. Tinetti, and P. von Allmen. Retrieval of Extra-Solar Planetary Spectra Using Evolutionary Computational Methods. In *AAS/Division for Planetary Sciences Meeting Abstracts #37*, volume 37 of *Bulletin of the American Astronomical Society*, page 1566, December 2005.

M. Tessenyi, G. Savini, G. Tinetti, J. Tennyson, M. Dhesi, and M. Joshua. TWINKLE - A Low Earth Orbit Visible and Infrared Exoplanet Spectroscopy Observatory. In *Revista Mexicana de Astronomia y Astrofisica Conference Series*, volume 49 of *Revista Mexicana de Astronomia y Astrofisica, vol. 27*, pages 148–148, July 2017.

A. Tettamanzi, J. Janßen, and M. Tomassini. *Soft Computing: Integrating Evolutionary, Neural, and Fuzzy Systems*. Studies in fuzziness and soft computing. Springer, 2001. ISBN 9783540422044. URL https://books.google.it/books?id=86jQw6v30KoC.

G. Tinetti, A. Vidal-Madjar, M.-C. Liang, J.-P. Beaulieu, Y. Yung, S. Carey, R. J. Barber, J. Tennyson, I. Ribas, N. Allard, G. E. Ballester, D. K. Sing, and F. Selsis. Water vapour in the atmosphere of a transiting extrasolar planet. *Nature*, 448:169–171, July 2007. doi: 10.1038/nature06002.

G. Tinetti, P. Deroo, M. R. Swain, C. A. Griffith, G. Vasisht, L. R. Brown, C. Burke, and P. McCullough. Probing the Terminator Region Atmosphere of the Hot-Jupiter XO-1b with Transmission Spectroscopy. *ApJ*, 712:L139–L142, April 2010. doi: 10.1088/2041-8205/712/2/L139.

G. Tinetti, J. Tennyson, C. A. Griffith, and I. Waldmann. Water in exoplanets. *Philosophical Transactions of the Royal Society of London Series A*, 370:2749–2764, June 2012. doi: 10.1098/rsta.2011.0338.

G. Tinetti, P. Drossart, P. Eccleston, P. Hartogh, A. Heske, J. Leconte, G. Micela, M. Ollivier, G. Pilbratt, L. Puig, D. Turrini, B. Vandenbussche, P. Wolkenberg, E. Pascale, J. P.

Beaulieu, M. Güdel, M. Min, M. Rataj, T. Ray, I. Ribas, J. Barstow, N. Bowles, A. Coustenis, V. Coudé du Foresto, L. Decin, T. Encrenaz, F. Forget, M. Friswell, M. Griffin, P. O. Lagage, P. Malaguti, A. Moneti, J. C. Morales, E. Pace, M. Rocchetto, S. Sarkar, F. Selsis, W. Taylor, J. Tennyson, O. Venot, I. P. Waldmann, G. Wright, T. Zingales, and M. R. Zapatero-Osorio. The science of ARIEL (Atmospheric Remote-sensing Infrared Exoplanet Large-survey). In *Space Telescopes and Instrumentation 2016: Optical, Infrared, and Millimeter Wave*, volume 9904, page 99041X, July 2016. doi: 10.1117/12.2232370.

G. Tinetti, P. Drossart, P. Eccleston, P. Hartogh, A. Heske, J. Leconte, G. Micela, M. Ollivier, G. Pilbratt, L. Puig, and et al. A chemical survey of exoplanets with ARIEL. *Experimental Astronomy*, September 2018. doi: 10.1007/s10686-018-9598-x.

Kamen O Todorov, D Deming, H A Knutson, A Burrows, J Fortney, Nikole K Lewis, N B Cowan, Eric Agol, Jean-Michel Desert, Pedro V Sada, D Charbonneau, Gregory Laughlin, Jonathan Langton, and Adam P Showman. Warm Spitzer Photometry of Three Hot Jupiters: HAT-P-3b, HAT-P-4b and HAT-P-12b. *ApJ*, 770(2):102, June 2013.

G. Torres, J. N. Winn, and M. J. Holman. Improved Parameters for Extrasolar Transiting Planets. *ApJ*, 677:1324–1342, April 2008a. doi: 10.1086/529429.

G. Torres, J. N. Winn, and M. J. Holman. Improved Parameters for Extrasolar Transiting Planets. *ApJ*, 677:1324-1342, April 2008b. doi: 10.1086/529429.

A. H. M. J. Triaud, A. A. Lanotte, B. Smalley, and M. Gillon. Colour-magnitude diagrams of transiting Exoplanets - II. A larger sample from photometric distances. *MNRAS*, 444:711–728, October 2014. doi: 10.1093/mnras/stu1416.

A. H. M. J. Triaud, M. Gillon, D. Ehrenreich, E. Herrero, M. Lendl, D. R. Anderson, A. Collier Cameron, L. Delrez, B.-O. Demory, C. Hellier, K. Heng, E. Jehin, P. F. L. Maxted, D. Pollacco, D. Queloz, I. Ribas, B. Smalley, A. M. S. Smith, and S. Udry. WASP-80b has a dayside within the T-dwarf range. *MNRAS*, 450:2279–2290, July 2015. doi: 10.1093/mnras/stv706.

R. Trotta. Applications of Bayesian model selection to cosmological parameters. *MNRAS*, 378: 72–82, June 2007. doi: 10.1111/j.1365-2966.2007.11738.x.

R. Trotta. Bayes in the sky: Bayesian inference and model selection in cosmology. *Contemporary Physics*, 49:71–104, March 2008. doi: 10.1080/00107510802066753.

A. Tsiaras, M. Rocchetto, I. P. Waldmann, O. Venot, R. Varley, G. Morello, M. Damiano, G. Tinetti, E. J. Barton, S. N. Yurchenko, and J. Tennyson. Detection of an Atmosphere

Around the Super-Earth 55 Cancri e. *ApJ*, 820:99, April 2016a. doi: 10.3847/0004-637X/820/2/99.

A. Tsiaras, M. Rocchetto, I. P. Waldmann, O. Venot, R. Varley, G. Morello, M. Damiano, G. Tinetti, E. J. Barton, S. N. Yurchenko, and J. Tennyson. Detection of an Atmosphere Around the Super-Earth 55 Cancri e. *ApJ*, 820:99, April 2016b. doi: 10.3847/0004-637X/820/2/99.

A. Tsiaras, I. P. Waldmann, M. Rocchetto, R. Varley, G. Morello, M. Damiano, and G. Tinetti. A New Approach to Analyzing HST Spatial Scans: The Transmission Spectrum of HD 209458 b. *ApJ*, 832:202, December 2016c. doi: 10.3847/0004-637X/832/2/202.

A. Tsiaras, I. P. Waldmann, T. Zingales, M. Rocchetto, G. Morello, M. Damiano, K. Karpouzas, G. Tinetti, L. K. McKemmish, J. Tennyson, and S. N. Yurchenko. A Population Study of Gaseous Exoplanets. *AJ*, 155:156, April 2018. doi: 10.3847/1538-3881/aaaf75.

Ayşegül Uçar, Yakup Demir, and Cüneyt Güzeliş. Object recognition and detection with deep learning for autonomous driving applications. *SIMULATION*, 93(9):759–769, 2018/07/04 2017. doi: 10.1177/0037549717709932. URL `https://doi.org/10.1177/0037549717709932`.

D. Ulyanov, A. Vedaldi, and V. Lempitsky. It Takes (Only) Two: Adversarial Generator-Encoder Networks. *ArXiv e-prints*, April 2017.

D. Valencia. Internal Structure and Evolution of Super-Earths. In *American Astronomical Society Meeting Abstracts*, volume 39 of *Bulletin of the American Astronomical Society*, page 858, December 2007.

D. Valencia, D. D. Sasselov, and R. J. O'Connell. Detailed Models of Super-Earths: How Well Can We Infer Bulk Properties? *ApJ*, 665:1413–1420, August 2007. doi: 10.1086/519554.

D. Valencia, T. Guillot, V. Parmentier, and R. S. Freedman. Bulk Composition of GJ 1214b and Other Sub-Neptune Exoplanets. *ApJ*, 775:10, September 2013. doi: 10.1088/0004-637X/775/1/10.

AÃđron van den Oord, Yazhe Li, Igor Babuschkin, Karen Simonyan, Oriol Vinyals, Koray Kavukcuoglu, George van den Driessche, Edward Lockhart, Luis Carlos Cobo Rus, Florian Stimberg, Norman Casagrande, Dominik Grewe, Seb Noury, Sander Dieleman, Erich Elsen, Nal Kalchbrenner, Heiga Zen, Alexander Graves, Helen King, Thomas Walters, Dan Belov, and Demis Hassabis. Parallel wavenet: Fast high-fidelity speech synthesis. Technical report, Google Deepmind, 2017. URL `https://arxiv.org/abs/1711.10433`.

O. Venot, E. Hébrard, M. Agúndez, M. Dobrijevic, F. Selsis, F. Hersant, N. Iro, and R. Bounaceur. A chemical model for the atmosphere of hot Jupiters. *A&A*, 546:A43, October 2012. doi: 10.1051/0004-6361/201219310.

von Paris, P., Gratier, P., BordÃľ, P., Leconte, J., and Selsis, F. Inferring asymmetric limb cloudiness on exoplanets from transit light curves. *A&A*, 589:A52, 2016. doi: 10.1051/0004-6361/201527894. URL `https://doi.org/10.1051/0004-6361/201527894`.

H. R. Wakeford, D. K. Sing, D. Deming, N. P. Gibson, J. J. Fortney, A. S. Burrows, G. Ballester, N. Nikolov, S. Aigrain, G. Henry, H. Knutson, A. Lecavelier des Etangs, F. Pont, A. P. Showman, A. Vidal-Madjar, and K. Zahnle. HST hot Jupiter transmission spectral survey: detection of water in HAT-P-1b from WFC3 near-IR spatial scan observations. *MNRAS*, 435: 3481–3493, November 2013. doi: 10.1093/mnras/stt1536.

H. R. Wakeford, K. B. Stevenson, N. K. Lewis, D. K. Sing, M. López-Morales, M. Marley, T. Kataria, A. Mandell, G. E. Ballester, J. Barstow, L. Ben-Jaffel, V. Bourrier, L. A. Buchhave, D. Ehrenreich, T. Evans, A. García Muñoz, G. Henry, H. Knutson, P. Lavvas, A. Lecavelier des Etangs, N. Nikolov, and J. Sanz-Forcada. HST PanCET program: A Cloudy Atmosphere for the Promising JWST Target WASP-101b. *ApJ*, 835:L12, January 2017. doi: 10.3847/2041-8213/835/1/L12.

I. P. Waldmann. Dreaming of Atmospheres. *ApJ*, 820:107, April 2016. doi: 10.3847/0004-637X/820/2/107.

I. P. Waldmann, M. Rocchetto, G. Tinetti, E. J. Barton, S. N. Yurchenko, and J. Tennyson. Tau-REx II: Retrieval of Emission Spectra. *ApJ*, 813:13, November 2015a. doi: 10.1088/0004-637X/813/1/13.

I. P. Waldmann, G. Tinetti, M. Rocchetto, E. J. Barton, S. N. Yurchenko, and J. Tennyson. Tau-REx I: A Next Generation Retrieval Code for Exoplanetary Atmospheres. *ApJ*, 802:107, April 2015b. doi: 10.1088/0004-637X/802/2/107.

G. A. H. Walker, A. R. Walker, A. W. Irwin, A. M. Larson, and S. L. S. Yang. Intriguing, low-amplitude periodicity in the radial velocities of δ Sagittarii. In B. J. Butler and D. O. Muhleman, editors, *Bulletin of the American Astronomical Society*, volume 27 of *Bulletin of the AAS*, page 1430, December 1995.

D. Q. Wark. On Indirect Temperature Soundings of the Stratosphere from Satellites. *Journal of Geophysics Research*, 66:77–82, January 1961. doi: 10.1029/JZ066i001p00077.

D. Q. Wark. SIRS: An experiment to measure the free air temperature from a satellite. *Applied Optics*, 9:1761–1766, 1970. doi: 10.1364/AO.9.001761.

L. M. Weiss, G. W. Marcy, J. F. Rowe, A. W. Howard, H. Isaacson, J. J. Fortney, N. Miller, B.-O. Demory, D. A. Fischer, E. R. Adams, A. K. Dupree, S. B. Howell, R. Kolbl, J. A. Johnson, E. P. Horch, M. E. Everett, D. C. Fabrycky, and S. Seager. The Mass of KOI-94d and a Relation for Planet Radius, Mass, and Incident Flux. *ApJ*, 768:14, May 2013. doi: 10.1088/0004-637X/768/1/14.

M. W. Werner, T. L. Roellig, F. J. Low, G. H. Rieke, M. Rieke, W. F. Hoffmann, E. Young, J. R. Houck, B. Brandl, G. G. Fazio, J. L. Hora, R. D. Gehrz, G. Helou, B. T. Soifer, J. Stauffer, J. Keene, P. Eisenhardt, D. Gallagher, T. N. Gautier, W. Irace, C. R. Lawrence, L. Simmons, J. E. Van Cleve, M. Jura, E. L. Wright, and D. P. Cruikshank. The Spitzer Space Telescope Mission. *The Astrophysical Journal Supplement Series*, 154:1–9, September 2004. doi: 10.1086/422992.

R. G. West, C. Hellier, J.-M. Almenara, D. R. Anderson, S. C. C. Barros, F. Bouchy, D. J. A. Brown, A. Collier Cameron, M. Deleuil, L. Delrez, A. P. Doyle, F. Faedi, A. Fumel, M. Gillon, Y. Gómez Maqueo Chew, G. Hébrard, E. Jehin, M. Lendl, P. F. L. Maxted, F. Pepe, D. Pollacco, D. Queloz, D. Ségransan, B. Smalley, A. M. S. Smith, J. Southworth, A. H. M. J. Triaud, and S. Udry. Three irradiated and bloated hot Jupiters:. WASP-76b, WASP-82b, and WASP-90b. *A&A*, 585:A126, January 2016. doi: 10.1051/0004-6361/201527276.

Peter J. Wheatley, Andrew Collier Cameron, Joseph Harrington, Jonathan J. Fortney, James M. Simpson, David R. Anderson, Alexis M. S. Smith, Suzanne Aigrain, William I. Clarkson, Michael Gillon, Carole A. Haswell, Leslie Hebb, Guillaume Hébrard, Coel Hellier, Simon T. Hodgkin, Keith D. Horne, Stephen R. Kane, Pierre F. L. Maxted, Andrew J. Norton, Don L. Pollacco, Frederic Pont, Ian Skillen, Barry Smalley, Rachel A. Street, Stephane Udry, Richard G. West, and David M. Wilson. The thermal emission of the exoplanets WASP-1b and WASP-2b. *ArXiv e-prints*, art. arXiv:1004.0836, April 2010.

M. J. White and F. Feroz. MSSM dark matter measurements at the LHC without squarks and sleptons. *Journal of High Energy Physics*, 7:64, July 2010. doi: 10.1007/JHEP07(2010)064.

J. N. Winn. Transits and Occultations. *ArXiv e-prints*, January 2010.

A. Wolszczan and D. A. Frail. A planetary system around the millisecond pulsar PSR1257 + 12. *Nature*, 355:145–147, January 1992. doi: 10.1038/355145a0.

Y. Wu, M. Schuster, Z. Chen, Q. V. Le, M. Norouzi, W. Macherey, M. Krikun, Y. Cao, Q. Gao, K. Macherey, J. Klingner, A. Shah, M. Johnson, X. Liu, Ł. Kaiser, S. Gouws, Y. Kato, T. Kudo, H. Kazawa, K. Stevens, G. Kurian, N. Patil, W. Wang, C. Young, J. Smith, J. Riesa, A. Rudnick, O. Vinyals, G. Corrado, M. Hughes, and J. Dean. Google's Neural Machine Translation System: Bridging the Gap between Human and Machine Translation. *ArXiv e-prints*, September 2016.

S. Xiang and H. Li. On the Effects of Batch and Weight Normalization in Generative Adversarial Networks. *ArXiv e-prints*, April 2017.

G. Yamamoto and D. Q. Wark. Discussion of the Letter by R. A. Hanel, 'Determination of Cloud Altitude from a Satellite'. *Journal of Geophysics Research*, 66:3596–3596, October 1961. doi: 10.1029/JZ066i010p03596.

Ke Yan, Yaowei Wang, Dawei Liang, Tiejun Huang, and Yonghong Tian. Cnn vs. sift for image retrieval: Alternative or complementary? In *Proceedings of the 2016 ACM on Multimedia Conference*, pages 407–411. ACM, 2016.

R. A. Yeh, C. Chen, T. Yian Lim, A. G. Schwing, M. Hasegawa-Johnson, and M. N. Do. Semantic Image Inpainting with Deep Generative Models. *ArXiv e-prints*, July 2016.

S. N. Yurchenko and J. Tennyson. ExoMol line lists - IV. The rotation-vibration spectrum of methane up to 1500 K. *MNRAS*, 440:1649–1661, May 2014. doi: 10.1093/mnras/stu326.

S. N. Yurchenko, R. J. Barber, and J. Tennyson. A variationally computed line list for hot NH_3. *MNRAS*, 413:1828–1834, May 2011. doi: 10.1111/j.1365-2966.2011.18261.x.

K. Zahnle, M. S. Marley, R. S. Freedman, K. Lodders, and J. J. Fortney. Atmospheric Sulfur Photochemistry on Hot Jupiters. *ApJ*, 701:L20–L24, August 2009. doi: 10.1088/0004-637X/701/1/L20.

Robert T Zellem, Caitlin A Griffith, P Deroo, Mark Swain, and I Waldmann. The Ground-based H-, K-, and L-band Absolute Emission Spectra of HD 209458b. *ApJ*, 796(1):48, November 2014.

Robert T. Zellem, Caitlin A. Griffith, Pieter Deroo, Mark R. Swain, and Ingo P. Waldmann. The Ground-based H-, K-, and L-band Absolute Emission Spectra of HD 209458b. *ApJ*, 796: 48, November 2014. doi: 10.1088/0004-637X/796/1/48.

Shanshan Zhang, Rodrigo Benenson, Bernt Schiele, et al. Filtered channel features for pedestrian detection. In *CVPR*, volume 1, page 4, 2015.

Y. T. Zhou and R. Chellappa. Computation of optical flow using a neural network. In *IEEE 1988 International Conference on Neural Networks*, pages 71–78 vol.2, July 1988. doi: 10.1109/ICNN.1988.23914.

Jun-Yan Zhu, Taesung Park, Phillip Isola, and Alexei A Efros. Unpaired image-to-image translation using cycle-consistent adversarial networkss. In *Computer Vision (ICCV), 2017 IEEE International Conference on*, 2017.

T. Zingales and I. P. Waldmann. ExoGAN: Retrieving Exoplanetary Atmospheres Using Deep Convolutional Generative Adversarial Networks. *AJ*, June 2018. doi: 10.3847/1538-3881/aae77c. URL `https://doi.org/10.3847/1538-3881/aae77c`.

Tiziano Zingales, Giovanna Tinetti, Ignazio Pillitteri, Jérémy Leconte, Giuseppina Micela, and Subhajit Sarkar. The ariel mission reference sample. *Experimental Astronomy*, Feb 2018. ISSN 1572-9508. doi: 10.1007/s10686-018-9572-7. URL `https://doi.org/10.1007/s10686-018-9572-7`.

Y. Zuo, G. Avraham, and T. Drummond. Generative Adversarial Forests for Better Conditioned Adversarial Learning. *ArXiv e-prints*, May 2018.